

Quantum Optomechanics with Silicon Nanostructures

Thesis by
Amir H. Safavi-Naeini

In Partial Fulfillment of the Requirements
for the Degree of
Doctor of Philosophy



California Institute of Technology
Pasadena, California

2013
(Defended May 21st, 2013)

© 2013

Amir H. Safavi-Naeini

All Rights Reserved

For maman, baba, and all who have taught me.

Acknowledgments

I'm not sure if I'll ever be able to properly thank Oskar for his caring guidance and instruction. Perhaps these debts are best paid forward, by some day guiding other young scientists through their journeys. If I were to choose one aspect of my interactions with Oskar as most important and effective, it would be his encouragement to pursue ideas that seemed crazy. There were many instances where I would try something, only because he, with his sharp physical intuition, for which I have always had enormous respect, believed it might work. Such encouragement, in the truest sense of the word, has been the key to our success. Oskar helped us muster the courage to try things that were crazy, and supported us in substantial ways through the ensuing struggles. In retrospect, many of these ideas are no longer crazy. To quote Batman, "everything is impossible, until someone does it".

There are other teachers, scientists, and engineers who have trained me over the years. There are those who left their mark long before I started at Caltech. I thank my mother and father for teaching me the importance of education, by devoting themselves to me and my brother, and providing us with whatever book, magazine, telescope, chemistry set, and computer program we fancied. I thank my father for spending those lazy afternoons lying around the living room talking about math and physics. I remember you slogging through words and equations trying to get me to understand Coulomb's law and how it follows just a few general concepts. When you were done, I *intuitively* understood for the first time that there was a logical structure in mathematics that was beautiful, and that could explain everything around us. I remember the feeling of clarity and power that followed, knowing that it all boils down to just a few equations solvable by even a clever high school student. I thank my high school math teacher Michael J. Burns, who made math class the one we always looked forward to ("Done like dinner!"), and who would spend his lunch breaks enjoying a sandwich while talking to us about general relativity and black holes.

During my time at the University of Waterloo, I thank the following people: Phat Tran, my supervisor at RIM (now Blackberry), for teaching me how to write good code. Amir Khandani, for letting me learn information theory in his lab. Giuseppe Tenti, for making math fun. Joseph Emerson, for letting me into his advanced quantum mechanics class. Norbert Lütkenhaus for his excellent instruction of electromagnetics and relativity. Omar Ramahi for teaching me that if you

want people to believe your simulations, you need to make the darn thing and test it. Hamed Majedi and Gregor Weihs, for getting me into optics and quantum information.

At Caltech, I owe Oskar and the generations of previous graduate students who built the clean-room: Tom Johnson, Matt Borselli, Paul Barclay, Kartik Srinivasan. I owe Raviv Perahia for teaching me fabrication. I owe Thiago Alegre for re-teaching me (and teaching me much more...), and Jeff Hill for re-re-teaching me (while helping keep my life in order, among other things). Thank you, Matt Eichenfield for inventing optomechanical crystals, Alex Krause for science (in general), Jasper Chan for being such an amazing hacker, Simon Gröblacher for always getting things to work somehow, Qiang Lin for those late night discussions. I benefited greatly from an environment that had people like Klemens Hammerer, Aashish Clerk, Florian Marquardt, and Markus Aspelmeyer, passing through, imparting wisdom and excitement. Thank you Darrick Chang for showing me what's important, and what's not. Thank you Ryan Camacho, Dennis Callahan, and Tim Blasius for putting up with my messy desk and random outbursts. Thank you Sean Meenehan for those factors of two. Thanks Justin Cohen, Martin Winger, Tao Paraiso, Chris Michael, and others I've surely forgotten to thank. Michel van Garrel, you're an excellent house-mate, thanks for dragging me to the LA Opera all those times, and introducing me to Chopin. Thank you Ari Weinstein for getting me to play soccer.

Kasra, thanks for being a great brother. I couldn't have asked for more.

To my wonderful and lovely girlfriend, Kirsi Muona, thank you for getting me through it all. I'm not sure what I did to deserve you.

Abstract

Mechanical resonators are the most basic and ubiquitous physical systems known. In on-chip form, they are used to process high frequency signals in every cell phone, television, and laptop. They have also been in the last few decades in different shapes and forms, a critical part of progress in quantum information sciences with kilogram-scale mirrors for gravitational wave detection measuring motion at its quantum limits, and the motion of single ions being used to link qubits for quantum computation.

Optomechanics is a field primarily concerned with coupling light to the motion of mechanical structures. This thesis contains descriptions of recent work with mechanical systems in the megahertz to gigahertz frequency range, formed by nanofabricating novel photonic/phononic structures on a silicon chip. These structures are designed to have both optical and mechanical resonances, and laser light is used to address and manipulate their motional degrees of freedom through radiation pressure forces. We laser cool these mechanical resonators to their ground states, and observe for the first time the quantum zero-point motion of a nanomechanical resonator. Conversely, we show that engineered mechanical resonances drastically modify the optical response of our structures, creating large effective optical nonlinearities not present in bulk silicon. We experimentally demonstrate aspects of these nonlinearities by proposing and observing “electromagnetically induced transparency” and light slowed down to 6 m/s, as well as wavelength conversion, and generation of nonclassical optical radiation. Finally, the application of optomechanics to longstanding problems in quantum and classical communications are proposed and investigated.

Contents

Acknowledgments	v
Abstract	vii
List of Figures	xiii
Preface	xv
1 Introduction to linearized optomechanical systems	1
1.1 Quantum description of the optomechanical system	1
1.1.1 Maxwell's equations for a photonic resonator and second quantization	1
1.1.2 Mechanical waves and their quantization	3
1.1.3 Optomechanical Coupling	5
1.1.3.1 Perturbation theory of dielectric cavities	5
1.1.3.2 Boundary perturbation	7
1.1.3.3 Photoelastic coupling	8
1.1.4 Vacuum coupling rate	8
1.2 Lossy optical and mechanical resonators	9
1.2.1 An optical cavity loaded by a waveguide	9
1.2.1.1 Waveguide-Cavity Interaction	9
1.2.1.2 Markov Approximation	10
1.2.1.3 Relation to Transmission-Line Theory	11
1.2.1.4 Relation to Coupled Mode Theory	12
1.2.2 Intrinsic and extrinsic losses	12
1.2.3 Mechanical resonators	14
1.3 Dynamical back-action in the Heisenberg-Langevin picture	14
1.4 Simplified results for sideband-resolved systems	15
1.4.1 Quantum-limited laser cooling and damping	15

2	Quantum and classical noise in optomechanical systems	19
2.1	The basic ideas	20
2.1.1	Measuring position with light	20
2.1.2	Interference effects	21
2.1.3	Electromagnetically induced transparency in optomechanics	21
2.1.4	Classical laser noise in thermometry: squashing and anti-squashing	22
2.1.5	Quantum back-action interference and Squeezing	24
2.2	Sideband-resolved systems	25
2.2.1	Electromagnetically induced transparency and amplification	25
2.2.1.1	Electromagnetically induced transparency	26
2.2.1.2	Group delay	27
2.2.1.3	Electromagnetically induced absorption and amplification	29
2.2.2	Thermometry using the detected photocurrent	29
2.2.2.1	Interpretation as quantum noise squashing	31
2.2.3	Motional sideband asymmetry thermometry	32
2.2.4	Laser phase noise	34
2.2.4.1	Heating	35
2.2.4.2	Effect on calibrated cooling beam thermometry	36
2.2.4.3	Effect on sideband asymmetry thermometry	39
2.3	Sideband-unresolved systems	40
2.3.1	Approximate quasi-static theory	41
2.3.2	The effect of dynamics and the correlations between shot-noise and position	43
2.3.3	General derivation of squeezing	45
2.3.3.1	The effect of imperfect optical coupling and inefficient detection	47
3	Thin-film phononic and photonic nanostructures	49
3.1	The basic ideas	49
3.1.1	Construction of a photonic crystal cavity	49
3.1.2	Phononic bandgaps	50
3.2	Full bandgap phononic crystal designs [1]	51
3.2.1	Origin of the gap: from effective medium to tight-binding	52
3.2.2	Quasi-1D phononic tight-binding bands: symmetry and dispersion in a toy model	53
3.2.3	Quasi-2D “Cross” crystal	55
3.2.4	Quasi-2D “Snowflake” crystal	57
3.3	Phononic crystal resonators and waveguides	59

3.3.1	Experimental verification of cross phononic crystal properties	59
3.3.2	Design of snowflake phononic-photonic crystal waveguides and resonators . .	64
3.3.2.1	Waveguide Design	64
3.3.2.2	Optomechanical Coupling Relations	68
3.3.2.3	Snowflake Optomechanical Cavity Design	70
3.4	Thermal noise spectroscopy of micromechanical resonators	72
3.4.1	Phenomenological dispersive noise model: the effect of structural damping . .	73
3.4.2	Phenomenological absorptive noise model	74
4	Quasi-two-dimensional silicon optomechanical resonators	77
4.1	Two-dimensional slotted photonic crystal cavities [1]	77
4.2	Optomechanics of a simultaneous bandgap phononic-photonic crystal	81
5	Main experimental results	85
5.1	Electromagnetically induced transparency and slow light with optomechanics [2] . .	85
5.2	Detection of zero-point motion [3]	92
5.2.1	Role of phase noise in measurement	99
5.3	Observation of squeezed light from an optomechanical resonator [4]	101
5.3.1	Measurement of optical losses	110
5.3.2	Data collection procedure	111
5.3.3	Relation between detuning and quadrature	111
5.3.4	Locking the cavity	113
6	Optomechanical System Proposals	115
6.1	The basic ideas	115
6.1.1	Red-side driving and state transfer	115
6.1.2	Optical damping rate in the weak-coupling regime	115
6.1.3	Matching to mechanical loss channels	116
6.1.4	Dynamic tuning of polaritons	117
6.2	Proposal for an optomechanical phonon-photon translator [5]	118
6.2.1	Photons and phonons on a chip	119
6.2.2	Optomechanical crystal implementation proposal	122
6.2.3	Detailed analysis of wavelength conversion [6]	124
6.2.4	Efficiency, Bandwidth, and Noise	127
6.3	Proposal for an optomechanical quantum memory [7]	129
6.3.1	Description of the system	130
6.3.2	Derivation of dispersion relation	130

6.3.3	Fractional Occupation Calculation	133
6.3.4	Slowing and stopping light	133
6.3.5	Storage of optical pulse	134
6.3.6	Optomechanical crystal implementation	135
A	Mathematical Definitions and Derivations	137
A.1	Definitions	137
A.2	Mechanical resonator spectral density	138
A.3	Quantum noise squashing	139
A.4	Scattering matrix elements	140
A.4.1	Red-side driving: $\Delta = \omega_m$	141
A.4.2	Blue-side driving: $\Delta = -\omega_m$	141
B	Characterization of laser phase noise in semiconductor diode lasers	143
B.1	Laser phase noise measurement at megahertz frequencies	143
B.1.1	Homodyne measurement with laser noise	143
B.1.1.1	Without optical cavity	143
B.1.1.2	With optical cavity	145
B.1.2	Measurement and characterization of laser noise	145
B.2	Laser phase noise measurement at gigahertz frequencies	147
B.2.1	Phase noise calibration	148
C	Definitions	151
C.1	Acronyms	151
D	Publications	153
	Bibliography	156

List of Figures

1.1	Optical coupling schemes	13
2.1	Detection of motion with an optomechanical system	20
2.2	Electromagnetically Induced Transparency in an Optomechanical System	21
2.3	Classical laser noise in a sideband-resolved optomechanical system	23
2.4	Squeezed light from a sideband-unresolved optomechanical system	24
2.5	Squashing and anti-squashing in calibrated mode thermometry	37
2.6	Squeezing theory	41
3.1	Construction of a photonic crystal cavity	50
3.2	A one-dimensional phononic crystal	52
3.3	Tight-binding 1D phononic crystal bands	54
3.4	The crosses crystal	56
3.5	Cross gap maps	57
3.6	The snowflake crystal	58
3.7	Snowflake gap maps	59
3.8	Optomechanical heterostructure with separate confinement for phonons and photons .	60
3.9	Tuning the “cross” lattice	61
3.10	Experimental and theoretical mode maps on a “cross” phononic crystal	63
3.11	Linear and point defect cavity designs on a snowflake lattice	64
3.12	Photonic and phononic snowflake waveguide band diagrams	65
3.13	Optical and mechanical waveguide designs on the snowflake crystal	67
3.14	Optical and mechanical simulations of co-localized photons and phonons on the snowflake crystal	71
3.15	Noise model and experimental results for zipper cavity	74
3.16	Power spectral density of noise contributions with varying powers	75
4.1	Optical and mechanical simulations of slotted photonic crystal cavity	78
4.2	Optical and mechanical spectroscopy of the slotted photonic crystal cavity	80
4.3	Fabricated snowflake cavity and mode profiles	82

4.4	Mechanical Spectroscopy of Snowflake Cavities	83
5.1	Optomechanical System	86
5.2	Optical Reflection Response ($T = 8.7$ K)	89
5.3	Measured Temporal Shifts and Amplification	90
5.4	Device used for sideband asymmetry measurement	93
5.5	Schematic of the experimental set-up	94
5.6	Two-shot detection method	95
5.7	Experimental Result	97
5.8	Ruling out phase-noise in sideband asymmetry measurements	99
5.9	Optomechanical device	105
5.10	Experimental setup and device characterization	106
5.11	Optomechanical squeezing of light	107
5.12	Spectral and power dependence of noise	109
5.13	Detuning and phase lock points	112
6.1	Emergence of polaritons in optomechanical arrays	117
6.2	Scattering matrix elements for phonon-photon translator	120
6.3	Proposed optomechanical crystal implementation	123
6.4	Response of optomechanical array element	130
6.5	Illustration of band structure of optomechanical crystal array	131
6.6	Simulated band structure of optomechanical crystal array	136
B.1	Laser noise characterization	146
B.2	High-frequency phase noise measurement setup	149
B.3	High-frequency phase noise measurements	150
B.4	Contributions to measured frequency noise results	150

Preface

Beginnings

I met Oskar Painter briefly in the February 2008, after a sleepless thirty-hour journey from beautiful Switzerland. My memory of the event is anything but clear, but there is ample evidence of both my initial infatuation with his research, and his willingness to take me on despite a less-than-stellar first meeting. My first email to him set the stage of many more incoherent emails:

February 17, 2008

Hi Prof Painter

During my meeting with you on Friday you mentioned a type of non-linear effect you have been studying. I didn't understand very much then. I was wondering if there is some literature I could look at regarding this particular effect.

Thanks, Amir

To which I received a typically kind response starting with:

February 18, 2008

Hello Amir,

Thank you for making the long trip to Caltech. I know the flight took its toll...

When I finally arrived a few months later in June 2008, I was well rested and ready to dive into the research. Within the first week, I had been paired with Raviv Perahia, a senior graduate student working on metallo-dielectric structures in the context of lasing. The hours were long, but I quickly learned the basics of every tool in the cleanroom largely thanks to Raviv's deep knowledge and systematic technique. I vividly remember taking a day off to visit Santa Monica beach for the first time with Kirsi and her sister, Kaisa, and taking with me a copy of Hitachi scanning electron microscope manual. Oskar provided me with leeway to work on the aspects of the project I found interesting and I rapidly gravitated towards the theory side. Lasers, and the lasing "phase transition" are fundamentally interesting as the system size is reduced in a nanofabricated structure and I was ambitious enough to try understand these effects. After a few weeks, we were joined by Thiago

Alegre, a post-doc from Brazil, and Raviv’s project moved more into the measurement phase. This involved long days of experiments in a vacuum chamber and significant amounts of data processing.

In the midst of all this excitement, the school year was starting, and new students had arrived. This is when I met Jeff Hill again, and managed to convince him that Oskar’s lab was the place to be. Jeff and I were soon paired and assigned a different project, working on nitrogen-vacancy centers together. This involved taking over a confocal microscopy set-up from Alex Krause, a summer student from Boston University with impenetrable handwriting who would later join us as a grad student. Jeff and I would work on this project a couple of days a week in the lab, often with Oskar helping us align and make measurements.

Dipping my feet into the waters of optomechanics

Around this time, there was also a significant amount of excitement in the lab with optical forces in nanostructures, with graduate students Matt Eichenfield and Jasper Chan working on photonic crystals, and post-doc Qiang Lin working on double-disk structures. The excitement and the intensity of people who were part of this work largely kept me away. I was however interested in understanding how the zipper structures worked, but the group had no papers on these results, and I found the treatment in the literature opaque. There was jargon I didn’t quite understand like gradient and scattering forces, as well as words that were constantly used (like “transduction”), which were unfamiliar to me at the time. One night, I simply started from the beginning. I wrote down what I understood of the zipper experiment, that there are two optical modes (one on each beam), and a mechanical mode (modulating the distance between the beams). I assumed that the motion modulates the coupling between the two optical modes in a roughly linear fashion. The problem was reduced, and now looked like the atom-cavity system I was used to from my studies of cavity QED. After a few approximations (which were wildly incorrect for the actual zipper experiment), I could convince myself fairly easily that cooling, and spring shifts were possible. I could also see how a simple state transfer protocol involving pulses could convert the state of the cavity to motion, and back. The beginning of 2009 started with a new effort by Matt and Jasper to demonstrate high frequency “optomechanical crystals”. Jeff and I were still nominally working on NV centers, but heavy course work and my drifting interests kept that work in a safely unproductive sphere. I simply wanted to know what “quantum” effects could be observed in optomechanics. This became a bit of an obsession with me spending long hours with Tze Tan’s Quantum Optics toolbox, trying to understand what the required parameters are to see anti-bunching in light emitted from an optomechanical cavity. Trying to apply master equation techniques to these systems, I was looking in the wrong places, going to higher and higher mechanical quality factors, and hitting instabilities. I was in way over my head. Two years later, Peter Rabl, and Andreas Nunnenkamp showed in a beautiful pair of PRLs that vacuum strong coupling is needed [8, 9], and that the mechanical

quality factor is not relevant. Oskar suggested that I consider squeezing of the mechanical motion instead. This was an excellent suggestion. I became very comfortable with Gaussian noise in the input-output formalism, and started to see everything as scattering matrices between inputs and outputs. Perhaps what struck me the most when reading the “classics” [10, 11] on input-output and squeezing was that the intracavity field wasn’t really all that important. It was the traveling field that had the most squeezing, and would end up being detected at the measurement setup. Slowly I started to appreciate the technological prospects for coupling linearly a mechanical and optical resonator on a chip, and the “phonon-photon translator” concept was born. At first, I was mostly interested in creating very narrow linewidth optical filters, by using the dispersion of mechanics at optical frequencies. Then, one Saturday morning, I sent the following email to Oskar:

May 9, 2009

Hi Oskar

I was thinking about the fact that one of the main limitations of circuit QED is making flying qubits; with the phonon-photon state transfer technique we could solve this problem. i.e. take the 5-6 GHz Photon on the superconductive circuit, using piezoelectric actuation (same technique used on BAW devices) create high frequency bulk waves ..., shine them on a phonon PBG circuit, capture them in a phononic crystal waveguide and then a phonon cavity, and do state transfer to an optical photon using the state transfer method we spoke about.

Amir

Within ten minutes (!), Oskar responded outlining what has now become an experiment actively pursued in several labs world-wide (including ours), and one of the most exciting applications of optomechanics to quantum science:

May 9, 2009

Amir,

If efficient, this could be a very useful technique. It would so very nicely enable microwave to optical conversion in circuit QED.

I would think a triple cavity of phonon, microwave photon, and photon would be ideal to consider.

OJP.

Around this time, I was enrolled in Keith Schwab’s condensed matter physics course. Keith would spend a portion of the class everyday presenting us with a varied and colorful description of research in the real world. One class, he spoke of a theoretical proposal by Cleland on coupling a qubit

to a mechanical resonator. I was mesmerized: this is exactly what I needed for the piezoelectric proposal, and people were already working on it! I finally felt that I was getting traction with my research, and that I was on the right track. I could feel a strong current pulling me in the direction of optomechanics, and I wasn't going to fight it anymore. Little did I know that O'Connell's demonstration [12] of the proposal was now only months away, and would become Science Magazine's breakthrough of the year.

Phononic structures

Starting in the summer of 2009, I had finished most of my required course work and had a fairly good understanding of what experiments I wanted to attempt in the coming years. I'd drifted away from Raviv and Thiago, who continued their work on active III-V materials. Jeff had joined Alex and Ryan Camacho, a sub-group working on an ambitious experiment to measure radiation pressure back-action. Matt and Jasper were also continuing work on the nanobeams, while Qiang and Jessie worked on double-disk structures. I was the only person in the group not paired with anyone, and was lacking concrete short-term goals. This allowed me to manage my own time and interests without a great deal of external pressure. I also benefited from routine informal meetings with Oskar, and Darrick Chang, an IQI post-doc with interests in optomechanics. During the summer, I focused most of my effort on designing two-dimensional structures phononic-photon structures (most of this work is presented in section 3.2). We envisioned this to be the first step to a viable phonon-photon interface. This was a design problem with a certain amount of history, going back to the 1990s. In the mid-2000s, simultaneous phonon-photon defect states had been proposed by a group at MIT, and in the preceding months, Matt and Jasper had demonstrated in experiments with 1D structures, that such systems are viable. However, 1D structures have a particular property that makes their design much simpler: there is no need for a full bandgap. Designing and fabricating 2D optomechanical crystals ended up being quite a challenge. Moving onto experiments with Thiago, we began by demonstrating a photonic crystal embedded in a phononic crystal cage. The cross crystal still used in our group to obtain the reported record high mechanical quality factors, is a relic of this effort. We quickly moved to developing the 'snowflake' geometry. The initial structures had excellent optical properties, but our measurement capabilities at the time, and a lack of microwave equipment, prevented us from being able to observe the roughly 10 GHz mechanical resonances in the structure for another two years.

Electromagnetically induced transparency

The sharp lines which Oskar and I thought would be useful for optical filtering meant something completely different to Darrick. He had noted interesting analogies between the optomechanical system and Electromagnetically Induced Transparency (EIT) in atoms. Along with Mohammad

Hafezi, a post-doc at JQI, we started to develop the theory for periodic arrays of optomechanical systems, to see if arrays of these structure could be made to act as a quantum memory, as atoms had roughly a decade ago. Darrick and Mohammed, who were from Misha Lukin's group, and had been intimately involved in atom cloud theory and experiments, approached the problem from that view. I was more familiar with work in the integrated optics setting, and Coupled Resonator Optical Waveguide (CROW) work by Amnon Yariv's group at Caltech. Interestingly, a complete picture required a synthesis of both approaches, which ended up being an excellent educational opportunity for me, thanks to Darrick's caring a careful tutelage. We rapidly wrote a theory paper and presented it at several conferences, including the Gordon Research Conference in March 2010. Thiago and I began work on the experimental realization of EIT, if only as a way to make detection of mechanical modes in our snowflake devices easier.

Early morning on June 5th 2010, I was sitting at the small airport in Kuopio, Finland, waiting for a flight to Helsinki. I logged into the free airport WiFi, and saw that the night before, Tobias Kippenberg's group in Lausanne had submitted a preprint onto arXiv with the title "Optomechanically Induced Transparency". I remember feeling my heart rate rise rapidly, as I read through what was my first experience of being "scooped". The flights back weren't pleasant. I simply looked out the window and thought about the situation I had suddenly found myself in. Thiago and I had quickly shot a few emails back and forth on how we should switch the direction of our research. Emotions were running high. The long flights were a blessing as I had time to sort out my thoughts and feelings. On the last leg of my thoughtful twenty hour journey, I wrote an email to Oskar:

June 6, 2010

Hi Oskar,

...

I've been thinking about future directions after their result and I don't think it affects anything we want to 'do' in any way whatsoever. I mean we need to observe EIT anyway, since it's the preliminary step to both wavelength conversion and optomechanical delays. (in all three experiments we have to put a probe one mechanical frequency blue of the pump, while having similar requirements on G.)

...

I think I've learned a few lessons though:

- 1. Don't underestimate the competition. I had completely written them off. In fact when I first saw the paper I just assumed it was a theory paper. I was pretty dejected/surprised when I realized it's experimental.*

2. *Good measurement techniques can compensate for bad devices. Maybe it's best to improve both instead of sticking to the same technique and perfecting devices, though I personally have the tendency to find new devices more interesting which may be a bad thing. Also I think in this field in particular there's a lot of untapped potential for devices.*

3. *Its not good for me to become too complacent/cozy, I'm not entitled to anything, if we don't do it someone else will.*

Best Amir

Oskar had already come to the same conclusions and in the next few days, successfully raised our spirits for the difficult tasks ahead. I still stand by the list I wrote in that email, and I thank Prof. Tobias Kippenberg, Dr. Albert Schliesser, and the other authors of that paper for teaching us valuable lessons early on. I thank them for being worthy and serious scientific competitors over the years, who kept us (and continue to keep us) from becoming complacent, slow, and boring.

The next few months were anything but boring. Thiago and I had to demonstrate EIT, and try to do a better job than our swiss competitors, preferably “striking while the iron was still hot”. We cut the fat: work on snowflakes was halted. My dalliances with Darrick on theoretical ideas became rare. I was going to stay in the lab until we had a paper. At around the same time, our electron beam lithography tool at the shared cleanroom stopped functioning. We had no more samples. Matt Eichenfield and Jasper had a nanobeam sample which they donated to us. In August we started to do low temperature measurements. On our first cool-down on Friday, August 13th, the stage jumped, and the chip flipped with the device side into thermal grease. I stared blankly at Thiago, learned a few new Brazilian swear words, packed my bag, and went home. Thiago emailed me a few hours later to tell me that the chip had been revived after what I can only imagine was the most heroic silicon cleaning effort in semiconductor history. By late September 2010, we had all of the data. The paper took approximately one month to write, and we submitted it in early December to Nature.

The silicon crew

Once our paper had been accepted, the group was in for a re-organization. Thiago and Jasper paired up to work on cooling the nanobeams, while Jeff and I assisted and simultaneously started back on the two-dimensional structures, while experimenting with ideas for wavelength conversion. This was the core of the “silicon crew” in the Painter lab (Simon Gröblacher would also be soon joining us as a post-doc from Vienna). In March 2011, we were again “scooped”. John Teufel from NIST released an incredibly beautiful preprint on using sideband cooling to reach the ground state

of motion in a microwave electromechanical system. At the same time, we knew of steady progress in the Kippenberg lab on producing the same result in the optical domain. The other groups had released a series of incremental results on the way to reaching the ground state, but we were late to game. If we were to publish anything it would have to be significant. To make up for being behind, all of our efforts were again redirected to the cooling experiment, and Jeff and I also began assisting Jasper in obtaining the result (abandoning the snowflake crystals again...).

The story of our efforts in those months on achieving ground state cooling, and the string of results that followed, can fill many pages. At this point, it is best to defer the reader to the actual results presented throughout this thesis, and also those of Jasper Chan and Jeff Hill. Perhaps most importantly, thanks to Oskar's careful selection of people and energetic leadership, we benefitted from having an amazing team in the last few years consisting of Jeff, Jasper, Simon, Thiago, and myself. It's been an honor to be part of this group of friends and scientists, and I can only hope that I will find myself in similar conditions in the future. This work is dedicated to the long hours we spent together in and out of the lab, every moment of which I cherish (even the time you slapped me, Jasper), and in the hopes of having our paths cross frequently in the coming years.

Chapter 1

Introduction to linearized optomechanical systems

1.1 Quantum description of the optomechanical system

A proper understanding the quantum behavior of a general optomechanical system requires recourse to quantum field theory, and quantization of a mesoscopic to macroscopic system with complicated geometry and interactions. Luckily, several well-justified simplifications allow us to express the full dynamics of such a system with a simple two-boson Hamiltonian containing only a few parameters. The values of these parameters can be simulated or measured to excellent accuracy. Perhaps more surprisingly, this Hamiltonian holds well for systems spanning roughly 20 orders of magnitude in mass, 10 orders of magnitude in mechanical frequency, and 5 orders of magnitude in optical frequency, with experimental results in a variety of domains agreeing extremely well with the basic theory.

In this section, we derive the optomechanical Hamiltonian for on-chip systems such those studied in our experiments. We also describe the simulations required to find the various parameters which are used to model the system.

1.1.1 Maxwell's equations for a photonic resonator and second quantization

Optically, we describe the nanofabricated structure with an inhomogeneous dielectric tensor $\bar{\bar{\epsilon}}(\mathbf{r})$. In most of this work, $\bar{\bar{\epsilon}}(\mathbf{r}) = \epsilon_{\text{Si}}$ in regions containing silicon, and $\bar{\bar{\epsilon}}(\mathbf{r}) = 1$ otherwise. The time-harmonic Maxwell's equations for such a system are given by:

$$\text{curl } \mathbf{E}(\mathbf{r}) = i\omega\mu_0\mathbf{H}(\mathbf{r}) - \mathbf{J}(\mathbf{r}), \quad \text{curl } \mathbf{H}(\mathbf{r}) = -i\omega\epsilon_0\bar{\bar{\epsilon}}(\mathbf{r}) \cdot \mathbf{E}(\mathbf{r}). \quad (1.1)$$

The source $\mathbf{J}(\mathbf{r})$ introduced here is a fictional magnetic current which will be used later in conjunction with the magnetic Green's function to find the effect of perturbations. In the absence of a source,

these equations lead to self-sustaining fields, or modes, represented by transverse (or solenoidal) and longitudinal (irrotational) eigenvectors, with the eigenvalue problem for the transverse magnetic fields given by

$$\mathbf{L}\mathbf{h}_j = \omega_j^2 \mathbf{h}_j, \quad \mathbf{L}(\cdot) = c^2 \text{curl} [(\bar{\epsilon}(\mathbf{r}))^{-1} \text{curl}(\cdot)]. \quad (1.2)$$

Additionally, for completeness, the irrotational fields given by $\mathbf{g}_j = \text{grad } \psi_j$, satisfying appropriate boundary conditions, where ψ_m is an eigenvector of $\text{div grad } \psi_j = -\nu_j \psi_j$, [13] must also be solved. This normal mode prescription is always valid for a volume enclosed in inside a perfectly reflective boundary. In the limit of an open system, however, complications arise as an open dielectric structure's resonances are typically not normal modes, but so-called 'quasi-normal' or leaky modes.

We use a Finite-Element Method (FEM) software package, COMSOL [14] to solve equation (1.2) with open or 'scattering' boundary conditions enclosing the simulation space. The very small loss rates for the obtained resonances, informs us of the accuracy of normal-mode approximation which is used throughout this work. As such, we take the numerically calculated high- Q solutions with frequency ω_j and field profile $\mathbf{h}_j(\mathbf{r})$ to be normal modes of the structures, and then add in losses 'by hand' at a later stage (c.f. section 1.2) to take into account the effects of a finite Q .

Quantization of the transverse electromagnetic field is accomplished in the standard way (see for example reference [15]) by associating bosonic creation and annihilation operators, \hat{a}_j^\dagger and \hat{a}_j respectively, with each modal solution $\{\mathbf{h}_j(\mathbf{r}), \mathbf{e}_j(\mathbf{r})\}$ of Maxwell's equation in the structure. The field operators are then expressed in the Heisenberg picture as

$$\hat{\mathbf{H}}(\mathbf{r}) = \sum_j \mathbf{h}_j(\mathbf{r}) \hat{a}_j e^{-i\omega_j t} + \text{h.c.} \quad (1.3)$$

$$\hat{\mathbf{E}}(\mathbf{r}) = \sum_j \mathbf{e}_j(\mathbf{r}) \hat{a}_j e^{-i\omega_j t} + \text{h.c.}, \quad (1.4)$$

and we obtain from eqn. (1.1) that $\mathbf{e}_j(\mathbf{r}) = i\omega^{-1} \overline{\overline{\epsilon^{-1}}}(\mathbf{r}) \cdot \text{curl } \mathbf{h}_j(\mathbf{r})$. To calculate the proper normalization of the field profiles, we assume a single photon state $|\psi\rangle = |1\rangle_j \prod_{\forall k \neq j} |0\rangle_k$ and find the expected value of additional field energy above vacuum ($|\text{vac}\rangle = \prod_k |0\rangle_k$):

$$\begin{aligned} U_{\text{em}} &= \langle \psi | \int d\mathbf{r} \hat{\mathbf{E}}(\mathbf{r}) \bar{\epsilon}(\mathbf{r}) \hat{\mathbf{E}}(\mathbf{r}) | \psi \rangle - \langle \text{vac} | \int d\mathbf{r} \hat{\mathbf{E}}(\mathbf{r}) \bar{\epsilon}(\mathbf{r}) \hat{\mathbf{E}}(\mathbf{r}) | \text{vac} \rangle \\ &= 2 \int d\mathbf{r} \mathbf{e}_j^*(\mathbf{r}) \bar{\epsilon}(\mathbf{r}) \mathbf{e}_j(\mathbf{r}) \\ &= 2V_{\text{eff}} \text{max}[\mathbf{e}_j^*(\mathbf{r}) \bar{\epsilon}(\mathbf{r}) \mathbf{e}_j(\mathbf{r})]. \end{aligned} \quad (1.5)$$

Assuming a maximum field amplitude inside the isotropic dielectric with index ϵ_{diel} , and $U_{\text{em}} = \hbar\omega_j$,

we obtain the maximum single-photon field

$$\max[|\mathbf{e}_j(\mathbf{r})|] = \sqrt{\frac{\hbar\omega_j}{2V_{\text{eff},j}\epsilon_{\text{diel}}}}, \quad (1.6)$$

where we have defined the effective mode volume for mode j to be

$$V_{\text{eff},j} = \frac{\int d\mathbf{r} \mathbf{e}_j^*(\mathbf{r})\bar{\epsilon}(\mathbf{r})\mathbf{e}_j(\mathbf{r})}{\max[\mathbf{e}_j^*(\mathbf{r})\bar{\epsilon}(\mathbf{r})\mathbf{e}_j(\mathbf{r})]}. \quad (1.7)$$

In many of the structures demonstrated in this work, the maximum field amplitude for a single photon can be surprisingly large, reaching values of 10^5 V/m.

1.1.2 Mechanical waves and their quantization

Analyzing mechanical vibrations, and their quantum description in terms of phonons in a crystal lattice can be approached in two ways. The first begins with the atomic structure of the crystal, the forces sensed by each ion, and studies the motion of these ions. The interested reader is referred to any of a wide array of excellent textbooks on condensed matter physics for such a treatment [16]. A second way, which is less general¹, as it only applies to phonons with wavelengths much longer than the atomic spacing, involves starting with an effective continuum mechanics description. This is the approach we take, as the motion of single ions is not of interest in this work. This is conceptually no different than the approach taken in section 1.1.1, where the macroscopic electromagnetic fields are quantized and the motion of the charges in the structure are only considered in terms how they contribute to the electric susceptibility of the material at optical frequencies. At this continuum limit, the material is characterized by an elasticity tensor \bar{c} (a fourth-rank tensor with components c_{ijkl} which depend on the Young's modulus E , and Poisson's ratio σ), its density $\rho(\mathbf{r})$, and its dynamical state represented by a time-dependent displacement vector field $\mathbf{Q}(\mathbf{r}, t)$ often also denoted $\mathbf{u}(\mathbf{r}, t)$ in the literature.

Fundamentally, it is the strain, a measure of the local deformation in a structure which is of interest. Local deformations arise from the spatial variation of $\mathbf{Q}(\mathbf{r}, t)$, and are found by taking the derivative of this vector field. This total derivative is symmetrized to do away with rotations, and is represented by a unit-less 3×3 matrix with components

$$S_{ij} = \frac{1}{2} (\partial_i Q_j + \partial_j Q_i). \quad (1.8)$$

Stress in a structure is also a 3×3 matrix T , which gives for every infinitesimal volume element in the structure the local forces which act on its surfaces. For a surface with normal vector \hat{n} , this force

¹In a way, this approach is more general, since it applies to non-crystalline materials as well.

is $T \cdot \hat{n}$. Hooke's law (i.e. the linear relationship between forces on a structure and the resulting deformation) extended to this formalism can be expressed as a linear relation between strain and stress, which is compactly stated as²

$$T_{ij} = c_{ijkl} S_{kl}. \quad (1.9)$$

At this point Newton's law can be used to express the acceleration of volume element due to the stress in the structure,

$$\begin{aligned} \rho \partial_t^2 Q_i &= \partial_j T_{ji} = \frac{1}{2} \partial_j c_{jikl} (\partial_k Q_l + \partial_l Q_k) \\ \text{implying } \partial_t^2 \mathbf{Q} &= c_l^2 \nabla (\nabla \cdot \mathbf{Q}) - c_t^2 \nabla \times \nabla \times \mathbf{Q}, \end{aligned} \quad (1.10)$$

for an isotropic material with c_l and c_t , the speed of longitudinal and transverse waves in the solid, being related to elements of \bar{c} . The important point is that equation (1.10) is a full vectorial wave equation for acoustic waves, and can be written as an eigenvector equation much like equation (1.2):

$$\omega_j^2 \mathbf{Q}_j(\mathbf{r}) = \mathbf{L} \mathbf{Q}_j(\mathbf{r}), \quad \mathbf{L}(\cdot) = -c_l^2 \nabla (\nabla \cdot (\cdot)) + c_t^2 \nabla \times \nabla \times (\cdot). \quad (1.11)$$

A solution at frequency ω_j now has a mechanical mode profile $\mathbf{Q}_j(\mathbf{r})$.

Quantizing the motion follows an approach similar to that used for the electromagnetic field. We define \hat{b}_j^\dagger and \hat{b}_j respectively, with each modal solution $\mathbf{Q}_j(\mathbf{r})$ of the equations of elasticity in the structure. The field operator is then expressed the Heisenberg picture as

$$\hat{\mathbf{Q}}(\mathbf{r}) = \sum_j \mathbf{Q}_j(\mathbf{r}) \hat{b}_j e^{-i\omega_j t} + \text{h.c.} \quad (1.12)$$

To calculate the proper normalization of the field profiles, we assume a single phonon state $|\psi\rangle = |1\rangle_j \prod_{\mathbf{v}k \neq j} |0\rangle_k$ and find the expected value of additional field energy above vacuum ($|\text{vac}\rangle = \prod_k |0\rangle_k$):

$$\begin{aligned} U_{\text{mech}} &= \langle \psi | \int d\mathbf{r} \dot{\mathbf{Q}}(\mathbf{r}) \rho(\mathbf{r}) \dot{\mathbf{Q}}(\mathbf{r}) | \psi \rangle - \langle \text{vac} | \int d\mathbf{r} \dot{\mathbf{Q}}(\mathbf{r}) \rho(\mathbf{r}) \dot{\mathbf{Q}}(\mathbf{r}) | \text{vac} \rangle \\ &= 2\omega_j^2 \int d\mathbf{r} \mathbf{Q}_j^*(\mathbf{r}) \rho(\mathbf{r}) \mathbf{Q}_j(\mathbf{r}) \\ &= 2m_{\text{eff}} \omega_j^2 \max[|\mathbf{Q}_j(\mathbf{r})|^2]. \end{aligned} \quad (1.13)$$

Here we have taken the energy to be twice the kinetic energy. It is easy to show that for a mechanical mode, half of the energy will be kinetic, and the other half potential. Assuming the energy of a

²Summations are implied over repeated indices.

phonon to be $U_{\text{mech}} = \hbar\omega_j$, we obtain the maximum single-phonon displacement

$$x_{\text{zpf},j} \equiv \max[|\mathbf{Q}_j(\mathbf{r})|] = \sqrt{\frac{\hbar}{2m_{\text{eff},j}\omega_j}}, \quad (1.14)$$

where we've defined the effective mode volume for mode j to be

$$m_{\text{eff},j} = \frac{\int d\mathbf{r} \mathbf{Q}_j^*(\mathbf{r})\rho(\mathbf{r})\mathbf{Q}_j(\mathbf{r})}{\max[|\mathbf{Q}_j(\mathbf{r})|^2]}. \quad (1.15)$$

In all the structures demonstrated in this work, regardless what the effective mass is (ranging from $10^{-18} - 10^{-15}$ kg), the zero-point fluctuation amplitude is roughly on the order of a femtometer.

1.1.3 Optomechanical Coupling

1.1.3.1 Perturbation theory of dielectric cavities

Given a mode for the optical and mechanical modes, coupling rates can be calculated. This coupling arises from the perturbation of the optical cavity frequency due to mechanical deformation. Starting from the optical eigenvalue equation (1.2), we can formulate this perturbation theory by looking at the Green's function for the optical field. Given a source \mathbf{J} , the response of the transverse field is given by,

$$\mathbf{h}(\mathbf{r}) = -\frac{i\omega}{\mu_0} \int d\mathbf{r}' \overline{\overline{\mathbf{G}}}(\mathbf{r}, \mathbf{r}'|\omega) \cdot \mathbf{J}(\mathbf{r}) = -\frac{i\omega}{\mu_0} \mathbf{G}(\omega) \mathbf{J}(\mathbf{r}), \quad (1.16)$$

where $\overline{\overline{\mathbf{G}}}(\mathbf{r}, \mathbf{r}'|\omega)$ is the transverse Green's function for the system, given by the expression

$$\overline{\overline{\mathbf{G}}}(\mathbf{r}, \mathbf{r}'|\omega) = \sum_m \frac{\mathbf{h}_m(\mathbf{r}) \otimes \mathbf{h}_m(\mathbf{r}')}{\omega_m^2 - \omega^2}. \quad (1.17)$$

Additionally, we can write

$$(\mathbf{L} - \omega^2) \mathbf{G}(\omega) = \mathbf{1}_{\mathbf{T}}. \quad (1.18)$$

In the context of photonic nanostructures, the *electric* Green's function, defined analogously, has been used to study optical bistability, and calculate the coupling between atoms and photons in inhomogeneous environments [17–19]. It is more natural to consider magnetic Green's functions for several reasons. First of all the operator \mathbf{L} is Hermitian in this case (see [20]). Secondly, an electric field solution for a non-perturbed structure, is not a valid solution of Maxwell's equations for a perturbed structure (since the electric boundary condition depends on the position of the dielectric boundary). For magnetic fields, since we assume $\mu(\mathbf{r}) = \mu_0$, this is not the case, thus a treatment based on magnetic fields is expected to hold to higher orders in the perturbation theory [21].

Nonperturbative expressions for modifications to the Green's function can be calculated using techniques borrowed from atomic physics [22]. Given a dielectric structure characterized by $\overline{\overline{\epsilon}}_0(\mathbf{r})$,

modifications due to, for example, deformations can be taken into account with the expression

$$\bar{\bar{\epsilon}}(\mathbf{r}) = \bar{\epsilon}_0(\mathbf{r}) + \bar{\delta\bar{\epsilon}}(\mathbf{r}). \quad (1.19)$$

An operator L_0 corresponding to the unmodified structure, is defined as in equation (1.2), and we define the deformation-dependent interaction potential as $V = L - L_0$. Additionally, both L and L_0 have corresponding Green's functions $G(\omega)$ and $G_0(\omega)$, and complete sets of eigenfunctions, $\mathbf{h}_m(\mathbf{r})$ and $\mathbf{h}_m^{(0)}(\mathbf{r})$. To see how the modes of interest are modified, we define an operator P projecting onto a subspace of modes (the modes of interest) with a position space representation

$$\bar{\bar{P}}(\mathbf{r}, \mathbf{r}' | \omega) = \sum_m \mathbf{h}_m^{(0)}(\mathbf{r}) \otimes \mathbf{h}_m^{(0)}(\mathbf{r}'), \quad (1.20)$$

and define additionally $Q = 1_{\mathbb{T}} - P$. In the subspace of interest, the range of P , equation (1.18) is modified:

$$P \left[L - \omega^2 - VQ \frac{1}{L - \omega^2} QV \right] PG(\omega)P = P. \quad (1.21)$$

This, in turn, may be expressed using the unpertrubed system operator and a level-shift operator [22] $R(\omega)$:

$$P [L_0 + R(\omega) - \omega^2] PG(\omega)P = P, \quad \text{with} \quad (1.22)$$

$$R(\omega) = V + V \frac{1}{\omega^2 - QLQ} V. \quad (1.23)$$

The last expression can be written as an expansion

$$\begin{aligned} R(\omega) = & V + V \frac{1}{\omega^2 - QL_0Q} V + \\ & + V \frac{1}{\omega^2 - QL_0Q} QVQ \frac{1}{\omega^2 - QL_0Q} V + \dots, \end{aligned} \quad (1.24)$$

and evaluated directly in the basis of eigenmodes for the original structure, R_{jk} ,

$$\begin{aligned} R_{jk}(\omega) = & V_{jk} + \sum_{p \neq m} \frac{V_{jp} V_{pk}}{\omega^2 - \omega_p^2} + \\ & + \sum_{p \neq m} \sum_{q \neq m} \frac{V_{jp} V_{pq} V_{qk}}{(\omega^2 - \omega_p^2)(\omega^2 - \omega_q^2)} + \dots \end{aligned} \quad (1.25)$$

The matrix elements V_{ij} can be calculated for moving boundaries using the limit conditions derived by Johnson et al. [21] as elaborated below.

By making a formal replacement $V \rightarrow \lambda V$, we can use λ as an ordering parameter to the shift in the photonic resonance frequencies at different orders. Taking a single mode of interest, $\mathbf{h}_0^{(0)}(\mathbf{r})$,

equation (1.22) becomes simply a scalar relation, from which the level shifts may be calculated. At $\omega = \omega_0$, the level shift is given by

$$R_{00} \cong \lambda V_{00} + \lambda^2 \sum_{p \neq 0} \frac{|V_{p0}|^2}{\omega_0^2 - \omega_p^2} + \mathcal{O}(\lambda^3) \quad (1.26)$$

Now assuming $\omega(\lambda) = \omega_0 + \omega^{(1)}\lambda + \omega^{(2)}\lambda^2 + \dots$, we find for the first two orders,

$$\omega^{(1)} = \frac{V_{00}}{2\omega_0}, \quad (1.27)$$

$$\omega^{(2)} = \frac{1}{2\omega_0} \sum_{p \neq 0} \frac{|V_{p0}|^2}{\omega_0^2 - \omega_p^2} - \frac{1}{2\omega_0} \frac{|V_{00}|^2}{4\omega_0^2}. \quad (1.28)$$

A notable aspect of equation (1.28) is that there is *always* a second-order (or quadratic) coupling term present in an optomechanical system that goes as $(\omega^{(1)})^2/(2\omega_0)$. This conclusion only follows from a full treatment of Maxwell's equation, and is typically not considered in the simple phenomenological Hamiltonian used in most of the optomechanics literature. The second-order time-derivative in the eigenvalue equation (1.2) causes this.

Using equation (1.27) we arrive at a simple relationship between the dielectric perturbation and the frequency shift of a single optical resonator,

$$\omega^{(1)} = -\frac{\omega_0}{2} \frac{\langle \mathbf{e} | \overline{\delta\epsilon} | \mathbf{e} \rangle}{\langle \mathbf{e} | \overline{\epsilon} | \mathbf{e} \rangle}, \quad (1.29)$$

where

$$\langle \mathbf{a} | \overline{\mathbf{b}} | \mathbf{c} \rangle = \int \mathbf{a}(\mathbf{r}) \cdot \overline{\mathbf{b}}(\mathbf{r}) \cdot \mathbf{c}(\mathbf{r}) \, d^3\mathbf{r}. \quad (1.30)$$

Having calculated the optical cavity frequency shift due to a perturbation in the dielectric tensor, we now calculate the perturbation of the dielectric tensor due to deformation. There are two main sources such a coupling, both of which are presented below.

1.1.3.2 Boundary perturbation

A deformation of the optical resonator affects the dielectric tensor at the boundaries between different materials. This is because the high-contrast step profile of $\overline{\epsilon}(\mathbf{r})$ across a boundary is shifted by deformations of the structure. By relating a deformation to a change in the dielectric constant, we can use equation (1.29) to calculate the optomechanical coupling. Johnson has derived a robust expression [21] for this shift in frequency, which, when adapted to optomechanics [23], gives a

frequency shift per unit length of

$$g_{\text{OM,Bnd}} = -\frac{\omega_0}{2} \frac{\int (\mathbf{Q}(\mathbf{r}) \cdot \mathbf{n}) (\Delta \bar{\bar{\epsilon}} |e^\parallel|^2 - \Delta(\bar{\bar{\epsilon}}^{-1}) |d^\perp|^2) dA}{\max(|\mathbf{Q}|) \int \bar{\bar{\epsilon}}(\mathbf{r}) |e(\mathbf{r})|^2 d^3\mathbf{r}} \quad (1.31)$$

for a mechanical vector displacement field $\mathbf{Q}(\mathbf{r})$.

1.1.3.3 Photoelastic coupling

The photoelastic contribution to the optomechanical coupling arises from local changes in the refractive index due to strain in the structure. For a particular displacement vector $\mathbf{Q}(\mathbf{r})$ (and the corresponding strain tensor $\bar{\bar{S}}$, see eqn. (1.8)), the dielectric perturbation is given by

$$\bar{\bar{\delta\epsilon}}(\mathbf{r}) = \bar{\bar{\epsilon}} \cdot \frac{\bar{\bar{p}} \cdot \bar{\bar{S}}}{\epsilon_0} \cdot \bar{\bar{\epsilon}} \quad (1.32)$$

which reduces to $\delta\epsilon_{ij} = -\epsilon_0 n^4 p_{ijkl} S_{kl}$ for an isotropic medium. The fourth-rank tensor $\bar{\bar{p}}$ with components p_{ijkl} is called the photoelastic tensor. Often, when considering the symmetries in a crystal, a reduced tensor is used with elements p_{ij} . At this point, a simple volume integral, such as that shown in equation (1.29), can be used to find the frequency shift for a given displacement

$$g_{\text{OM,PE}} = -\frac{\omega_0}{2} \frac{\int \mathbf{e} \cdot \bar{\bar{\delta\epsilon}} \cdot \mathbf{e} d^3\mathbf{r}}{\max(|\mathbf{Q}|) \int \bar{\bar{\epsilon}}(\mathbf{r}) |e(\mathbf{r})|^2 d^3\mathbf{r}}, \quad (1.33)$$

where $\mathbf{e} \cdot \bar{\bar{\delta\epsilon}} \cdot \mathbf{e}$ for the surface of silicon with x and y being in [100] and [010] crystal directions is given by [24]

$$\begin{aligned} \mathbf{e} \cdot \bar{\bar{\delta\epsilon}} \cdot \mathbf{e} = & -\epsilon_0 n^4 \left[2\Re\{E_x^* E_y\} p_{44} S_4 + 2\Re\{E_x^* E_z\} p_{44} S_5 + \Re\{E_y^* E_z\} p_{44} S_6 \right. \\ & + |E_x|^2 (p_{11} S_1 + p_{12} (S_2 + S_3)) + |E_y|^2 (p_{11} S_2 + p_{12} (S_1 + S_3)) \\ & \left. + |E_z|^2 (p_{11} S_3 + p_{12} (S_1 + S_2)) \right] \end{aligned} \quad (1.34)$$

and the components of the photoelastic tensor are $(p_{11}, p_{12}, p_{44}) = (-0.094, 0.017, -0.051)$ [25].

1.1.4 Vacuum coupling rate

The expressions derived above give us the boundary and photoelastic components for a shift in the optical cavity frequency per unit displacement of the maximum deflection point of a deformation profile $\mathbf{Q}(\mathbf{r})$. The vacuum coupling rate g_0 is the shift in the optical cavity frequency due to a deformation equal in amplitude to the zero-point fluctuations of a single mechanical mode $\mathbf{Q}_j(\mathbf{r})$. We can find $g_{0,\text{Bnd}}$ and $g_{0,\text{PE}}$ simply by multiplying the expressions (1.31) and (1.33) by the zero-point fluctuation length $x_{\text{zpf}} = \sqrt{\hbar/(2m\omega_m)}$ (see eqn. 1.14). The total coupling rate is then simply

their sum $g_0 = g_{0,\text{Bnd}} + g_{0,\text{PE}}$. Finally, the optomechanical interaction is

$$\begin{aligned} H_{\text{OM,int}} &= \hbar(g_{\text{OM,PE}} + g_{\text{OM,Bnd}})\hat{x}\hat{a}^\dagger\hat{a} \\ &= \hbar g_0(\hat{b}^\dagger + \hat{b})\hat{a}^\dagger\hat{a}. \end{aligned} \tag{1.35}$$

1.2 Lossy optical and mechanical resonators

It is important to account for the loss-rate of excitations in optical and mechanical cavities. Typically in chip-scale optical experiments, the resonator is coupled to a waveguide. A quantum-mechanical treatment of this interaction is provided below in section 1.2.1. Such a treatment may seem daunting as first: the optical waveguide is described by an infinite continuum of propagating modes, each coupled to the optical cavity. However, several approximations significantly reduce the complexity of the problem such that it is fully described by essentially a single number, κ_e , which is the optical coupling rate to the waveguide. In real experiments, there are also other channels of *intrinsic* loss often lumped together into a term κ_i . Additionally, cavity-waveguide coupling occurs in a variety of different geometrical arrangements which we treat in section 1.2.2.

1.2.1 An optical cavity loaded by a waveguide

In this section, we derive the effects of coupling between a waveguide and a resonator. The basic assumptions leading to the input-output formalism [10, 26] are shown. For completeness, we relate these results to both transmission line theory [27] and to coupled mode theory [28] often used in engineering literature to treat classical photonic circuits.

1.2.1.1 Waveguide-Cavity Interaction

The system's Hamiltonian \hat{H}_{tot} is composed from the Hamiltonian for the optical resonator $\hat{H}_{\text{cav}} = \hbar\omega_c\hat{a}^\dagger\hat{a}$, the waveguide Hamiltonian \hat{H}_{WG} , and linear coupling interaction term \hat{H}_{int} between the cavity and waveguide. The waveguide consists of an infinite number of modes indexed with k , and with annihilation operator $\hat{A}(k, t)$. The index k can be thought of as a general mode index, representing freespace modes, modes on one band of a photonic crystal waveguide, or even modes of a simple optical fiber. The waveguide Hamiltonian is then given by

$$\hat{H}_{\text{WG}} = \hbar \int dk \omega(k)\hat{A}^\dagger(k, t)\hat{A}(k, t), \tag{1.36}$$

with $\omega(k)$ representing the energy of mode k . If k is a wavenumber, $\omega(k)$ would be the dispersion relation for the waveguide band of interest. The linear interaction between the waveguide and cavity

is provided by the interaction Hamiltonian

$$\hat{H}_{\text{int}} = -i\hbar \int dk \left\{ \hat{A}(k, t) \hat{a}^\dagger(t) f(k) - \text{h.c.} \right\}, \quad (1.37)$$

where $f(k)$ is the coupling rate between mode k and the resonator. Solving for the Heisenberg equations of motion for this Hamiltonian we find a system of differential equations

$$\dot{\hat{A}}(k, t) = -i\omega(k) \hat{A}(k, t) + f^*(k) \hat{a}(t), \quad (1.38)$$

$$\dot{\hat{a}}(t) = -\frac{1}{i\hbar} [H_{\text{cav}}, \hat{a}(t)] - \int dk \hat{A}(k, t) f(k). \quad (1.39)$$

The equation of motion for $\hat{A}(k, t)$ can be formally integrated giving (t_i is some initial time):

$$\hat{A}(k, t) = \hat{A}(k, t_i) e^{-i\omega(k)(t-t_i)} + \int_{t_i}^t d\tau \hat{a}(\tau) f^*(k) e^{-i\omega(k)(t-\tau)}. \quad (1.40)$$

Substituting this term into the last term of equation (1.39), we arrive at an equation

$$\int dk \hat{A}(k, t) f(k) = \int dk f(k) \hat{A}(k, t_i) e^{-i\omega(k)(t-t_i)} + \int dk \int_{t_i}^t d\tau \hat{a}(\tau) |f(k)|^2 e^{-i\omega(k)(t-\tau)}. \quad (1.41)$$

Equivalently, we can write this equation by in terms of final interaction time t_f :

$$\int dk \hat{A}(k, t) f(k) = \int dk f(k) \hat{A}(k, t_f) e^{-i\omega(k)(t-t_f)} - \int dk \int_t^{t_f} d\tau \hat{a}(\tau) |f(k)|^2 e^{-i\omega(k)(t-\tau)}. \quad (1.42)$$

1.2.1.2 Markov Approximation

To proceed any further, approximations must be made. A common way to simplify these types of the equations is to make the Markov approximation, or, equivalently, a first-order Born approximation of the integro-differential equation. The Markov approximation is easiest to justify physically by considering the slowly varying amplitude of the cavity mode, i.e. $\tilde{a}(t)$ where $\hat{a}(t) = \tilde{a}(t) e^{-i\omega_c t}$. The term under the integral is then $\hat{a}(\tau) = \tilde{a}(\tau) e^{-i\omega_c \tau} e^{+i\omega_c(t-\tau)}$. Here we claim that $\tilde{a}(\tau) \approx \tilde{a}(t)$ over the range of interest. Then the following simplification can be made

$$\int dk \int_{t_i}^t d\tau \hat{a}(\tau) |f(k)|^2 e^{-i\omega(k)(t-\tau)} = \hat{a}(t) \int dk \int_{t_i}^t d\tau |f(k)|^2 e^{-i(\omega(k) - \omega_c)(t-\tau)}. \quad (1.43)$$

The dissipative component is captured by the real part of the integral multiplying $\hat{a}(t)$, which we define as $\kappa_e/2$ with κ_e equal to:

$$\kappa_e = 2\pi \cdot \left| \frac{dk}{d\omega} \right| \cdot |f(k_c)|^2. \quad (1.44)$$

Defining $\hat{a}_{\text{in}}(t)$ and $\hat{a}_{\text{out}}(t)$ as

$$\hat{a}_{\text{in}}(t) = \sqrt{\frac{v_g}{2\pi}} \int dk \hat{A}(k, t_i) e^{-i\omega(k)(t-t_i)}, \quad \text{and} \quad (1.45)$$

$$\hat{a}_{\text{out}}(t) = \sqrt{\frac{v_g}{2\pi}} \int dk \hat{A}(k, t_f) e^{-i\omega(k)(t-t_f)}, \quad (1.46)$$

the equation of motion of $\hat{a}(t)$ (i.e., equation (1.39)) becomes

$$\dot{\hat{a}}(t) = -\frac{1}{i\hbar} [H_{\text{cav}}, \hat{a}(t)] - \frac{\kappa_e}{2} \hat{a}(t) - \sqrt{\kappa_e} \hat{a}_{\text{in}}(t). \quad (1.47)$$

The solutions of the equation of motion for the $\hat{A}(k, t)$ modes, (i.e., equation (1.41) and (1.42)) give us the input-output boundary condition

$$\hat{a}_{\text{out}}(t) - \hat{a}_{\text{in}}(t) = \sqrt{\kappa_e} \hat{a}(t). \quad (1.48)$$

1.2.1.3 Relation to Transmission-Line Theory

To obtain the relation between the inputs and outputs and transmission line theory, we take the spatial Fourier transform of the radiation modes in the waveguide.

$$\hat{A}_+(z, t) = \int_0^\infty dk e^{ikz} \hat{A}(k, t) \quad (1.49)$$

$$\hat{A}_-(z, t) = \int_0^\infty dk e^{-ikz} \hat{A}(-k, t) \quad (1.50)$$

Physically these operators represent, respectively, the annihilation operators for a single forward (towards the cavity) or backward traveling photon at a point z inside the guiding structure. Classically, these are the amplitudes of a forward or backward traveling signals on a transmission line. We can now relate them to the input and output operators. For simplicity, we consider only the linear dispersion case where $\omega(k) = v_g|k|$. Then

$$\begin{aligned} \hat{a}_{\text{in}}(t) &= \sqrt{\frac{v_g}{2\pi}} \int dk \hat{A}(k, t_i) e^{-i\omega(k)(t-t_i)} \\ &= \sqrt{\frac{v_g}{2\pi}} \int dk \hat{A}(k, t_i) e^{-iv_g|k|(t-t_i)} \\ &= \sqrt{\frac{v_g}{2\pi}} \hat{A}_-(z = v_g \cdot (t - t_i), t_i) \end{aligned} \quad (1.51)$$

Similarly, one finds for the output the relation:

$$\hat{a}_{\text{out}}(t) = \sqrt{\frac{v_g}{2\pi}} \hat{A}_+(z = v_g \cdot (t_f - t), t_f) \quad (1.52)$$

1.2.1.4 Relation to Coupled Mode Theory

A common formalism often used in integrated optics is the coupled-mode formalism. Here we connect to this literature [28–34] and show its relation to the input-output treatment more common in quantum optics. Starting with the equation of motion for $\hat{A}(k, t)$, we take the Fourier transform in time, to find

$$-i\omega\hat{A}(k, \omega) = -i\omega(k)\hat{A}(k, \omega) + f^*(k)\hat{a}(\omega) \quad (1.53)$$

We then approximate the function $\omega(k)$ linearly around a frequency ω of interest.

$$\omega(k) = \omega + (k - k(\omega))v_g \quad (1.54)$$

This is exactly equivalent to the slowly varying amplitude approximation made commonly in the optics literature to convert second-order differential equations in the spatial variable to first-order differential equations. The equation of motion can be written as

$$ik\hat{A}(k, \omega) = ik(\omega)\hat{A}(k, \omega) + \frac{f^*(k)}{v_g}\hat{a}(\omega). \quad (1.55)$$

Taking the inverse spatial Fourier transform of this equation, we arrive at:

$$\frac{d\hat{A}(z, \omega)}{dz} = ik(\omega)\hat{A}(z, \omega) + \frac{f^*(z)}{v_g}\hat{a}(\omega). \quad (1.56)$$

This is the coupled mode equation for the interaction between a waveguide and resonator (See appendix of [31]). Interestingly, it shows in a very clear manner that lower group velocity in a waveguide close to cavity increases the rate of coupling to the cavity. This intuitively expected conclusion results from the fact that in a one dimensional waveguide, v_g and the density of states are simply related.

Finally we note that the approximations made in coupled mode theory and input-output formalism are similar. In the coupled-mode treatment, we use the *spatial* slowly varying amplitude of $A(z, t)$ to truncate the dispersion at linear order. In the input-output formalism, we use the *temporal* slowly varying amplitude of $\tilde{a}(\tau)$, to truncate the higher orders of the integrodifferential equation of motion. From equations (1.51) and (1.52) it is evident that the validity of one of these approximations implies the validity of the other.

1.2.2 Intrinsic and extrinsic losses

The effect of cavity-waveguide coupling discussed in section 1.2.1 is captured in a single coupling rate κ_e , and a noise input $\hat{a}_{\text{in}}(t)$. The coupling scheme giving rise to this system is represented

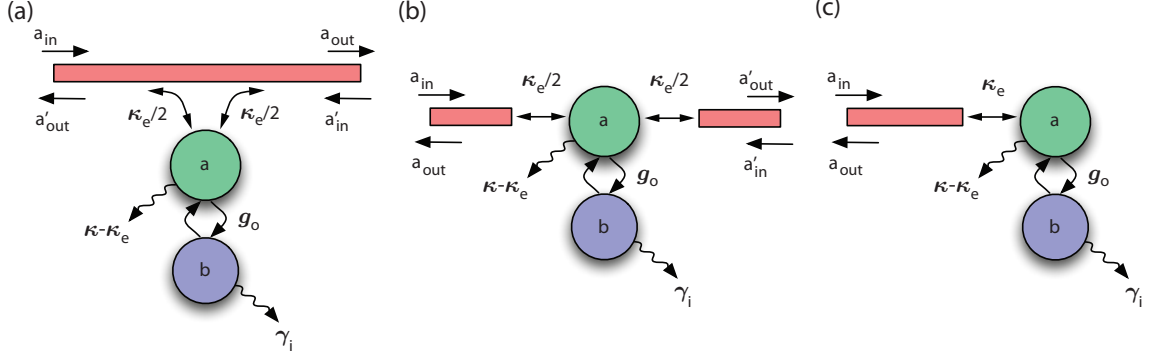


Figure 1.1: **Optical coupling schemes.** **a**, Bi-directional evanescent coupling geometry, in which the “transmitted” field goes into the forward a_{out} waveguide channel and the “reflected” field goes into the backward a'_{out} waveguide channel. This is the coupling geometry we will be focusing on in this work, in which the laser input channel is a_{in} and the detection channel is the forward waveguide channel, a_{out} . **b**, Double-sided end-fire coupling geometry. This is the geometry one would have in a Fabry-Perot cavity. Note that in this geometry what we call the “transmission” and “reflection” channels are typically opposite of that in the evanescent coupling geometry (a direct map between the two geometries would relate the “reflected” channel in (a) to the conventional transmission of a Fabry-Perot, for instance). **c**, Single-sided end-fire coupling geometry. This is the ideal measurement geometry since $\kappa = \kappa_e$, in which all of the optical signal that is coupled into the cavity can be, in principle, collected and detected in the a_{out} channel. In principle one does not have excess vacuum noise coupled into the optical cavity, only that from the detection channel $\kappa - \kappa_e$.

pictorially in Figure 1.1c. In reality, the loss into the waveguide will not be the only one present - other loss channels both load the cavity, and add fluctuations to the system. The subscript ‘e’ shows that κ_e represents the engineered or extrinsic losses from the resonator. The other losses are called lumped together into $\kappa_i = \kappa - \kappa_e$, representing the intrinsic losses in the cavity, with κ denoting now that total photon loss rate from the optical resonator.

Often it is convenient for a variety of technical reasons to make measurements “in transmission”. In such instances, a double-sided coupling is effectively induced. Excitation of one input channel in these measurements can lead to photons exiting through two different output channels, and the system as a whole is a two-port as opposed to a one-port device in microwave parlance. The two different balanced double-sided coupling geometries are shown in Figures 1.1a and b.

The Heisenberg equations for the cases outlined in Figure 1.1 are the following:

$$\begin{aligned} \text{a, b:} \quad \dot{\hat{a}}(t) &= -\frac{1}{i\hbar} [H_{\text{cav}}, \hat{a}(t)] - \frac{\kappa}{2} \hat{a}(t) - \sqrt{\kappa_e/2} \hat{a}_{\text{in}}(t) - \sqrt{\kappa'} \hat{a}_{\text{in},i}(t) \\ \text{c:} \quad \dot{\hat{a}}(t) &= -\frac{1}{i\hbar} [H_{\text{cav}}, \hat{a}(t)] - \frac{\kappa}{2} \hat{a}(t) - \sqrt{\kappa_e} \hat{a}_{\text{in}}(t) - \sqrt{\kappa_i} \hat{a}_{\text{in},i}(t) \end{aligned}$$

For a and b we have defined $\kappa' = \kappa - \kappa_e/2$ so that it accounts for the losses from the intrinsic cavity loss channel (κ_i), along with the losses from the second coupling channel ($\kappa_e/2$).

1.2.3 Mechanical resonators

The same analysis which was presented here for optical loss channels transfers directly to mechanical resonators. We use the symbol γ_i to denote the intrinsic loss rate of the mechanical resonator. It is also possible to create mechanical waveguides [5], and these can be used to load mechanical resonators, leading to an extrinsic loss channel for the mechanics, γ_e . Mechanical waveguides and their role in optomechanical circuits are investigated in section 6.2.

1.3 Dynamical back-action in the Heisenberg-Langevin picture

As shown in section 1.1.3, the optomechanical interaction between a mechanical system and an optical field occurs through radiation pressure, a force proportional to the optical field intensity. This can be modeled by a Hamiltonian

$$H = \hbar\omega_o\hat{a}^\dagger\hat{a} + \hbar\omega_m\hat{b}^\dagger\hat{b} + \hbar g_0\hat{a}^\dagger\hat{a}(\hat{b}^\dagger + \hat{b}), \quad (1.57)$$

with \hat{a} and \hat{b} the annihilation operators for photons and phonons in the system. In the presence of a laser emitting light at frequency ω_L , it is convenient to work in an interaction frame where $\omega_o \rightarrow \Delta$ in the above Hamiltonian with $\Delta = \omega_o - \omega_L$. To incorporate the effect of the environment, we use the quantum-optical Langevin equations for the system [10, 11, 26] as derived in section 1.2.1,

$$\dot{\hat{b}}(t) = -\left(i\omega_m + \frac{\gamma_i}{2}\right)\hat{b} - ig\hat{a}^\dagger\hat{a} - \sqrt{\gamma_i}\hat{b}_{\text{in}}(t) \quad (1.58)$$

and

$$\dot{\hat{a}}(t) = -\left(i\Delta + \frac{\kappa}{2}\right)\hat{a} - ig\hat{a}(\hat{b}^\dagger + \hat{b}) - \sqrt{\kappa}\hat{a}_{\text{in}}(t). \quad (1.59)$$

Here $\hat{a}_{\text{in}}(t)$ is the vacuum noise from the optical loss channels (extrinsic and intrinsic) entering the cavity. The noise operator $\hat{b}_{\text{in}}(t)$ arises from the coupling of the mechanical system to the surrounding bath degrees of freedom, which, in most current systems, resides in a high temperature thermal state with average bath occupancy $n_b \gg 1$.

We linearize the equations about a large optical field intensity by displacing $\hat{a} \rightarrow \alpha_0 + \hat{a}$. Such an approximation is valid for systems such as ours, where $g_0 \ll \kappa$, and the optical vacuum alone only marginally affects the dynamics of the system, i.e., the *vacuum weak coupling* regime. All experimental systems to date are in this regime. For systems in the *vacuum strong coupling* ($g_0 > \kappa$) regime, more elaborate treatments taking into account the quantum nature of the nonlinearity must

be pursued [8, 9, 35]. In the Fourier domain, the operators for the mechanical and optical modes are found to be³

$$\hat{b}(\omega) = \frac{-\sqrt{\gamma_i}\hat{b}_{\text{in}}(\omega)}{i(\omega_m - \omega) + \gamma_i/2} - \frac{iG(\hat{a}(\omega) + \hat{a}^\dagger(\omega))}{i(\omega_m - \omega) + \gamma_i/2} \quad (1.60)$$

and

$$\hat{a}(\omega) = \frac{-\sqrt{\kappa}\hat{a}_{\text{in}}(\omega) - iG(\hat{b}(\omega) + \hat{b}^\dagger(\omega))}{i(\Delta - \omega) + \kappa/2}, \quad (1.61)$$

respectively, where $G = g|\alpha_0|$.

Using equations (1.60-1.61) we arrive at the operator for the mechanical fluctuations,

$$\hat{b}(\omega) = \frac{-\sqrt{\gamma_i}\hat{b}_{\text{in}}(\omega)}{i(\omega_m - \omega) + \gamma/2} + \frac{iG}{i(\omega_m - \omega) + \gamma/2} \left(\frac{\sqrt{\kappa}\hat{a}_{\text{in}}(\omega)}{i(\Delta - \omega) + \kappa/2} + \frac{\sqrt{\kappa}\hat{a}_{\text{in}}^\dagger(\omega)}{-i(\Delta + \omega) + \kappa/2} \right), \quad (1.62)$$

where we have absorbed the spring shift $\delta\omega_m$ into the mechanical frequency ($\omega_m \leftarrow \omega_m + \delta\omega_m$) and $\gamma = \gamma_i + \gamma_{\text{OM}}$ is the optically damped (or amplified) mechanical loss-rate. Expressions for the optical springing and damping terms are given by

$$\delta\omega_m = |G|^2 \text{Im} \left[\frac{1}{i(\Delta - \omega_m) + \kappa/2} - \frac{1}{-i(\Delta + \omega_m) + \kappa/2} \right] \quad (1.63)$$

and

$$\gamma_{\text{OM}} = 2|G|^2 \text{Re} \left[\frac{1}{i(\Delta - \omega_m) + \kappa/2} - \frac{1}{-i(\Delta + \omega_m) + \kappa/2} \right], \quad (1.64)$$

respectively. From these expressions it is evident that in the sideband-resolved regime the maximum optical damping occurs for a laser red-detuned from the optical cavity with $\Delta = \omega_m$, resulting in a damping rate of $\gamma_{\text{OM}} \cong 4|G|^2/\kappa$. The ratio between this optical contribution to the mechanical damping and the intrinsic mechanical damping is the co-operativity, $C \equiv \gamma_{\text{OM}}/\gamma_i$.

1.4 Simplified results for sideband-resolved systems

1.4.1 Quantum-limited laser cooling and damping

The expression for the noise power spectrum of the laser driven mechanical system can be calculated using eqn. (1.62) for $\hat{b}(\omega)$. More specifically, we calculate $S_{bb}(\omega)$ (see A.2), corresponding in the high- Q regime to the ability of the mechanical system to *emit* noise power into its environment [36]. The

³In this thesis I use the notation where $\hat{a}^\dagger(\omega)$ is the Fourier transform of $\hat{a}^\dagger(t)$ and equal to $(\hat{a}(-\omega))^\dagger$. This is outlined in Appendix A.

area under $S_{bb}(\omega)$ is the average mode occupancy of the mechanical quantum oscillator. In the absence of the optical coupling to the mechanics ($G = 0$), the result in A.2 is obtained. Allowing for optical coupling and including the optical noise terms, we arrive at an expression involving the correlations $\langle \hat{a}_{\text{in}}^\dagger(\omega)\hat{a}_{\text{in}}(\omega') \rangle$, and $\langle \hat{a}_{\text{in}}(\omega)\hat{a}_{\text{in}}^\dagger(\omega') \rangle$ that must be calculated from the properties of the optical bath. Assuming that our source of light is a pure coherent tone, and thus the optical bath is in a vacuum state, as is approximately the case in many optical experiments, the former correlation can be set to zero, while the latter gives $\delta(\omega + \omega')$. As described in A.2, for the mechanical system that is in contact with a thermal bath of occupancy n_b , we have noise input correlations of $\langle \hat{b}_{\text{in}}(\omega)\hat{b}_{\text{in}}^\dagger(\omega') \rangle = (n_b + 1)\delta(\omega + \omega')$ and $\langle \hat{b}_{\text{in}}^\dagger(\omega)\hat{b}_{\text{in}}(\omega') \rangle = n_b\delta(\omega + \omega')$. The expression for $S_{bb}(\omega)$ is then found to be,

$$S_{bb}(\omega) = \frac{\gamma n_f(\omega)}{(\omega_m + \omega)^2 + (\gamma/2)^2}, \quad (1.65)$$

where $n_f(\omega)$, the back-action modified phonon occupation number, is given by

$$n_f(\omega) = \frac{\gamma_i n_b}{\gamma} + \frac{|G|^2 \kappa}{\gamma} \frac{1}{(\Delta - \omega)^2 + (\kappa/2)^2}. \quad (1.66)$$

In the *driven weak-coupling* regime ($\kappa \gg \gamma$), the mechanical lineshape is not strongly modified from that of a Lorentzian, and $n_f(\omega)$ can simply be replaced by $n_f(-\omega_m)$ in eqn. (1.65). An input laser beam tuned to a mechanical frequency red of the cavity for optimal laser cooling ($\Delta = \omega_m$), results in a back-action modified average mechanical mode occupation number equal to

$$\langle \hat{n} \rangle |_{\Delta=\omega_m} = \frac{\gamma_i n_b}{\gamma} + \frac{\gamma_{\text{OM}}}{\gamma} \left(\frac{\kappa}{4\omega_m} \right)^2. \quad (1.67)$$

The term $n_{\text{qbl}} \equiv (\kappa/4\omega_m)^2$ is the quantum limit on back-action cooling, as derived in [37, 38] using master-equation methods and in [39] by taking into account the spectral density of the optical back-action force. This small (in the good cavity limit) residual heating comes from the non-resonant scattering of red pump photons to one mechanical frequency lower, or a total of $2\omega_m$ detuned from the optical cavity.

We note briefly that for other laser detunings different back-action occupancies are achieved, such as

$$\langle \hat{n} \rangle |_{\Delta=0} = n_b + \frac{4|G|^2}{\gamma_i \kappa} \left(\frac{\kappa}{2\omega_m} \right)^2 \quad (1.68)$$

and

$$\langle \hat{n} \rangle |_{\Delta=-\omega_m} = \frac{\gamma_i n_b}{\gamma} + \frac{|\gamma_{\text{OM}}|}{\gamma}, \quad (1.69)$$

where again the resolved-sideband limit is assumed, and for $\Delta = -\omega_m$ one has amplification of the mechanical motion with $\gamma_{\text{OM}} \cong -4|G|^2/\kappa$ (which must be smaller than γ_i to avoid triggering instabilities.)

Chapter 2

Quantum and classical noise in optomechanical systems

ای چرخ فلک خرابی از کینه توست بیدادگری شیوه دیرینه توست

خیام

Cosmic wheel of heavens!

Decay, you impose upon us,

with anarchy, your ancient method.

— (Omar Khayyám 1048-1131)

Much of optomechanics concerns the study of noise, the effect of noise on detecting a signal, and the decay of coherences caused by the process of measurement. Whether it is the unpredictable thermal motion of a warm mechanical system, or the quantum fluctuations of the electromagnetic vacuum imparting random forces on a mechanical structure, the propagation and detection of noise is at the core of nearly all optomechanical experiments. In this chapter we present noise in optomechanical structures in the context of two different limits.

Both limits concern the weak-coupling regime ($g_0, G < \kappa$). In the first limit treated (Sec. 2.2), we assume that the cavity lifetime is much longer than the period of the mechanical oscillations ($\kappa \ll \omega_m$). This implies that each photon experiences many cycles of the mechanical motion before leaving the cavity. As such, the spectral selectivity of the resonator can be used to select out certain phonon-photon processes, while blocking others. Thus, the analysis of the problem is significantly simplified if a detuning roughly equal in magnitude to the mechanical frequency is selected. The

treatment in Sec. 2.2 is an expanded version of what was published in Safavi-Naeini et al. [4]. The second case treated (Sec. 2.3) concerns the bad-cavity or sideband-unresolved limit ($\kappa \gg \omega_m$). Under this assumption, the optical cavity can be adiabatically eliminated. The treatment in Sec. 2.3 has been previously presented in Safavi-Naeini et al. [40]. In both cases, the roles played by both classical and quantum noise are crucial to the experiments performed, and thus treated in detail. Additionally, since the *vacuum* weak-coupling regime is assumed ($g_0 \ll \kappa$), both treatments involve coupled linear systems. By performing Fourier analysis on the Heisenberg equations of motion, the analysis is reduced to simple algebraic manipulations resulting in simple analytic expressions with excellent accuracy. We start off, however, with an introduction to the basic ideas that provide a hopefully coherent strand connecting these experiments to one another.

2.1 The basic ideas

2.1.1 Measuring position with light

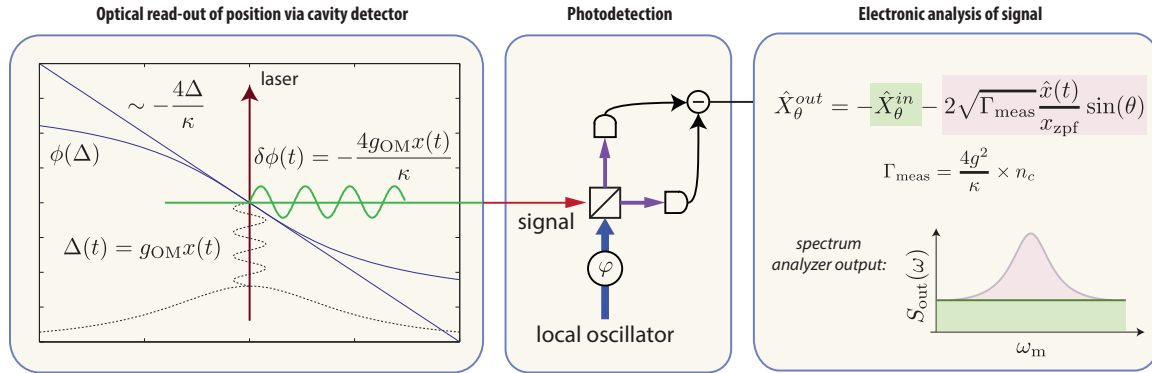


Figure 2.1: **Detection of motion with an optomechanical system.** See text for description.

Fluctuations in the position of the mechanical resonator cause the cavity frequency and hence the detuning between the laser and cavity to fluctuate. Assuming that the dynamics of the light in the cavity are not important at the time scale of these fluctuations and that the light is immediately lost to the detection channel (i.e. $\kappa \gg \omega_m$), the input light will be reflected from the cavity with additional fluctuations proportional to the motion. If the frequency of the laser is set nominally equal to that of the cavity, these fluctuations will be predominantly in the phase quadrature, since the magnitude of the reflection coefficient (and so the intensity of the reflected light) does not change to linear order at resonance. These phase fluctuations can be detected by a balanced homodyne setup, and an electronic signal is obtained containing both the phase fluctuations due to motion, and the quantum limited fluctuations of the light leading to shot-noise. By analyzing the noise Power Spectral Density (PSD) of this electronic signal, we can extract a variety of parameters of the mechanical

system, including its linewidth, and the average amplitude of its motion. The equipartition theorem then allows us to convert this average amplitude of motion to a mode temperature. As such, we call this type of measurement (and the analogous measurement in the sideband-resolved regime $\kappa \ll \omega_m$), “thermometry” or “calibrated thermometry” in this work.

2.1.2 Interference effects

Light propagating through an optomechanical system can take two paths. One is the path through the optical system, while the other involves going “through” the mechanics. The fact that there are two paths means that interference plays a crucial role in the optical response of these structures. Both destructive and constructive interference can occur. An example of constructive interference is the transparency window in EIT discussed in section 2.1.3. Destructive interference can cause a reduction in the noise on the light coming from an optomechanical resonator, which can lead to squeezed light. We introduce three basic manifestations of these interference effects, which have played a key role in the experiments presented in this thesis, in sections 2.1.3–2.1.5 below, and study these theoretically throughout the rest of this chapter.

2.1.3 Electromagnetically induced transparency in optomechanics

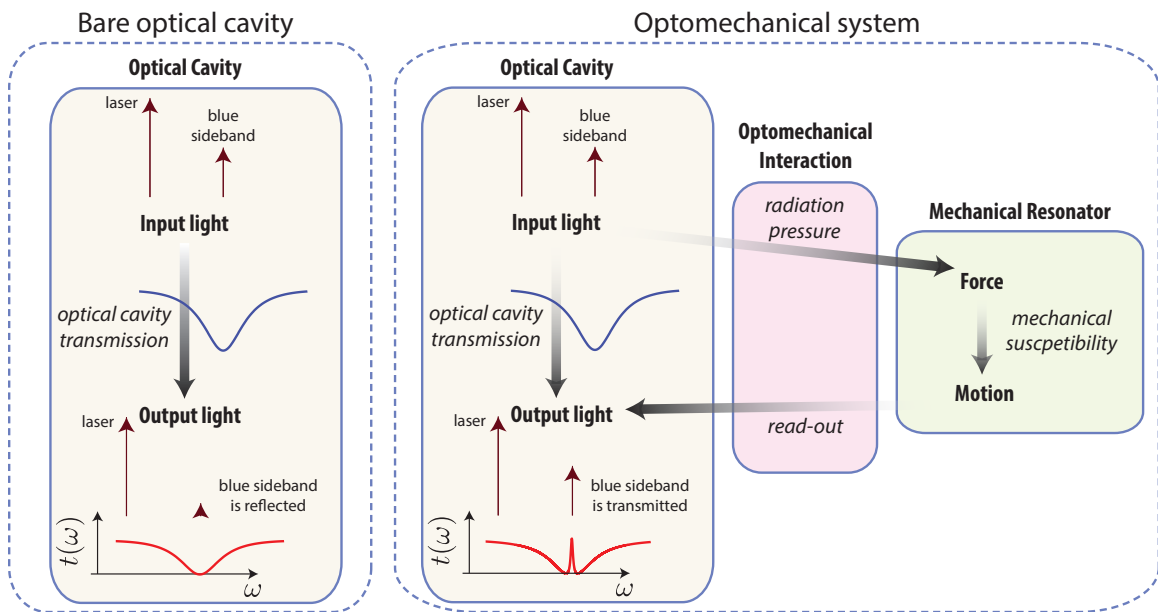


Figure 2.2: **Electromagnetically Induced Transparency in an Optomechanical System.** See text for description.

The radiation pressure force imparted on a mechanical resonator is proportional to the intensity of the light in the cavity. Modulation of the light causes this force to fluctuate, and by matching the

frequency of the modulation to the mechanical resonator’s natural frequency, large amplitude motion can be induced. Due to optomechanical coupling, this large amplitude motion, which is coherent with the input light modulation, is modulated back onto the light beam and significantly impacts the effective transmissivity and reflectivity of the modulated components of the light propagating through the system.

Modulated light in frequency domain has spectral components called sidebands. It is possible in principle to generate light with a single sideband as shown in Figure 2.2. The spectral response of a simple optical cavity allows one to filter this sideband, if its separation from the carrier is greater than the optical linewidth κ . For example, by placing the laser at a detuning $\Delta \gg \kappa$ equal to the sideband modulation frequency ($\Delta_{\text{mod}} = \Delta$), the sidebands becomes completely resonant with the cavity, and are thus reflected. The situation is different for an optomechanical cavity. As shown in Figure 2.2, the time dependent radiation pressure force generated by the beating between the laser and its sideband causes the mechanical system to oscillate at a large amplitude. This motion, up-converts light from the laser beam to exactly the sideband frequency, which is then emitted from the cavity. As we will show in section 2.2.1, at frequencies resonant with the mechanical motion, the sideband is fully transmitted and the reflection of the optical cavity is completely canceled. Thus, the cavity becomes transparent at a “two-photon detuning” (Δ) equal to the mechanical resonance frequency, thereby demonstrating EIT.

At its core, EIT in optomechanics arises from interference between two paths that light can take – a direct path, and an indirect path through the mechanical resonator (see figure 2.2). More specifically, a single sideband is imprinted onto the motion of the mechanical system, and then converted back to light on the same channel, thereby leading to this interference. In a double slit experiment, the visibility of the interference pattern can be washed out by measurement of which-path information. In the case of the optomechanical system, an analogous “measurement” can be either accomplished by a second laser beam, or by the mechanical bath that the system is coupled to. Large transparency can only be achieved when the coupling of the mechanical system to other degrees of freedom is minimized (high co-operativity). Often, we present this effect in its entirety in terms of sideband reflection and transmission coefficients $r(\omega)$ and $t(\omega)$, respectively (see section 2.2.1).

2.1.4 Classical laser noise in thermometry: squashing and anti-squashing

The propagation of laser noise through the driven optomechanical cavity follows essentially the same physics outlined above. Instead of considering a single coherently generated sideband, we consider all the noise photons that surround the laser frequency over a much larger bandwidth. One must consider the type noise (intensity or phase), and the type of detection being performed in the experiment (direct detection of intensity or measurement of quadratures).

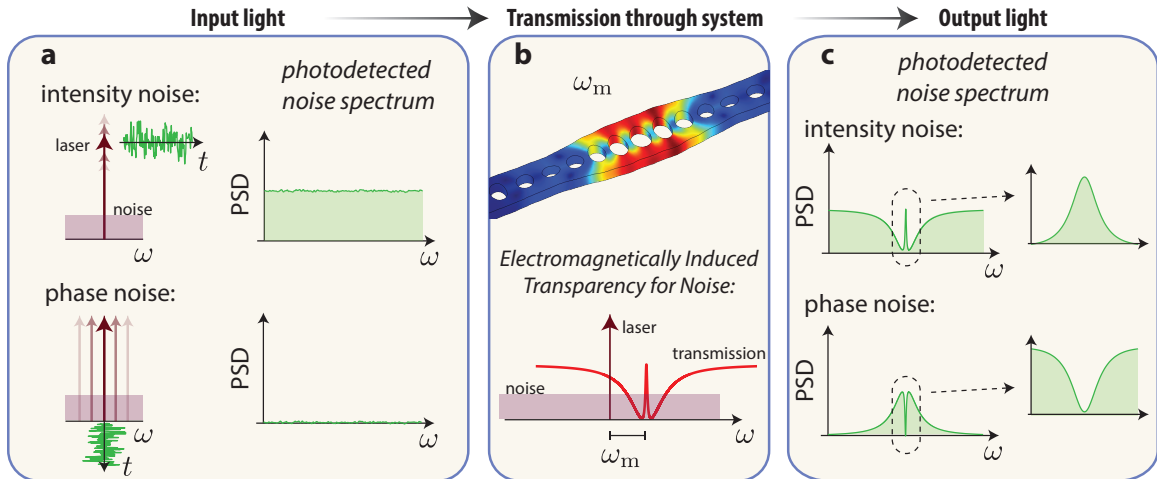


Figure 2.3: **Classical laser noise in a sideband-resolved optomechanical system.** See text for description.

For laser light exhibiting classical intensity fluctuations, the detected signal in a direct detection scheme measuring the intensity of incident light will have some noise PSD (taken here to be flat over some frequency range) as shown in Fig. 2.3a. Classical phase fluctuations involve no change in the intensity, and so no noise will be detected in a direct detection measurement¹. Propagation through a dispersive optical element with transmission $t(\omega)$ changes the type of noise detected, leading to qualitatively different spectral features at the detector.

The transmission spectrum of the cavity filters out some of the intensity fluctuations at frequencies ω where ω is within the cavity linewidth, but detuned from the mechanical system (i.e., for ω satisfying $\gamma < |\omega - \Delta| < \kappa$ and $\Delta \approx \omega_m$). This causes a drop in the noise floor. At the mechanical frequency, and within the transparency window, all intensity fluctuations travel through the system and the larger noise floor, expected without the presence of the optical cavity, will be detected. Effectively, the spectrum will exhibit a Lorentzian peak with the mechanical linewidth (see Fig. 2.3c). The mechanical resonator motion will be heated due to the noise on the laser; however if one is unaware of the intensity noise on the laser, an estimation of the temperature from the size of this peak will lead to an enhanced *inferred* bath temperature. This is essentially due the constructive interference between the motion undergoing fluctuations correlated with the laser noise, and the laser noise itself.

The situation is perhaps more interesting for the case of phase noise. Here the light will seem “quiet” in a direct detection measurement unless it interacts with a dispersive component (such as an optical cavity) converting frequency fluctuations to intensity fluctuations. For $\Delta = \omega_m$, a transparency window will appear about $\omega = \omega_m$, making the system transparent over the bandwidth

¹There will still be shot-noise due to quantum fluctuations that are treated in the following section.

of the mechanical, and thus the noise floor will exhibit a minimum (since the phase noise will not be converted to intensity fluctuations). On the other hand, the noise floor at frequencies ω outside the mechanical linewidth, but inside the optical linewidth ($\gamma < |\omega - \Delta| < \kappa$), will be enhanced from optical filtering of half the phase noise spectrum. This means that a measurement of the noise PSD will show an inverted Lorentzian with the same frequency and linewidth expected from the mechanical system. Any additional thermal noise will add to this noise floor. This effect is called noise squashing, as any calculation of a phonon occupation number from such a spectrum will yield smaller (and even negative!) inferred phonon occupancies. This squashing effect is analyzed in detail in section 2.2.

2.1.5 Quantum back-action interference and Squeezing

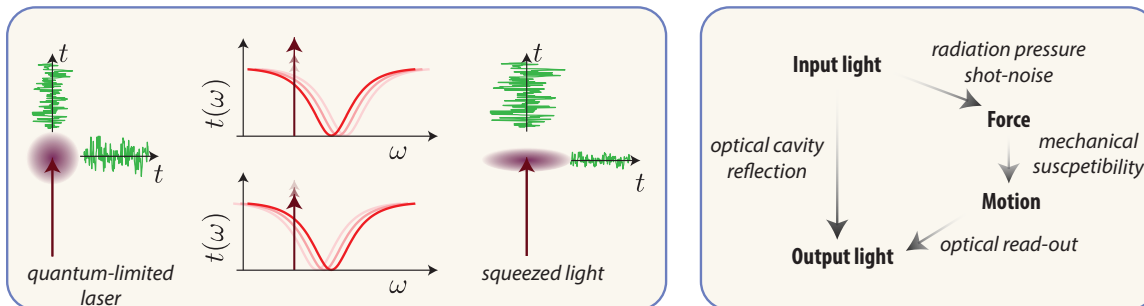


Figure 2.4: **Squeezed light from a sideband-unresolved optomechanical system.** See text for description.

Combining Maxwell’s equations with quantum mechanics leads to the conclusion that fields fluctuate. Effectively, this means that a perfectly ‘noise-less’ laser cannot exist. We can represent these fluctuations by a density or an “uncertainty ball” in phase space, shown in figure 2.4. The size or area of this ball is bounded below by quantum mechanics and the uncertainty principle, but otherwise an experimentalist is free to change its shape.

Just as classical noise can be imprinted onto the motion, and subsequently read out, leading to interesting modifications of the noise spectrum, quantum noise can also be modified in the same way. We observe this effect explicitly in two of our experiments. The first experiment (presented in section 5.2 and Ref. [3]), which is in the good-cavity regime ($\kappa < \omega_m$), consists of a measurement of an asymmetry in the motional sidebands. We show in section 2.2.2.1 (see Ref. [4, 41]), that this effect can be interpreted to arise exactly from such interference in the quantum noise of light. In a second experiment, presented in section 5.3 (see Ref. [40]), we show that this interference can be used to obtain light that is squeezed, i.e quieter than the electromagnetic vacuum in certain respects. We present below a simple physical picture of how squeezing works in optomechanical resonators. A fully rigorous derivation is presented in section 2.3.

The arguments made above in sections 2.1.3 and 2.1.4, treat primarily the sideband-resolved case, and here we consider this effect in a sideband-unresolved system (where $\kappa \gg \omega_m$) for simplicity. It is apparent that the intensity fluctuations of light cause a fluctuating force on the mechanical system due to radiation pressure. This fluctuating force shifts the optical resonator's frequency due to optomechanical coupling. Considering the case of a detuned cavity, this fluctuation of the cavity frequency causes the cavity transmission to also fluctuate, modulating the amount of light that is transmitted. By placing the laser on the red side of the cavity, this fluctuation of the cavity transmission effectively counter-acts the laser's intensity fluctuations, and so the reflected light will have a smaller amount of intensity noise. For example, an increasing intensity causes the cavity to shift red, so the transmission on the red side of the cavity drops, counter-acting the increased intensity (see Figure 2.4). The flip-side is that a fluctuating cavity means that the phase of the light transmitted will have excess noise due to the optical resonator's phase response. So in effect, intensity fluctuations are traded for phase fluctuations in this simple heuristic model.

2.2 Sideband-resolved systems

We present here some of the basic theoretical results for quantum and classical noise propagation through a sideband-resolved optomechanical system. The experiments relating to this section were performed with direct coupling via a fiber taper coupler; hence, a two-sided coupling is assumed. This means that the total optical decay rate $\kappa = \kappa_i + \kappa_e$ is composed of an intrinsic component κ_i and two extrinsic components, with magnitude $\kappa_e/2$ each, to the forward and backward propagating waves in the fiber (see section 1.2.2 and Figure 1.1a). The Langevin equations used are given by²

$$\dot{\hat{b}}(t) = -\left(i\omega_m + \frac{\gamma_i}{2}\right)\hat{b} - ig\hat{a}^\dagger\hat{a} - \sqrt{\gamma_i}\hat{b}_{\text{in}}(t)$$

and

$$\dot{\hat{a}}(t) = -\left(i\Delta + \frac{\kappa}{2}\right)\hat{a} - ig\hat{a}(\hat{b}^\dagger + \hat{b}) - \sqrt{\kappa_e/2}\hat{a}_{\text{in}}(t) - \sqrt{\kappa'}\hat{a}_{\text{in},i}(t). \quad (2.1)$$

2.2.1 Electromagnetically induced transparency and amplification

We start with deriving the optical response of an optomechanical system being driven by a laser tone at frequency ω_L . This can be done by formally replacing the optical cavity annihilation operator with time varying amplitude consisting of the laser tone, and its two sidebands α_- and α_+

$$\hat{a} \rightarrow \alpha_0 e^{-i\omega_L t} + (\alpha_- e^{-i(\omega_L + \Delta_{\text{mod}})t} + \alpha_+ e^{-i(\omega_L - \Delta_{\text{mod}})t}). \quad (2.2)$$

²Compare to equation 1.47. These equations hold just as well for the sideband-unresolved case. We simply re-state them here, to clarify the coupling scheme used in all the results presented in this section.

The mechanical motion will experience a time varying force at frequency Δ_{mod} , and thus the phonon amplitude will also consist of a static part β_0 , due to a DC radiation pressure shift, and a time varying part at frequency β_- .

$$\hat{b} \rightarrow \beta_0 + \beta_- e^{-i\Delta_{\text{mod}}t}. \quad (2.3)$$

The Langevin equations of motion of equation (1.59) are then reduced to the following algebraic equations ($\beta_+ = \beta_-^*$):

$$\pm i\Delta_{\text{mod}}\alpha_{\pm} = -\left(i\Delta + \frac{\kappa}{2}\right)\alpha_{\pm} - ig\alpha_0\beta_{\pm} - \sqrt{\frac{\kappa_e}{2}}\alpha_{\text{in},\pm}, \quad (\Delta = \omega_c - \omega_L) \quad (2.4)$$

$$-i\Delta_{\text{mod}}\beta_- = -\left(i\omega_m + \frac{\gamma_i}{2}\right)\beta_- - ig(\alpha_0^*\alpha_- + \alpha_0\alpha_+^*) - \sqrt{\gamma_i}\beta_{\text{in},-}. \quad (2.5)$$

At this point, we make approximations that simplify the derivations and apply well to the sideband resolved regime. First, we assume that, in addition to the laser (α_0), only intracavity population in the blue sideband (α_-) is involved in the dynamics and set $\alpha_+ = 0$ (see section 2.2.1.1). This rotating wave approximation holds when $\Delta \approx \omega_m \gg \kappa$. Then, we make a very similar approximation for the opposite detuning case ($-\Delta \gg \kappa$), i.e. set $\alpha_- = 0$ (see section 2.2.1.3). The fully general derivation of the optical cavity response is required to understand squeezing and is presented later in section 2.3.3.

2.2.1.1 Electromagnetically induced transparency

For $\alpha_+ = 0$, $\Delta \gg \kappa$ we obtain

$$\alpha_- = \frac{-\sqrt{\kappa_e/2}}{i(\Delta - \Delta_{\text{mod}}) + \frac{\kappa}{2} + \frac{|G|^2}{i(\omega_m - \Delta_{\text{mod}}) + \gamma_i/2}}\alpha_{\text{in},-}. \quad (2.6)$$

Assuming here that $\Delta = \omega_m$, and that the intrinsic mechanical loss-rate is negligible ($\gamma_i \approx 0$), several interesting properties of this relation immediately become apparent. First, at driving resonant with the mechanical frequency $\Delta_{\text{mod}} = \omega_m$, the denominator of equation (2.6) blows up, and $\alpha_- \rightarrow 0$. In other words, photons *directly resonant* with the optical cavity are prevented from entering it, due to the presence of the coupled mechanical resonator. This counter-intuitive behaviour gives rise to an interesting optical transmission spectrum. We are interested in the response due to the mechanical system, and so to ignore the cavity dispersion, we assume $\kappa \gg |\Delta - \Delta_{\text{mod}}|$. In this limit,

$$\alpha_- \approx \frac{-\sqrt{\kappa_e/2}\alpha_{\text{in},-}}{i(\omega_m - \Delta_{\text{mod}}) + 2|G|^2/\kappa} \times \frac{2}{\kappa} \times i(\omega_m - \Delta_{\text{mod}}), \quad (2.7)$$

the transmission given by the input-output boundary condition (eqn. (1.48)) is given by

$$\alpha_{\text{out},-} \approx \alpha_{\text{in},-} \left[\left(1 - \frac{\kappa_e}{\kappa}\right) + \frac{\kappa_e}{\kappa} \frac{\gamma_{\text{OM}}/2}{i(\omega_m - \Delta_{\text{mod}}) + \gamma_{\text{OM}}/2} \right]. \quad (2.8)$$

where $\gamma_{\text{OM}} = 4|G|^2/\kappa$. Note that the loaded mechanical linewidth derived here agrees with the sideband-resolved limit of equation (1.64). It is clear that over a bandwidth of γ_{OM} , the optomechanical cavity becomes transparent, hence the effect is called EIT. The full transmission coefficient for sideband α_- (assuming $\alpha_+ = 0$) can be found easily from equation (2.6) and the input-output boundary condition (eqn. (1.48))

$$t(\Delta_{\text{mod}}) = 1 - \frac{\kappa_e/2}{i(\Delta - \Delta_{\text{mod}}) + \frac{\kappa}{2} + \frac{|G|^2}{i(\omega_m - \Delta_{\text{mod}}) + \gamma_i/2}}. \quad (2.9)$$

The sideband reflection coefficient is also found in a similar manner, and is given by

$$r(\Delta_{\text{mod}}) = -\frac{\kappa_e/2}{i(\Delta - \Delta_{\text{mod}}) + \frac{\kappa}{2} + \frac{|G|^2}{i(\omega_m - \Delta_{\text{mod}}) + \gamma_i/2}}. \quad (2.10)$$

Both of these expressions can be simplified for $\kappa \gg |\Delta - \Delta_{\text{mod}}|$, $\Delta = \omega_m$, as shown in Appendix A.4.

2.2.1.2 Group delay

For the red-detuned system, the existence of an effective transparency on transmission makes the group delay imparted on the pulse an interesting quantity. To calculate the reflection and transmission group delays we consider a pulse

$$f(t_o) = \int_0^\infty f(\omega) e^{-i\omega t_o} d\omega, \quad (2.11)$$

where most of the spectrum is confined to a small window ($< 4G^2/\kappa$) about a central signal frequency ω_s . Then the transmitted signal $f^{(\text{T})}(t_o)$ may be written as

$$\begin{aligned} f^{(\text{T})}(t_o) &= \int_0^\infty t(\omega) f(\omega) e^{-i\omega t_o} d\omega \\ &= e^{-i\omega_s t_o} \int_{-\infty}^\infty t(\omega_s + \delta) f(\omega_s + \delta) e^{-i\delta t_o} d\delta \\ &= e^{-i\omega_s t_o} \int_{-\infty}^\infty t(\omega_s) \left(1 + \frac{1}{t(\omega_s)} \frac{dt}{d\omega} \Big|_{\omega_s} \delta + o(\delta^2) \right) f(\omega_s + \delta) e^{-i\delta t_o} d\delta \\ &\approx e^{-i\omega_s t_o} \int_{-\infty}^\infty t(\omega_s) f(\omega_s + \delta) e^{-i\delta(t_o - \tau^{(\text{T})})} d\delta \end{aligned} \quad (2.12)$$

The last line implies that $f^{(\text{T})}(t_o) \approx f(t_o - \tau^{(\text{T})})$, where

$$\tau^{(\text{T})} = \text{Re} \left\{ \frac{-i}{t(\omega_s)} \frac{dt}{d\omega} \right\}. \quad (2.13)$$

The reflection group delay may also be defined analogously,

$$\tau^{(\text{R})} = \text{Re} \left\{ \frac{-i}{r(\omega_s)} \frac{dr}{d\omega} \right\}. \quad (2.14)$$

With the signal sent at a two-photon detuning $\Delta_{\text{mod}} = \omega_m$, we find

$$\tau^{(\text{T})}|_{\Delta_{\text{mod}}=\omega_m} = \frac{2}{\gamma_i} \frac{(\kappa_e/\kappa)C}{(1+C)(1 - (\kappa_e/\kappa) + C)}, \quad (2.15)$$

where the cooperativity $C = 4G^2/\kappa\gamma_i$ is a measure of the coupling between the mechanical oscillator and the optical bath. Under the same conditions, we find that group delay for reflection is given by

$$\tau^{(\text{R})}|_{\Delta_{\text{mod}}=\omega_m} = -\frac{2}{\gamma_i} \frac{C}{1+C}, \quad (2.16)$$

resulting in the limit $C \gg 1$

$$\tau^{(\text{T})}|_{\Delta_{\text{mod}}=\omega_m} \rightarrow \frac{2}{\gamma_i} \frac{\kappa_e}{\kappa} \frac{1}{C} \quad \text{and} \quad \tau^{(\text{R})}|_{\Delta_{\text{mod}}=\omega_m} \rightarrow -\frac{2}{\gamma_i}. \quad (2.17)$$

A quantity of interest, the delay-bandwidth product, can be calculated for the transmitted signal by taking the product of the signal delay $|\tau^{(\text{T})}|_{\text{max}}$ and the bandwidth $\Delta\omega = \gamma_i C$, to give us the delay bandwidth product which is independent from the parameters of the optomechanical system, and depends only on the coupling efficiency from the feeding waveguide to the resonator:

$$\Delta\omega \cdot t_d = \frac{2\kappa_e}{\kappa}. \quad (2.18)$$

Using equations 2.15 and 2.43, we can estimate the maximum delay for our system. The reflection and transmission coefficients at resonance ($\Delta_{\text{mod}} = \Delta = \omega_m$) are given by

$$r_{\text{max}} = -\frac{(\kappa_e/\kappa)}{1+C} \quad \text{and} \quad t_{\text{max}} = \frac{1 - (\kappa_e/\kappa) + C}{1+C}. \quad (2.19)$$

For the case where intrinsic optical losses are negligible, i.e. $\kappa_e = \kappa$, the equations for transmission coefficient contrast and delay can be written as

$$t_{\text{max}} = \frac{C}{1+C}, \quad \tau_{\text{max}}^{(\text{T})} = \frac{2}{\gamma_i} \frac{1}{(1+C)}, \quad (2.20)$$

respectively.

2.2.1.3 Electromagnetically induced absorption and amplification

An effect similar to EIT occurs for laser pump frequencies detuned to the blue side of optical cavity ($-\Delta = \omega_m$). These effects have been experimentally observed by several different groups [2, 42, 43], and in our experiments as described in section 5.1. A brief classical treatment of this result is provided here.

Starting from equations (2.4) and (2.5), we make the approximation that $\alpha_- = 0$ (valid for $-\Delta \approx \omega_m \gg \kappa$), and arrive at

$$\alpha_+ = \frac{-\sqrt{\kappa_e/2}}{i(\Delta + \Delta_{\text{mod}}) + \frac{\kappa}{2} + \frac{|G|^2}{i(\omega_m - \Delta_{\text{mod}}) - \gamma_i/2}} \alpha_{\text{in},+}. \quad (2.21)$$

The basic amplification properties are already apparent from this expression, and from the reflection $r^A(\Delta_{\text{mod}}) = \sqrt{\kappa_e/2} \alpha_+ / \alpha_{\text{in},+}$:

$$r_A(\Delta_{\text{mod}}) = -\frac{\kappa_e/2}{i(\Delta + \Delta_{\text{mod}}) + \kappa/2 + \frac{|G|^2}{i(\omega_m - \Delta_{\text{mod}}) - \gamma_i/2}}. \quad (2.22)$$

To find the response modification due to the mechanical system, we assume $\kappa \gg |\Delta + \Delta_{\text{mod}}|$ (so we look at sidebands well within the cavity linewidth). In this limit,

$$r_A(\Delta_{\text{mod}}) \rightarrow -\frac{\kappa_e/2}{i(\omega_m - \Delta_{\text{mod}}) - (\gamma_i - |\gamma_{\text{OM}}|)/2} \times \frac{2}{\kappa} \times [i(\omega_m - \Delta_{\text{mod}}) - \gamma_i/2]. \quad (2.23)$$

We have kept γ_i in these expressions, since an additional requirement that does not exist for red-side pumping is that $|\gamma_{\text{OM}}| < \gamma_i$, otherwise the mechanical resonator will start oscillations otherwise. From here it is apparent that a total gain of of $\kappa_e/\kappa \times \gamma_i/(\gamma_i - |\gamma_{\text{OM}}|)$ can be obtained on resonance, with a bandwidth of roughly $\gamma_i - |\gamma_{\text{OM}}|$. The full simplified expressions for both reflection and transmission are provided in the Appendix (see A.4.2), and are used below to understand the properties of sideband thermometry.

2.2.2 Thermometry using the detected photocurrent

One of the simplest methods of inferring the mechanical mode occupancy is to detect the imprinted mechanical motion on the cooling laser beam itself. Upon transmission through the cavity-optomechanical system, the laser cooling beam, typically detuned to $\Delta = \omega_m$ in the resolved sideband regime, preferentially picks up a blue-shifted sideband at frequency $\omega_L + \omega_m$ ($\approx \omega_o$) due to removal of phonon quanta from the mechanical resonator (anti-Stokes scattering). Upon detection with a photodetector, the beating of the anti-Stokes sideband with the intense cooling tone produces an electrical signal at the mechanical frequency [44–46]. By careful calibration and accurate measurement of the magnitude of this signal, and through independent measurements of other system

parameters such as g , $|\alpha_0|$, κ_e , and κ , the mechanical resonator's average phonon number occupancy can be inferred. Note that no other thermometry is required for this procedure, though as a sanity check, we verify the inferred temperature at room temperature and find agreement in our experiments [3, 24, 46].

The optical fluctuations in the transmitted laser cooling beam at the output port of the optomechanical cavity are given approximately in the sideband resolved regime by

$$\hat{a}_{\text{out}}(\omega)|_{\Delta=\omega_m} \approx t(\omega; \Delta)\hat{a}_{\text{in}}(\omega) + n_{\text{opt}}(\omega; \Delta)\hat{a}_{\text{in},i}(\omega) + s_{12}(\omega; \Delta)\hat{b}_{\text{in}}(\omega), \quad (2.24)$$

where t , n_{opt} , and s_{12} are the scattering matrix elements evaluated for a laser cooling beam of red-detuning $\Delta = \omega_m$ (see A.4 and equation (2.8)). This expression is derived using eqns. (1.60-1.61) and input-output boundary condition $\hat{a}_{\text{out}}(\omega) = \hat{a}_{\text{in}}(\omega) + \sqrt{\kappa_e/2}\hat{a}(\omega)$. Expressions of this form will be used later in section 6.2 in the context of state-transfer [5, 6]. In this case, we have simplified eqn. (2.24) by ignoring input noise terms from the creation operators $\hat{a}_{\text{in}}^\dagger(\omega)$ and $\hat{a}_{\text{in},i}^\dagger(\omega)$. These terms gives rise to the quantum-limit of laser cooling found in eqn. (1.67) above, but insignificantly modify the optically transduced signal of the mechanical motion as long as $\langle \hat{n} \rangle \gg n_{\text{qbl}}$.

The strong cooling laser tone beats with the optical noise sidebands at the photodetector, generating a photocurrent proportional to $\hat{a}_{\text{out}}(t) + \hat{a}_{\text{out}}^\dagger(t)$,

$$\begin{aligned} \hat{I}(\omega)|_{\Delta=\omega_m} &= t(\omega)\hat{a}_{\text{in}}(\omega) + n_{\text{opt}}(\omega)\hat{a}_{\text{in},i}(\omega) + s_{12}(\omega)\hat{b}_{\text{in}}(\omega) + \\ &+ \text{h.c.}(-\omega) \end{aligned}$$

where $\text{h.c.}(-\omega)$ is a convenient short-hand ($f(\omega) + (f(-\omega))^\dagger = f(\omega) + \text{h.c.}(-\omega)$). The resulting photocurrent PSD, as read out from a spectrum analyzer, is given by

$$\begin{aligned} S_{II}(\omega)|_{\Delta=\omega_m} &= \int_{-\infty}^{\infty} d\omega' \langle \hat{I}^\dagger(\omega)\hat{I}(\omega') \rangle \\ &= \int_{-\infty}^{\infty} t(\omega)t(-\omega')^* \langle \hat{a}_{\text{in}}(\omega)\hat{a}_{\text{in}}^\dagger(\omega') \rangle + n_{\text{opt}}(\omega)n_{\text{opt}}(-\omega')^* \langle \hat{a}_{\text{in},i}(\omega)\hat{a}_{\text{in},i}^\dagger(\omega') \rangle \\ &+ s_{12}(\omega)s_{21}(-\omega')^* \langle \hat{b}_{\text{in}}(\omega)\hat{b}_{\text{in}}^\dagger(\omega') \rangle + s_{12}(-\omega)s_{21}(\omega')^* \langle \hat{b}_{\text{in}}^\dagger(\omega)\hat{b}_{\text{in}}(\omega') \rangle d\omega', \end{aligned} \quad (2.25)$$

where we have assumed the same optical (vacuum) and mechanical (thermal) noise correlations as above in evaluating eqn. (1.65). Using the normalization property of the scattering matrix coefficients ($|t(\omega)|^2 + |n_{\text{opt}}(\omega)|^2 + |s_{12}(\omega)|^2 = 1$), we find the simplified expression

$$S_{II}(\omega)|_{\Delta=\omega_m} = 1 + n_b(|s_{12}(\omega)|^2 + |s_{12}(-\omega)|^2). \quad (2.26)$$

Substituting for the expression of the phonon-photon scattering element $s_{12}(\omega)$, given in appendix A.4

for $\Delta = \omega_m$ yields

$$S_{II}(\omega)|_{\Delta=\omega_m} = 1 + \frac{\kappa_e}{2\kappa} \frac{8|G|^2}{\kappa} \bar{S}_{bb}(\omega; \langle \hat{n} \rangle), \quad (2.27)$$

for the transduced noise PSD, where $\langle \hat{n} \rangle$ is the actual mechanical mode occupancy including back-action effects of the cooling laser (see eqn. (1.67)).

Several points are worth mentioning with regard to this expression. Firstly, the signal to noise goes as the coupling efficiency $\eta = \kappa_e/2\kappa$. In the case of non-ideal measurement, i.e., losses in the optical path from cavity to detector, or an imperfect detector, the efficiency would be multiplied by an additional factor $\eta_{\text{detection}}$ which is taken to be unity throughout this work. Secondly, the detected signal is proportional to $\langle \hat{b}^\dagger \hat{b} \rangle$, as opposed to $\langle \hat{b}^\dagger \hat{b} \rangle + 1/2$, and so the resulting signal is exactly what would be expected classically, vanishing as the temperature and phonon occupation go to zero. In other words, this measurement is insensitive to the zero-point motion of the resonator. The spectral density $S_{bb}(\omega, \langle \hat{n} \rangle)$, represents the ability of the mechanical system to *emit* energy [36]. By tuning the laser to $\Delta = \omega_m$ in the sideband-resolved regime, it is exceedingly unlikely for the tone to drive the mechanics (since the required Stokes scattering process becomes non-resonant by $2\omega_m$), and so we gain little information about how the mechanical system *absorbs* energy from the optical bath. Finally, we note that equation (2.27) is general and holds for both low and high cooperativity.

2.2.2.1 Interpretation as quantum noise squashing

Though the scattering matrix formulation provides a consistent and systematic way of deriving the form of the detected signals, it does so by elimination of the position operator from the equations. It is interesting to reinterpret the experiment as a measurement of the position of the mechanical system [36], and we attempt to do so here³. For simplicity, the perfect coupling condition is assumed, i.e., $\kappa_e/2 = \kappa$. The output signal is then given by

$$\hat{a}_{\text{out}}(\omega)|_{\Delta=\omega_m} \approx -\hat{a}_{\text{in}}(\omega) - \frac{i2G}{\sqrt{\kappa}} \hat{b}(\omega)$$

The normalized heterodyne current is found to be

$$\hat{I}(t)|_{\Delta=\omega_m} = -i\hat{a}_{\text{in}}(t) + i\hat{a}_{\text{in}}^\dagger(t) + \frac{2G}{\sqrt{\kappa}}(\hat{b}(t) + \hat{b}^\dagger(t)) \quad (2.28)$$

and so it would seem that the signal $\hat{I}(t)$ is composed of optical shot-noise and a component which is proportional to \hat{x} , making $S_{II} = 1 + \text{const} \times \langle \hat{x}^2 \rangle$. This, however, contradicts the above derivations which show that $S_{II} = 1 + \text{const} \times \langle \hat{n} \rangle$ for $\Delta = \omega_m$. The inconsistency comes after careful calculation

³A much more thorough treatment of the implications of quantum back-action and measurement theory in this type of system is presented in the work by Khalili, et al. [41].

of the correlation function $\langle \hat{I}(t + \tau) \hat{I}(t) \rangle$. In fact, $\hat{a}_{\text{in}}^\dagger(t)$ and $\hat{b}(t)$ are correlated, and the view that the shot-noise simply creates a constant noise floor is incorrect [47, 48]. Proper accounting for the correlations (see A.3) leads us again to eqn. (2.27), showing that the measured quantity is \bar{S}_{bb} , and the area of the detected spectrum is proportional to $\langle \hat{n} \rangle$.

The blue-side driving with $\Delta = -\omega_m$ causes the opposite effect, i.e., quantum noise anti-squashing. The squashing and anti-squashing are signatures of quantum back-action. This effect is, in spirit, similar to classical noise squashing, which we study in Section 2.2.4.2, where correlations between the noise-induced motion and *classical* noise of the detection beam destructively interfere at the photodetector. It is important to note that this signature of quantum back-action does not involve detection of quantum back-action heating (as demonstrated by Purdy et al. [49]), and can be apparent at arbitrarily low powers, far below those required to reach the standard quantum limit.

2.2.3 Motional sideband asymmetry thermometry

An alternate method of measuring the temperature of the mechanical subsystem, one which uses the mechanical zero-point motion to self-calibrate the measured phonon occupancy, involves comparing the measured signal from a weak probe beam (low cooperativity) at both $\Delta = \pm\omega_m$ in the sideband resolved regime [3]. In such experiments, the mechanics can be either laser cooled with a different laser and/or optical cavity mode, or the system can be cryogenically pre-cooled to a temperature which requires no further cooling to approach the quantum ground state. As the optical read-out beam can be arbitrarily weak in such measurements, it only marginally affects the dynamics of the mechanical system [3, 50, 51]. By working at low read-out beam power, such that the optically-induced damping and amplification rates are much smaller than the bare mechanical linewidth, optical back-action by the probe beam only minimally affects the dynamics of the mechanical system and measurements can be taken at detunings both red ($\Delta = \omega_m$) and blue ($\Delta = -\omega_m$) of the cavity without triggering any optomechanical instabilities [52]. Operating in the resolved sideband regime allows for the separate cavity filtering of the Stokes and anti-Stokes motionally induced sidebands on the probe beam, which are respectively proportional to $\langle \hat{n} \rangle + 1$ and $\langle \hat{n} \rangle$. It can be shown that the additional vacuum contribution to the Stokes scattering, which provides the intrinsic calibration for $\langle \hat{n} \rangle$, arises in these measurements equally from the shot noise on the probe laser and zero-point motion of the mechanical resonator [41]. We will also see in the following sections, that such a measurement at both $\Delta = \pm\omega_m$ can provide additional resilience to systematic errors from non-idealities such as laser phase noise.

We derive here the blue-detuned ($\Delta = -\omega_m$) result analogous to the red-detuned ($\Delta = \omega_m$) laser cooling case given above in eqn.(2.27). In the sideband-resolved regime, the approximations that led to eqn. (2.24), lead to a similar expression in the case of $\Delta = -\omega_m$ for the electromagnetic field

output from the optomechanical cavity

$$\hat{a}_{\text{out}}(\omega)|_{\Delta=-\omega_m} \approx t(\omega; \Delta)\hat{a}_{\text{in}}(\omega) + n_{\text{opt}}(\omega; \Delta)\hat{a}_{\text{in},i}(\omega) + s_{12}(\omega; \Delta)\hat{b}_{\text{in}}^\dagger(\omega). \quad (2.29)$$

where we have neglected the terms proportional to the photon noise creation operators, as their effect is minimal on the optically transduced signal of the mechanical motion in the sideband-resolved weak coupling regime when $\langle n \rangle \gg n_{\text{qbl}}$. The scattering relation, which was partially derived in section 2.2.1.3 and whose exact form is shown in the appendix A.4, allows the optomechanical system to act as an amplifier, and has been studied experimentally at microwave [42] and optical frequencies [2], and studied more generally in the context of optomechanics by Botter, et al. [53]. The scattering elements satisfy the equation $|t(\omega)|^2 + |n_{\text{opt}}(\omega)|^2 + |s_{12}(\omega)|^2 = 1$, which, along with the standard bath correlation relations used above, allows us to write

$$S_{II}(\omega)|_{\Delta=-\omega_m} = 1 + (n_b + 1)(|s_{12}(\omega; \Delta)|^2 + |s_{12}(-\omega; \Delta)|^2) \quad (2.30)$$

$$= 1 + \frac{\kappa_e}{2\kappa} \frac{8|G|^2}{\kappa} \bar{S}_{b^\dagger b^\dagger}(\omega; \langle \hat{n} \rangle), \quad (2.31)$$

where $\langle \hat{n} \rangle$ is the actual mode occupancy including back-action of the laser input (see eqn. (1.69)). As before, the signal lies on top of a flat shot noise background of unity, and is proportional to the detection efficiency η and the measurement rate γ_{OM} . Now, however, the signal is proportional to the creation operator spectral density $\bar{S}_{b^\dagger b^\dagger}(\omega; \langle \hat{n} \rangle)$, which itself is proportional to $\langle \hat{n} \rangle + 1$. The spectral density $\bar{S}_{b^\dagger b^\dagger}(\omega; \langle \hat{n} \rangle)$ can be interpreted as the mechanical system's ability to *absorb* energy [54], which even at zero temperature (occupation) can absorb energy through spontaneous scattering process, which arises due to the zero-point motion of the mechanical resonator.

For a constant laser driving power, the optomechanical damping and amplification rates for detuning $\Delta = \pm\omega_m$ are equal in magnitude but opposite in sign, with

$$\gamma_\pm \equiv \gamma_i \pm |\gamma_{\text{OM}}|, \quad \text{where} \quad (2.32)$$

$$|\gamma_{\text{OM}}| \cong 4|G|^2/\kappa, \quad (2.33)$$

in the sideband resolved, weak coupling regime. Weak probing entails using a probe intensity such that $|\gamma_{\text{OM}}| \ll \gamma_i$, or $C_r \ll 1$, where we define $C_r \equiv |\gamma_{\text{OM}}|/\gamma_i$ as the read-out beam cooperativity. In this limit the mechanical mode occupation numbers for $\Delta = \pm\omega_m$ detunings are given approximately by $\langle \hat{n} \rangle_\pm \cong \gamma_i n_b / \gamma_\pm$, where n_b is the mechanical mode occupancy in absence of the probe field⁴. Denoting the integrated area under the Lorentzians in eqns. (2.27) and (2.31) as I_+ and I_- , respectively, we find a relation between their ratios and the read-out cooperativity that provides a

⁴Referring to eqns. (1.67) and (1.69), this is an accurate relation if $C_r \ll n_b$.

quantum calibration of the unperturbed thermal occupancy [3]:

$$\eta \equiv \frac{I_-/I_+}{1 + C_r} - \frac{1}{1 - C_r} = \frac{1}{n_b}. \quad (2.34)$$

2.2.4 Laser phase noise

Although various other noise sources (laser intensity noise, internal cavity noise [55], etc.) can be treated similarly, here we focus on laser phase noise, as it is typically the most important source of nonideality in the laser cooling and thermometry of cavity optomechanical systems. In our measurements, we have ruled out intensity noise as a significant source of systematic error, as described in Appendix B. Detection of laser phase noise and its effect on the experiment is more involved, and recent measurements of phase noise in lasers of a similar make and model as ours have been reported [56]. The effect of phase noise on optomechanical systems has also been of great interest and studied at depth in the context of heating [57] and entanglement [58–60] of light and mechanics. However, laser light often acts as both a means by which the mechanical system is cooled as well as its temperature measured, and thus laser noise can effect both the true and inferred mechanical mode occupancy. Here we complement previous studies of laser noise heating with a unified analysis that also quantifies the effects of quantum and classical (phase) laser noise on the optically-transduced mechanical mode spectra.

The optical laser field amplitude input to the optomechanical system, in a rotating reference frame at frequency ω_L and in units of $\sqrt{\text{photons/s}}$, we denote by E_0 . Due to processes internal to the laser, some fundamental in nature, others technical, this amplitude undergoes random phase fluctuations which are captured by adding a random rotating phase factor [61]

$$E_0(t) = |E_0|e^{i\phi(t)}. \quad (2.35)$$

As long as the phase fluctuations are small, we expand this expression to first order yielding $E_0(t) \approx |E_0|(1 + i\phi(t) + O(\phi^2))$ [57]. Then

$$\langle E_0^*(\tau)E_0(0) \rangle = |E_0|^2 (1 + \langle \phi(\tau)\phi(0) \rangle).$$

In this way, we can express the noise PSD of the optical field amplitude, $S_{EE}(\omega)$, as

$$S_{EE}(\omega) = |E_0|^2 (2\pi\delta(\omega) + \bar{S}_{\phi\phi}(\omega)), \quad (2.36)$$

where we have also used the realness of $\phi(t)$ to set $S_{\phi\phi}(\omega) = \bar{S}_{\phi\phi}(\omega)$. The $\delta(\omega)$ term is due to the carrier. We are interested in fluctuations of laser light away from the carrier and so we will ignore this term from here onward. This relates the phase noise power spectral density to the optical power

spectrum of the noisy laser beam, with the optical power away from the carrier at $\omega = 0$ due to phase noise. This phase noise can then be taken into account as an additional noise input to the cavity,

$$\hat{a}_{\text{in,tot}}(\omega) = \hat{a}_{\text{in}}(\omega) + a_{\text{in},\phi}(\omega), \quad (2.37)$$

where $a_{\text{in},\phi}(\omega)$ is a stochastic input with $\langle a_{\text{in},\phi}^\dagger(\omega)a_{\text{in},\phi}(\omega') \rangle = S_{EE}(\omega)\delta(\omega + \omega')$ (here the averages used for correlation functions correspond to classical ensemble averages and $a_{\text{in},\phi}^\dagger(\omega) \equiv (a_{\text{in},\phi}(-\omega))^*$).

There is, however, an additional subtlety when performing mechanical mode thermometry with a laser beam affected by phase noise; correlations between the positive and negative frequency components of the phase noise can cause cancellations in the optically transduced signal, and therefore must be carefully taken into account. For example, for a pure sinusoidal tone phase modulated onto a laser we have,

$$\begin{aligned} E_0 e^{i\phi(t)} &\simeq E_0 \left(e^{i\beta_c \cos \omega t + i\beta_s \sin \omega t} \right) \\ &\simeq E_0 \left(1 + \frac{1}{2}(\beta_s + i\beta_c)e^{i\omega t} - \frac{1}{2}(\beta_s - i\beta_c)e^{-i\omega t} \right). \end{aligned}$$

The positive and negative frequency optical sideband amplitudes are negative complex conjugates of one another. More generally, the positive and negative frequency components of the noisy optical input have the following relation for an optical signal with phase noise,

$$a_{\text{in},\phi}^{(-)}(\omega) = - \left(a_{\text{in},\phi}^{(+)}(-\omega) \right)^* \quad (2.38)$$

where $a_{\text{in},\phi}^{(-)}(\omega) = \theta(-\omega)a_{\text{in},\phi}(\omega)$, and $a_{\text{in},\phi}^{(+)}(\omega) = \theta(\omega)a_{\text{in},\phi}(\omega)$ (with $\theta(\omega) = 1$ for $\omega > 0$, $\theta(\omega) = 0$ for $\omega < 0$). The total phase noise signal can then be expressed as $a_{\text{in},\phi}(\omega) = a_{\text{in},\phi}^{(+)}(\omega) - a_{\text{in},\phi}^{(+)\dagger}(-\omega)$. For calculations that follow, this explicit separation of positive and negative frequency phase noise components is useful in simplifying calculations of the optically transduced mechanical motion. In terms of positive frequency phase noise components only, then, we have

$$\langle a_{\text{in},\phi}^{(+)\dagger}(\omega)a_{\text{in},\phi}^{(+)}(\omega') \rangle = S_{EE}(\omega)\delta(\omega + \omega')\theta(\omega), \quad (2.39)$$

with a similar relation holding for the negative frequency components of the phase noise input and the negative frequency optical power spectrum.

2.2.4.1 Heating

To find the actual thermal occupation of the mechanical system in the presence of phase noise on the laser cooling beam, we use, once again, a form of eqn. (1.62) for $\hat{b}(\omega)$ (slightly modified

for the coupling scheme used in this section), replacing $\hat{a}_{\text{in}}(\omega)$ with $\hat{a}_{\text{in,tot}}(\omega)$ which includes the classical phase noise on the input laser. From the non-zero correlation $\langle \hat{a}_{\text{in,tot}}^\dagger(\omega)\hat{a}_{\text{in,tot}}(\omega') \rangle = S_{EE}(\omega)\delta(\omega + \omega')$ for $\omega, \omega' > 0$, we find another source of noise phonons, in addition to those coming from the thermal bath and quantum back-action of the laser light. This is expressed as new terms proportional to $S_{EE}(\omega)$ in the noise spectrum of the mechanical motion given by eqn. (1.65),

$$S_{bb}(\omega) = \frac{\gamma n_{f,\phi}(\omega)}{(\omega_m + \omega)^2 + (\gamma/2)^2}, \quad (2.40)$$

where

$$\begin{aligned} n_{f,\phi}(\omega)|_{\Delta=\omega_m} &= \frac{\gamma_i n_b}{\gamma} + \frac{|G|^2 \kappa}{\gamma} \frac{1 + (\kappa_e/2\kappa) S_{EE}(\omega)}{(\Delta - \omega)^2 + (\kappa/2)^2} \\ &+ \frac{|G|^2 \kappa}{\gamma} \frac{(\kappa_e/2\kappa) S_{EE}(\omega)}{(\Delta + \omega)^2 + (\kappa/2)^2}. \end{aligned} \quad (2.41)$$

As before, assuming a high mechanical Q -factor and the driven weak-coupling regime ($\kappa \gg \gamma$), we substitute $n_{f,\phi}(-\omega_m)$ for $n_{f,\phi}(\omega)$ and relate it to the average mode occupancy in the presence of laser phase noise, $\langle \hat{n} \rangle_\phi$,

$$\langle \hat{n} \rangle_\phi |_{\Delta=\omega_m} = \frac{\gamma_i n_b}{\gamma} + \frac{\gamma_{\text{OM}}}{\gamma} \left[\left(\frac{\kappa}{4\omega_m} \right)^2 + \left(\frac{\kappa_e}{2\kappa} \right) n_\phi \right], \quad (2.42)$$

where we have defined $n_\phi \equiv S_{EE}(\omega_m)$ [57].

The additional phase noise heating in equation (2.42) can be understood as the product of the number of noise photons present in the light field at a mechanical frequency detuned from the central laser frequency (n_ϕ), multiplied by the efficiency with which they are coupled into the cavity ($\kappa_e/2\kappa$), and finally multiplied by the efficiency with which the light field couples to the mechanics ($\gamma_{\text{OM}}/\gamma$). For detuning $\Delta = \omega_m$ used in resolved sideband laser cooling, the optomechanical system only samples the input laser phase noise at a mechanical frequency blue of the central laser frequency, and thus the relationship between the negative and positive frequency components of the laser phase noise has no role to play in heating in the sideband-resolved regime (as we will see below, this is not the case in the thermometry).

2.2.4.2 Effect on calibrated cooling beam thermometry

Since direct photodetection is sensitive to the total field intensity and not the phase, laser light with phase noise detected without first passing through a system with frequency dependent transmission will fail to exhibit any fluctuations in excess of shot-noise. Ignoring the mechanical part of the system for the moment, a laser detuned from an optical cavity by Δ will, however, cause the phase noise of the laser near frequency Δ to appear as an increased noise floor level in the photodetected spectrum

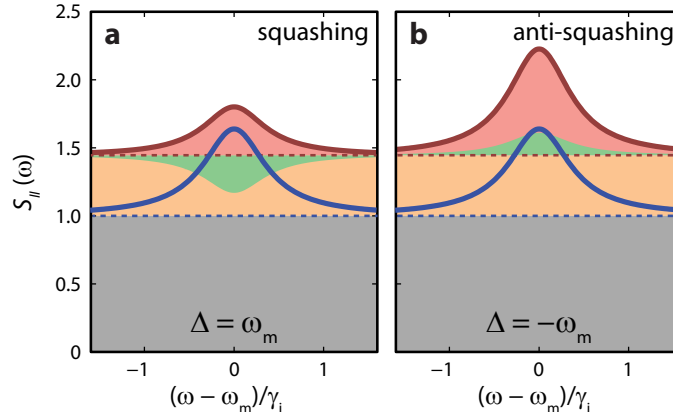


Figure 2.5: **Squashing and anti-squashing in calibrated mode thermometry.** The red traces in **a**, and **b** show the spectral density of the detected signal, $S_{II}(\omega)$ for a large phonon occupation $\bar{n} \gg 1$, about the mechanical frequency. The contributions from phase noise (in orange), thermal Brownian motion (in blue) and shot-noise (in gray), are highlighted. In **a**, the effect of noise squashing, arising from the cancellation of phase noise near the mechanical frequency is apparent (green shaded area). Without phase noise, the spectrum in blue would be detected, with an area corresponding to the actual phonon population. The dip from the phase noise background reduces the area under this curve, causing the area to be underestimated. In **b** the spectra from blue-side detection are presented. Here we note that the phase noise is amplified, causing a larger temperature. Though **a** and **b** are for large phonon occupation numbers, an asymmetry still appears due to classical laser phase noise.

of the transmitted optical signal. The noise from the mechanical system undergoing random motion appears as a Lorentzian peak on top of this noise floor in the photocurrent spectrum. Depending on the exact experimental geometry, i.e. whether the measurement is done on reflection or transmission, and whether the probe laser is red- or blue-detuned from the cavity, the amplitude of this Lorentzian signal above the raised noise floor can be in excess or below that expected in an ideal measurement lacking laser phase noise. At very high relative noise levels, it is even possible for the signal peak to invert and become a dip in the noise floor. Such an effect has been called noise squashing [62], and results from correlations in the input laser noise and the optically transduced mechanical motion noise due to radiation pressure fluctuations stemming from the same input laser noise.

Figures 2.5a and b display a model of the photocurrent noise power spectrum for the transmitted laser field of an evanescently-coupled cavity-optomechanical geometry (Fig. 1.1a) for red ($\Delta = \omega_m$) and blue ($\Delta = -\omega_m$) laser detuning from the optical cavity resonance, respectively. The shaded orange area denotes the part of the photocurrent noise power spectrum that is generated due to phase noise on the probe laser. It can be seen that the aforementioned interference effect, in the transmission geometry considered here, causes a dip (shaded green) in the phase noise background for red-side laser driving and a peak for blue-side laser driving⁵. Note that, over a broader bandwidth

⁵In the case of detecting in the reflection channel for this geometry, the reverse is seen, with red-side laser detuning resulting in anti-squashing and blue-side detuning resulting in squashing.

than that shown in Fig. 2.5, the phase noise contribution to the photocurrent noise spectrum is modulated by the optical cavity lineshape, $\kappa \gg \gamma$.

Formally, the photocurrent noise power spectrum of Fig. 2.5 can be understood by considering the properties of a *driven* cavity-optomechanical system, EIT [2, 63–65], and Electromagnetically Induced Absorption (EIA) [42, 43, 53]. As discussed in sections 2.2.1.1 and 2.2.1.3 for the evanescently coupled geometry of Fig. 1.1a, the reflection coefficient of (weak) probe light at frequencies ω from an intense laser drive tone at frequency $\omega_L = \omega_o \mp \Delta$, is given by

$$r^\pm(\omega) = -\frac{\kappa_e/2}{i(\Delta \mp \omega) + \kappa/2 + \frac{|G|^2}{i(\omega_m - \omega) \pm \gamma/2}}. \quad (2.43)$$

Here reflection is into the backwards waveguide direction ($a_{\text{out},-}$ of Fig. 1.1a). The transmission coefficient into the output channel in the forward waveguide direction is $t^\pm(\omega) = 1 + r^\pm(\omega)$.

The photocurrent of the detected signal in the forward waveguide direction output, due to laser phase noise present at the input, is

$$I_\phi(\omega) = t(\omega)a_{\text{in},\phi}(\omega) + \text{h.c.}(-\omega), \quad (2.44)$$

which, taking into account the above relation between the transmission and reflection coefficients and the correlation between the positive and negative frequency components of the phase noise, yields in terms of the positive phase noise components only

$$I_\phi(\omega) = r(\omega)a_{\text{in},\phi}^{(+)}(\omega) + \text{h.c.}(-\omega). \quad (2.45)$$

Using eqns. (A.3) and (2.39), the resulting photocurrent noise power spectrum in the output channel due to laser phase noise is then calculated to be:

$$S_{I_\phi I_\phi}(\omega) = (|r(\omega)|^2\theta(\omega) + |r(-\omega)|^2\theta(-\omega)) S_{EE}(\omega). \quad (2.46)$$

Evaluating the reflection coefficient at laser detuning $\Delta = \pm\omega_m$ yields,

$$\frac{S_{I_\phi I_\phi}^\pm(\omega)}{S_{EE}(\omega)} = \left(\frac{\kappa_e}{\kappa}\right)^2 \mp \left(\frac{\kappa_e}{\kappa}\right)^2 \frac{|\gamma_{\text{OM}}|}{2} \frac{\gamma_i \pm |\gamma_{\text{OM}}/2|}{(\omega_m \mp \omega)^2 + (\gamma/2)^2}. \quad (2.47)$$

The expression in eqn. (2.47), which is the phase noise contribution to the detected PSD, is plotted in orange and green in Fig. 2.5. Adding this noise spectrum with detuning set to $\Delta = \omega_m$, to that found in eqn. (2.27) for the laser cooling beam output noise spectrum in the absence of classical laser noise, we find the total transduced noise power spectral density near the mechanical resonance

in the large cooperativity limit ($\gamma_i \ll \gamma_{\text{OM}}$) is

$$S_{II}(\omega)|_{\Delta=\omega_m} = 1 + \left(\frac{\kappa_e}{\kappa}\right)^2 n_\phi + \frac{\kappa_e}{2\kappa} \frac{8|G|^2}{\kappa} \bar{S}_{bb}(\omega; n_{\text{inf}}), \quad (2.48)$$

where $n_{\text{inf}} = \gamma_i n_b / \gamma - \kappa_e n_\phi / 2\kappa$ and n_b is mechanical mode occupancy in the absence of the cooling beam. This is the noise output power spectral density in experiments in which the laser cooling beam is also used for transduction/thermometry of the mechanical mode. Laser phase noise on the cooling beam, then, not only adds additional heating of the mechanical resonator (as captured by eqn. (2.42)), but the naively inferred phonon number represented by n_{inf} is also in error relative to the actual average mode occupancy,

$$\langle \hat{n} \rangle_\phi |_{\Delta=\omega_m} - n_{\text{inf}} = \frac{\kappa_e}{\kappa} n_\phi, \quad (2.49)$$

where we have assumed, again, the high cooperativity, deeply sideband resolved limit. As mentioned above, similar relations for heating and transduction error may be derived for other forms of classical noise, such as laser intensity noise and internal cavity noise.

2.2.4.3 Effect on sideband asymmetry thermometry

As indicated pictorially in Fig. 2.5 and mathematically in eqn. (2.47), the contribution to the detected photocurrent noise power spectrum due to laser phase noise takes on a different sign for red and blue detuned driving. In the evanescent coupling geometry considered, the former causes a dip in the phase noise background at the mechanical frequency resulting in noise *squashing*, while the latter leads to a reflection peak in the photodetected noise corresponding to noise *anti-squashing*. For the sideband asymmetry thermometry described in Section 2.2.3, this classical noise asymmetry can mask the quantum asymmetry associated with zero-point fluctuations of the mechanical resonator, and thus must be carefully accounted for in such measurements.

From eqns. (2.27), (2.31), and (2.47) we find the inferred mechanical mode populations for probe measurements at detuning $\Delta = \pm\omega_m$,

$$n_{\text{inf}}^\pm = \frac{\gamma_i n_b}{\gamma_\pm} + \frac{|\gamma_{\text{OM}}|}{\gamma_\pm} \frac{(\kappa/2)^2}{(\omega_m \pm \omega_m)^2 + (\kappa/2)^2} \mp \left(\frac{\kappa_e}{\kappa}\right) \frac{\gamma_i \pm |\gamma_{\text{OM}}/2|}{\gamma_\pm} n_\phi, \quad (2.50)$$

where n_b is the average phonon occupancy of the mechanical resonator in the absence of the probe field, and γ_\pm are the probe back-action modified damping rates defined in eqn. 2.32. In the limit of low probe power (low cooperativity, $C_r = |\gamma_{\text{OM}}|/\gamma_i \ll 1$) applicable to measurements performed in Ref. [3] this simplifies to,

$$n_{\text{inf}}^\pm |_{C_r \ll 1} = \frac{\gamma_i n_b}{\gamma_\pm} \mp \frac{\kappa_e}{\kappa} \frac{\gamma_i}{\gamma_\pm} n_\phi. \quad (2.51)$$

Note that in this limit, averaging the two detuning measurements of n_{inf}^{\pm} , results in a cancellation of the noise squashing for $\Delta = \omega_m$ and the noise anti-squashing for $\Delta = -\omega_m$. This hints at a method of accurately determining the unperturbed phonon occupation number, i.e. $n_b = (\gamma_+ n_{\text{inf}}^+ + \gamma_- n_{\text{inf}}^-) / 2\gamma_i$, even in the presence of laser phase noise.

For thermometry based upon the motional sideband asymmetry (Section 2.2.3), however, the effects of classical laser phase noise cannot so easily be separated from the quantum noise asymmetry generated by the zero-point fluctuations of the mechanical resonator and the quantum back-action of the vacuum fluctuations of the probe laser. In the low cooperativity regime, the motional sideband asymmetry parameter described in Section 2.2.3 is modified to include the effects of probe laser phase noise,

$$\eta^{(\phi)} = \frac{1 + 2\kappa_e n_\phi / \kappa}{n_b - \kappa_e n_\phi / \kappa}. \quad (2.52)$$

One way to differentiate the asymmetry effects related to classical laser phase noise, from those caused by quantum noise is to analyze the dependence of the measured asymmetry on the laser probe power or n_ϕ . This analysis is performed on our measured sideband asymmetry data in Section 5.2.1.

2.3 Sideband-unresolved systems

Sideband-unresolved systems operate in the so-called bad-cavity limit ($\kappa > \omega$), and have features which are qualitatively different than the sideband-resolved case. Since the Stokes and anti-Stokes sidebands generated are of the same order of magnitude in these systems, they are not suited for sideband-cooling and perfect state transfer. However, the relatively “floppy” and compliant nature of their mechanical modes can lead to surprising and interesting phenomena. A particular effect, which we study theoretically here, and experimentally in section 5.3, is squeezing of the light reflected from these structures. This effect is basically similar to the quantum-noise squashing outlined in section 2.2.2.1. As shown in section 2.3.2, correlations between the radiation-pressure shot noise driving the mechanical resonator, and the quantum fluctuations of the light at the detector lead to cancellations. Here we show that at certain quadratures, this cancellation can cause the detected noise floor to below shot-noise, i.e., the reflected light can be squeezed.

It is convenient to define here what we mean by a quadrature, as it is the observable of the light field to which our measurement device (the balanced homodyne detector (BHD) setup) is sensitive:

$$\hat{X}_\theta^{(j)}(t) = \hat{a}_j(t)e^{-i\theta} + \hat{a}_j^\dagger(t)e^{i\theta}. \quad j = \text{in, out, vac, ...} \quad (2.53)$$

We are interested in the properties of $\hat{X}_\theta^{(\text{out})}$ for various quadrature angles θ , given the influence of

the mechanical system.

The measurement of the field provides us with a record $\hat{I}(t) = \hat{X}_\theta^{(\text{out})}(t)$ for a certain θ . We use a spectrum analyzer to perform Fourier analysis on this signal and obtain a symmetrized classical PSD $\bar{S}_{II}(\omega)$, as defined in the mathematical appendix (Appendix A).

For a vacuum field such as the input field, the measured quadrature $\hat{X}_\theta^{(\text{vac})}(t)$ will have a power spectral density

$$\bar{S}_{II}^{\text{vac}}(\omega) = 1. \quad (2.54)$$

This is the shot-noise level which is due to the quantum fluctuations of the electromagnetic field. Mathematically, it arises from the correlator $\langle \hat{a}_{\text{vac}}(\omega) \hat{a}_{\text{vac}}^\dagger(\omega') \rangle = \delta(\omega + \omega')$, with all other correlators $\langle \hat{a}_{\text{vac}}^\dagger(\omega) \hat{a}_{\text{vac}}(\omega') \rangle$, $\langle \hat{a}_{\text{vac}}^\dagger(\omega) \hat{a}_{\text{vac}}^\dagger(\omega') \rangle$, $\langle \hat{a}_{\text{vac}}(\omega) \hat{a}_{\text{vac}}(\omega') \rangle$, arising in the expression $\langle \hat{I}^\dagger(\omega) \hat{I}(\omega') \rangle$ equal to zero.

2.3.1 Approximate quasi-static theory

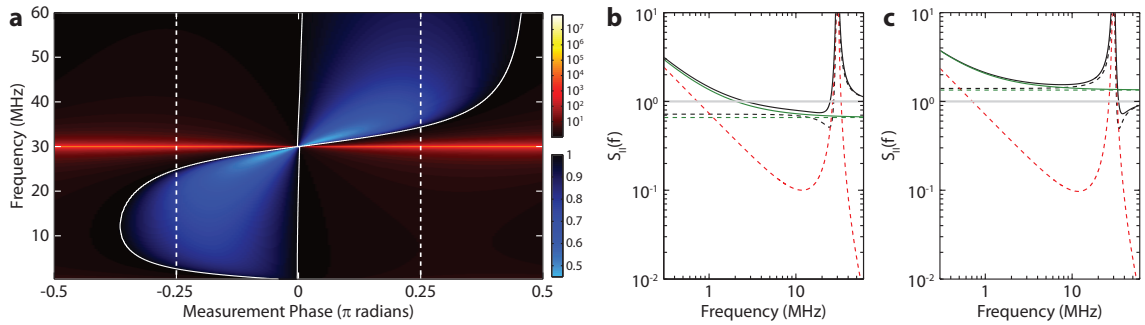


Figure 2.6: **Squeezing theory.** **a**, Density plot of the predicted squeezing $\bar{S}_{II}^{\text{out}}(\omega)$ vs. phase angle and frequency, normalized to the shot-noise. The mechanical mode can clearly be seen at $\omega_m/2\pi = 30$ MHz. The solid white lines outline the region where the power spectral density falls below 1 (the shot-noise level) indicating the presence of squeezing for that phase and frequency. The dashed white lines at $\theta = -\pi/4$ and $\theta = +\pi/4$ correspond to regions where squeezing can be obtained below and above the mechanical frequency, respectively, and the components of the noise model for these phases is shown in detail in figures **b** and **c**. In these figures the spectra are again normalized to the shot-noise level plotted as a grey line. The simple squeezing model without thermal noise (Eq. (2.57)) is represented by the dashed green line and the simple model with thermal noise (Eq. (2.58)) is the solid green line. The solid black line is the full squeezing model $\bar{S}_{II}^{\text{out}}(\omega)$ corresponding to **a** with the constituent components: the contribution from the optical vacuum fluctuations ($\bar{S}_{II,a}^{\text{out}}(\omega)$; Eq. (2.72)) represented by the dashed black line and the thermal noise ($\bar{S}_{II,b}^{\text{out}}(\omega)$; Eq. (2.73)) represented by the dashed red line.

In this section, we present a simplified derivation of how squeezing is obtained in the studied optomechanical system to elucidate the important system parameters and their role in squeezing. We make a few approximations to simplify the derivation:

1. $\Delta = 0$: The laser is tuned exactly to the optical cavity frequency.
2. $\kappa_e = \kappa$: Perfect single-sided coupling (Figure 1.1c).
3. $\kappa \gg \omega_m$: Bad cavity limit.
4. $\omega \ll \omega_m$: We are only interested in the quasi-static response, so the resonant response of the mechanical resonator does not play a role.

Under these assumptions, equations (1.60) and (1.62) can be written as (using the relation for the optical output field $\hat{a}_{\text{out}}(\omega) = \hat{a}_{\text{in}}(\omega) + \sqrt{\kappa}\hat{a}(\omega)$):

$$\begin{aligned} i\omega_m \hat{b}(\omega) &= -\sqrt{\gamma_i} \hat{b}_{\text{in}}(\omega) + \frac{2iG}{\sqrt{\kappa}} (\hat{a}_{\text{in}}(\omega) + \hat{a}_{\text{in}}^\dagger(\omega)), \\ \hat{a}_{\text{out}}(\omega) &= -\hat{a}_{\text{in}}(\omega) - \frac{2iG}{\sqrt{\kappa}} (\hat{b}(\omega) + \hat{b}^\dagger(\omega)). \end{aligned} \quad (2.55)$$

The first equation shows the response of the mechanical resonator subsystem to the thermal bath fluctuations ($\hat{b}_{\text{in}}(\omega)$) and the optical vacuum noise from the measurement back-action. We define $\Gamma_{\text{meas}} \equiv 4|G|^2/\kappa$, and interpret it as the measurement rate [36], such that the factor appearing in front of the optical vacuum noise operators is $\sqrt{\Gamma_{\text{meas}}}$. This rate also appears in the second equation for the output field, in front of the normalized position operator $\hat{x}(\omega)/x_{\text{zpf}} = \hat{b}(\omega) + \hat{b}^\dagger(\omega)$, which is the observable that is being measured.

Note, from the expression for $\hat{a}_{\text{out}}(\omega)$ it follows that since the position is a real observable with an imaginary prefactor, the effects we consider depend strongly on the quadrature being probed, i.e. the real part of the expression, $\hat{X}_{\theta=0}^{(\text{out})}$, will not be affected by the optomechanical coupling.

At this point, we can easily calculate the properties of the detected spectrum $\bar{S}_{II}^{\text{out}}(\omega)$ by writing \hat{a}_{out} in terms of \hat{a}_{in} and \hat{b}_{in} for which the correlators are known:

$$\begin{aligned} \hat{a}_{\text{out}}(\omega) &= -\hat{a}_{\text{in}}(\omega) - 2i \frac{\Gamma_{\text{meas}}}{\omega_m} (\hat{a}_{\text{in}}(\omega) + \hat{a}_{\text{in}}^\dagger(\omega)) \\ &\quad + \frac{\sqrt{\gamma_i} \Gamma_{\text{meas}}}{\omega_m} (\hat{b}_{\text{in}}(\omega) - \hat{b}_{\text{in}}^\dagger(\omega)). \end{aligned} \quad (2.56)$$

Ignoring thermal noise for the moment ($\gamma_i = 0$), and dropping terms of order $(\Gamma_{\text{meas}}/\omega_m)^2$ (assuming $\Gamma_{\text{meas}} \ll \omega_m$) we arrive at:

$$\begin{aligned} \bar{S}_{II}^{\text{out}}(\omega) &= \int_{-\infty}^{\infty} d\omega' \langle \hat{X}_{\theta}^{(\text{out})}(\omega) \hat{X}_{\theta}^{(\text{out})}(\omega') \rangle \\ &= 1 + 4(\Gamma_{\text{meas}}/\omega_m) \sin(2\theta). \end{aligned} \quad (2.57)$$

Note that for certain values of θ , the detected spectral density can be smaller than what one would expect for a vacuum field. For $\theta = -\pi/4$, we achieve the maximum squeezing with a noise floor of

$1 - 4(\Gamma_{\text{meas}}/\omega_m)$, which strongly depends on the ratio $\Gamma_{\text{meas}}/\omega_m$.

To understand the effect of thermal noise, we assume the form of the correlator to be $\langle \hat{b}_{\text{in}}(\omega)\hat{b}_{\text{in}}^\dagger(\omega') \rangle = (\bar{n}(\omega) + 1)\delta(\omega + \omega')$, $\langle \hat{b}_{\text{in}}^\dagger(\omega)\hat{b}_{\text{in}}(\omega') \rangle = \bar{n}(\omega)\delta(\omega + \omega')$, $\langle \hat{b}_{\text{in}}^\dagger(\omega)\hat{b}_{\text{in}}^\dagger(\omega') \rangle = 0$, and $\langle \hat{b}_{\text{in}}(\omega)\hat{b}_{\text{in}}(\omega') \rangle = 0$ (these expressions are discussed in section 3.4.1). Then, a calculation similar to the one leading to equation (2.57) gives

$$\begin{aligned} \bar{S}_{II}^{\text{out}}(\omega) &= 1 + 4(\Gamma_{\text{meas}}/\omega_m)\sin(2\theta) \\ &\quad + 4\frac{\Gamma_{\text{meas}}}{\omega_m}\frac{\bar{n}(\omega)}{Q_m}(1 - \cos(2\theta)), \end{aligned} \quad (2.58)$$

where we have assumed $\bar{n}(\omega)$, the bath occupation at frequency ω , to be much larger than unity. At $\theta = -\pi/4$, we have

$$\bar{S}_{II}^{\text{out}}(\omega) = 1 - 4(\Gamma_{\text{meas}}/\omega_m)(1 - \bar{n}(\omega)/Q_m). \quad (2.59)$$

In this model, there is no squeezing at $\theta = -\pi/4$ and frequency ω if $\bar{n}(\omega) > Q_m$. Some squeezing is always present, but is shifted to other quadratures and the amount of detectable squeezing is reduced at higher temperatures. Most of the squeezing (59%) is washed out by the thermal noise at $\bar{n}(\omega) = Q_m$. The squeezing arises from the time evolution of the mechanical resonator maintaining coherence over the time scale of the fluctuations. Requiring coherent evolution over the mechanical cycle is equivalent to demanding that the rate at which phonons enter the mechanical system from the bath ($\gamma_i\bar{n}$) be smaller than the mechanical frequency ω_m . In conclusion, the important requirements to achieve squeezing are to make Γ_{meas} comparable to ω_m and to reduce the thermal occupancy or increase the mechanical quality factor to achieve $\bar{n}(\omega) \lesssim Q_m$.

2.3.2 The effect of dynamics and the correlations between shot-noise and position

As a next step, we take into account the dynamics of the mechanical resonator while keeping the approximations of the bad-cavity limit ($\kappa \gg \omega_m$) and on-resonant probing ($\Delta = 0$). In addition to further clarifying some of the observed features, this treatment elucidates the role of correlations between the mechanical system's position and the back-action force.

The response of the mechanical system to a force is captured by its susceptibility:

$$\chi_m(\omega) = \frac{1}{m(\omega_m^2 - \omega^2 - i\gamma_i\omega_m)}. \quad (2.60)$$

The form of the damping considered here is the strongly sub-ohmic structural damping which is observed in our measurements [66, 67] (cf. Section 3.4.1). The mechanical system responds to

random noise forces $F_T(t)$ from the thermal bath and to the quantum back-action from the cavity $F_{BA}(t)$, both of which are taken into account below.

The back-action force for the resonant case can simply be found by linearizing the expression for the radiation pressure force $\hat{F}_{RP}(t) = -\hbar g \hat{a}^\dagger \hat{a} / x_{zpf}$. We find the force imparted on the mechanics due to the shot-noise of the cavity field to be

$$\hat{F}_{BA}(t) = \frac{\hbar \cdot \sqrt{\Gamma_{\text{meas}}}}{x_{zpf}} \hat{X}_{\theta=0}^{(\text{in})}(t) \quad (2.61)$$

for the case of resonant driving. The fluctuations imparted on the mechanics are from the intensity quadrature of the light ($\theta = 0$). Using equation (2.55), we can write the output field quadrature as:

$$\hat{X}_{\theta}^{(\text{out})}(t) = -\hat{X}_{\theta}^{(\text{in})}(t) - 2 \frac{\sqrt{\Gamma_{\text{meas}}}}{x_{zpf}} \hat{x}(t) \cdot \sin(\theta). \quad (2.62)$$

We note here that the mechanical position fluctuations are primarily imprinted on the phase quadrature of the output light, with $\theta = \pm\pi/2$. The intensity quadrature is unmodified ($\hat{X}_{\theta=0}^{(\text{out})}(t) = -\hat{X}_{\theta=0}^{(\text{in})}(t)$) since changes in the cavity frequency are not transduced as changes in intensity when the laser is resonant with the cavity (see section 2.3.3 for the general $\Delta \neq 0$ case).

The output of the homodyne detector normalized to the shot-noise level is found by taking the auto-correlation of eqn. (2.62). The correlations between radiation pressure shot-noise and the mechanical motion are important in this calculation [3, 4, 41, 48, 68–70] and must be taken into account. In the time-domain we find the auto-correlation to be:

$$\begin{aligned} \langle \hat{X}_{\theta}^{(\text{out})}(t) \hat{X}_{\theta}^{(\text{out})}(t') \rangle &= \delta(t-t') + 4\Gamma_{\text{meas}} \sin^2(\theta) \frac{\langle \hat{x}(t) \hat{x}(t') \rangle}{x_{zpf}^2} \\ &\quad + 2\hbar^{-1} \sin(\theta) \cos(\theta) \langle \hat{F}_{BA}(t) \hat{x}(t') + \hat{x}(t) \hat{F}_{BA}(t') \rangle. \end{aligned} \quad (2.63)$$

The $\cos(\theta)$ in the last term comes from the general expression for a quadrature $\hat{X}_{\theta}^{(\text{in})}(t) = \hat{X}_{\theta=0}^{(\text{in})}(t) \cos(\theta) + \hat{X}_{\theta=\pi/2}^{(\text{in})}(t) \sin(\theta)$, and equation (2.61). The key components of equation (2.63) are the shot-noise level, the thermal noise, and the cross-correlation between the back-action noise force and mechanical position fluctuations. It is only the latter that can give rise to squeezing, by reducing the fluctuation level below shot-noise. This squeezing can be calculated spectrally:

$$\begin{aligned} S_{\text{sq}}(\omega) &= \hbar^{-1} \sin(2\theta) \times \int_{-\infty}^{\infty} d\tau [\langle \hat{F}_{BA}(t) \hat{x}(t-\tau) \rangle + \langle \hat{x}(t) \hat{F}_{BA}(t-\tau) \rangle] e^{i\omega\tau} \\ &= 2\hbar \text{Re} \{ \chi_m(\omega) \} \Gamma_{\text{meas}} / x_{zpf}^2 \sin(2\theta). \end{aligned} \quad (2.64)$$

The full detected spectral density is then

$$\bar{S}_{II}^{\text{out}}(\omega) = 1 + \frac{4\Gamma_{\text{meas}}}{x_{\text{zpf}}^2} \left[\bar{S}_{xx} \sin^2(\theta) + \frac{\hbar}{2} \text{Re}\{\chi_m\} \sin(2\theta) \right], \quad (2.65)$$

At the DC or quasi-static limit ($\omega \rightarrow 0$) the susceptibility $\chi_m \rightarrow 1/m\omega_m^2$ can be used and we reobtain the results from section 2.3.1 (cf. equation (2.57)). We see that for $\theta < 0$, squeezing is obtained in this limit. At frequencies larger than ω_m , $\chi_m(\omega)$ changes sign, and we expect to see squeezing at quadrature angles $\theta > 0$. Additionally, since $\chi_m(\omega)$ becomes larger around the mechanical frequency, we expect the maximum squeezing to be enhanced. More specifically, at a detuning $\delta = \omega_m - \omega$ ($|\delta| \gg \gamma_i$) from the mechanical resonance, we expect the parameter characterizing the squeezing to be proportional to $\Gamma_{\text{meas}}/\delta$, and the detected spectrum shown in equation (2.65) becomes $\bar{S}_{II}^{\text{out}}(\omega > 0) \approx 1 + (2\Gamma_{\text{meas}}/\delta)[(\omega_m/\delta)(\bar{n}(\omega)/Q_m)(1 - \cos(2\theta)) + \sin(2\theta)]$. These features are evident in the spectra represented in Fig. 2.6.

It is important to note here that in the absence of other nonlinearities in the system, any reduction of the noise below the vacuum fluctuations can only be caused by the correlations between the Radiation Pressure Shot-Noise (RPSN) and the position fluctuations of the system. This makes the problem of proving the correlations between RPSN and mechanical motion equivalent to the problem of proving that the reflected light from the optomechanical cavity is squeezed.

Conceptually this form of probing the RPSN is similar to quantum noise squashing presented in section 2.2.2.1 for a sideband-resolved system, and studied in Refs. [3, 4, 41]. It also shares features with the cross-correlation measurements proposed by Heidmann et al. [68], and Børkje et al. [48], and recent experiments by Purdy et al. [49]. The distinguishing feature of this type of measurement is that the quantum correlations between the fluctuations of the position and the electromagnetic vacuum manifest themselves as squeezed light.

The effects of RPSN also play a role in the second term of equation (2.65). Part of the position fluctuation power spectral density $\bar{S}_{xx}(\omega)$ can be attributed to the motional heating due to RPSN, an effect first measured in a solid state system by Purdy et al. [49]. In our measurements, at the largest powers ($\sim 3,100$ intracavity photons), roughly 65% of the displacement fluctuations are thermal, while 32% are due to RPSN heating. An additional 2% heating arises from the phase noise of the laser.

2.3.3 General derivation of squeezing

Among the approximations made in section 2.3.1, the quasi-static approximation is the least correct. In fact, in our experiments, the most observable squeezing occurs with ω close to ω_m and even slightly larger than ω_m , so $\omega \ll \omega_m$ is not valid. Near the mechanical frequency, resonant enhancement of the optical vacuum fluctuations by the mechanical resonator causes squeezing greater than that

predicted in the quasi-static regime to be possible.

Here we show the results of a derivation that does not rely on most of the assumptions used in the approximate model. Of the assumptions in the previous section, the only simplification we keep here is to assume perfect coupling $\kappa_e = \kappa$. The effect of imperfect coupling can be taken into account trivially and is explained after this section (2.3.3.1).

By substitution of equation (1.62) into the equation for $\hat{a}(\omega)$ (1.60), we arrive at:

$$\sqrt{\kappa}\hat{a}(\omega) = A_1(\omega)\hat{a}_{\text{in}}(\omega) + A_2(\omega)\hat{a}_{\text{in}}^\dagger(\omega) + B_1(\omega)\hat{b}_{\text{in}}(\omega) + B_2(\omega)\hat{b}_{\text{in}}^\dagger(\omega), \quad (2.66)$$

with

$$A_1(\omega) = \frac{\kappa}{i(\Delta - \omega) + \kappa/2} \times \left[\frac{|G|^2}{i(\Delta - \omega) + \kappa/2} \frac{1}{i(\omega_m - \omega) + \gamma/2} - \frac{|G|^2}{i(\Delta - \omega) + \kappa/2} \frac{1}{-i(\omega_m + \omega) + \gamma/2} - 1 \right] \quad (2.67)$$

$$A_2(\omega) = \frac{\kappa}{i(\Delta - \omega) + \kappa/2} \times \left[\frac{|G|^2}{-i(\Delta + \omega) + \kappa/2} \frac{1}{i(\omega_m - \omega) + \gamma/2} - \frac{|G|^2}{-i(\Delta + \omega) + \kappa/2} \frac{1}{-i(\omega_m + \omega) + \gamma/2} \right] \quad (2.68)$$

$$B_1(\omega) = \frac{\sqrt{\kappa\gamma_i}}{i(\Delta - \omega) + \kappa/2} \left[\frac{iG}{i(\omega_m - \omega) + \gamma/2} \right] \quad (2.69)$$

$$B_2(\omega) = \frac{\sqrt{\kappa\gamma_i}}{i(\Delta - \omega) + \kappa/2} \left[\frac{iG}{-i(\omega_m + \omega) + \gamma/2} \right] \quad (2.70)$$

The expressions give us the output field in terms of the input fields, since

$$\begin{aligned} \hat{a}_{\text{out}}(\omega) &= \hat{a}_{\text{in}}(\omega) + \sqrt{\kappa}\hat{a}(\omega) \\ &= (1 + A_1(\omega))\hat{a}_{\text{in}}(\omega) + A_2(\omega)\hat{a}_{\text{in}}^\dagger(\omega) \\ &\quad + B_1(\omega)\hat{b}_{\text{in}}(\omega) + B_2(\omega)\hat{b}_{\text{in}}^\dagger(\omega). \end{aligned} \quad (2.71)$$

We can calculate $\bar{S}_{II}^{\text{out}}(\omega)$ from this expression, which we split into two parts, one only due to the optical vacuum fluctuations, and the other containing the contribution from thermal noise:

$$\bar{S}_{II}^{\text{out}}(\omega) = \bar{S}_{II,a}^{\text{out}}(\omega) + \bar{S}_{II,b}^{\text{out}}(\omega).$$

$$\bar{S}_{II,a}^{\text{out}}(\omega) = |A_2(-\omega)|^2 + |1 + A_1(\omega)|^2 + 2\text{Re}\{e^{-2i\theta}(1 + A_1(\omega))A_2(-\omega)\} \quad (2.72)$$

$$\begin{aligned} \bar{S}_{II,b}^{\text{out}}(\omega) &= |B_1(\omega)|^2(\bar{n}(\omega) + 1) + |B_1(-\omega)|^2\bar{n}(\omega) \\ &\quad + |B_2(-\omega)|^2(\bar{n}(\omega) + 1) + |B_2(\omega)|^2\bar{n}(\omega) \\ &\quad + 2\text{Re}\{e^{-2i\theta}B_1(\omega)B_2(-\omega)\}(\bar{n}(\omega) + 1) + 2\text{Re}\{e^{-2i\theta}B_1(-\omega)B_2(\omega)\}\bar{n}(\omega) \end{aligned} \quad (2.73)$$

2.3.3.1 The effect of imperfect optical coupling and inefficient detection

At every junction in an experiment where the optical transmission efficiency is less than unity ($\eta < 1$), an equivalent optical circuit can be defined involving an $\eta : (1 - \eta)$ beam splitter with the output being η times the input and $(1 - \eta)$ times the vacuum. Therefore, the effect of optical losses and coupling inefficiencies on the detected spectra can be calculated by replacing the measured field quadrature with:

$$\hat{X}_\theta^{(\text{det})} = \sqrt{\eta}\hat{X}_\theta^{(\text{out})} + \sqrt{1 - \eta}\hat{X}_\theta^{(\text{vac})} \quad (2.74)$$

This source of vacuum noise is completely unrelated to the cavity output, and there are no cross-correlation terms, so the detected current spectral density will be given by

$$\bar{S}_{II}^{\text{det}}(\omega) = \eta\bar{S}_{II}^{\text{out}}(\omega) + (1 - \eta)\bar{S}_{II}^{\text{vac}}(\omega), \quad (2.75)$$

where $\bar{S}_{II}^{\text{vac}}(\omega) = 1$ is the shot-noise.

Measurement inefficiencies take two forms: one is due to inefficiencies in the detection, while the second is because of excess electronic noise or “dark current” present due to the circuitry of the detector and amplifier. This excess noise can also be thought of as a detection inefficiency by considering the amount of optical shot-noise inserted into the signal that would produce it. Since the dark-current is measured with no optical input, and the real shot-noise level increases linearly with the local oscillator (LO) power, this inefficiency is power dependent and can be minimized for large LO powers. In our measurements with sideband-unresolved systems (presented in section 5.3), the dark current was found to be 10.4 dB below the detected shot-noise. The total detector inefficiency was measured to be $\eta_{\text{HD}} = 66\%$.

Chapter 3

Thin-film phononic and photonic nanostructures

3.1 The basic ideas

There are several motivations in using chip-scale optomechanical resonators. On one hand, by using techniques of nanofabrication one is positioned well to profit from advances in the field of nanotechnology, which is expected to advance rapidly due to significant industrial and scientific backing across a variety of fields. Secondly, optomechanical systems fabricated using these techniques are expected to be more easily expandable with chips containing many optical and mechanical elements providing us with possibly new functionality and dynamics. Thirdly, and perhaps most importantly for the experiments presented in this thesis, nanofabrication allows confinement of mechanical and optical energy in exceedingly small interaction volumes, boosting the rates at which the phonons and photons couple. These large coupling rates simplify the experimental requirements and allow us access to regimes that had been previously off-limits.

3.1.1 Construction of a photonic crystal cavity

Our goal is to confine a photon on a chip. A simple beam of silicon confines light in two dimensions, and acts as a single-mode waveguide if patterned at the scale of the wavelengths being confined (see figure 3.1a). This effect can be thought of as arising due to total internal reflection of light propagating down the beam. To confine the light in all three dimensions, we need to have mirrors at each end. A hole drilled into this beam will act as a scatterer. Such a scatterer will act as a mirror and reflect some of the light back in the opposite direction in the waveguide. Some of the light will go through the scatterer and continue propagation along the waveguide (transmission loss). Additionally, much of the light will be scattered out of plane, as the total internal reflection condition is broken by the hole. This leads to some far-field radiation from the scatterer (see figure 3.1b). Perhaps counter-intuitively, this far-field radiation can be eliminated by putting in more holes to form

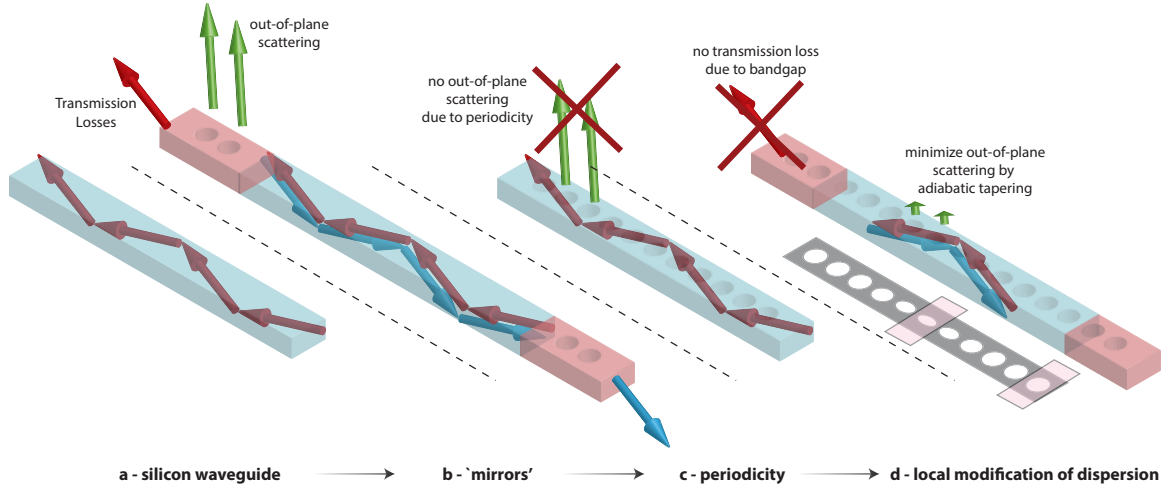


Figure 3.1: **Construction of a photonic crystal cavity.** See text for description.

an array, but spacing them such that the far-field radiation from consecutive scatterers cancels. The structure that arises from this construction is called a photonic crystal waveguide (see figure 3.1c).

Since the dispersion of the photonic crystal depends strongly on the spacing and shape of the individual scatterers, small changes can have large effects. The optical engineer is thus given fine control over the propagation of light, which is experimentally realizable given the current state of nanofabrication technology.

A stunning manifestation of the strong modification of the photonic dispersion in such a periodic structure is the emergence of bandgaps. These are regions of frequency where no photons are allowed to exist in the waveguide. Such regions act as perfect mirrors for photons in those energy ranges. A detailed study of the properties of photonic crystals can be found in Joannopoulos et al. [20].

By creating a photonic heterostructure, i.e. a photonic crystal where the properties are varied along the propagation direction, we can create a central region where photons of a certain frequency are allowed, while the bandgap in the surrounding regions reflects the light at that frequency, and acts as perfect mirrors (see figure 3.1d). By changing the properties of the photonic crystal slowly along the propagation direction, out-of-plane scattering is minimized (since locally the waveguide is loss-less due to the far-field cancellation effect). Thus, optical resonances with very large quality factors can be engineered. High quality factor photonic crystals based on slow modulation of line defect waveguides were first demonstrated by Song et al. [71]. The first demonstration of ultra-high Q optical resonances on nanobeams came from Marko Loncar's group at Harvard [72].

3.1.2 Phononic bandgaps

Periodicity of the atomic lattice in a crystal gives rise to many of the interesting properties of semiconductors. In a similar way, the micro- and nanofabricated arrays of holes comprising the

lattice of a photonic crystal cause a bandgap to form for light, and provide us with new means to control the optical response of a fabricated structure. The same periodic lattice, can give rise to a bandgap for phonons. Due to the difference between the speed of light and sound, we expect the frequencies to be different by roughly five orders of magnitude.

A confined phonon can be scattered into a non-confined phonon of the same energy due to impurities, fabrication imperfections, or just finite mode intensity at the “clamps”. A phononic bandgap is thus a particularly powerful tool if used properly, since it can shut off all of these linear sources of loss. Additionally, phononic bandgaps allow one to create waveguides with interesting dispersion properties, and transfer many of the design techniques developed in the optical domain to phononics.

A basic property of phonons that is unique to acoustic waves is applied to create robust large bandgap phononic crystals in section 3.2. Phonons, unlike light, cannot propagate in vacuum. Therefore, small constrictions or bridges can very strongly affect their propagation.

We create a large bandgap phononic crystal by constructing an array of squares connected to one another with small bridges (see Figure 3.4). At very low frequencies, the phonons in the structure see only an effective medium, and have energies that are highly dependent on the thickness of the connecting bridges (since the whole structure becomes significantly floppier as the bridges are made thinner). At high frequencies, the resonances of the squares define the propagating modes. These have frequencies that are not strongly dependent on the connecting bridge width. Thus, a bandgap is formed between these two types of phonons in the structure.

3.2 Full bandgap phononic crystal designs [1]

In this section we study two types of crystal structures, one with a square lattice and the other with a hexagonal lattice. Most photonic and phononic crystals to date have utilized circular holes. Here we investigate the degree of freedom associated with hole shape. Circular holes are the simplest holes to fabricate and the most symmetric. Considering that it is desirable for the hole to have at least as much (point-group) symmetry as the underlying lattice, circular holes seem like the obvious choice. Unfortunately, for quasi-two-dimensional phononics crystals, circular holes fail to provide large mechanical bandgaps at desirable frequencies, and fail completely at providing a bandgap for a variety of slab thicknesses. In cases where full simultaneous phononic-photonic bandgaps are achievable, e.g. the square lattice proposed by Mohammadi, et al., in Refs. [73, 74], the large hole sizes make the crystal unsuitable for fabrication of ultrahigh- Q optical cavities. Thankfully, by exploring the shape degree of freedom of the hole it is possible to do better when it comes to phononic bandgap materials.

3.2.1 Origin of the gap: from effective medium to tight-binding

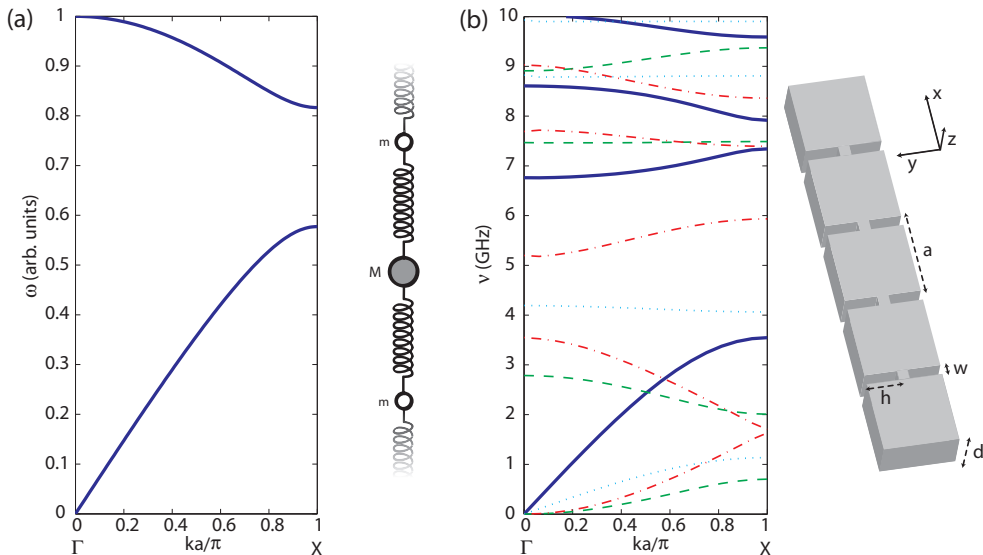


Figure 3.2: **A one-dimensional phononic crystal.** Band diagram for a simple (a) spring-mass system and (b) its quasi-1D nanomechanical analogue. The nanomechanical structure band diagram is plotted for a silicon structure with $(d, h, w, a) = (220, 200, 100, 500)$ nm. In (b) waveguide bands are plotted as $(—)$, $(\cdot \cdot \cdot)$, $(- - -)$ and $(\cdot - \cdot)$ for vibrational modes with (σ_y, σ_z) symmetry of $(+, +)$, $(-, -)$, $(-, +)$ and $(+, -)$ respectively. Here, σ_y is a mirror plane symmetry of the structure about the y -axis. σ_z is the corresponding vertical mirror symmetry about the z -axis.

We start with the toy model consisting of alternating small and large masses coupled by springs typically studied in solid-state physics [16]. As shown in Figure 3.2(a), this system results in a large bandgap in the frequency spectrum of the mechanical vibrations of this linear chain. The bandgap arises from the existence of modes of oscillation with widely different frequencies. Traveling phonon modes where the large masses are predominantly excited (low frequency “acoustic”-like phonons) are split in frequency from those where the small masses are predominantly excited (high frequency “optical”-like phonons). The frequency bandgap between low and high frequency vibrations becomes more pronounced with increasing difference in particle masses. A quasi-1D nanomechanical realization of the linear chain of alternating small and large masses coupled by springs is shown in Figure 3.2(b). This structure consists of a linear array of square “drumheads” joined together by narrower “connector” pieces. Here, and throughout the rest of this article, the material of the mechanical structure is assumed to be silicon (Si), with Young’s modulus of 170 GPa and mass density of 2329 kg/m^3 . These and the following mechanical simulations were done using COMSOL Multiphysics [14], a FEM solver. We see that large phononic bandgaps exist in this structure just as in the elementary periodic array of small and large masses coupled via springs.

To more accurately understand the origin of the bandgap in the quasi-1D nanomechanical structure of Figure 3.2(b), we consider the low and high frequency bands separately. In the low-frequency,

large wavelength ($\lambda \gg a$) regime, an effective medium theory [75] can be used to calculate the exact values of wave velocities and the dispersion at the origin. For our purposes, we wish to push these low frequency bands to as low a frequency as possible. This can be achieved by reducing the width of the connector piece, $a - 2h$. The reasoning heuristic is as follows. The stiffness of a beam is in a sense dependent on the stiffness of its weakest link. In this case, the connectors, acting as contacts between the larger square drumhead sections, make the beam much floppier than an unperturbed beam of uniform cross-section. At higher frequencies, as ν approaches the resonances, ν_j , of each square drumhead, a tight-binding model may be used to model the dispersion. This sort of model is valid as long as the interaction between each square is made small, which we have achieved by making $a - 2h$ small. To get a bandgap then, the effective medium bands are squeezed down to low frequencies by reducing $a - 2h$, which does not affect the tight-binding bands since their frequency is set by the internal resonances of the larger square drumhead section. Simultaneously, the interaction strength between the coupled drumhead sections is reduced, and therefore so is the slope of the tight-binding bands making them more flat. These two effects conspire together to produce a large phononic bandgap.

3.2.2 Quasi-1D phononic tight-binding bands: symmetry and dispersion in a toy model

As will be evident below in the design of phononic waveguides and cavities, it is useful to study the properties of the tight-binding bands in a little more detail. Considering the simple linear lattice example introduced above (refer to Fig. 3.2(b)), the group of the wavevector at the Γ and X points of the Brillouin zone possesses the full point group symmetry of the crystal itself. As such, the Bloch modes (\mathbf{Q}) at these high symmetry points can be characterized according to their vector symmetry with respect to reflection $\sigma_x(x, y, z) = (-x, y, z)$ about the x -axis in a plane intersecting the middle of the unit cell of the linear nanomechanical structure. We have for x -symmetric ($\mathbf{Q}^{(x+)}$) and x -antisymmetric ($\mathbf{Q}^{(x-)}$) Bloch modes, for which $\sigma_x \mathbf{Q}^{(x\pm)}(\sigma_x \mathbf{r}) = \pm \mathbf{Q}^{(x\pm)}(\mathbf{r})$, the following relation for the displacement vector (\mathbf{Q}) at the unit-cell boundaries (\mathbf{r}_b):

$$\mathbf{Q}^{(x+)}(\mathbf{r}_b + a\mathbf{e}_x) = +\sigma_x \mathbf{Q}^{(x+)}(\mathbf{r}_b), \quad (3.1)$$

$$\mathbf{Q}^{(x-)}(\mathbf{r}_b + a\mathbf{e}_x) = -\sigma_x \mathbf{Q}^{(x-)}(\mathbf{r}_b), \quad (3.2)$$

On the other hand, we have the usual phase shift acquired by the different Bloch modes, which for the X -point and Γ -point modes yields,

$$\mathbf{Q}_\Gamma(\mathbf{r} + a\mathbf{e}_x) = +\mathbf{Q}_\Gamma(\mathbf{r}), \quad (3.3)$$

$$\mathbf{Q}_X(\mathbf{r} + a\mathbf{e}_x) = -\mathbf{Q}_X(\mathbf{r}). \quad (3.4)$$

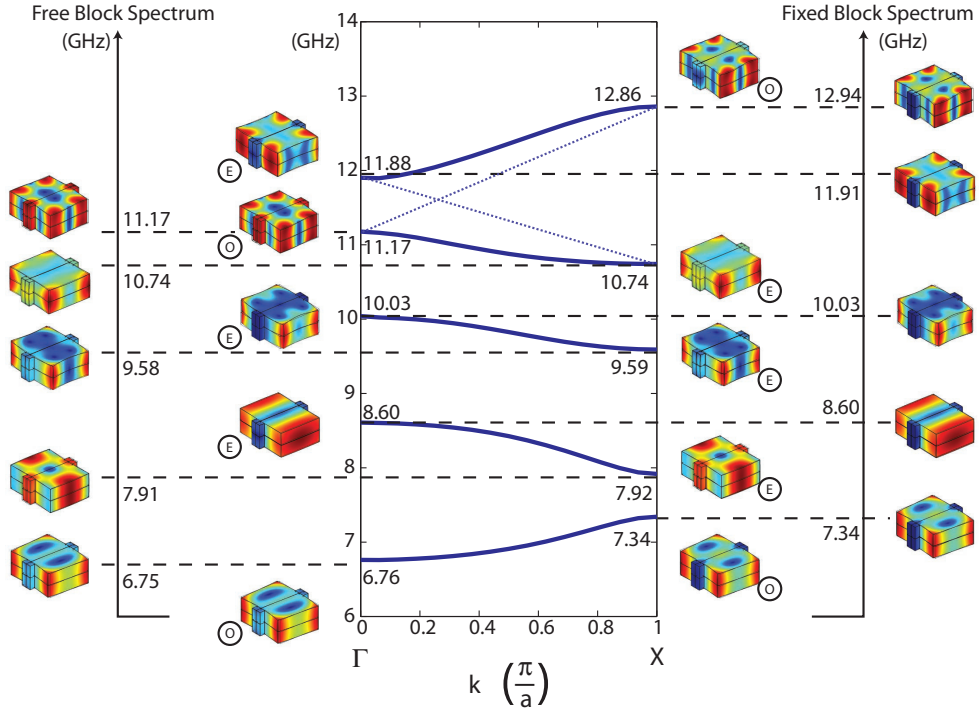


Figure 3.3: **Tight-binding 1D phononic crystal bands.** The tight-binding bands of symmetry $(\sigma_y, \sigma_z) = (+, +)$ are plotted for the quasi-1D nanomechanical system of Fig. 3.2(b), along with the unit cell solved for fixed and free boundary conditions. The E (O) symbol below the Bloch function plots designates $\sigma_x = +(-)$ symmetry of the vibrational modes. We see that in every case where bands don't mix, i.e. the bottom three bands, the E bands slope downwards in frequency from Γ to X , while the O band slopes upwards. In plots of the mechanical modes, color indicates the magnitude of the displacement field (blue no displacement, red large displacement) and the displacement of the structure has been exaggerated for viewing purposes.

These constraints together imply that x -symmetric modes at the Γ - and X -points must obey respectively the conditions

$$\mathbf{e}_x \cdot \mathbf{Q}_\Gamma^{(x+)}(\mathbf{r}_b) = 0, \quad (3.5)$$

$$\mathbf{e}_x \times \mathbf{Q}_X^{(x+)}(\mathbf{r}_b) = \mathbf{0}. \quad (3.6)$$

In many cases the excitation is of a dominant polarization. For example, for the $(\sigma_y, \sigma_z) = (+, +)$ vector symmetry vibrational modes, the dominant polarization is found to be Q_x (not surprising, as for this symmetry the displacement in y or z would have to be of higher order, involving a stretching/compression of the membrane along these directions). For this symmetry of modes then, the boundary condition given by Eqn. (3.5) is approximately equivalent to a fixed boundary condition, whereas the boundary condition of Eqn. (3.6) can be approximated as a free boundary condition. Since, intuitively, one expects the frequency of a free resonator to increase by fixing part of it, the above argument implies that, for the given polarization mode symmetry, $(\sigma_y, \sigma_z) = (+, +)$, x -symmetric modes bend up while x -antisymmetric modes slope downwards as the in-plane wavevector k varies from $\Gamma - X$. This correspondence is elucidated in Figure 3.3, where the tight-binding bands are shown for the aforementioned quasi-1D system. In all cases, the frequencies calculated with fixed or free boundary conditions on the square drumhead correspond to their respective high symmetry Bloch function frequencies to within a factor 10^{-2} . In what follows, we use these features of the tight-binding bands to help identify vibrational bands that will strongly couple to optical waves.

3.2.3 Quasi-2D “Cross” crystal

In going to a quasi-2D system, we begin with the simplest extension of the quasi-1D structure of Fig. 3.2(b), that being the same elements of square blocks and thin connectors, but now arrayed in two dimensions as shown in Fig. 3.4(c). We call this the “cross” substrate, since it results from a square array of crosses cut into a slab. Each cross is characterized by a height h and a width w , which along with the lattice spacing a and slab thickness d , serve to fully parametrize geometrically the system. For reference, the reciprocal space representation of the lattice is shown in Fig. 3.4(d), in which the common notation of the high symmetry points of the first Brillouin zone in a square lattice are used. The phononic bandstructure, including all symmetries of vibrational modes, of the cross substrate is shown in Fig. 3.4(b) for the same set of parameters as used in the quasi-1D structure of Fig. 3.2. A large bandgap opens up between 5.3 and 6.8 GHz. The phononic gap maps for a variety of relevant parameters of the cross substrate are shown in Figure 3.5, indicating the robustness of the phonon bandgap to each parameter.

Despite the encouraging mechanical properties of the cross substrate, as we will see, it is difficult to realize this substrate as an Optomechanical Crystal (OMC) due to its unfavorable optical

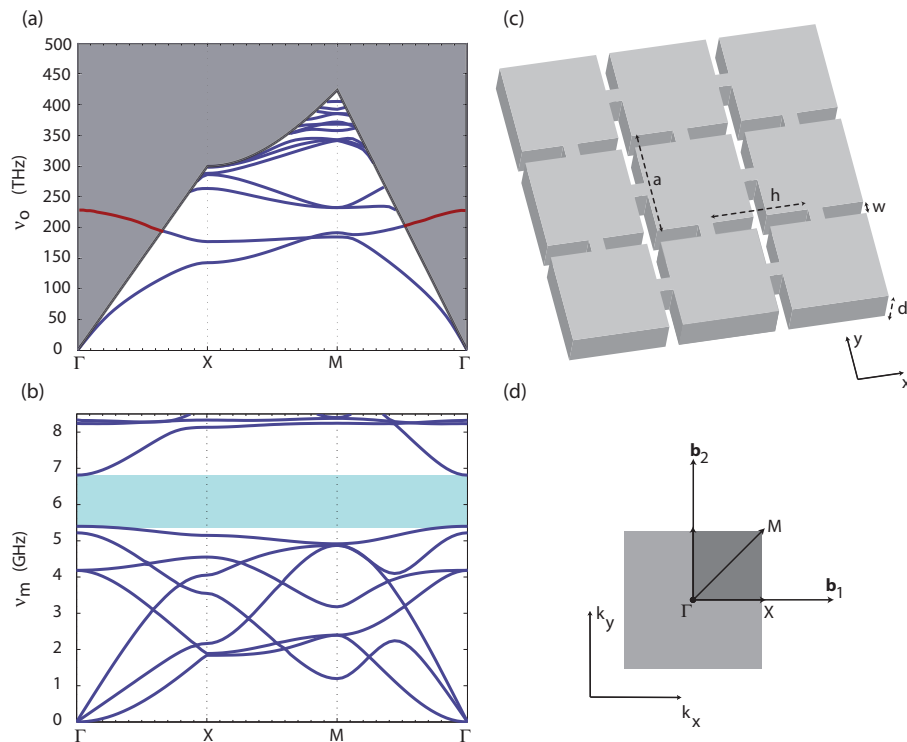


Figure 3.4: **The crosses crystal.** (a) Photonic and (b) phononic bandstructure of the quasi-2D Si cross substrate shown schematically in (c) real space and (d) reciprocal space. The photonic bandstructure is for the even symmetry modes of the slab only. The band diagrams were calculated for a Si structure with parameters $(d, h, w, a) = (220, 200, 100, 500)$ nm. Notably, there is not even a photonic pseudo in-plane bandgap for the even vertical symmetry optical modes of the slab.

properties. In general, design of photonic bandgaps in materials with refractive index of order $n \sim 3$ (semiconductors) is more suited to a plane-wave expansion approach as opposed to the tight-binding picture discussed above for nanomechanical vibrations. The square lattice, with its low symmetry, behaves differently for plane waves propagating in different directions, such as at the high symmetry X and M points of the first Brillouin zone boundary. This results in a much smaller in-plane photonic bandgap for the square lattice in comparison to a higher symmetry lattice, such as the hexagonal lattice. Note also, that for quasi-2D photonic structures we usually talk about an *in-plane* bandgap only, as light (unlike sound) can also propagate vertically into the surrounding vacuum cladding. The photonic bandstructure of the Si cross substrate, assuming a refractive index for Si of 3.48, is shown in Fig. 3.4(a) for the even vertically symmetric optical modes of the Si slab (these modes include the fundamental TE-like bands). These and the following photonic simulations were done using the software package MPB [76]. The photonic bandstructure consists of two distinct regions: (i) the guided mode region below the light line (shown as a black line) in which there are a discrete number of mode bands, all of which are evanescent into the surrounding cladding, and (ii) the re-

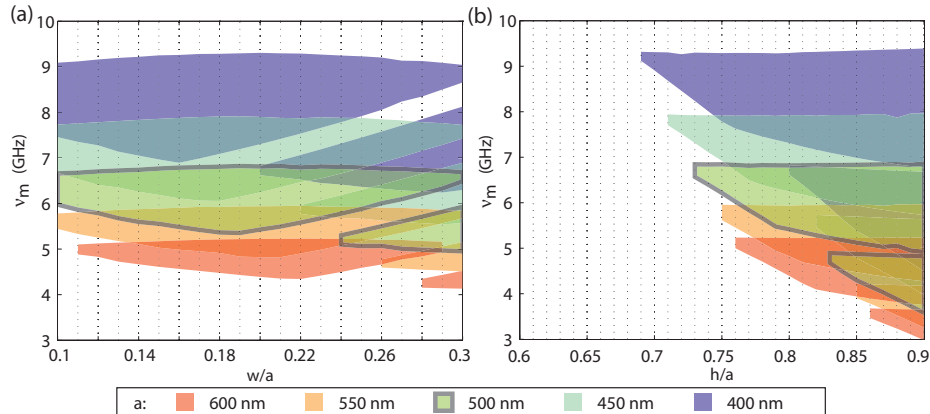


Figure 3.5: **Cross gap maps.** Phononic gap maps for a Si quasi-2D cross structure. The cross width is varied in (a) and the cross height is varied in (b). The nominal structure about which the variations are performed is characterized by parameters $(d, h, w, a) = (220, 400, 100, 500)$ nm. The lattice constant a is varied while keeping the ratios $h/a = 0.8$ and $w/a = 0.2$ constant in (a) and (b), respectively.

gion above the light line (shown in grey) in which *leaky* guided mode resonances and a continuum of radiation modes exist. We have shown the extension of the lowest lying guided mode band above the light line as a red line, where it behaves as a *leaky*, but highly localized resonance of the Si slab.

Due to the presence of the continuum of radiation modes above the light line, it is clear that in the photonic case one can only talk about a pseudo in-plane bandgap in the case of a quasi-2D slab structure. Much more problematic is the presence of *leaky* guided mode resonances above the light line, which can strongly couple to the guided modes of the structure in the presence of perturbations of the lattice. These perturbations can both be unintentional, such as in fabrication imperfections, or intentional, such as in the formation of resonant cavities and linear waveguides. Here, we will adopt a practical definition of a pseudo in-plane photonic bandgap as one where the bandgap extends across *both* guided mode and leaky resonances. As can be seen in the photonic bandstructure of Fig. 3.4(d), the cross structure lacks even a pseudo in-plane photonic bandgap for the TE-like modes of the slab structure (the odd symmetry modes of the slab, which include the fundamental TM-like modes, do not even possess a guided mode bandgap). Due, then, to leaky resonances with large local density of states in the slab, the cross substrate is ruled out as a suitable structure from which to form important photonic elements such as ultrahigh- Q optical cavities. This is the same problem faced by the “honey-comb” crystal proposed in Ref. [73].

3.2.4 Quasi-2D “Snowflake” crystal

The hexagonal lattice counterpart of the cross substrate is shown in Fig. 3.6; this we term the “snowflake” substrate. Each snowflake pattern is characterized by radius r , and a width w ; which

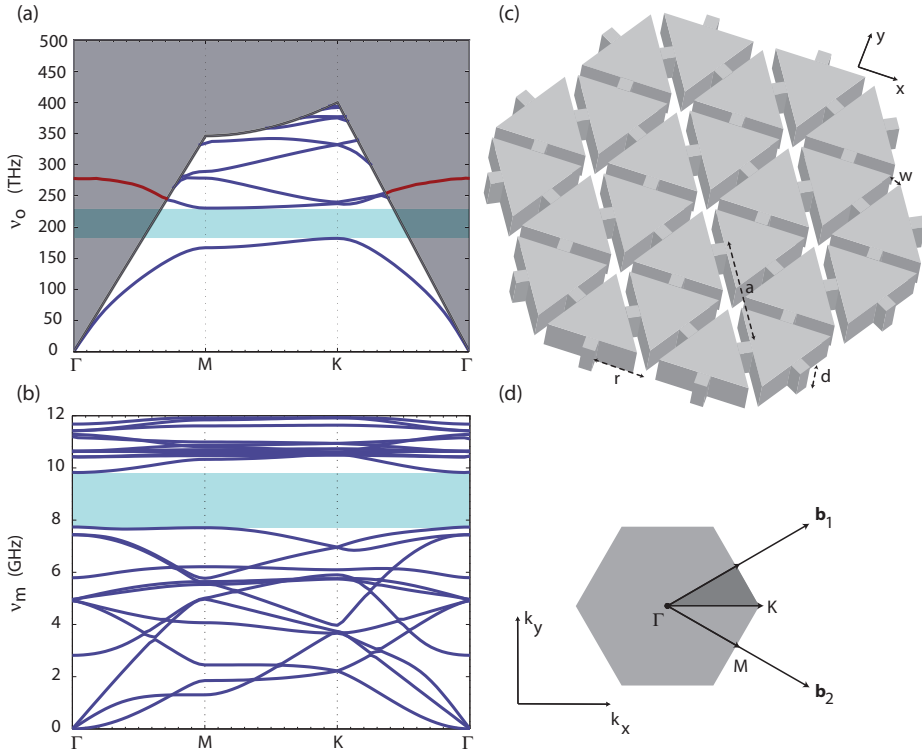


Figure 3.6: **The snowflake crystal.** (a) Photonic and (b) phononic bandstructure of the quasi-2D Si snowflake substrate. Schematic of the snowflake slab substrate in (c) real space and (d) reciprocal space. The band diagrams were calculated for a Si structure with parameters $(d, r, w, a) = (220, 200, 75, 500)$ nm. For these parameters, there are large simultaneous phononic and photonic bandgaps.

along with the lattice spacing a and slab thickness d , serve to fully parametrize geometrically the system. The phononic gap maps for a variety of relevant parameters of the snowflake substrate are shown in Figs. 3.7(a) and 3.7(b). The snowflake substrate, unlike the cross substrate, does possess favorable optical properties. Gap maps for the photonic properties are shown in Figs. 3.7(c) and 3.7(d), where again we focus on the even vertical symmetry optical modes of the slab (which includes the fundamental TE-like bands of primary interest). Due to the fact that the phononics is more sensitive to connector width, $a - 2r$, while the photonics is more sensitive to the air-slot width, w , this crystal provides us with two different tunable parameters for control over the photonic and phononic properties of the system. This property, which is apparent from the respective gap maps, is highly valuable for designing optomechanical devices which must simultaneously manipulate sound and light.

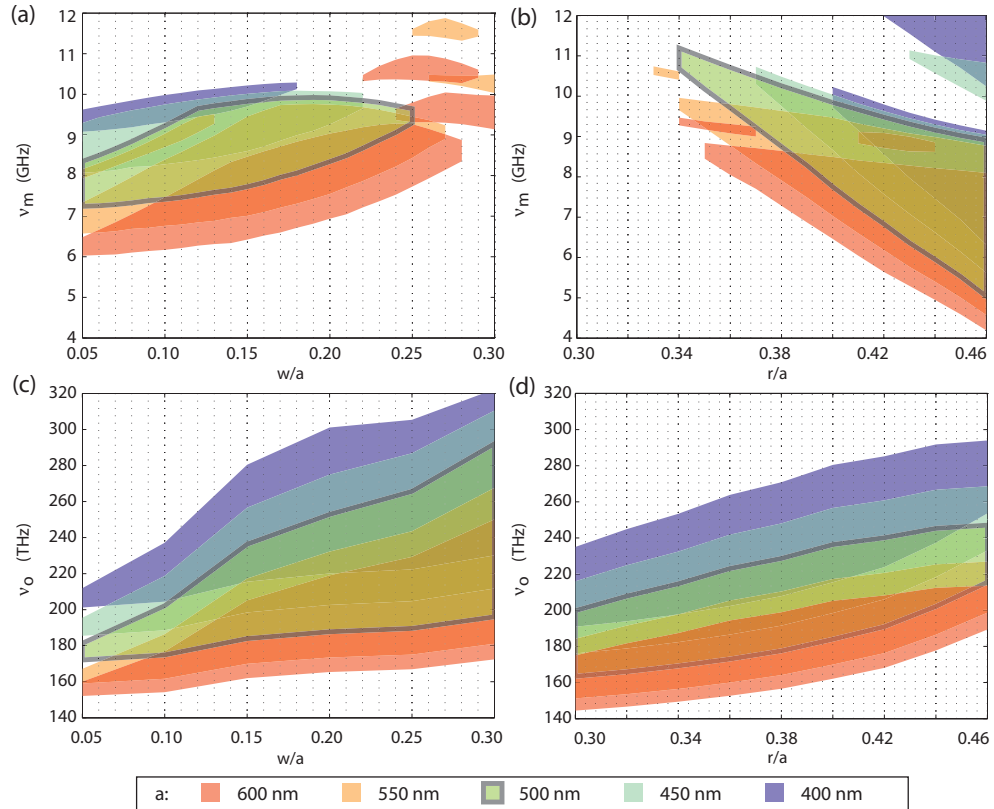


Figure 3.7: **Snowflake gap maps.** Phononic (a,b) and photonic (c,d) gap maps for a quasi-2D snowflake substrate. The photonic gap maps are for the even vertical symmetry modes of the slab only. In (a,c) we vary the snowflake width and (b,d) the snowflake radius. The nominal structure about which the variations are performed is characterized by parameters $(d, r, w, a) = (220, 200, 75, 500)$ nm. The lattice constant a is varied while keeping the ratios $r/a = 0.4$ and $w/a = 0.15$ constant in (a,c) and (b,d), respectively.

3.3 Phononic crystal resonators and waveguides

3.3.1 Experimental verification of cross phononic crystal properties

In this section, experimental studies of the 2D “cross” phononic crystals (introduced in section 3.2.3 and Ref. [77]) are covered. This work is primarily aimed at demonstrating that a phononic bandgap can be engineered in the thin-film systems presented, and is focused on studying the properties of the localized mechanical resonances, as the geometric properties of the crystal are tuned. As described previously, the structure consists of an array of squares connected to each other by thin bridges, or equivalently, a square lattice of cross-shaped holes. The phononic bandgap in this structure arises from the frequency separation between higher frequency tight-binding bands, which have similar frequencies to the resonances of the individual squares, and lower frequency effective-medium bands with frequencies strongly dependent on the width of the connecting bridges, $b = a - h$ as described above.

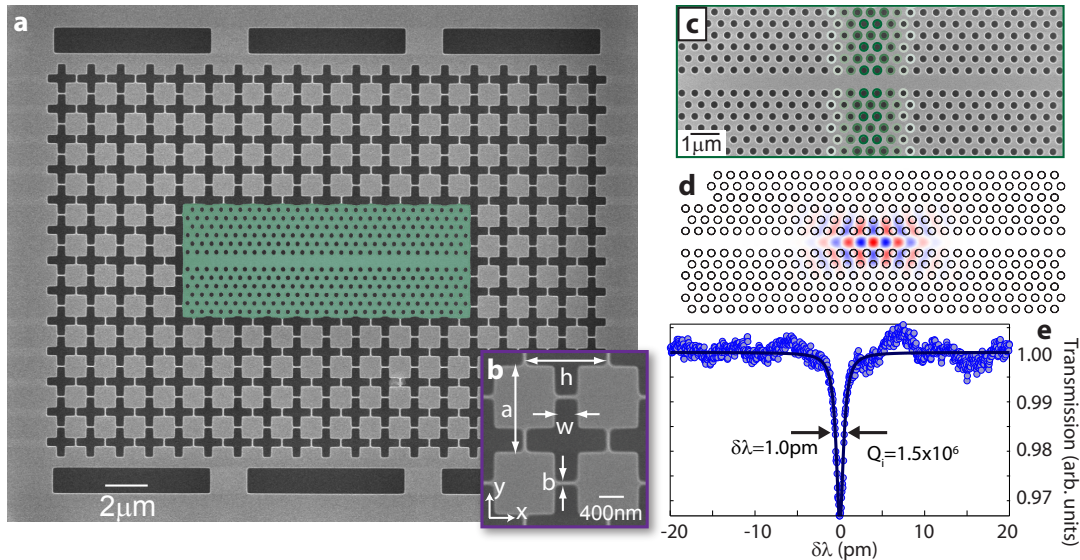


Figure 3.8: **Optomechanical heterostructure with separate confinement for phonons and photons.** **a**, Scanning electron micrograph (SEM) of one of the fabricated 2D-OMC structures. The photonic nanocavity region is shown in false green color. In **b**, Zoom-in SEM image of the cross crystal phononic bandgap structure. **c**, Zoom-in SEM image of the optical nanocavity within embedded in the phononic bandgap crystal. Darker (lighter) false colors represents larger (smaller) lattice constant in the optical cavity defect region. **d**, FEM simulation of E_y electrical field for the optical cavity. **e**, Typical measured transmission spectra for the optical nanocavity, showing a bare optical Q -factor of $Q_i = 1.5 \times 10^6$.

As shown in Figs. 3.8a-c, the cross crystal is used as a phononic cage (cavity) for an embedded optical nanocavity [71] (highlighted in a green false color) consisting of a quasi-2D photonic crystal waveguide with a centralized “defect” region for localizing photons. This embedding of an optical cavity within an acoustic cavity enables, through the radiation-pressure-coupling of optical and acoustic waves, the probing of the properties of the bandgap-localized phonons via a light field sent through the optical nanocavity. The theoretical electric field mode profile and the measured high- Q nature of the optical resonance of the photonic crystal cavity are shown in Figs. 3.8d and 3.8e, respectively. Such a phonon-photon heterostructure design allows for completely independent tuning of the mechanical and optical properties of our system, and in what follows, we use this feature to probe arrays of structures with different geometric parameters. In particular, by varying the bridge width b of the outer phononic bandgap crystal, the lower frequency edge of the bandgap can be swept in frequency and the resulting change in the *lifetime*, *density of states*, and *localization* of the trapped acoustic waves interacting with the central optical cavity can be monitored. Two different phonon cavity designs, S_1 and S_2 , were fabricated in this study. We focus first on the lower acoustic frequency S_1 structure (shown in Figs. 3.8a), for which an array of devices with bridge width varying from $b = 53$ nm to 173 nm (in 6 nm increments) was created.

A typical band diagram for a nominal structure ($a = 1.265$ μm , $h = 1.220$ μm , $w = 340$ nm) is

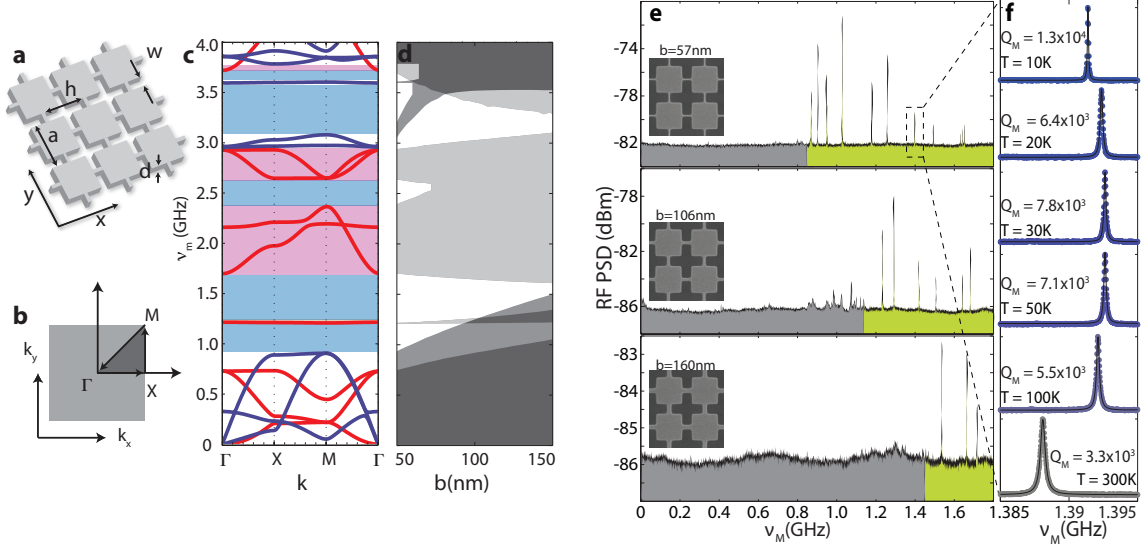


Figure 3.9: **Tuning the “cross” lattice.** **a**, Real space crystal lattice of the cross crystal with lattice constant a , cross length h , cross width w , and membrane thickness d . The bridge width is defined as $b = a - h$. **b**, Reciprocal lattice of the first Brillouin zone for the cross crystal. **c**, Phononic band diagram for the nominal cross structure with $a = 1.265 \mu\text{m}$, $h = 1.220 \mu\text{m}$, $w = 340 \text{ nm}$. Dark blue lines represent the bands with even vector symmetry for reflections about the $x - y$ plane, while the red lines are the flexural modes which have odd vector mirror symmetry about the $x - y$ plane. **d**, Tuning of the bandgap with bridge width, b . Light gray, dark gray, and white areas indicate regions of a symmetry-dependent (i.e., for modes of only one symmetry) bandgap, no bandgap, and full bandgap for all acoustic modes, respectively. **e**, Optically transduced RF power spectral density of the thermal Brownian motion of S_1 structures with $b = 57 \text{ nm}$ (top), $b = 106 \text{ nm}$ (middle), and $b = 160 \text{ nm}$ (bottom). The inferred region below the phononic bandgap is shaded gray (see main text). **f**, Temperature dependence of the mechanical quality factor for the 1.4 GHz acoustic mode of the S_1 structure with $b = 57 \text{ nm}$.

shown in Fig. 3.9c. Blue (red) lines represent bands with even (odd) vector symmetry for reflections about the $x - y$ plane. The lowest frequency bandgap for the even modes of the simulated cross structure extends from 0.91 GHz to 3.6 GHz (with a $\approx 100 \text{ MHz}$ interruption by flat bands at roughly 3.0 GHz). Within this bandgap, there are regions of full phononic bandgap (shaded blue) where no mechanical modes of any symmetry exist, and regions of partial symmetry-dependent bandgap (shaded red) where out-of-plane flexural modes with odd symmetry about the $x - y$ plane are allowed. As the bridge width is increased, the lower frequency effective-medium bands become stiffer, causing an increase in their frequency, while the higher frequency tight-binding band frequencies remain essentially constant. A gap-map show in in Fig. 3.9d, showing how the bandgaps in the structure change as a function of phononic crystal bridge width, illustrates this general feature.

Experimentally we observe the thermally excited acoustic modes of the photonic-phononic crystal. The detection scheme consists of direct detection of the transmitted light, as described in section 2.2.2. In all of these measurements, due to a combination of low optomechanical coupling, and optical power, no dynamical back-action was observed. In other words, the mechanical linewidths

and quality factors represent the intrinsic properties of the mechanical systems. This also means that the calibration of the g_0 cannot be done by sweeping the power and observing the back-action, and so the mode temperature is assumed from an independent thermometry reading as described below. The detected RF-spectra from three different S_1 structures with small ($b = 57$ nm), medium ($b = 106$ nm), and large ($b = 160$ nm) bridge widths are shown in Fig. 3.9e. Each narrow tone in the RF-spectra corresponds to a different acoustic resonance interacting with the central optical nanocavity. Through careful calibration of the optical power and electronic detection, one can extract both the mechanical Q -factor (from the linewidth) and the level of optomechanical coupling (from the magnitude of the transduced thermal motion) of each acoustic resonance. A measurement of the temperature dependence of the acoustic mode spectrum is also performed, and is shown in Fig. 3.9f for one of the acoustic resonances over a cryostat base temperature range of 300 K to 10 K (measured via a cernox thermometer). Therefore, the temperature was assumed to be that reported by the cryostat thermometer.

By measuring the entire set of S_1 devices in this way, a map may be produced of the localized acoustic modes' properties versus bridge width. In Figs. 3.10a and 3.10b we plot the numerically simulated and experimentally measured mode map for the S_1 structure. Each marker in these plots corresponds to a different acoustic resonance, with the position of the marker indicating the mode frequency and the size of the marker indicating the mechanical Q -factor of the mode (for the numerical simulations all mechanical Q -factors above 10^7 are shown with the same marker size). Numerical simulations of the optical, mechanical, and optomechanical properties of the structure are performed using the COMSOL [14] FEM software package, with an absorbing boundary condition applied at the exterior of the phononic cage [23]. The various bandgap regions are indicated in Fig. 3.10a with the same color coding as in Fig. 3.9c. Due to the weak radiation pressure coupling to the optical nanocavity of the flexure acoustic modes of odd symmetry about the x - y plane of the slab (red mode bands in Fig. 3.9c), we only show in the simulated mode plot of the even symmetry, in-plane acoustic resonances.

The striking similarity of the simulated and measured mode plots is evidence that the optical nanocavity is able to sensitively probe the in-plane localized acoustic modes of the phononic bandgap structure (the acoustic band with light blue marker in Fig. 3.10a is the one localized in-plane mode which does not show up in the measured plot of Fig. 3.10b; numerical simulations show this mode to be a surface mode at the inner edge of the cross crystal, which does not couple well to the central optical cavity). Within the bandgap, modes are tightly localized (see Fig. 3.10c) and do not radiate acoustic energy, whereas below the bandgap the acoustic modes spread into the exterior cross crystal (see Fig. 3.10d), leaking energy into the surrounding substrate region. The boundary where the mechanical Q -factor drops off is clearly identifiable in the experimentally measured mode plot of Fig. 3.10b (the spectral region below the apparent full phononic bandgap is shaded gray as

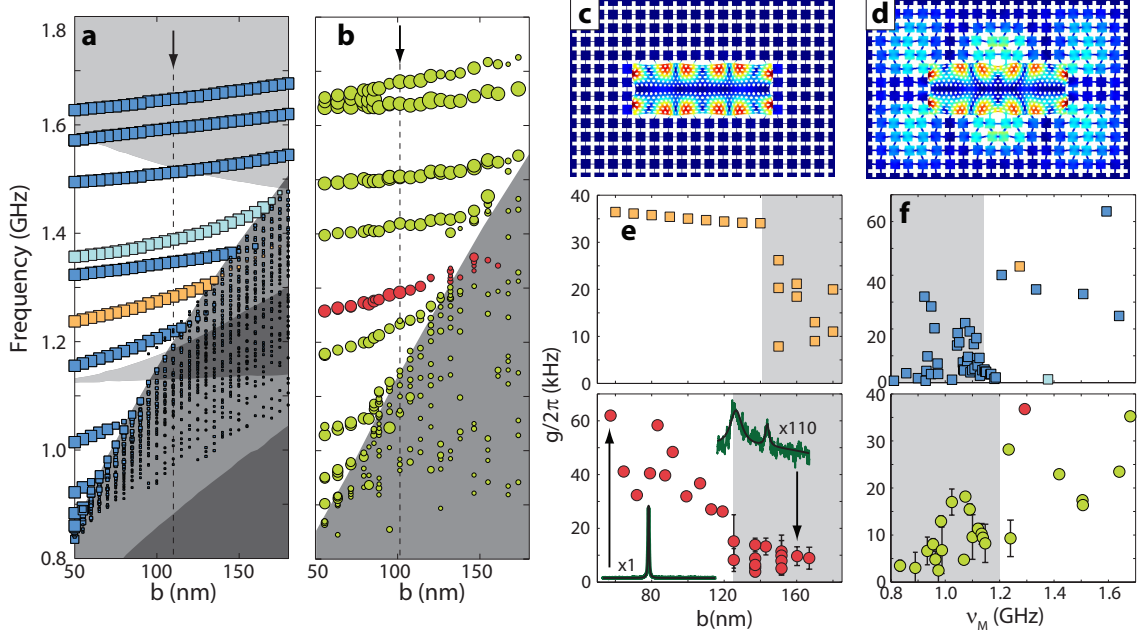


Figure 3.10: **Experimental and theoretical mode maps on a “cross” phononic crystal.** **a**, Plot of the 3D-FEM simulated in-plane localized acoustic modes of the S_1 structure as a function of bridge width b . Each marker corresponds to a single acoustic mode, with the marker size proportional to the logarithm of the calculated acoustic radiation Q -factor. The light blue shaded markers correspond to acoustic bands which are optically dark. The shading corresponds to the same color coding of the phononic bandgaps as that used in Fig. 3.9d. **b**, Measured mode plot of the optically-transduced localized acoustic modes for an array of S_1 structures with varying bridge width. The marker size of each resonance is related to the logarithm of the measured mechanical Q -factor. The inferred spectral region below the phononic bandgap is shaded grey. **c** and **d**, FEM simulations of the displacement field amplitude ($|\mathbf{Q}(\mathbf{r})|$) for the acoustic mode in the orange colored band around 1.35 GHz in **a**. In **c** the mode is within the phononic band gap resulting in a radiation-limited $Q_M^{(\text{rad})} \approx 10^9$. In **d** the mode is on the edge of the bandgap and has a reduced $Q_M^{(\text{rad})} < 10^3$. **e**, Simulated (\square) and measured (\circ) optomechanical coupling rate g for the orange (red) highlighted acoustic band in **a** (**b**). **f**, Simulated (\square) and measured (\circ) optomechanical coupling rate g for the series of acoustic modes of the S_1 structure with $b \sim 100$ nm (vertical dashed curves in **a** and **b**)

a guide to the eye), and matches up well with the theoretical lower frequency band-edge of the full phononic bandgap of the cross crystal.

Two other distinguishing features between modes inside and outside a bandgap are the spectral mode density and the strength of the optomechanical coupling. Below the phononic bandgap, acoustic modes can fill the entire volume of the cross crystal (out to the boundary of the undercut structure where it is finally clamped), resulting in an increase of the mode density (proportional to volume) and a decrease in the optomechanical coupling (proportional to the inverse-square-root of mode volume [77]). In Fig. 3.10e we have plotted the theoretically computed and experimentally measured values of the optomechanical coupling (g_0) for an acoustic resonance lying near the middle of the full phononic bandgap (this resonance is highlighted in orange in the theoretical plot of Fig. 3.10a and red in the measured plot of Fig. 3.10b). The measured trend of optomechanical

coupling nicely matches that of the theoretical one, and highlights the sharp drop off in optomechanical coupling as the mode crosses the bandgap. Similarly, in Fig. 3.10f we plot the optomechanical coupling for the acoustic resonances of a single device with bridge width $b \sim 100$ nm (corresponding to a vertical slice in Figs. 3.10a and 3.10b as indicated by a dashed vertical line). Again we see good correspondence between theory and experiment, with the drop off in g and the large increase in spectral mode density clearly evident in both plots below the bandgap (note that the frequency position of the bandgap edge is not the same in the theoretical and experimental plots of Figs. 3.10e and 3.10f due to the slight differences in bridge width).

3.3.2 Design of snowflake phononic-photonic crystal waveguides and resonators

3.3.2.1 Waveguide Design

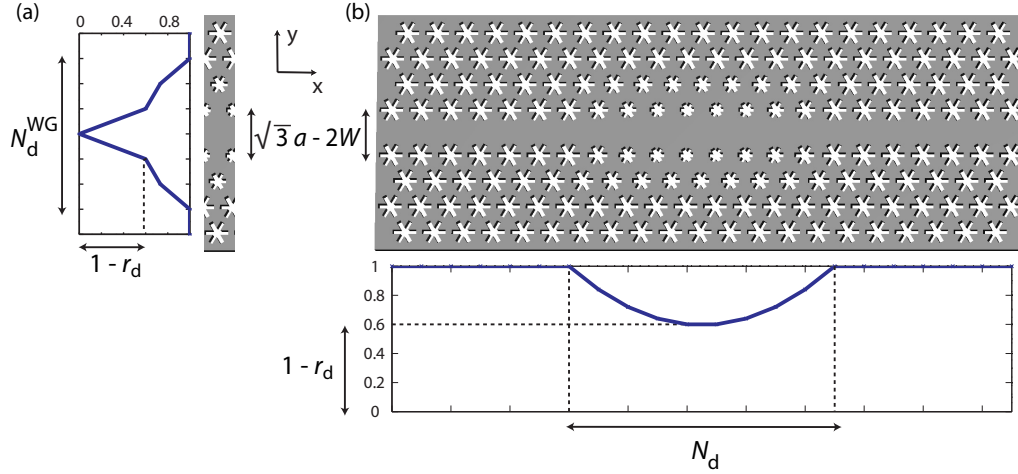


Figure 3.11: **Linear and point defect cavity designs on a snowflake lattice.** (a) Schematic of a $W1$ -like linear defect waveguide in the quasi-2D snowflake crystal slab structure. The central row of snowflake holes is completely removed along the x -direction (Γ - K in reciprocal space), and the remaining top and bottom pieces of the lattice are shifted by a value W towards each other (effectively a strip of $2W$ is removed from the center of the waveguide). A transverse radius variation of the snowflake holes is also applied. N_d^{WG} is the number of rows of holes which take part in forming this defect. The number r_d represents the factor by which the radius of holes on the two rows neighbouring the center of the waveguide are reduced; i.e. the radius is changed to $r \times (1 - r_d)$, where r is the nominal radius. Rows going further out from the center of the waveguide have radii which scale quadratically to the nominal value of r . (b) Cavities are formed from this line-defect waveguide by a longitudinal modulation of the waveguide parameters. In this case, the r_d scale factor is varied quadratically from 0 to a desired value at the cavity center along the length of the waveguide over a period of N_d lattice periods. The cavity structure shown here has $r_d = 0.4$ at the cavity center, $N_d = 10$ and $N_d^{\text{WG}} = 7$.

A line-defect in a photonic bandgap material will act as a waveguide for light [78, 79]. In a quasi-

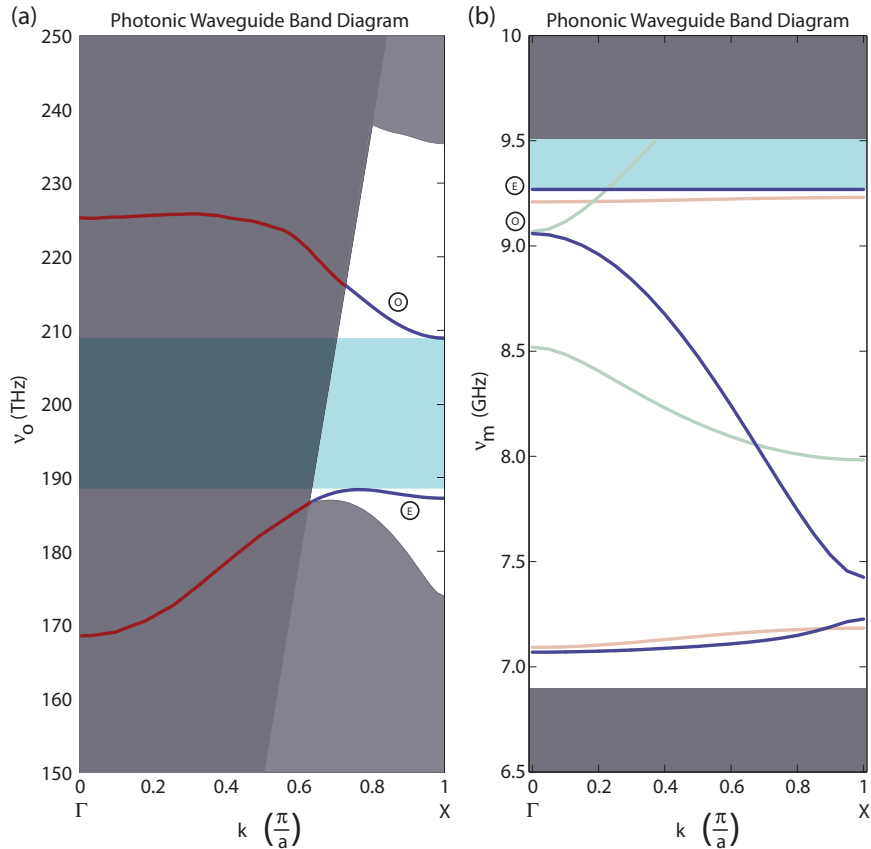


Figure 3.12: **Photonic and phononic snowflake waveguide band diagrams.** (a) Photonic and (b) phononic waveguide bands for an optomechanical waveguide on a snowflake substrate with $(d, r, w, a) = (220, 210, 75, 500)$ nm, and a $W1$ -like waveguide with properties $W = 200$ nm and $r_d = 0$. The E and O symbols represent even and odd vector parity, respectively, of the zone boundary modes with respect to σ_y reflections for the optical and σ_x reflections for the mechanical modes. The same mode labels are used in Figure 3.13. In (a), only the even vertical symmetry modes are shown (those including the fundamental TE-like modes, but not the fundamental TM-like modes). In (b), guided modes with different transverse symmetries (σ_y, σ_z) are colored (—), (—) and (—) for symmetries (+, +), (\pm , -), and (-, +), respectively. In both diagrams frequencies above and below the in-plane bandgap are colored light gray, and in (a) the light cone is region is colored dark grey. Above the light-line in (a), the leaky mode bands are colored red (—). In both (a) and (b) we have highlighted the bandgap regions which will be relevant in the cavity design pursued below.

2D crystal structure with simultaneous in-plane photonic and phononic bandgaps, such a defect should be able to direct both light and sound around in the plane of the crystal. In this section, we study the guided modes in these types of linear-defect waveguides of the snowflake crystal slab. It is of interest to understand the properties of these modes, since it has been shown for photonic crystal slabs that good waveguides also yield ultrahigh- Q optical cavities [71, 80] as described in section 3.1.1. In Section 3.3.2.3 we follow this design technique to demonstrate ultrahigh- Q optomechanical cavities in which both light and sound are effectively localized in the same volume with very little radiative

loss. Although we are primarily interested here in *cavity* optomechanics, the coupling between guided photons and phonons in periodic structures is also an interesting subject of study which has been recently explored in photonic crystal fiber systems [81]. As will be discussed further below, studying *guided-mode* optomechanical properties also allows one to simplify the design and optimization of *cavity* optomechanical devices.

When designing optical and mechanical cavities and waveguides, it is desirable to have control over where the waveguide bands are placed within the frequency bandgap [78]. For example, previous demonstrations of photonic crystal cavities have often involved a line defect waveguide in which a localized cavity resonance was formed by locally tuning the line defect guided mode out of the bandwidth of the waveguide band and into the bandgap. In previous work, this tuning has been achieved by changing locally the longitudinal lattice constant along the guiding direction [71], the width of the line-defect forming the waveguide [80], or the radii of the holes adjacent to the line-defect region [32]. Figure 3.11(a) shows an example of a linear defect waveguide formed in the snowflake crystal slab. This waveguide consists of a row of snowflake holes which have been removed (a *W1*-like waveguide), and a transverse variation of the snowflake hole size has been applied (see Fig. 3.11 caption for details). Figure 3.11(b) shows a corresponding resonant cavity structure formed from the linear defect waveguide.

The photonic and phononic bandstructures of a linear defect waveguide with $W = 200$ nm is shown in Fig. 3.12. In this diagram only the vertically (z) symmetric optical bands are shown. The waveguide dielectric structure also has a transverse mirror symmetry, σ_y , about the y -axis in the middle of the waveguide. The transverse symmetry of each of the mechanical bands is indicated in Fig. 3.12 by the color of the band, whereas for the optical waveguide bands we use the labels E (even) and O (odd) to indicate the σ_y parity of the fields. A similar E and O labeling scheme is used for the mechanical waveguide modes at the Γ -point, although in this case the parity relates to the σ_x symmetry of the mechanical displacement field within each unit cell along the x -direction of the waveguide. Also, in the photonic band diagram we have indicated the light cone with a dark gray shade. The regions above and below the guided mode bandgap of the unperturbed snowflake crystal are shaded a light gray in both the photonic and phononic band diagrams, with the leaky regions of the photonic waveguide bands colored in red. For this waveguide width, a significant pseudo-bandgap can be seen in the photonic bandstructure (shaded in light blue). At the same time, several phononic bandgaps can be seen in the bands of the mechanical band diagram of the waveguide. Our primary interest when forming a resonant cavity in the next section will be the bandgap highlighted in light blue between the highest frequency phononic waveguide band and the upper frequency band-edge of the unperturbed snowflake crystal. This mechanical waveguide band has the desirable property of very flat dispersion which allows for highly localized phonon cavity states in the presence of waveguide perturbations.

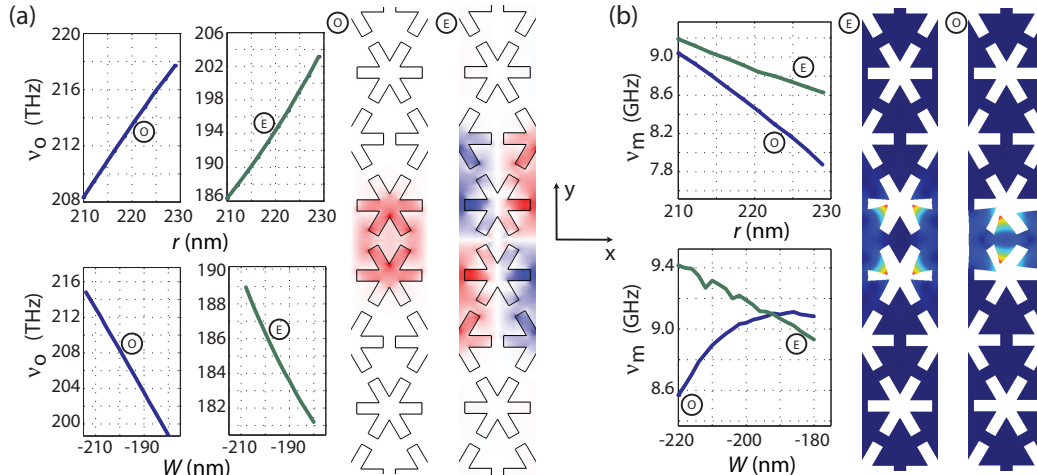


Figure 3.13: **Optical and mechanical waveguide designs on the snowflake crystal.** Tuning of the (a) X -point optical and (b) Γ -point mechanical waveguide modes of a $W1$ -like waveguide in a snowflake substrate with parameters $(d, r, w, a) = (220, 210, 75, 500)$ nm. Tuning is shown versus both waveguide width W and snowflake radius r . In this case we have taken $r_d = 0$, and $N_d^{\text{WG}} = 1$. See Fig. 3.11(a) for line-defect waveguide description. The E and O symbols represent respectively the even and odd vector parity of $\mathbf{E}(\mathbf{r})$ with respect to mirror reflection σ_y about the middle of the waveguide and $\mathbf{Q}(\mathbf{r})$ with respect to mirror reflection σ_x about the middle of each waveguide unit cell. In the optical field plots we show a snapshot in time of the y -polarization of the electric field ($E_y(\mathbf{r})$), with red and blue indicating positive and negative values of the field, respectively. In the mechanical mode plots, color indicates the magnitude of the displacement field (blue no displacement, and red large displacement), and the displacement of the structure has been exaggerated for viewing purposes.

In the design of an optomechanical device, one in which light and sound must be simultaneously manipulated, the independent control of the two types of wave excitations is desired. The tuning of the optical and mechanical waveguide bands of a $W1$ -like line-defect waveguide is shown in Fig. 3.13 for two different types of waveguide geometry perturbations. For simplicity we have only shown the tuning of the waveguide modes at the zone boundary (X -point for the optical and Γ -point for the mechanical waveguide modes). From these plots, it is evident that radius modulations of the snowflake hole tend to tune the optical and mechanical modes in differing directions, whereas for width modulations (through W) of the waveguide the optical and mechanical frequencies tend to tune in a similar direction (this is not true of the odd symmetry mechanical mode in this narrow waveguide). A heuristic argument for this behavior goes as follows. For an optical mode, regions of high refractive index, such as the silicon, tend to reduce the optical frequency for a given curvature (wavevector) of the optical wave. Quite the opposite is true for mechanical excitations in which the material adds to the stiffness of the structure, thereby generally raising the frequency of acoustic waves. This suggests that by using a perturbation where the hole sizes are slightly reduced, since we are increasing the amount of high-index(stiffness) material the photon (phonon) sees while keeping the wavelength constant, the frequency of the mode will decrease (increase). On the other hand, when

the waveguide width is increased, one is in some sense increasing the “transverse” lattice constant of the crystal. Since the lattice constant sets the wavelength for both the optical and mechanical modes, increasing it will cause the frequencies of both waves to drop. By using these perturbations simultaneously, within a certain small range, photonic and phononic bands may be raised and lowered independently. This is a powerful consequence of using differing tuning mechanisms, and allows us to design independently the longitudinal (cavity) confining potentials for phonons and photons.

3.3.2.2 Optomechanical Coupling Relations

In the design methodology followed in this paper, a resonant cavity is formed by locally modulating the properties of a linear defect, or waveguide, in a planar crystal structure. This methodology has been used previously in the design of high- Q photonic crystal cavities, and due to the similarities in the kinematic properties of the wave equations of phonons and photons, we expect it to also produce phononic crystal cavities in the snowflake crystal structure. For our purposes, however, having the photonic and phononic resonances simply co-localized does not suffice, as their interaction must also be tailored, and maximized. To better understand the origin of the optomechanical coupling, it is useful to study the interaction at the level of the waveguide modes, from which the localized cavity resonances are formed.

The coupling between guided optical and mechanical waves has been studied previously in both theoretical and experimental settings [81, 82] for photonic crystal fiber structures with *continuous* longitudinal symmetry. These analyses have generally expanded on calculations of acousto-optical scattering in bulk materials [83]. For this work, we are interested in the case of *discrete* longitudinal symmetry, and a calculation of the coupling per unit cell. Instead of extending the aforementioned analysis to the case of discrete longitudinal symmetry, our approach will be to start with the known *cavity* optomechanical coupling relations, and then to work backwards to a relevant per unit cell guided-mode coupling. This has the benefit of providing a direct relation between the guided-mode and cavity-mode optomechanical couplings. Specifically, using Johnson’s formulation of perturbation theory for moving dielectric boundaries [21], which has been previously applied successfully to the calculation of cavity optomechanical properties [23, 84], we find the cavity optomechanical coupling in terms of the localized mechanical vibration field and an effective optical energy density. Then, using the Wannier function formalism [85–88], we relate (approximately) the cavity and waveguide modes to one another, providing a relation for the guided-mode optomechanical coupling from the cavity-mode optomechanical coupling.

$$g = \sqrt{\frac{\hbar}{2\omega_m}} \frac{\omega_o}{2} \frac{\int (\mathbf{Q}(\mathbf{r}) \cdot \mathbf{n}) (\Delta\epsilon |\mathbf{E}^\parallel|^2 - \Delta(\epsilon^{-1}) |\mathbf{D}^\perp|^2) dA}{\sqrt{\int \rho |\mathbf{Q}(\mathbf{r})|^2 d^3\mathbf{r}} \int \epsilon(\mathbf{r}) |\mathbf{E}(\mathbf{r})|^2 d^3\mathbf{r}} \quad (3.7)$$

This is a pure rate, and is found by multiplying the dispersion of the optical cavity resonance

with mechanical oscillator displacement ($g_{\text{OM}} \equiv \partial\omega_c/\partial x$) by the zero-point fluctuation amplitude of the mechanical oscillator ($x_{\text{ZPF}} = \sqrt{\frac{\hbar}{2m_{\text{eff}}\omega_m}}$). To relate the cavity optomechanical coupling to the properties of the waveguides, we assume that our acoustic and optical cavity fields can both be written in terms of a waveguide Bloch function multiplied by a smoothly varying envelope function. In general these cavity fields can be represented as superpositions of terms of the type $\mathbf{E}_{\pm}(\mathbf{r}) = \mathbf{E}_e(\mathbf{r})e^{\pm i\mathbf{k}_e \cdot \mathbf{r}} f_e(x)$ ($\mathbf{Q}_{\pm}(\mathbf{r}) = \mathbf{Q}_m(\mathbf{r})e^{\pm i\mathbf{k}_m \cdot \mathbf{r}} f_m(x)$), where \mathbf{E}_e (\mathbf{Q}_m) is a periodic Bloch function, k_e (k_m) the reduced wavevector, and $f_e(x)$ ($f_m(x)$) the envelope of the electric (mechanical displacement) cavity field. Note that both the co- and counter-propagating terms ($\pm k_{e,m}$) are necessary to describe the localized standing-wave resonances of a linear cavity.

While a general analysis is possible, we limit ourselves here to the case where the optical cavity mode is formed from the X -point of the waveguide band diagram (see Fig. 3.12(a)), with $\mathbf{k}_e = \mathbf{k}_X$, and the mechanical cavity mode is a Γ -point mode with $\mathbf{k}_m = 0$. The condition on the optical mode is necessary in a quasi-2D slab structure to achieve a high- Q optical cavity, as small k -vector components in the plane of slab can radiate into the light cone of the low-index cladding surrounding the slab. The mechanical mode condition is a phase matching requirement for the coupling of the two counter-propagating optical waves of a standing-wave cavity resonance, $\mathbf{k}_X + (-\mathbf{k}_X) = \mathbf{k}_m = 0$. Hence, starting with

$$\mathbf{E}_{\pm}(\mathbf{r}) = \mathbf{E}_X(\mathbf{r})e^{\pm i\mathbf{k}_X \cdot \mathbf{r}} f_e(\mathbf{x}), \quad (3.8)$$

$$\mathbf{Q}(\mathbf{r}) = \mathbf{Q}_{\Gamma}(\mathbf{r})f_m(\mathbf{x}), \quad (3.9)$$

and assuming that the envelope functions vary slowly over a lattice spacing, and that they have no zero-crossings, we separate the integrals into a product of two integrals, one over a single waveguide unit-cell and the other across multiple unit-cells. For example,

$$\int |\mathbf{Q}(\mathbf{r})|^2 d\mathbf{r} \approx \frac{1}{a} \int_{\Delta} |\mathbf{Q}_{\Gamma}(\mathbf{r})|^2 d^3\mathbf{r} \int |f_m(x)|^2 dx. \quad (3.10)$$

From here, we arrive at the following expression for g :

$$g \approx \sqrt{a}g_{\Delta} \frac{\langle f_e | f_m | f_e \rangle}{\sqrt{\langle f_m | f_m \rangle \langle f_e | f_e \rangle}}, \quad (3.11)$$

where g_{Δ} is the guided-mode optomechanical coupling given by

$$g_{\Delta} = \sqrt{\frac{\hbar}{2\omega_m}} \frac{\omega_o}{2} \frac{\int_{\Delta} (\mathbf{Q}_{\Gamma}(\mathbf{r}) \cdot \mathbf{n}) (\Delta\epsilon |\mathbf{E}_X^{\parallel}|^2 - \Delta(\epsilon^{-1}) |\mathbf{D}_X^{\perp}|^2) dA}{\sqrt{\int_{\Delta} \rho |\mathbf{Q}_{\Gamma}(\mathbf{r})|^2 d^3\mathbf{r} \int_{\Delta} \epsilon(\mathbf{r}) |\mathbf{E}_X(\mathbf{r})|^2 d^3\mathbf{r}}}. \quad (3.12)$$

Equation (3.11) shows that the optomechanical coupling achievable is the product of a term

g_Δ depending only on the linear waveguide properties and a second term which is a function of the envelope functions $f_e(x)$ and $f_m(x)$ describing the localization of the cavity resonances along the length of the waveguide. In many relevant systems, the optical and mechanical modes may be approximated as Gaussians with standard deviation in intensity profile of L_m and L_e . In this case the envelope-dependent component of the cavity optomechanical coupling is,

$$\langle f_e | f_m | f_e \rangle = \frac{1}{(2\pi)^{\frac{1}{4}}} \frac{1}{\sqrt{L_m + \frac{1}{2} \frac{L_e^2}{L_m}}}. \quad (3.13)$$

The largest value of the envelope dependent part of the optomechanical coupling from equation (3.13) is achieved by making $L_m = L_e/\sqrt{2}$. For this ratio of mechanical and optical cavity Gaussian profiles one arrives at a maximum optomechanical coupling rate of

$$g_{\text{optimal}} \approx \frac{1}{(4\pi)^{\frac{1}{4}}} g_\Delta \sqrt{\frac{a}{L_e}}. \quad (3.14)$$

Clearly, the more localized the optical and mechanical resonances the larger the optomechanical coupling, all other things being equal.

3.3.2.3 Snowflake Optomechanical Cavity Design

As mentioned above, higher- Q optical cavity resonances will be formed from optical modes near the X -point of the linear-defect waveguide as they lie underneath the out-of-plane light cone. Phase-matching then requires the mechanical resonance to be formed primarily from the Γ -point in order to have significant optomechanical interaction of the two localized resonances. Given the even symmetry along x within each unit cell of the *intensity* of the optical field for waveguide modes at the X -point (again, all X -point modes can be classified by their σ_x parity, and thus their intensity must be symmetric), and considering the form of Eqn. (3.12) for the per unit cell optomechanical coupling, we see that only the even symmetry (E) mechanical modes at the Γ -point yield a non-zero g_Δ . As such, we choose to form the localized phononic cavity resonance from the uppermost phononic waveguide band in Figure 3.12(b) (the lowermost phononic waveguide band, also of even parity at the Γ -point, was found to have a smaller g_Δ). To avoid coupling to mechanical waveguide bands below this upper band, we choose to form a cavity defect perturbation which *increases* the frequency of the upper mechanical waveguide band, thus localizing the phononic resonance in the highlighted blue pseudo-bandgap of Fig. 3.12(b).

In the case of the optical field, we can choose to form the localized cavity resonance from either the upper or the lower frequency waveguide bands that define the photonic pseudo-bandgap of

the waveguide (see Fig. 3.12(a)). We choose here to use the upper frequency waveguide band due to its more central location in the pseudo-bandgap of the unperturbed snowflake crystal. The curvature of the upper frequency waveguide band near the X -point is positive, so we need to have the cavity perturbation cause a local *decrease* in the band-edge frequency; the opposite frequency shift required for that of the mechanical waveguide band. From Figure 3.13, it is evident that the radius modulation satisfies this requirement, i.e. it tunes the optical and mechanical band-edge modes in opposing directions. Here we use a combination of transverse and longitudinal quadratic modulations with parameters $(r_d, N_d, N_d^{\text{WG}}) = (0.03, 14, 5)$ to form the optomechanical cavity. The resulting cavity geometry is depicted in Figure 3.11(b).

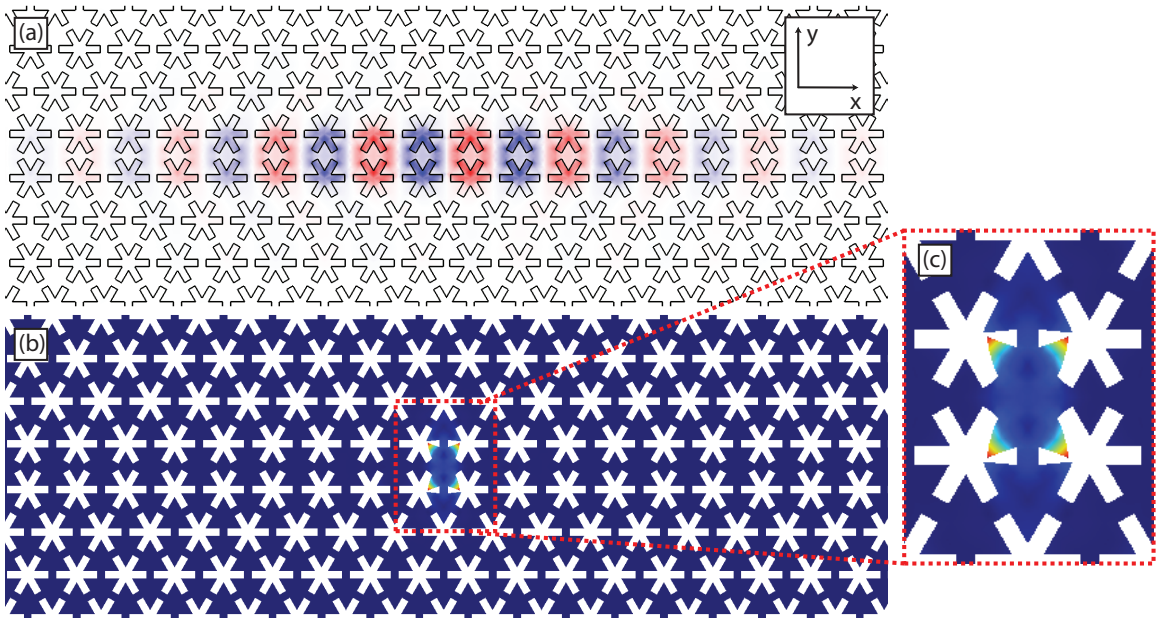


Figure 3.14: Optical and mechanical simulations of co-localized photons and phonons on the snowflake crystal. Plots of the localized ultrahigh- Q resonances of an optomechanical cavity formed in a Si snowflake thin-film substrate with parameters $(d, r, w, a) = (220, 210, 75, 500)$ nm. (a) Optical field ($E_y(\mathbf{r})$) and (b) magnitude of the mechanical displacement field ($Q(\mathbf{r})$). (c) Zoom-in of the mechanical displacement field. In the optical field plot we show a snapshot in time of the y -polarization of the electric field, with red and blue indicating positive and negative values of the field, respectively. In the mechanical mode plots, color indicates the magnitude of the displacement field (blue no displacement, and red large displacement), and the displacement of the structure has been exaggerated for viewing purposes. The mechanical resonance is at a frequency of $\nu_m = 9.50$ GHz, and the optical mode at a wavelength of $\lambda_0 = 1.459 \mu\text{m}$. The defect cavity design, with parameters $(r_d, N_d, N_d^{\text{WG}}) = (0.03, 14, 5)$, is described in Fig. 3.11. The lowest-order optomechanical coupling between the photon and phonon cavity resonances is calculated to be $g_0 = 2\pi \times 146$ kHz.

As hoped, the resulting optomechanical cavity supports a localized fundamental mechanical mode of frequency $\nu_m = 9.5$ GHz and a fundamental optical mode of frequency $\nu_o = 205.6$ THz, the latter corresponding to a free-space wavelength of $\lambda_0 = 1.459 \mu\text{m}$. Plots of the FEM-simulated electric and mechanical displacement fields of both localized cavity resonances are shown in Fig. 3.14. Owing

to the extremely flat dispersion of the mechanical waveguide band, the cavity phonon resonance is localized almost entirely to the central unit cell of the cavity. The resulting effective motional mass of this localized phonon is only $m_{\text{eff}} = 3.85 \text{ fg}$. The optomechanical coupling of photons and phonons in this cavity is calculated to be $g_0/2\pi = 146 \text{ kHz}$. This value represents an enormous radiation pressure coupling of the optical and mechanical fields, being only a factor of two or so weaker than that found in the strongly-coupled zipper cavity [23] and only slightly below the approximate upper-bound calculated using equation (3.14) of $g_{\text{optimal}}/2\pi = 191 \text{ kHz}$.

The radiation-limited optical Q -factor was also computed for this cavity using perfectly-matched-layer radiation boundary conditions, and found to be limited to $Q \approx 5.1 \times 10^7$ due to out-of-plane radiation. The corresponding mechanical Q -factor of the localized phonon resonances is $Q_m \gg 10^7$ for 40 unit cells surrounding the cavity region. Unlike in the optical case, this mechanical Q can be made arbitrarily large by increasing the number of unit cells surrounding the cavity due to the lack of an out-of-plane loss mechanism and a pseudo-bandgap in-plane. The important practical limiting factor in both the mechanical and optical Q will of course be the presence of perturbations in a real fabricated structure. From Fig. 3.12 we see that in the absence of perturbations breaking the z -mirror symmetry, the mechanical radiation loss can be made effectively zero due to the complete lack of states to which the phononic resonance can couple. Perturbations breaking the z -mirror symmetry will however induce loss by coupling to odd vertical symmetry mechanical waveguide modes, colored light green in Fig. 3.12. Terminating the waveguide, i.e. transitioning back into the bulk snowflake crystal after some number of unit cells, eliminates this component of mechanical radiative loss as well.

3.4 Thermal noise spectroscopy of micromechanical resonators

The noise spectroscopy and sideband-resolved mode thermometry presented in section 2.2 is predominantly concerned with the resonant response of the structure. In our experiments with sideband-resolved systems, the detected noise floor is typically overwhelmed by optical shot-noise at frequencies far from the mechanical resonance. The optomechanical resonators presented in this thesis are typically higher frequency than those considered by other groups. A higher frequency resonator provides less sensitive transduction for low frequency thermal noise. This can be simply understood as a conserved gain-bandwidth product, where a less stiff mechanical system provides higher “gain” (motion per unit force) but exhibits a correspondingly smaller bandwidth (i.e., resonance frequency). The lowest frequency resonators in this thesis are the zipper cavities presented in section 5.3. These systems are also the ones that we use for the squeezing experiment, where the broadband mechanical response gives rise to the desired effect. As shown below, in these systems, the broadband mechanical response to thermal noise is detectable, i.e., far enough above the shot-noise that its exact form

can be determined and studied.

3.4.1 Phenomenological dispersive noise model: the effect of structural damping

Mechanical damping of resonators and the associated fluctuations from coupling to the thermal bath has long been considered as an impediment to measuring weak forces in gravitational wave detectors [66, 67, 89–91]. In these studies the effect of the bath has often been encapsulated in a parameter $\Psi(\omega)$, representing the lag angle in the response of the material to a force. This lag angle is the complex part of the spring constant: $F = -k(1 + i\Psi(\omega))x$. The quality factor of the resonator is given by the narrow-band properties of the lag angle and its value at the mechanical resonance frequency, $Q = \Psi(\omega_m)^{-1}$. We are interested in the wideband properties of $\Psi(\omega)$, since the spectral properties of the thermal fluctuations are related to the spectrum $\Psi(\omega)$, following the fluctuation-dissipation theorem.

In the case of our experiments, we observed noise floors for S_{xx} following a ω^{-1} power law on the low frequency end. This sort of noise power law corresponds to a flat spectrum for the lag angle $\Psi(\omega) = \text{const.}$ over the frequency range of interest. Unlike viscous damping which can be simply shown to have $\Psi(\omega) \propto \omega$ (since the force is proportional to velocity), a lag angle constant in frequency lacks a simple physical explanation, though it is ubiquitous in many types of mechanical resonators and commonly called “structural damping” [67].

In the input-output formalism outlined in section 2.3 we model this type of noise by taking the mechanical damping rate γ_i to be spectrally flat, and using frequency dependent bath correlation functions $\langle \hat{b}_{\text{in}}(\omega)\hat{b}_{\text{in}}^\dagger(\omega') \rangle = (\bar{n}(\omega) + 1)\delta(\omega + \omega')$, $\langle \hat{b}_{\text{in}}^\dagger(\omega)\hat{b}_{\text{in}}(\omega') \rangle = \bar{n}(\omega)\delta(\omega + \omega')$, $\langle \hat{b}_{\text{in}}^\dagger(\omega)\hat{b}_{\text{in}}^\dagger(\omega') \rangle = 0$, and $\langle \hat{b}_{\text{in}}(\omega)\hat{b}_{\text{in}}(\omega') \rangle = 0$. This constitutes our single-mode thermal noise model.

In any real optomechanical system, a family of mechanical modes couples to the optical resonance. In the modal picture which we use here, each of these mechanical resonances can be thought to add to the detected noise floor with its contribution scaling at the low-frequency end as ω^{-1} . The contribution of each mode is proportional to the bath temperature, $g_{0,k}^2$, $\gamma_{i,k}$, and $\omega_{m,k}^{-2}$. We lump all of these contributions into a single effective mechanical resonance, with its properties (not all independent) determined by fitting to the low frequency end of the noise floor. This mechanical resonator is modeled with a mechanical frequency $\omega_m/2\pi = 50$ MHz (so we operate in the low frequency tail), a mechanical quality factor $Q_m = 100$, and a total coupling rate of $g_0/2\pi = 100$ kHz. We found that this model reproduced the magnitude and phase (the quadrature in which the noise is detected) of the ω^{-1} noise well, if an additional intracavity photon-dependent heating of $c_0 = 3.2 \times 10^{-4}$ K/photons is assumed. These background noise floors are plotted in figure 3.15. This cavity heating rate leads to the effective bath temperature to nearly double at the highest input

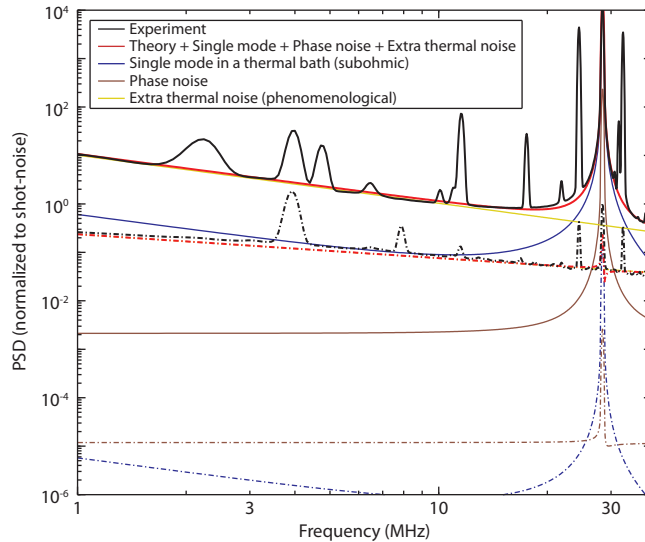


Figure 3.15: **Noise model and experimental results for zipper cavity.** The complete noise model, and constituent components, are plotted and compared to the experimental, shot-noise-subtracted PSD for a quadrature sensitive to the mechanical motion (solid curves) and an insensitive quadrature (dotted dashed curves), in the zipper cavity presented in section 5.3. The black lines are the experimental PSDs. The red lines represent the full noise model including contributions from a single mechanical mode (blue line), phase noise of the laser (brown line), and the extra thermal noise (yellow line) as described in section 3.4.1. The deviation between the modeled and experimental data predominantly results from additional mechanical modes.

powers, going from 16 K to over 30 K. This amount of heating is in line with what we expect from thin-film photonic crystals we have fabricated in the past operating in the same cryostat [46].

3.4.2 Phenomenological absorptive noise model

In addition to the noise in the quadrature of the mechanical motion (which arises from fluctuations in the cavity frequency ω_o , and we suspect is mechanical in origin), we observed a significant amount of noise in the opposite quadrature, which can be interpreted to arise from fluctuations of the cavity decay rate κ . Additionally, we observed a different noise floor power law ($\omega^{-1/2}$) for this noise, which may rule out an optomechanical origin. The power law scaling agreed with thermorefractive noise studied extensively in the context of gravitational wave detection [90], microspheres [92], and microtoroids [93], but it is expected that thermorefractive coupling is predominantly in the same quadrature as the mechanical noise, which is not observed here. Also, if thermorefractive, the noise should show strong variation with temperature through both a quadratic temperature scaling (T^2) and an extremely steep variation of dn/dT in the temperature range of 16 K to 30 K [94], which was not observed. At this point, we have no noise model to explain the observed fluctuations, and the origin of this noise will be the subject of further investigation to be presented at a later

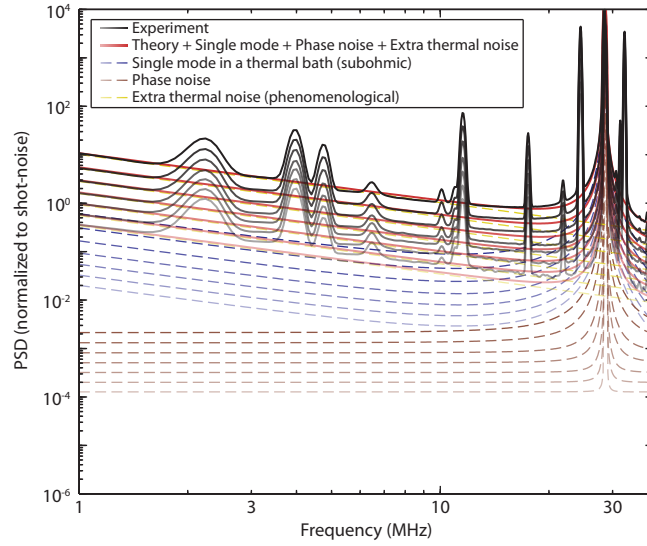


Figure 3.16: **Power spectral density of noise contributions with varying powers.** The complete noise model along with its constituent components and experimental data are shown for varying optical powers. All curves have been normalized to the shot-noise level. The experimental data are shown in black with the full noise model in red consisting of the single mechanical mode (dashed blue), phase noise (dashed brown), and extra thermal noise (dashed yellow). The optical power scaling is represented by the transparency of the individual curves with curves becoming less transparent with increasing optical power. The traces from highest power to lowest power correspond to intracavity photon numbers of $n_c = 3140, 1990, 1250, 792, 498, 314,$ and 196 photons (2 dB steps).

time. A phenomenological noise model was instead used, where fluctuations in the cavity linewidth proportional to the intracavity power with a $\omega^{-1/2}$ noise spectrum are assumed.

Chapter 4

Quasi-two-dimensional silicon optomechanical resonators

4.1 Two-dimensional slotted photonic crystal cavities [1]

In this work we design, fabricate, and measure the optomechanical properties of a slotted two-dimensional (2D) photonic crystal cavity formed in a Silicon membrane. Due to the strong optical confinement provided by a sub-100 nm slot and a two-dimensional photonic bandgap, this cavity structure is demonstrated to have an optical quality factor $Q > 10^6$, large optomechanical coupling rate g_0 , and a deep sub-cubic-wavelength optical mode volume.

A common approach to forming photonic crystal optical circuits is to etch a pattern of holes into a thin dielectric film such as the top Silicon device layer in a Silicon-On-Insulator (SOI) microchip. An effective means of forming resonant cavities in such quasi-2D slab photonic crystal structures is to weakly modulate the properties of a line-defect waveguide [71, 78, 79]. Applying this same design principle to slotted photonic crystal waveguides [95], optical cavities with $Q \leq 5 \times 10^4$ have been experimentally demonstrated [96, 97]. A major source of optical loss in real fabricated structures is light scattering out of the plane of the slab. One class of optical states which play an important role in determining scattering loss are the resonant leaky modes of the slab. These optical resonances are localized to the slab and yet have wavevector components which radiate energy into the surrounding cladding. To reduce the effects of these modes it is preferable to engineer a structure where the photonic crystal waveguide has no leaky mode bands crossing the localized cavity mode frequency. For the popular W1 waveguide [78, 79] with a slot added in the waveguide center, we have found that the choice of the slot width is crucial to avoiding coupling to leaky resonances. Figure 4.1(a) shows the bandstructure of a slotted W1 waveguide with a hole radius $r = 0.285a = 134$ nm, slot size $s = 0.2a = 94$ nm, thickness $t = 220$ nm, and nominal lattice constant of $a = 470$ nm. A large bandgap for both guided and leaky modes (a “quasi-bandgap”) is clearly present in this structure for the TE-like (even vector parity) modes of the waveguide. On the otherhand, for slot widths

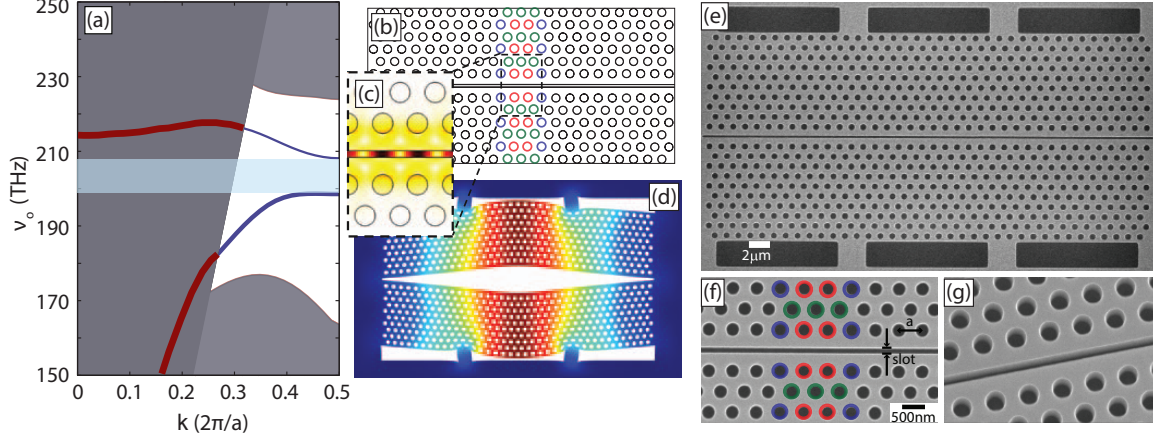


Figure 4.1: **Optical and mechanical simulations of slotted photonic crystal cavity.** (a) Band diagram for a slotted W1 waveguide formed in a thin ($t = 220$ nm) Silicon layer. The waveguide slot size is $s = 0.2a$, with lattice hole radius $r = 0.285a$ for a nominal lattice constant of $a = 470$ nm. The light gray shade indicates the guided mode continua, while the dark gray represents the unguided continua of radiation modes. The blue curve is the waveguide band used to create the heterostructure cavity. Leaky resonant modes are shown by the thick red line. The photonic quasi-bandgap (for TE-like modes of even vector parity) is highlighted in blue. (b) Electric field intensity, $|\mathbf{E}(\mathbf{r})|^2$ of the optical mode. (c) Zoom-in of the slotted region showing strong optical field confinement. (d) Total displacement field $|\mathbf{Q}(\mathbf{r})|$ of the simulated fundamental mechanical mode at 146.1 MHz. (e) SEM image of the fabricated sample. (f) Zoom-in SEM image of the cavity region, with the heterostructure defect cavity region highlighted in false color, and (g) SEM image showing the etched sidewalls of the slot and holes.

$s > 0.25a$ the quasi-bandgap of the waveguide closes due to the presence of leaky resonant bands.

In order to form a localized cavity resonance, we begin with the slotted cavity waveguide structure of Figure 4.1(a). A localized resonance is created from the lower frequency waveguide band by reducing smoothly the local lattice constant from a nominal value of $a = 470$ nm to a value of $a = 450$ nm in the center of the cavity. Three-dimensional FEM simulations of the optical and mechanical properties of the resulting cavity structure were performed. The simulated electric field intensity of the fundamental confined optical mode is shown in Fig. 4.1(b). This mode has a resonance wavelength of $\lambda_o \approx 1550$ nm, a theoretical radiation-limited $Q > 10^6$ and an effective optical mode volume of $V_{\text{eff}} = 0.04 (\lambda_o)^3$.

To allow for mechanical motion of the structure, three rectangular holes of dimensions $4.9 \mu\text{m} \times 1.0 \mu\text{m}$ are cut on each side of cavity device as shown in Fig. 4.1(d). FEM simulations show that this allows for a fundamental in-plane mechanical mode of motion with frequency $\omega_m/2\pi = 146.1$ MHz and an effective motional mass of $m_{\text{eff}} = 20$ pg. The optomechanical coupling between the localized optical and mechanical modes is computed to be optical frequency shift per nanometer of mechanical displacement of $g_{\text{OM,Bnd}} = 2\pi \times 480$ GHz/nm (see section 1.1.3), or in the quantum realm a phonon-photon coupling rate of $g_0 = g_{\text{OM,Bnd}} \sqrt{\hbar/2m_{\text{eff}}\omega_m} = 2\pi \times 800$ kHz.

Slotted cavities with the dimensions stated above are fabricated using a Silicon-On-Insulator wafer from SOITEC ($\rho = 4\text{-}20 \Omega \cdot \text{cm}$, device layer thickness $t = 220 \text{ nm}$, buried-oxide layer thickness $2 \mu\text{m}$). The cavity geometry is defined by electron beam lithography followed by reactive-ion etching to transfer the pattern through the 220 nm silicon device layer. The cavities are undercut using $\text{HF}:\text{H}_2\text{O}$ solution to remove the buried oxide layer, and cleaned using a piranha/HF cycle [98]. A scanning electron microscope (SEM) micrograph of a final device is shown in Fig.4.1(e). Fig. 4.1(f) and Fig. 4.1(g) show the local waveguide defect and slotted region of the cavity, respectively.

The resulting devices are characterized optically using a swept-wavelength external-cavity laser ($\lambda = 1510 - 1590 \text{ nm}$, $\Delta\lambda < 300 \text{ kHz}$), connected to a dimpled fiber-taper probe [99]. A broadband cavity transmission spectrum is shown in Fig. 4.2(a), with the first- and second-order optical cavity modes separated by roughly by 10 nm , in agreement with simulations. For the first-order mode, optical Q on the order of 10^6 is measured consistently in these devices. A narrowband optical transmission spectrum (calibrated using a fiber Mach-Zender interferometer) for one such device is shown in the inset of Fig. 4.2(a), with a measured intrinsic optical $Q_i = 1.2 \times 10^6$.

The mechanical properties of the slotted photonic crystal cavity are measured by driving the system with the laser frequency locked to a detuning of a half-linewidth (blue or red) from the cavity resonance. The transmitted cavity laser light is sent through an erbium doped fiber amplifier and then onto a high-speed photodetector. The photodetected signal is sent to an oscilloscope (2 GHz bandwidth) where the electronic PSD is computed. An example of the measured RF-spectrum from a typical slotted cavity device is shown in Fig. 4.2(b). The fundamental in-plane mode, corresponding to the largest peak in the spectrum, is found to occur at a frequency of $\omega_m/2\pi = 151 \text{ MHz}$, very close to the simulated value of 146 MHz . RF spectra for various dropped optical powers into the cavity are shown in Fig. 4.2(c). The corresponding mechanical linewidth is plotted in Fig. 4.2(d). The effects of the retarded component of the dynamical back-action [100] of the light field on the mechanical resonance are clear in both plots, with red (blue) detuning resulting in a reduction (amplification) in the mechanical resonance peak height and a broadening (narrowing) of the mechanical linewidth. One curious aspect of the measured mechanical spectra, however, are the two smaller side peaks on either side of the main resonance line. These side peaks are thought to arise due to a mixing of the in-plane mode with nearby flexural (out-of-plane) resonances of the slab. FEM simulations indicate the presence of several flexural modes located within a few MHz of the fundamental in-plane mode, which can mix with in-plane motion through a breaking of the vertical symmetry of the slab. As an example, SEM images show that the membranes are subject to weak stress-induced bowing, which can lead to this effect.

The optomechanical coupling of the fundamental in-plane mechanical resonance can be estimated using two different methods. The first method involves calibration of the optical powers and electronic detection system, and uses the fact that the transduced thermal Brownian motion of the

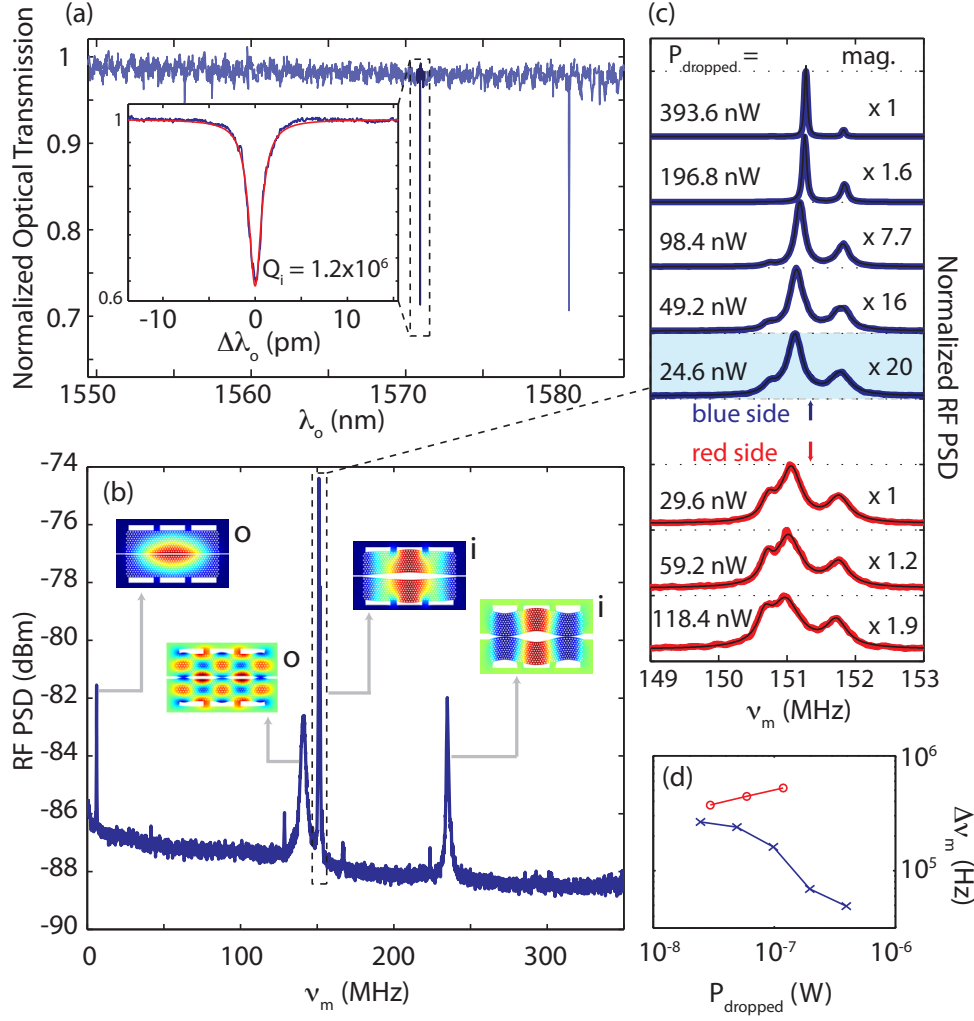


Figure 4.2: **Optical and mechanical spectroscopy of the slotted photonic crystal cavity.** (a) Normalized optical transmission spectrum showing the first and second order optical cavity modes. (inset) Transmission spectrum for the first order mode showing an intrinsic quality factor of $Q_i = 1.2 \times 10^6$. (b) PSD of the photodetected signal, indicating a series of resonance peaks corresponding to mechanical motion of the patterned slab. (c) PSD around the frequency of the fundamental in-plane mechanical resonance for various optical powers dropped into the cavity. A pair of optical attenuators is used, one at the input and one at the output of the cavity, so that the optical power reaching the photodetector is constant and the measured PSD is only dependent upon the amplitude of mechanical motion. The red (bottom three) and blue (top five) spectra represent spectra taken with red and blue input laser detuning from the cavity resonance, respectively. Denoted for each spectrum is the optical power dropped into the cavity and a scale factor used to normalize the peak height in each spectrum to a common value. (d) Linewidth of the fundamental in-plane mechanical mode extracted from the spectra in (c). \times = blue detuning, \circ = red detuning.

mechanical resonator is proportional to $g_{\text{OM}}^2/m_{\text{eff}}$ [101]. The second method compares the ratio of the RF power in the first and second harmonic of the mechanical frequency. This method is independent of the absolute optical power and detection efficiency, and relies only on accurate knowledge of the optical linewidth. Both of these methods were found to yield an experimental optomechanical

coupling of $g_{\text{OM}}^* = 2\pi \times 140$ GHz/nm for the fundamental in-plane mechanical resonance (assuming $m_{\text{eff}} = 20$ pg), roughly a factor of 3.4 times smaller than the FEM-estimated value. As alluded to above, this discrepancy is thought to result from mixing of in-plane motion with optomechanically “dark” (i.e., no coupling to first-order in motional amplitude) flexural modes of the patterned slab.

In summary, the slotted photonic crystal cavity described here reduces optical scattering loss through the avoidance of resonant leaky modes of the structure while simultaneously allowing for large electric field enhancement in the cavity slot region. The demonstrated optical loss rate of the cavity is $\kappa/2\pi \approx 160$ MHz, which in conjunction with the high mechanical frequency ($\omega_m/2\pi = 151$ MHz) of the fundamental in-plane mechanical resonance, puts this system in the resolved sideband limit of cavity optomechanics ($\kappa/2\omega_m < 1$). The resolved sideband limit is important for a variety of applications, including optical cooling of the mechanical motion to the quantum mechanical ground-state [37, 39]. The optomechanical coupling is estimated to be $g_{\text{OM}}^*/2\pi = 140$ GHz/nm for the slotted cavity. The estimated Q/V_{eff} ratio for the measured devices is $3 \times 10^7(\lambda)^{-3}$, indicating that these slotted cavities may also find use in other applications such as Silicon-based cavity-QED [96] and sensing [97].

4.2 Optomechanics of a simultaneous bandgap phononic-photonic crystal

The snowflake cavity design introduced in section 3.3.2.3 was fabricated and its optomechanical properties were measured using EIT spectroscopy described in section 2.2.1.1. Due to fabrication constraints, the perfectly rectangular shapes making the snowflakes were not transferred faithfully onto the silicon. Effectively, the corners were rounded in the beamwrite due to resolution and proximity effect constraints. This modified the mechanical and optical mode spectra of the devices, which were resimulated. In figure 4.3c we show the resimulated optical mode profile for the fabricated structure (figure 4.3a). Fiber-taper coupling to the optical cavity was used to measure a linewidth $\kappa/2\pi = 2.1$ GHz, and an extrinsic coupling of $\kappa_e/2\pi = 1.0$ GHz.

The extremely flat dispersion of the mechanical waveguide mode (see Fig. 3.12b) means that a shallow defect can generate large number of localized mechanical resonances, all closely spaced and sensitive to local perturbations. This makes identification of the detected mechanical mode difficult. An example spectrum is shown in figure 4.4a. In this case there are two modes that are closely spaced, with a frequency spacing of 7 MHz.

Fitting of the detected spectra is done in two steps. First, given a known κ (from a separate optical transmission measurement), the wideband spectrum (Fig. 4.4a,b) is fit to find the detuning Δ . Afterwards, the narrowband spectrum (Fig. 4.4a,b inset), now only a function of the mechanical resonator linewidths (γ_{OM} , γ_i for each resonator) and frequencies (ω_m for each resonator), is fit.

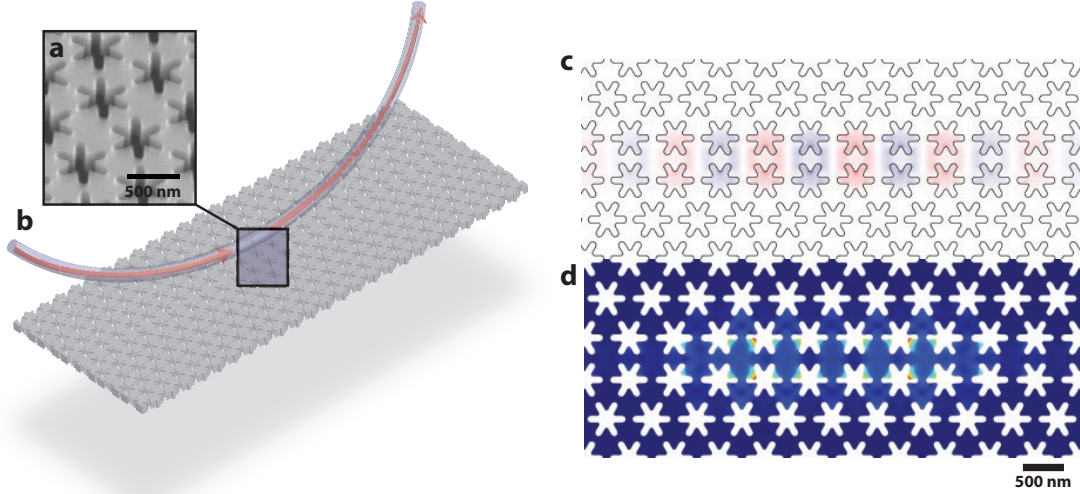


Figure 4.3: **Fabricated snowflake cavity and mode profiles.** **a**, The fabricated structure is shown. **b**, A fiber taper is used to couple to the optomechanical resonator. In **c**, we show the simulated mode profile for the optical resonance and **d**, mechanical mode which is studied. The mechanical mode has a calculated coupling rate of $g_0/2\pi = 330$ kHz. There are other modes spaced by about 30 MHz higher and lower frequency of this mode. We identify this mode as closest to the one measured shown in Fig. 4.4 because it is the highest frequency mode with significant optomechanical coupling.

Roughly speaking, the ratio of the intrinsic and total linewidths determines the visibility of the feature, while the total width is given by the sum of the intrinsic and optomechanical linewidths. The fit intrinsic mechanical linewidth and back-action rates are plotted in figure 4.4c. As expected, the back-action rates fall on a line, showing that this component of the mechanical linewidth goes linearly with optical power. Also, the intrinsic mechanical loss rate γ_i changes with optical power, going from around 200 kHz to nearly 750 kHz, as shown in Fig 4.4. The source of this deterioration of the mechanical quality factor is not fully understood, but experiments in a silicon nanobeam suggest free carriers generated optically in the silicon to be the culprit. For further details of such parasitic heating effects in silicon OMC cavities, the interested reader is referred to the Supplementary Information of Ref. [46].

The slope of the line shown in figure 4.4c can be used to find the g_0 , since $\gamma_{OM} \approx 4g_0^2 n_c / \kappa$. The two modes are found to have values of g_0 of 220 kHz and 180 kHz respectively. These numbers are roughly in line with the simulated value of 330 kHz, for the mode shown in Figure 4.3d. We expect the slightly lower measured value and the double moded-ness to be due to mode splitting from symmetry breaking about the $y - z$ plane.

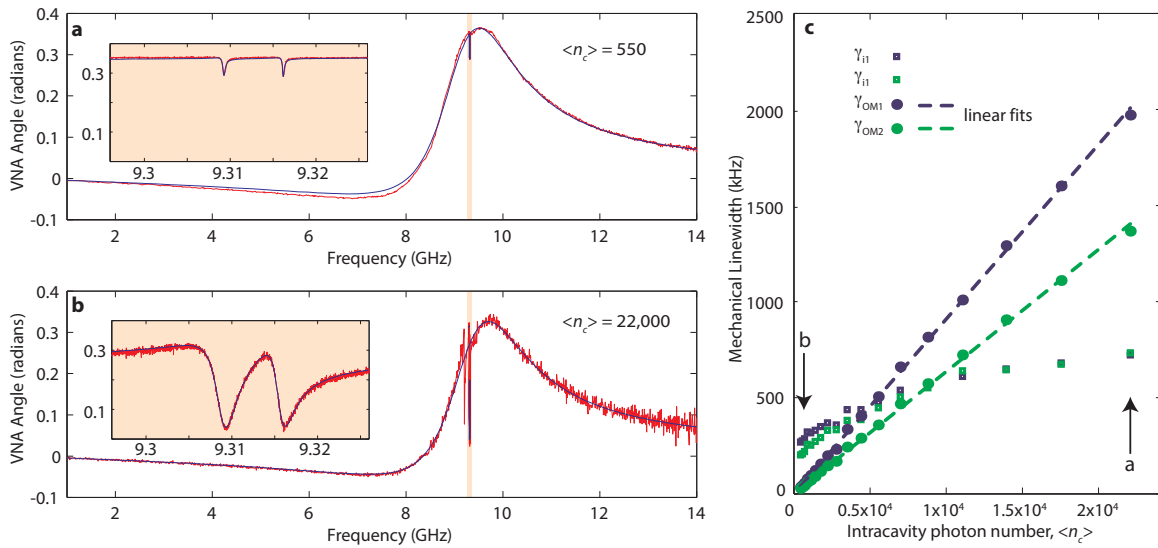


Figure 4.4: **Mechanical Spectroscopy of Snowflake Cavities.** **a,b** show the low and high power (550 and 22,000 intracavity photons respectively) EIT spectra taken using a vector network analyzer. The insets show the highlighted frequencies in more detail. The fits shown in the insets are used to extract the optomechanical coupling (γ_{OM}) and intrinsic mechanical loss rate (γ_i) for every optical power. These are plotted in **c**.

Chapter 5

Main experimental results

5.1 Electromagnetically induced transparency and slow light with optomechanics [2]

Controlling the interaction between localized optical and mechanical excitations has recently become possible following advances in micro- and nano-fabrication techniques [100, 102]. To date, most experimental studies of optomechanics have focused on measurement and control of the mechanical subsystem through its interaction with optics, and have led to the experimental demonstration of dynamical back-action cooling and optical rigidity of the mechanical system [100, 103]. Conversely, the optical response of these systems is also modified in the presence of mechanical interactions, leading to strong nonlinear optical effects such as EIT [64] and parametric normal-mode splitting [104]. In atomic systems, seminal experiments [105] and proposals to slow and stop the propagation of light [106], and their applicability to modern optical networks [83], and future quantum networks [107], have thrust EIT to the forefront of experimental study during the last two decades. In a similar fashion, here we use the optomechanical nonlinearity to control the velocity of light via engineered photon-phonon interactions. Our results demonstrate EIT and tunable optical delays in a nanoscale OMC device, fabricated by simply etching holes into a thin film of silicon (Si). At low temperature (8.7 K), we show an optically-tunable delay of 50 ns with near-unity optical transparency, and superluminal light with a 1.4 μ s signal advance. These results, while indicating significant progress towards an integrated quantum optomechanical memory [108], are also relevant to classical signal processing applications. Measurements at room temperature and in the analogous regime of EIA show the utility of these chip-scale optomechanical systems for optical buffering, amplification, and filtering of microwave-over-optical signals.

It is by now well known that the optical properties of matter can be dramatically modified by using a secondary light beam, approximately resonant with an internal process of the material system. As an example, an opaque object can be made transparent in the presence of a control beam,

in what is referred to as EIT. A remarkable feature of EIT is the drastic reduction in the group velocity of light passing through the material, achieved inside a practically lossless transparency window. This aspect of the effect has been utilized to conjure schemes whereby light may be slowed and stopped, making it an important building block in quantum information and communication proposals, as well as of great practical interest in classical optics and photonics. A simple upper-bound for the storage time in EIT-based proposals is the lifetime related to the internal processes of the material. These lifetimes are longest in pure atomic gas and lattice systems, with storage times up to 240 ms having been demonstrated [109]. Part of the vision for future scalable quantum networks has involved extending the remarkable results achieved in atomic experiments to a more readily deployable domain [110].

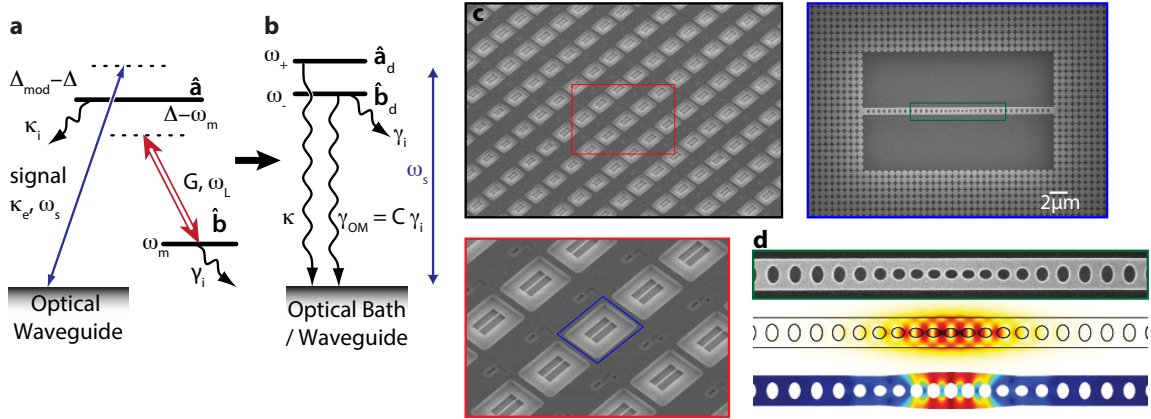


Figure 5.1: **Optomechanical System.** **a**, Level-diagram picture, showing three “levels” representing the optical mode \hat{a} , mechanical mode \hat{b} and the “bath” of optical waveguide modes. **b**, The control beam at ω_c drives the transition between the optical and mechanical mode, dressing the optical and mechanical modes, resulting in the dressed state picture with dressed modes \hat{a}_d and \hat{b}_d . **c**, Scanning electron micrographs (SEM) of an array of OMC nanocavities. **d**, From top to bottom: scanning electron micrograph (SEM) of a zoomed-in region showing the OMC defect region; FEM simulation results for the optical field showing the electrical field intensity $|\mathbf{E}(\mathbf{r})|$; FEM simulated mechanical mode with the total displacement $|\mathbf{Q}(\mathbf{r})|$ shown.

In the solid state, EIT has been demonstrated in quantum wells, dots, and N-V centers [111]. The fast dephasing rates and inhomogeneous broadening of solid state electronic resonances, however, has led to a plethora of other methods and techniques. Elegant experiments with stimulated Brillouin scattering (SBS) in fibers [112], and coherent population oscillations (CPO) [113] have been used to delay intense classical light. Alternatively, for quantum storage and buffering, techniques based on photon-echo spectroscopy (e.g. CRIB [114] and AFC [115]) have been used successfully to achieve solid-state quantum memories. In chip-scale photonics, proposals for dynamically tunable arrays of cavities, displaying EIT, are an intriguing analogy to ensembles of atoms and provide a route to slowing and stopping light all-optically [116]. Generally, the elements in the arrays have consisted

of coupled optical or plasmonic resonances, and have been demonstrated with couplings engineered to give rise to Fano-like interference [117]. A significant limitation in these all-photonic systems, however, is the short optical resonance lifetime. With optomechanics, EIT arising from optically controlled interactions between engineered optical and mechanical modes provides the means for tunable delays on the order of the mechanical resonance lifetime, which due to the lower mechanical frequency, can be orders of magnitude longer than the lifetime of the optical mode. Such delays are attainable at any wavelength and in any material which is of high optical and mechanical quality. Additionally, the on-chip nature and Si compatibility of many optomechanical systems [118] suggest that arrays of such structures may be possible [119], allowing for the dynamic slowing and storage of light pulses [108].

EIT in optomechanical systems can be understood physically as follows. The conventional radiation pressure interaction between a near-resonant cavity light field and mechanical motion is modeled by the nonlinear Hamiltonian $H_{\text{int}} = \hbar g \hat{a}^\dagger \hat{a} (\hat{b} + \hat{b}^\dagger)$, where \hat{a} and \hat{b} are the annihilation operators of photon and phonon resonator quanta, respectively, and g is the optomechanical coupling rate corresponding physically to the shift in the optical mode's frequency due to the zero-point fluctuations of the phonon mode. By driving the system with an intense red-detuned optical "control" beam at frequency ω_L , as shown in Fig. 5.1a, the form of the effective interaction changes (in the resolved sideband limit) to that of a beam-splitter-like Hamiltonian $H_{\text{int}} = \hbar G (\hat{a}^\dagger \hat{b} + \hat{a} \hat{b}^\dagger)$. Here, the zero-point-motion coupling rate g is replaced by a much stronger parametric coupling rate $G = g \sqrt{\langle n_c \rangle}$ between light and mechanics, where $\langle n_c \rangle$ is the stored intracavity photon number induced by the control beam. Viewed in a dressed-state picture, with the control beam detuning set to $\Delta \equiv \omega_o - \omega_L \cong \omega_m$, the optical and mechanical modes \hat{a} and \hat{b} become coupled (denoted \hat{a}_d and \hat{b}_d in Fig. 5.1b). The dressed mechanical mode, now effectively a phonon-photon polariton, takes on a weakly photonic nature, coupling it to the optical loss channels at a rate $\gamma_{\text{om}} \equiv C \gamma_i$, where the optomechanical cooperativity is defined as $C \equiv 4G^2 / \kappa \gamma_i$ for an optical cavity decay rate of κ .

The drive-dependent loss rate γ_{om} has been viewed in most previous studies as an incoherent, quantum-limited loss channel, and was used in recent experiments to cool the mechanical resonator close to its quantum ground state [55]. In the dressed mode picture, in analogy to the dressed state view of EIT [106], it becomes clear that a coherent cancellation of the loss channels in the dressed optical and mechanical modes is possible, and can be used to switch the system from absorptive to transmissive in a narrowband around cavity resonance. Much as in atomic EIT, this effect causes an extremely steep dispersion for the transmitted probe photons, with a group delay on resonance of (see section 2.2.1.1)

$$\tau^{(\text{T})}|_{\omega=\omega_m} = \frac{2}{\gamma_i} \frac{(\kappa_e/\kappa)C}{(1+C)(1 - (\kappa_e/\kappa) + C)}, \quad (5.1)$$

where κ_e is the optical coupling rate between the external optical waveguide and the optical cavity, and the delay is dynamically tunable via the control beam intensity through C .

Nano- and micro-optomechanical resonators take a variety of forms, among which OMC have been used to demonstrate large radiation-pressure-induced interaction strengths between gigahertz mechanical and near-infrared optical resonances [101]. The nanobeam OMC cavity used in this study (Figs. 5.1c and 5.1d) utilizes a periodic free-standing Si structure to create high- Q co-localized optical and mechanical resonances. These devices can be printed and etched into the surface of a Si chip in large arrays (Fig. 5.1c), and are designed to operate optically in the telecom band ($\lambda_o = 1550$ nm) and acoustically at microwave frequencies ($\omega_m/2\pi = 3.75$ GHz). The theoretical optomechanical coupling rate g between co-localized photon and phonon modes is $g/2\pi \approx 800$ kHz. By optimizing both the defect and crystal structure, an intrinsic optical decay rate of $\kappa_i/2\pi \approx 290$ MHz is obtained for the optical mode, placing the optomechanical system in the resolved sideband regime ($\omega_m/\kappa_i \gg 1$) necessary for EIT. The corresponding mechanical resonance is measured to have an intrinsic damping rate of $\gamma_i/2\pi \approx 250$ kHz ($T = 8.7$ K). Light is coupled into and out of the device using a specially prepared optical fiber taper, which when placed in the near-field of the nanobeam cavity couples the guided modes of the taper evanescently to the optical resonances of the nanobeam.

In order to characterize the near-resonance optical reflection of the cavity system, a sideband of the control beam is created using electro-optic modulation, forming a weak signal beam with tunable frequency ω_s . The results of measurements performed at a cryogenic temperature of 8.7 K are shown in Fig. 5.2. Here, the control beam laser power was varied from $6 \mu\text{W}$ ($\langle n_c \rangle = 25$) to nearly $250 \mu\text{W}$ ($\langle n_c \rangle = 1040$). The frequencies of both the control and signal beams are swept in order to map out the system dependence upon control-cavity detuning, Δ , and the two-photon detuning, $\Delta_{\text{mod}} = \omega_s - \omega_L$. The resulting reflected optical signal intensity, separated from the control beam via a modulation and lock-in technique, is shown in Fig. 5.2(a) for a series of control laser detunings. Visible in each of the plots is a broad resonance corresponding to the bare optical cavity response with loaded linewidth $\kappa/2\pi \approx 900$ MHz. A much narrower reflection dip feature, corresponding to the transparency window, can also be seen near the cavity line center. The position of the narrow reflection dip tracks with a two-photon detuning equal to the mechanical resonance frequency, $\Delta_{\text{mod}} \approx \omega_m$. This region is shown in more detail in Fig. 5.2b, where the Fano-like structure of the optical response is apparent. Each curve in Figs. 5.2a and 5.2b is a horizontal slice of the data presented in Fig. 5.2c, where the reflectivity is plotted as a function of both ω_L and Δ_{mod} . The transparency window is shown to be fully controllable via the applied light field, the window expanding and contracting with the control beam laser power (Fig. 5.2d). At the maximum stable control power (unstable regions due to a thermo-optic bistability induced by optical absorption are shown as hatched regions in Fig. 5.2c), a transparency window approaching 5 MHz is obtained.

A model fit to the reflection spectra (see section 2.2.1.1) are shown as solid curves in Figs. 5.2a

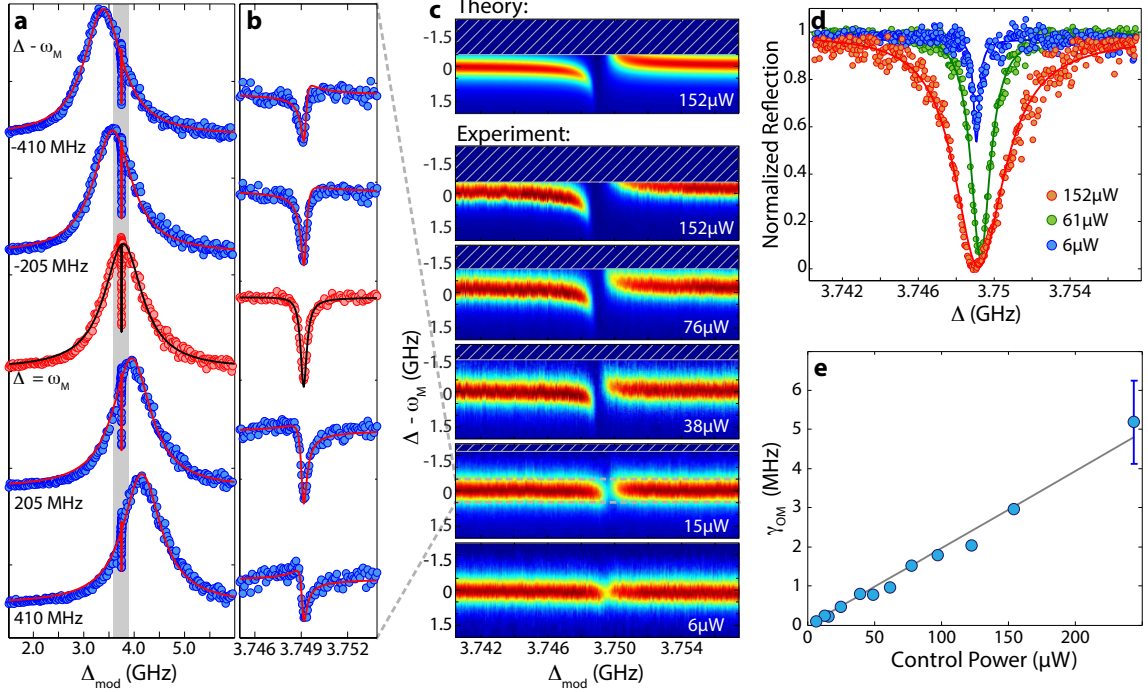


Figure 5.2: **Optical Reflection Response** ($T = 8.7$ K). **a**, Measured normalized reflection (dots) of the signal beam as a function of the two-photon detuning for a control beam power of $15 \mu\text{W}$. **b**, Zoom-in of the reflected signal about the transparency window. Each spectrum in **a** and **b** corresponds to a different control laser detuning ($\Delta - \omega_m$) as indicated. Solid curves correspond to model fits to the data. **c**, Intensity plots for the signal beam reflection as a function of both control laser detuning (Δ) and two-photon detuning (Δ_{mod}) for a series of different control beam powers (as indicated). The hatched areas are unstable regions for the control laser detuning at the given input power. The top plot is the theoretically predicted reflection spectrum for the highest control beam power. **d**, Transparency window versus control beam power for control laser detuning $\Delta \approx \omega_m$. **e**, Transparency window bandwidth ($\gamma_{\text{om}} = 4G^2/\kappa$) versus control beam power. The solid line represents the fit to the model which determines g .

and 5.2b. The resulting fit values for $\gamma_{\text{om}} = 4G^2/\kappa$ for each control power are shown in Fig. 5.2e. A linear fit to the extracted data yields a value for the zero-point-motion coupling constant of $g/2\pi = 800$ kHz, in agreement with the value obtained from independent optical transduction measurements of the thermal Brownian motion of the mechanical oscillator [101]. In addition to the intensity response of the optomechanical cavity there is the phase response, which provides a measure of the group delay of the modulated optical signal beam as it passes through the cavity. For the 89 kHz modulation of the signal beam used in our experiments, corresponding to a free-space signal wavelength of ~ 3.4 km, phase shifts between the modulation sidebands and the signal carrier on the order of a fraction of a radian are measured in the region where Δ_{mod} is within a mechanical linewidth of ω_m . The measured phase-shifts for the reflected signal beam correspond to advances in time of the modulated signal, pointing to causality-preserving superluminal effects. A plot of the peak effective signal advance versus control beam power is plotted in Fig. 5.3a, ascertained from a

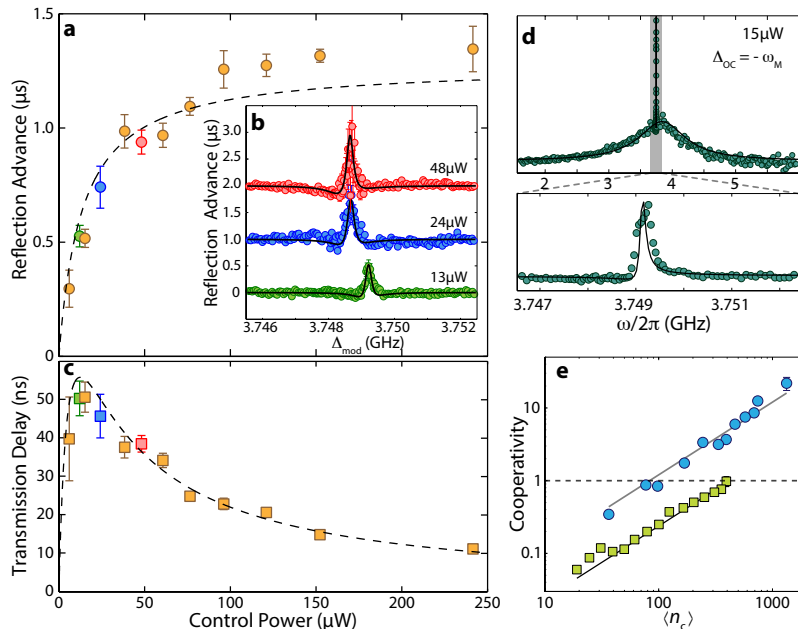


Figure 5.3: **Measured Temporal Shifts and Amplification.** **a**, Maximum measured reflected signal advance as a function of the control beam power. **b**, Measured reflected signal advance versus two photon detuning, Δ_{mod} . Solid curves correspond to fit from model. Curves at different control powers are shifted for clarity. **c**, Inferred maximum transmitted signal delay versus control beam power. Dashed lines in **a** and **c** are theoretical advance/delay times predicted from model of optomechanical system based upon intensity response of the optomechanical system. **d**, Measured reflection signal as a function of two photon detuning for the control laser blue detuned from the cavity. **e**, Measured cooperativity for sample temperature of 296 K (\square) and 8.7 K (\circ) as a function of the average number of control photons inside the cavity.

fit to the reflection phase response spectra (Fig. 5.3b). For the highest control power, the reflected signal is advanced by $1.3 \mu\text{s}$, roughly 7000 times longer than the bare optical cavity lifetime.

The delay in transmission is directly related to the advance upon reflection through the bare cavity transmission contrast. As such, we plot the corresponding transmission group delay of the signal in Fig. 5.3c. The theoretical delay/advance of the modulated signal beam for system parameters given by fits to the EIT intensity spectra are shown as dashed curves in Figs. 5.3a and 5.3c, indicating good agreement with the measured phase response. As can be seen in this data, the maximum measured transmission delay is $\tau^{(\text{T})} \approx 50 \text{ ns}$, which although corresponds to significant slowing of light to a velocity of $v_g \approx 40 \text{ m/s}$ through the few micron long structure, is much smaller than the measured reflected signal advance or the limit set by the intrinsic mechanical damping ($2/\gamma_i \approx 1.4 \mu\text{s}$). This is due to the weak loading of the optical cavity in these experiments, and the resulting small fraction of transmitted light that actually passes through the cavity.

In addition to the observed EIT-like behavior of the optomechanical system, a similar phenomena to that of EIA [120] in atomic systems can be realized by setting the detuning of the control beam

to the blue side of the optomechanical cavity resonance ($\Delta < 0$). Under blue-detuned pumping, the effective Hamiltonian for the optical signal and mechanical phonon mode becomes one of parametric amplification, $H_{\text{int}} = \hbar G(\hat{a}^\dagger \hat{b}^\dagger + \hat{a} \hat{b})$. The measured reflection spectrum from the OMC is shown in Fig. 5.3d, where the reflectivity of the cavity system is seen to be enhanced around the two-photon detuning $\Delta_{\text{mod}} \sim \omega_m$, a result of the increased “absorption” (feeding) of photons into the cavity. At even higher control beam powers such that $C \gtrsim 1$, the system switches from EIA to parametric amplification, resulting in optical signal amplification, and eventually phonon-lasing (see section 2.2.1.3).

Reflection spectroscopy at room temperature (296 K) of the optomechanical cavity has also been performed, and yields similar results to that of the cryogenic measurements, albeit with a larger value of $\langle n_c \rangle$ required to reach a given cooperativity (see Fig. 5.3e) due to the larger intrinsic mechanical dissipation at room temperature ($\gamma_i = 2\pi \times 1.9$ MHz). Beyond the initial demonstrations of EIT and EIA behaviour in the OMC cavities presented here, it is fruitful to consider the bandwidth and signal delay limits that might be attainable with future improvements in device material or geometry. For instance, the transparency bandwidth of the current devices is limited by two-photon absorption of the control beam in the silicon cavities; a move to larger bandgap dielectric materials, such as silicon nitride, should allow intra-cavity photon numbers of 10^6 (limited by linear material absorption), resulting in a transparency window approaching $G = g\sqrt{\langle n_c \rangle} \sim 2\pi(1 \text{ GHz})$. Also, recent research into low-loss GHz mechanic resonators [121] should enable slow light optical delays approaching $10 \mu\text{s}$ at room temperature, roughly a path length of a kilometer of optical fiber. Much like the acoustic wave devices used in electronic systems [122], optomechanical devices with these attributes would enable chip-scale microwave photonic systems capable of advanced signal processing in the optical domain, such as that needed for emerging broadband wireless access networks or more specialized applications such as true-time delays in radar systems [123].

The limiting factor for quantum applications of optomechanical systems is the re-thermalization time of the mechanical resonator, $\tau_{\text{th}} = \hbar Q_m / kT$, which in the case of a quantum optical memory represents the average storage time of a single photon before excitation of the system by a thermal bath phonon. For the devices studied here, despite the small optically-cooled phonon occupancy of the resonator (~ 2.1 phonons from the measured cooperativity), the re-thermalization time is only $\tau_{\text{th}} \approx 12 \text{ ns}$ at the measurement temperature of 8.7 K (50 ps at room temperature). Reducing the operating temperature further to a value below 100 mK (routinely attained in a dilution refrigerator), would not only increase the re-thermalization time through a lower bath temperature, but should also result in a significant increase in the mechanical Q -factor. Taken together, the resulting re-thermalization time in the current OMC devices at $T = 100 \text{ mK}$ is likely to be on the order of $100 \mu\text{s}$, which although not nearly as long as what has been achieved in atomic systems [109], still represents a substantial storage time compared to the realizable GHz bandwidth of the system.

Additionally, optomechanical processes similar to the EIT behavior measured here have also been proposed [77, 124] to provide an optical interface between, for instance, atomic and superconducting circuit quantum systems, enabling the formation of hybrid quantum networks.

5.2 Detection of zero-point motion [3]

Experiments with trapped atomic ions and neutral atoms [125–127], dating back several decades, utilized techniques such as resolved sideband laser cooling and motional sideband absorption and fluorescence spectroscopy to cool and measure a single trapped particle in its vibrational quantum ground state. These experiments generated significant interest in the coherent control of motion and the quantum optics of trapped atoms and ions [128], and were important stepping stones towards the development of ion-trap based quantum computing [129, 130]. Larger scale mechanical objects, such as fabricated nanomechanical resonators, have only recently been cooled close to their quantum mechanical ground state of motion [12, 45, 46, 50, 51, 55, 131, 132]. In a pioneering experiment by O’Connell, et al. [12], a piezoelectric nanomechanical resonator has been cryogenically cooled ($T_b \sim 25$ mK) to its vibrational ground state and strongly coupled to a superconducting circuit qubit allowing for quantum state preparation and read-out of the mechanics. An alternate line of research has been pursued in circuit and cavity optomechanics [103], where the position of a mechanical oscillator is coupled to the frequency of a high- Q electromagnetic resonance allowing for back-action cooling [37, 39] and continuous position read-out of the oscillator. Such optomechanical resonators have long been pursued as quantum-limited sensors of weak classical forces [36, 50, 103, 133, 134], with more recent studies exploring optomechanical systems as quantum optical memories and amplifiers [2, 7, 42, 135], quantum nonlinear dynamical elements [35], and quantum interfaces in hybrid quantum systems [5, 124, 136, 137].

Despite the major advances in circuit and cavity optomechanical systems made in the last few years, all experiments to date involving the cooling of mesoscopic mechanical oscillators have relied on careful measurement and calibration of the motionally scattered light to obtain the average phonon occupancy of the oscillator, $\langle \hat{n} \rangle$. Approach towards the quantum ground state in such experiments is manifest only as a weaker measured signal, with no evident demarcation between the classical and quantum regimes of the oscillator. A crucial aspect of zero-point fluctuations of the quantum ground state is that they cannot supply energy, but can only contribute to processes where energy is absorbed by the mechanics. This is different from classical noise, and techniques that attempt to measure zero-point motion without being sensitive to this aspect (i.e., standard continuous linear position detection) can always be interpreted classically and described by some effective temperature.

A more direct method of thermometry and characterization of the quantized nature of a mechan-

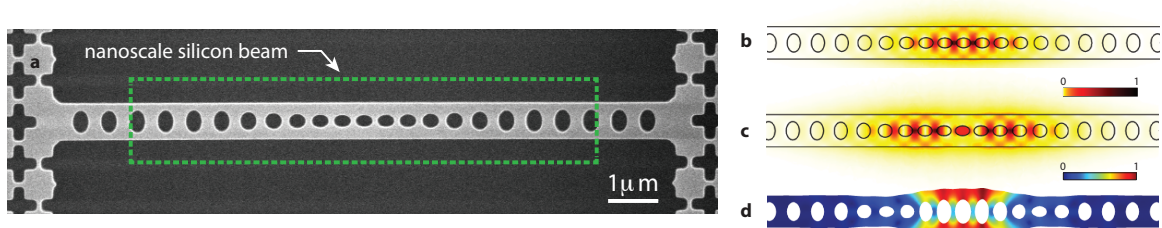


Figure 5.4: **Device used for sideband asymmetry measurement.** (a) A scanning electron micrograph of the silicon nanobeam optomechanical cavity. FEM numerical simulations of the electric field amplitude of the (b) first- and (c) second-order optical modes of the cavity which are used for cooling and probing the mechanical motion, respectively. (d) FEM numerical simulation showing the displacement amplitude of the coupled breathing mechanical mode.

ical oscillator, one particularly suited to small $\langle \hat{n} \rangle$ and utilized in the above-mentioned trapped atom experiments [125–127], is referred to as motional sideband spectroscopy. This method relies on the fundamental asymmetry in the quantum processes of phonon absorption from (proportional to $\langle \hat{n} \rangle$) and emission into (proportional to $\langle \hat{n} \rangle + 1$) the mechanical oscillator. In the case of atomic systems, this asymmetry can be measured in the motionally-generated Stokes and anti-Stokes sidebands in either the fluorescence or absorption spectrum of the atom. The ratio of the Stokes to anti-Stokes sideband amplitudes ($(\langle \hat{n} \rangle + 1)/\langle \hat{n} \rangle$) deviates significantly from unity as the quantum ground state is reached ($\langle \hat{n} \rangle \rightarrow 0$), and provides a self-calibrated reference for the phonon occupancy. In the present experiment we cool a nanomechanical resonator to near its quantum ground state, and measure the asymmetry in the motional sidebands utilizing a form of resolved sideband spectroscopy based upon the filtering properties of a high- Q optical cavity with linewidth narrower than the mechanical frequency.

The cavity optomechanical system studied in this work consists of a patterned silicon nanobeam which forms an OMC [84] capable of localizing both optical and acoustic waves (see Fig. 5.4). The cavity is designed to have two optical resonances, one for cooling and one for read-out of mechanical motion. The cooling mode is chosen as the fundamental mode of the patterned nanobeam cavity, with a frequency $\omega_c/2\pi = 205.3$ THz and a corresponding free-space wavelength of $\lambda_c = 1460$ nm. The read-out mode is the second-order mode of the cavity with $\omega_r/2\pi = 194.1$ THz ($\lambda_r = 1545$ nm). An in-plane mechanical breathing mode at $\omega_m/2\pi = 3.99$ GHz, confined at the center of the nanobeam due to acoustic Bragg reflection, couples via radiation pressure to both optical resonances.

An illustration of the experimental apparatus used to cool and measure the nanomechanical oscillator is shown in Fig. 5.5. In order to pre-cool the oscillator, the silicon sample is mounted inside a Helium flow cryostat. For a cold finger temperature of 6.3 K, the actual thermal bath temperature of the mechanical mode is measured to be 18 K (corresponding to a thermal phonon occupation of $n_b = 94$ phonons) through optical measurements described below. At this temperature

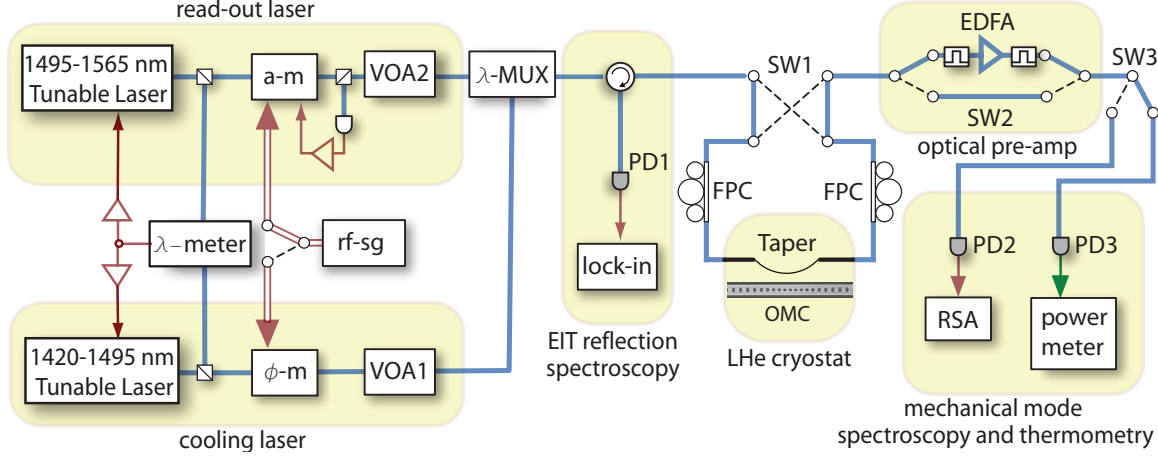


Figure 5.5: **Schematic of the experimental set-up.** Two narrowband lasers (linewidth ~ 300 kHz) are used to independently cool and read out the motion of the breathing mechanical mode of the OMC cavity. The 1500 nm (read-out) and 1400 nm (cooling) laser beams are passed through variable optical attenuators (VOAs) to set the laser power, and combined at a wavelength multiplexer (λ -MUX) before being sent into the cryostat through an optical fiber. Transmission of the 1500 nm read-out beam through the OMC cavity, collected at the output end of the optical fiber, is filtered from the 1400 nm cooling beam light via a bandpass filter, pre-amplified by an Erbium-doped fiber amplifier (EDFA), and detected on a high-speed photodetector (PD2) connected to a real-time spectrum analyzer (RSA). An optical wavemeter (λ -meter) is used to monitor both the cooling and read-out laser frequencies. The optical reflection from the cavity is used to perform EIT-like spectroscopy [2] on both the read-out and cooling cavity modes. Other components are: amplitude-modulation (a-m) and phase-modulation (ϕ -m) electro-optic modulators, fiber polarization controller (FPC), swept frequency radio-frequency signal generator (rf-sg), lock-in amplifier (lock-in), and optical switches (SW).

the breathing mode damping rate to the thermal bath is found to be $\gamma_i/2\pi = 43$ kHz. The optical resonances of the OMC cavity are measured to have total damping rates of $\kappa_c/2\pi = 390$ MHz and $\kappa_r/2\pi = 1.0$ GHz for the cooling and read-out modes, respectively. An optical fiber taper is used to evanescently couple light to and from the OMC cavity. Utilizing piezoelectric stages, the taper is positioned to the side of the nanobeam cavity and placed in contact with the surface of the silicon microchip in the peripheral region surrounding the suspended nanobeam. In this scheme, the fiber taper runs approximately parallel to the nanobeam, and can be rigidly mounted at a prescribed nanoscale gap from the nanobeam. For the taper-to-nanobeam gap used here ($\lesssim 200$ nm), the coupling rate to the fiber taper waveguide is approximately $\kappa_{e,c}/2\pi = 46$ MHz for the cooling mode and $\kappa_{e,r}/2\pi = 300$ MHz for the read-out mode.

The Hamiltonian of the coupled system is $\hat{H} = \hbar(\omega_r + g_r \hat{x}/x_{zpf}) \hat{a}^\dagger \hat{a} + \hbar(\omega_c + g_c \hat{x}/x_{zpf}) \hat{c}^\dagger \hat{c} + \hbar\omega_m \hat{b}^\dagger \hat{b}$, where \hat{c} (\hat{c}^\dagger) and \hat{a} (\hat{a}^\dagger) are the annihilation (creation) operators for photons in the cooling and read-out modes, respectively, and $\hat{x} \equiv x_{zpf}(\hat{b}^\dagger + \hat{b})$ is the displacement operator of the breathing mode with \hat{b}^\dagger (\hat{b}) the phonon creation (annihilation) operator and x_{zpf} the mode's zero-point fluctuation amplitude (see eqn. 1.14). The zero-point optomechanical coupling rates can be determined

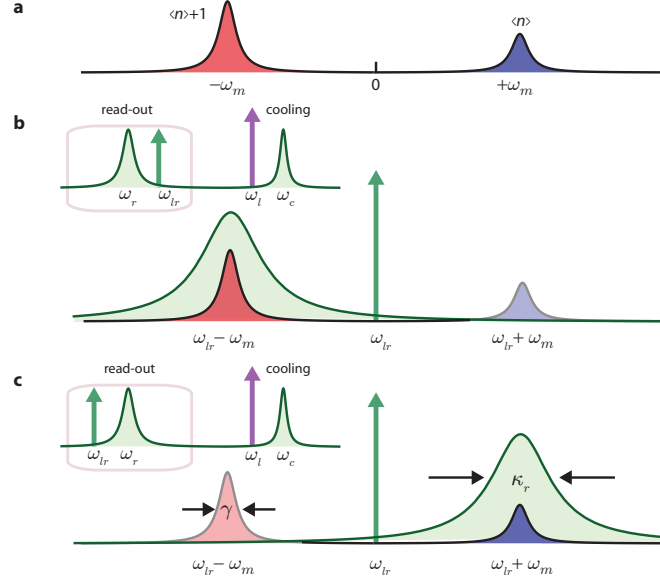


Figure 5.6: **Two-shot detection method.** (a) Displacement noise PSD, S_{xx} , of a quantum simple harmonic oscillator, plotted against $-\omega$ for clarity. (b) Scheme for measurement of the down-converted (Stokes) motional sideband. Here the read-out laser (green vertical arrow; frequency ω_{lr}) is detuned a mechanical frequency above that of the read-out cavity resonance (green solid curve). (c) Corresponding scheme for measurement of the up-converted (anti-Stokes) motional sideband. The linewidth of the readout cavity (κ_r) and the mechanical resonance (γ) are indicated. Insets to (b) and (c) show a zoomed-out spectra indicating the relative frequency of the cooling cavity mode and cooling laser.

from measurements of the optically-induced damping of the mechanical mode [46], and are found to be $g_c/2\pi = 960$ kHz and $g_r/2\pi = 430$ kHz for the cooling and read-out modes, respectively. Numerical simulation of the breathing mode yields a motional mass of only $m = 311$ fg, with corresponding $x_{z\text{pf}} = 2.7$ fm.

As alluded to above, resolved sideband cooling in optomechanical cavities follows physics which is formally similar to the Raman processes used to cool ions to their motional ground state [125]. A cooling laser, with frequency $\omega_l = \omega_c - \omega_m$, is tuned a mechanical frequency red of the cooling cavity resonance of the OMC, giving rise to an intra-cavity photon population n_c at frequency ω_l . Motion of the mechanical oscillator causes scattering of the intra-cavity cooling beam laser light into Stokes and anti-Stokes sidebands at $\omega_c - 2\omega_m$ and ω_c , respectively. Since the anti-Stokes sideband is resonant with the cavity at ω_c , and $\kappa_c < \omega_m$, the anti-Stokes optical up-conversion process is greatly enhanced relative to the Stokes down-conversion process, leading to cooling of the mechanical mode. Assuming a deeply resolved sideband system ($\kappa_c/\omega_m \ll 1$), the back-action cooled mechanical mode occupancy is approximately given by $\langle \hat{n} \rangle_c = \gamma_i n_b / (\gamma_i + \gamma_c)$ [37, 39].

Optical scattering of the intra-cavity light field can also be used to read out the motion of the coupled mechanical oscillator. For a quantum harmonic oscillator, the noise PSD of the oscillator's

position is equal to [36],

$$S_{xx}(\omega)/x_{\text{zpf}}^2 = \frac{\gamma\langle\hat{n}\rangle}{(\omega_m + \omega)^2 + (\gamma/2)^2} + \frac{\gamma(\langle\hat{n}\rangle + 1)}{(\omega_m - \omega)^2 + (\gamma/2)^2}, \quad (5.2)$$

where γ is the total mechanical damping rate. The asymmetric zero-point motion contribution to $S_{xx}(\omega)$ (illustrated in Fig. 5.6a) arises from the non-commutivity of position and momentum operators in quantum mechanics. This absorption-emission asymmetry has no classical analogue; of course, at high phonon occupation numbers where $\langle\hat{n}\rangle \approx \langle\hat{n}\rangle + 1$, the classically symmetric spectral density is recovered. Since the optical cavity frequency is linearly coupled to the position of the mechanical oscillator, the displacement noise spectrum is imprinted on the photons leaving the cavity and can be measured optically.

Specifically, consider a read-out laser with frequency ω_{lr} and detuning $\Delta \equiv \omega_r - \omega_{lr}$ from the read-out cavity mode. The optical power spectrum about ω_{lr} of the transmitted read-out beam leaving the cavity is given by [37],

$$S(\omega) = \frac{\kappa_{e,r}}{2\pi\kappa_r} \frac{A_-^{(r)}\gamma\langle\hat{n}\rangle}{(\omega_m - \omega)^2 + (\gamma/2)^2} + \frac{\kappa_{e,r}}{2\pi\kappa_r} \frac{A_+^{(r)}\gamma(\langle\hat{n}\rangle + 1)}{(\omega_m + \omega)^2 + (\gamma/2)^2}, \quad (5.3)$$

Here $A_+^{(r)}$ and $A_-^{(r)}$ are the detuning-dependent anti-Stokes and Stokes motional scattering rates, respectively, of the read-out laser, given by $A_{\pm}^{(r)} = g_r^2\kappa_r n_r / ((\Delta \pm \omega_m)^2 + (\kappa_r/2)^2)$.

As illustrated in Fig. 5.6b and c, the optical read-out cavity can be used to selectively filter the positive or negative frequency components of $S(\omega)$. For a detuning $\Delta = -\omega_m$ for the read-out laser, $A_+^{(r)} \gg A_-^{(r)}$, resulting in a Lorentzian signal with area I_- proportional to $\langle\hat{n}\rangle + 1$. Conversely, a detuning of $\Delta = \omega_m$ results in $A_-^{(r)} \gg A_+^{(r)}$, producing a signal of area I_+ proportional to $\langle\hat{n}\rangle$. Comparison of the area under the Lorentzian part of the measured photocurrent PSD of the transmitted read-out laser for detunings $\Delta = \pm\omega_m$, can then be used to infer the mechanical mode occupancy,

$$\eta \equiv I_-/I_+ - 1 = \frac{1}{\langle\hat{n}\rangle}. \quad (5.4)$$

This simple argument neglects the back-action of the read-out beam on the mechanical oscillator. In particular, the mechanical damping rate becomes detuning dependent, with $\gamma_{\pm} \equiv (\gamma_i + \gamma_c)(1 \pm C_r)$ for $\Delta = \pm\omega_m$. Here $C_r \equiv |A_+^{(r)} - A_-^{(r)}|/(\gamma_i + \gamma_c)$ is the effective cooperativity of the read-out beam in the presence of the strong cooling beam, and can be found from the measured spectra by the relation, $C_r = (\gamma_+ - \gamma_-)/(\gamma_+ + \gamma_-)$. The back-action of the read-out beam also results in a corresponding change in the phonon occupancy, given by $\langle\hat{n}\rangle_{\pm} = \langle\hat{n}\rangle_c/(1 \pm C_r)$ for $\Delta = \pm\omega_m$. Here $\langle\hat{n}\rangle_c$ is the mechanical mode occupancy due back-action from the cooling beam only. Adding in a correction for the read-out laser back-action, one finds the following relation between the measured motional

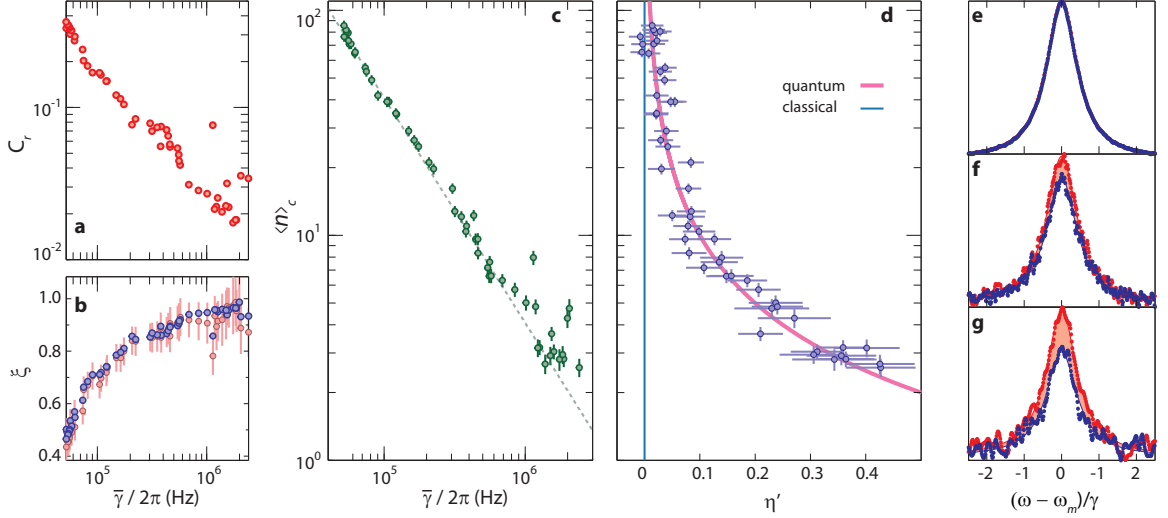


Figure 5.7: **Experimental Result.** (a) Plot of the cooperativity of the read-out beam as a function of damped mechanical linewidth. (b) Plot of the measured ratios γ_-/γ_+ (blue \circ) and $\langle \hat{n} \rangle_+/\langle \hat{n} \rangle_-$ (pink \circ). (c) Plot of the mechanical mode phonon occupancy, $\langle \hat{n} \rangle_c$, as a function of the optically damped mechanical linewidth, $\bar{\gamma}$. The dashed line is the predicted phonon number $\gamma_i n_b / \bar{\gamma}$ from an ideal back-action cooling model. Vertical error bars in (b) and (c) indicate uncertainty in the calibrated phonon occupancy due to uncertainty in the system parameters and a 95% confidence interval on the Lorentzian fits to spectra. (d) Plot of the asymmetry (η') in the measured Stokes and anti-Stokes sidebands of the read-out laser for each calibrated measurement of $\langle \hat{n} \rangle_c$. The horizontal error bars arise from a 2% uncertainty in the transmitted read-out laser beam power between detunings $\Delta = \pm\omega_m$, and a 95% confidence interval in the Lorentzian fits to the measured spectra. The vertical error bars in $\langle \hat{n} \rangle_c$ are the same as in (c). The classical (blue curve) and quantum mechanical (pink curve) relations for the sideband asymmetry are also plotted. (e-g) Plot of the measured Stokes (red curve) and anti-Stokes (blue curve) read-out beam spectra for (from top to bottom) $\langle \hat{n} \rangle_c = 85, 6.3$, and 3.2 phonons. For clarity, we have divided out the read-out back-action from each spectra by multiplying the measured spectra at detunings $\Delta = \pm\omega_m$ by γ_{\pm} . Additionally, we have plotted the horizontal axis in units of γ , and rescaled the vertical axis for different $\langle \hat{n} \rangle_c$ to keep the areas directly comparable. The difference in the Stokes and anti-Stokes spectra, which arises due to the quantum zero-point fluctuation of the mechanical system, is shown as a shaded region.

sidebands and the phonon occupancy of the cooled mechanical oscillator,

$$\eta' \equiv \frac{I_-/I_+}{1+C_r} - \frac{1}{1-C_r} = \frac{1}{\langle \hat{n} \rangle_c}, \quad (5.5)$$

where for $C_r \ll 1$ we recover the standard relation given in Equation (5.4).

Figure 5.7 summarizes the measurement results of the calibrated mechanical mode thermometry and motional sideband asymmetry for the silicon OMC cavity. These measurements are performed with the cooling laser locked a mechanical frequency to the red of the fundamental mode of the OMC cavity, and the cooling laser power swept from $n_c \sim 1$ to 330 (maximum input power of $250 \mu\text{W}$). A much weaker read-out laser ($C_r \ll 1$) is used to both estimate the mechanical mode

phonon occupancy and to compare the motional sideband amplitudes. Locking of the cooling and read-out lasers utilizes a high resolution wavemeter (10 MHz resolution) to set the absolute laser frequency and a weak probe beam to determine the laser-cavity detuning. Here the weak probe beam is generated from the cooling or read-out laser via electro-optic modulation, similar to the EIT-like spectroscopy described in Ref. [2]. The laser-cavity lock for both cooling and read-out lasers is performed every few minutes, multiplexed in time between measurements of the phonon occupancy. With the read-out laser set to a detuning $\Delta = \omega_m$ from the read-out cavity, a Lorentzian spectrum with linewidth γ_+ and integrated area I_+ is measured in the read-out laser photocurrent PSD, from which a mode occupancy of $\langle \hat{n} \rangle_+$ is inferred from a careful calibration of the optomechanical cavity and photodetection system parameters [46]). Similarly, by placing the read-out laser at $\Delta = -\omega_m$ we obtain spectra with linewidth γ_- and integrated area $I_- \propto \langle \hat{n} \rangle_- + 1$, from which we estimate $\langle \hat{n} \rangle_-$.

Figure 5.7a plots the read-out cooperativity C_r , calculated from the measured γ_{\pm} , versus the mechanical damping rate $\bar{\gamma} = (\gamma_+ + \gamma_-)/2$. The ratios $\xi \equiv \gamma_-/\gamma_+$ and $\langle \hat{n} \rangle_+/\langle \hat{n} \rangle_-$ are plotted in Fig. 5.7b. From $\langle \hat{n} \rangle_{\pm}$, the laser cooled phonon occupation number, $\langle \hat{n} \rangle_c$, is calculated and plotted in Fig. 5.7c versus $\bar{\gamma}$. As expected, $\langle \hat{n} \rangle_c$ drops approximately linearly with $\bar{\gamma}$, reaching a minimum value of approximately 2.6 ± 0.2 phonons. Further cooling below a single phonon quanta has been achieved in similar devices [46], however in this case cooling is limited by the available power of the 1400 nm cooling laser. Also evident in Fig. 5.7c, at the higher cooling powers, is an increased scatter and deviation from the ideal cooling curve (dashed curve). This can be attributed to optical absorption in the silicon nanobeam [46], which in this case produces a power-dependent variation in n_b and γ_i due to both the read-out and cooling laser beams.

In Fig. 5.7d, the measured values of the expression η' are plotted versus the calibrated value of $\langle \hat{n} \rangle_c$. Also plotted are the classical and quantum values of this expression, 0 and $1/\langle \hat{n} \rangle_c$, respectively. A clear divergence from the classical result of $\eta' = 0$ is apparent, agreeing with the deviation due to zero-point fluctuations of the mechanical oscillator. This deviation is directly apparent in the measured spectra, shown for $\langle \hat{n} \rangle_c = 85, 6.3,$ and 3.2 phonons in Fig. 5.7e-g, with the shaded region corresponding to the noise power contribution due to zero-point motion. At the largest powers, we measure asymmetry in the motional sideband amplitudes of $\sim 40\%$ in agreement with the inferred $\langle \hat{n} \rangle_c = 2.6$ phonons from calibrated thermometry.

While the quantum nature of a mechanical resonator will come as little surprise to most physicists, its observation through the zero-point motion is a significant step towards observing and controlling the quantum dynamics of mesoscopic mechanical systems. By demonstrating the fundamentally quantum behavior of an engineered mechanical nanostructure, we have shown that realizable optomechanical systems have the sensitivity and environmental isolation required for such quantum mechanical investigations.

5.2.1 Role of phase noise in measurement

Laser phase noise on the probe beam used in the sideband asymmetry measurement can affect both the inferred mode temperature (see section 2.2.4.2) and the magnitude of the detected asymmetry (see section 2.2.4.3). Therefore to make a strong claim about measuring a quantum effect, classical noise masking and mimicking the desired result must be understood.

Here we aim to re-present the data of Ref. [3], in a form suitable for analysis of the effects of laser noise (primarily phase noise) as per the theoretical analysis described above in section 2.2.4.3. We also compare the measured results with the expected noise effects from the calibrated laser phase noise of the read-out laser presented in B.2.

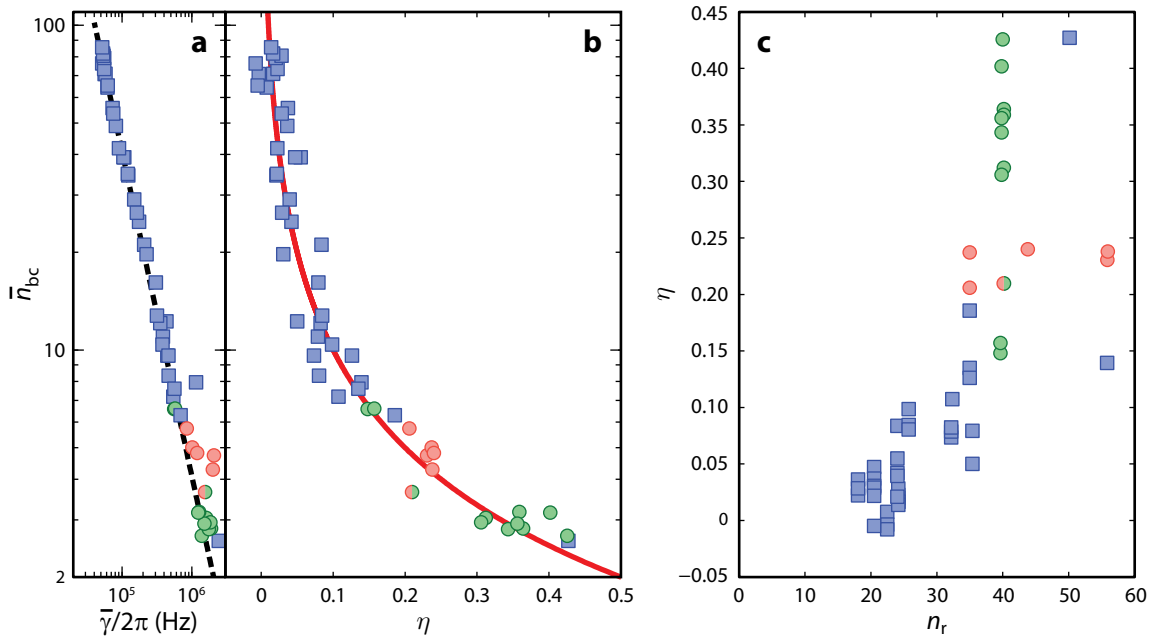


Figure 5.8: **Ruling out phase-noise in sideband asymmetry measurements.** **a** and **b** show laser cooling and motional sideband asymmetry data from the experiment reported in Ref. [3] presented above. In **a** we plot the measured optically enhanced mechanical damping rate ($\bar{\gamma}$) versus the inferred laser cooled mode occupancy of the breathing mechanical resonator (\bar{n}_{bc}). Here \bar{n}_{bc} represents the breathing mode occupancy due to laser cooling in the absence of the probe beam. It is computed as $\bar{n}_{bc} = (\gamma_+ n_{inf}^+ + \gamma_- n_{inf}^-) / 2\bar{\gamma}$, from the inferred mode occupancies (n_{inf}^\pm) and mechanical linewidths (γ_\pm and $\bar{\gamma} \equiv (\gamma_+ + \gamma_-) / 2$) measured with the weak probe beam at detunings $\Delta_r = \pm\omega_m$. As plotted in **b**, the weak probe beam signals for detunings $\Delta = \pm\omega_m$ are also used to calculate η of eqn.(2.34). The red line in **b** represents the expected theoretical asymmetry ($\eta = 1/\bar{n}_{bc}$) due to zero-point motion of the mechanical system in the absence of phase-noise effects. In **c** we also plot the measured asymmetry versus the probe read-out power as represented by the read-out intra-cavity photon number m_r . We have highlighted two subsets of data within the full set of data, represented by green and red circles. For the red circle data points the measured asymmetry is roughly constant at $\eta = 0.23 \pm 0.02$ while the probe beam power is varied over a factor of nearly two. For the green circle data, the probe beam power is held fixed at $n_r = 40$ and the asymmetry is measured to range over a factor of three.

Figure 5.8a shows a plot of the inferred phonon occupancy of the breathing mechanical mode at 3.99 GHz versus the mechanical linewidth of the breathing mechanical mode ($\bar{\gamma}_c$) for each cooling laser beam power. The cooling laser, a Model 6326 Velocity laser in this case, is tuned to a mechanical frequency red of the fundamental optical mode at $\lambda_c = 1460$ nm ($\Delta_c = \omega_m$). The inferred phonon occupancy in the absence of a read-out beam, \bar{n}_{bc} is measured using a read-out laser (the same Model 6328 Velocity laser used in the ground-state cooling experiments of Ref. [46]) that is tuned near resonance of the second-order optical mode of the OMC cavity at $\lambda_r = 1545$ nm. This occupancy (\bar{n}_{bc}) can be thought of as the occupation number of a new effective thermal bath coupled to the mechanics consisting of a combination of the intrinsic mechanical damping and optical damping from the cooling beam. \bar{n}_{bc} is measured by taking the average of the calibrated phonon occupancies measured for read-out beam detunings of $\Delta_r = \pm\omega_m$; $\bar{n}_{bc} \equiv 1/2(\gamma_+\bar{n}_+ + \gamma_-\bar{n}_-)/\bar{\gamma}$, where \bar{n}_+ and \bar{n}_- are the inferred phonon occupancies from the measured read-out beam photocurrent spectrum and γ_+ and γ_- are the measured mechanical linewidths for $\Delta_r = \omega_m$ and $\Delta_r = -\omega_m$, respectively. $\bar{\gamma}$ is the mechanical damping rate of the total system in the absence of the a read-out beam and is calculated from the measured probe beam spectra using $\bar{\gamma} \equiv 1/2(\gamma_+ + \gamma_-)$. At each of the cooling beam powers, the read-out laser beam power is adjusted such that the cooperativity of the read-out beam is substantially below unity (see Ref. [3]). As such, using this two-mode approach, one high power for cooling and one low power for read-out, separates the noise heating and noise squashing effects, and substantially reduces any effects due to laser phase noise on the mode thermometry.

In Fig. 5.8b we plot the measured asymmetry in the motional sidebands, η in eqn. (2.34), of the read-out laser beam versus the inferred laser-cooled mode occupancy of Fig. 5.8a. At the highest cooling powers, the mode occupancy shown in Fig. 5.8a begins to show a larger spread. This is due to extra substrate and mode heating from optical absorption of the probe and cooling beams. For further details of such parasitic heating effects in silicon OMC cavities, the interested reader is referred to the Supplementary Information of Ref. [46]. The red solid curve of Fig. 5.8b also plots the expected sideband asymmetry from the linear fit of the laser-cooled mode occupancy versus mechanical damping (dashed black-curve of Fig. 5.8a). The asymmetry is quite pronounced at lower mode occupancies as expected, and matches well the theoretical sideband asymmetry curve of eqn. (2.34) due to the behavior of the zero-point fluctuations of the mechanical mode and interference with the quantum back-action of the read-out laser shot-noise [3, 41]. As discussed in Section 2.2.4.3, such sideband asymmetry can also arise from classical laser noise on the read-out laser beam (see eqn.(2.52)). Owing to the fact that the read-out laser beam is of substantially lower power than that of the cooling laser beam in these experiments, the amount of classical laser phase noise is expected to be small. Also, the read-out laser beam power was only weakly correlated with the cooling beam power (and thus laser-cooled mode occupancy), making it highly unlikely that the measured motional sideband asymmetry curve of Fig. 5.8b is due to classical laser noise on the read-

out beam. Verification of this is shown in Fig. 5.8c, in which a scatter plot of the measured sideband asymmetry is plotted versus the read-out beam laser power (intra-cavity photon number, n_r). We have highlighted in this set of data two groups of points. The red circles correspond to a range of data points in which the read-out beam power is varied over a factor of nearly two ($n_r \approx 30$ -60), whereas the measured asymmetry varies by less than $\pm 10\%$ of its nominal value ($\eta = 0.23 \pm 0.02$). The green circle points show data in which the read-out beam power was held fixed ($n_r \approx 40$) as the cooling beam power was varied. For these data points the measured asymmetry is seen to vary by a factor of almost three ($\eta \approx 0.15$ -0.45). Both of these groups of data points serve to indicate a lack of correlation between the measured motional sideband asymmetry and the read-out beam power, strongly ruling out laser phase noise as the source of the measured asymmetry in the experiments of Ref. [3].

Finally, one can estimate the magnitude of the effects of laser phase noise of the read-out laser on the measured sideband asymmetry in these measurements by comparing to the calibrated laser phase noise presented in B.2. From Fig. B.3a, the laser frequency noise of the Model 6328 laser used in the read-out of the sideband asymmetry experiment has a value of $\bar{S}_{\omega\omega} \approx 5 \times 10^4 \text{ rad}^2\text{Hz}$ at a frequency of $\omega/2\pi = 3.99 \text{ GHz}$ (the mechanical mode frequency) and for a laser wavelength near $\lambda_r = 1545 \text{ nm}$. From Fig. 5.8c, the read-out beam laser power is at most $|E_0|_r^2 = n_r/(\kappa_e/2\omega_m^2) \lesssim 4 \times 10^{13} \text{ photons/s}$. The maximum read-out laser phase noise quanta in these measurements is then bounded by $n_\phi = (\bar{S}_{\omega\omega}/\omega_m^2)|E_0|_r^2 \lesssim 0.003$ quanta. The corresponding laser noise heating of the mechanical resonator by the weak read-out beam is $(C_r/1 + C_r)(\kappa_e/2\kappa)n_\phi$, which for the read-out beam cooperativity of these experiments ($C_r \lesssim 0.1$) is at most a negligible 4.3×10^{-5} phonons. Laser phase noise squashing and anti-squashing results in the modified motional sideband asymmetry given in eqn. (2.42) for a low-cooperativity read-out beam. The correction factor to the quantum asymmetry due to classical laser phase noise is given by $(1 + 2\kappa_e n_\phi/\kappa)/(1 - \kappa_e n_\phi/\kappa \bar{n}_c) - 1$, which for the measurement of Ref. [3] is smaller than 0.2%. We should also note that from the measured phase noise of the Model 6326 laser used to cool the mechanical mode in these experiments (see Fig. B.3c,f), the estimated laser phase noise heating from the cooling beam is less than $\bar{n}_\phi \approx 0.04$ phonons at the largest cooling beam powers ($n_c = 330$ intra-cavity photons), indicating that the minimum measured phonon occupancy of 2.6 is also not limited by laser noise in this experiment.

5.3 Observation of squeezed light from an optomechanical resonator [4]

Monitoring a mechanical object's motion, even with the gentle touch of light, fundamentally alters its dynamics. The experimental manifestation of this basic principle of quantum mechanics, its link to the quantum nature of light, and the extension of quantum measurement to the macroscopic

realm have all received extensive attention over the last half century [36, 138]. The use of squeezed light, with quantum fluctuations below that of the vacuum field, was proposed nearly three decades ago [139] as a means for beating the standard quantum limits in precision force measurements. Conversely, it has also been proposed that a strong continuous measurement of a mirror's position with light, may itself give rise to squeezed light [47, 140]. Such squeezed light generation has in fact recently been demonstrated in an analogous system consisting of the center-of-mass motion of ultracold gas phase atoms [135]. In this Letter, we present a continuous position measurement of a solid-state optomechanical system fabricated from a silicon microchip and composed of a micromechanical resonator coupled to a nanophotonic cavity. Laser light sent into the cavity is used to measure the fluctuations in the position of the mechanical resonator at a measurement rate comparable to its free dynamics and greater than its thermal decoherence rate. In spite of the mechanical resonator's highly excited thermal state (10^4 phonons), we observe through homodyne detection, squeezing of the reflected light's vacuum fluctuation spectrum at the level of $4.5 \pm 0.2\%$ below that of shot-noise over a few MHz bandwidth around the mechanical resonance frequency of $\omega_m/2\pi \approx 28$ MHz. With further device improvements, on-chip squeezing at significant levels should be possible, making such integrated microscale devices well-suited for precision metrology applications.

The generation of states of light with fluctuations below that of vacuum has been of great theoretical interest since the 1970s [139, 141–143]. Early experimental work demonstrated squeezing of a few percent below shot-noise in a large variety of different nonlinear systems, such as neutral atoms in a cavity [144], optical fibers [145], and crystals with bulk optical nonlinearities [146, 147]. Modern experiments exhibit squeezing of almost 13 dB [148]. The initial research was mainly pursued as a strategy to mitigate the effects of shot-noise given the possibility of improved optical communication [141] and better sensitivity in gravitational wave detectors [139, 142] and led to seminal experiments [149] demonstrating enhancement of sensitivity beyond the standard quantum limit. In recent years, in addition to being installed in gravitational wave detectors [150], squeezed light has enhanced metrology in more applied settings [151, 152].

The vacuum fluctuations arising from the quantum nature of light determine our ability to optically resolve mechanical motion and set limits on the perturbation caused by the act of measurement [153]. A well-suited system to experimentally study quantum measurement is that of cavity-optomechanics, where an optical cavity's resonance frequency can be designed to be sensitive to the position of a mechanical system. By monitoring the phase and intensity of the reflected light from such a cavity, a continuous measurement of mechanical displacement can be made. Systems operating on this simple premise have been realized in a variety of experimental settings, such as in large-scale laser gravitational wave interferometers [154], microwave circuits with electromechanical elements [131], solid-state mechanical elements [155–157] and ultracold gas phase atoms [135, 158] integrated with or comprising Fabry-Pérot cavities, and on-chip nanophotonic cavities sensitive to

mechanical deformations [23, 46].

The canonical cavity-optomechanical system consists of an optical cavity resonance which is dispersively coupled to the position of a mechanical resonance. The Hamiltonian describing the interaction between light and mechanics is $H_{\text{int}} = \hbar g_0 \hat{a}^\dagger \hat{a} \hat{x} / x_{\text{zpf}}$, where $\hat{x} = x_{\text{zpf}} \cdot (\hat{b}^\dagger + \hat{b})$ is the mechanical position, $x_{\text{zpf}} = \sqrt{\hbar / 2m_{\text{eff}}\omega_m}$ is the zero-point fluctuation amplitude (see eqn. 1.14), ω_m is the mechanical resonance frequency, m_{eff} is the effective motional mass of the resonator, and g_0 is the frequency shift of the optical resonance for a mechanical amplitude of x_{zpf} . Here \hat{a} (\hat{a}^\dagger) and \hat{b} (\hat{b}^\dagger) are the annihilation (creation) operators of optical and mechanical excitations, respectively. The optical cavity decay rate, κ , is the loss rate of photons from the cavity and the rate at which optical vacuum fluctuations, or shot-noise, are coupled into the optical resonance [11]. Similarly, the mechanical damping rate γ_i is the rate at which thermal bath fluctuations couple into the mechanical system. In all experimental realizations of solid-state optomechanics to date, including that presented here, the optomechanical coupling rate g_0 has been much smaller than the cavity decay rate κ . As such, without a strong coherent drive, the interaction of the vacuum fluctuations with the mechanics is negligible.

Under the effect of a coherent laser drive, the cavity is populated with a mean intracavity photon number $\langle n_c \rangle$, and one considers the optical fluctuations about the classical steady-state, $\hat{a} \rightarrow \sqrt{\langle n_c \rangle} + \hat{a}$. This modifies the optomechanical interaction resulting in a linear coupling between the fluctuations of the intracavity optical field ($\hat{X}_0 = \hat{a} + \hat{a}^\dagger$) and the position fluctuations of the mechanical system \hat{x} : $H_{\text{int}} = \hbar G \hat{X}_0 \hat{x} / x_{\text{zpf}}$. The parametric linear coupling occurs at an effective interaction rate of $G \equiv \sqrt{\langle n_c \rangle} g_0$. The mechanical motion is coupled to the intra-cavity optical field at a rate of $\Gamma_{\text{meas}} \equiv 4G^2 / \kappa$. Through this interaction, the intensity fluctuations of the vacuum field $\hat{X}_{\theta=0}^{(\text{in})}(t)$ entering the cavity impart a force on the mechanical system,

$$\hat{F}_{\text{BA}}(t) = \frac{\hbar \cdot \sqrt{\Gamma_{\text{meas}}}}{x_{\text{zpf}}} \hat{X}_{\theta=0}^{(\text{in})}(t). \quad (5.6)$$

This RPSN force has previously been measured in an ultracold atomic gas [158], and more recently on a macroscopic silicon nitride nanomembrane [49]. The mechanical motion is in turn recorded in the phase of the light leaving the cavity,

$$\hat{X}_{\theta}^{(\text{out})}(t) = -\hat{X}_{\theta}^{(\text{in})}(t) - 2 \frac{\sqrt{\Gamma_{\text{meas}}}}{x_{\text{zpf}}} \hat{x}(t) \cdot \sin(\theta), \quad (5.7)$$

where $\hat{X}_{\theta}^{(j)} = \hat{a}_j e^{-i\theta} + \hat{a}_j^\dagger e^{i\theta}$, \hat{a}_{in} and \hat{a}_{out} are the operators of the input and reflected optical fields from the cavity, respectively, and θ is the quadrature angle with $\theta = 0$ ($\pi/2$) referring to the intensity (phase) quadrature. In such a measurement, the optical cavity plays the role of the position detector, measuring observable \hat{x} at a rate Γ_{meas} , while the RPSN imposes a measurement back-action force

onto the mechanical system [36]. In addition to the back-action noise, thermal fluctuations from the bath also drive the mechanical motion, with their magnitudes becoming comparable as Γ_{meas} approaches the thermalization rate $\Gamma_{\text{thermal}}(\omega) \equiv \gamma_i \bar{n}(\omega)$, where $\bar{n}(\omega)$ is thermal bath occupancy.

Formally, the output noise PSD of the homodyne detector normalized to the shot-noise level is found by taking the Fourier transform of the auto-correlation of eqn. (5.7):

$$\bar{S}_{II}^{\text{out}}(\omega) = 1 + \frac{4\Gamma_{\text{meas}}}{x_{\text{zpf}}^2} \left[\bar{S}_{xx} \sin^2(\theta) + \frac{\hbar}{2} \text{Re}\{\chi_m\} \sin(2\theta) \right], \quad (5.8)$$

where $\bar{S}_{xx}(\omega)$ is the noise PSD of the mechanical position fluctuations of the resonator, and $\chi_m(\omega) = (m_{\text{eff}}(\omega_m^2 - \omega^2 - i\gamma_i\omega_m))^{-1}$ is the mechanical susceptibility characterizing the response of the mechanical system to an applied force. $\bar{S}_{xx}(\omega)$ contains noise stemming from coupling to the thermal bath, quantum back-action noise from the light field, and any other technical laser noise driving the mechanics. The components of $\bar{S}_{II}^{\text{out}}(\omega)$ in eqn. (5.8), from left to right, are due to shot-noise, mechanical position fluctuations, and the cross-correlation between the back-action noise force and mechanical position fluctuations. It is only the latter which can have a negative noise PSD and gives rise to squeezing.

The primary hurdle to observing such squeezing, as in many quantum measurements, is the strong coupling of a preferred detection channel simultaneous with the minimization of unwanted environmental perturbations of the mechanical system. Most relevant to the work presented here are frequencies detuned from resonance, $\omega_m > |\delta| \gg \gamma_i$, for which the approximate output noise PSD is $\bar{S}_{II}^{\text{out}}(\omega > 0) \approx 1 + (2\Gamma_{\text{meas}}/\delta)[(\omega_m/\delta)(\bar{n}(\omega)/Q_m)(1 - \cos(2\theta)) + \sin(2\theta)]$, where we have assumed that the mechanical position fluctuations are predominantly due to thermal bath coupling (at high optical power, back-action heating and laser noise also contribute to the mode occupancy). In this case, fluctuations from the thermal bath limit appreciable squeezing of the optical probe field to a regime in which $\bar{n}(\omega)/Q_m \lesssim 1$. This requirement is equivalent to having a Q -frequency product, $Q_m\omega_m \gtrsim k_B T_b/\hbar$, where k_B is the Boltzmann constant and T_b the bath temperature. The squeezing in this regime only becomes appreciable when the measurement rate of the mechanics by the light field is larger than the detuning $|\delta| = (\bar{n}(\omega)/Q_m)\omega_m$. This indicates that, in the presence of thermal bath noise, squeezing over a significant spectral bandwidth requires not only a large cooperativity between light and mechanics, as realized in recent cooling experiments [46, 131, 132], but the more stringent requirement that the effective measurement back-action force be comparable to all forces acting on the mechanics, including the elastic restoring force of the mechanical structure.

In order to meet the requirements of strong measurement and efficient detection, we designed a zipper-style optomechanical cavity [23] with a novel integrated waveguide coupler fabricated from the 220 nm thick silicon device layer of a silicon-on-insulator microchip (see Fig. 5.9a). The in-plane differential motion of the two beams at a fundamental frequency of $\omega_m/2\pi = 28$ MHz strongly

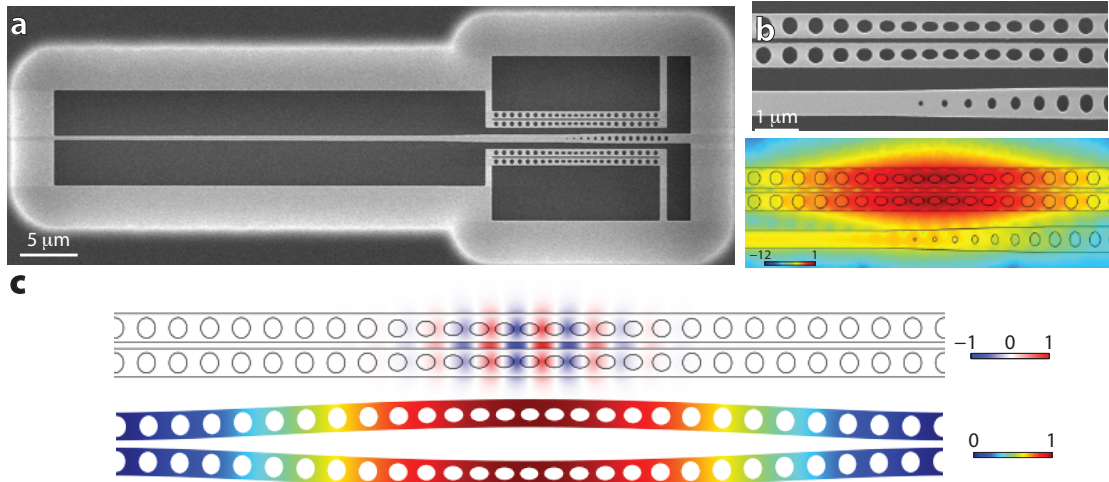


Figure 5.9: **Optomechanical device.** **a**, Scanning electron microscope image of a waveguide-coupled zipper optomechanical cavity. The waveguide width is adiabatically tapered along its length and terminated with a photonic crystal mirror next to the cavity. The tapering of the waveguide allows for efficient input/output coupling while the photonic crystal termination makes the coupling to the cavity single-sided. Two zipper cavities are coupled above and below the waveguide, each with a slightly different optical resonance frequency allowing them to be separately addressed. **b**, (left) Close-up of the coupling region between one of the cavities and the waveguide. (right) FEM simulation of the cavity field leaking into the waveguide (log scale). Note that the field does not leak into the mirror region of the waveguide. **c**, (top) FEM simulation showing the in-plane electrical field of the fundamental optical cavity mode. (bottom) FEM simulation of the displacement of the fundamental in-plane differential mode of the structure with frequency $\omega_m/2\pi = 28$ MHz. The mechanical motion, modifying the gap between the beams, shifts the optical cavity frequency leading to optomechanical coupling.

modulates the co-localized fundamental optical resonance of the cavity with a theoretical vacuum coupling rate of $g_0/2\pi = 1$ MHz. As shown in Fig. 5.9b, we use a silicon waveguide with a high reflectivity photonic crystal end-mirror to efficiently excite and collect light from the optical cavity. Coupling light from the silicon waveguide to a single-mode optical fiber is performed using an optical fiber taper and a combination of adiabatic mode coupling and transformation.

The experimental setup used to characterize the zipper cavity system and measure the optomechanical squeezing of light is shown in Fig. 5.10a. The silicon sample is placed in a continuous flow ^4He cryostat with a cold finger temperature of 10 K. A signal laser beam is used to probe the optomechanical system and measure the mechanical motion of the zipper cavity. A wavelength scan of the reflected signal from the cavity is plotted in Fig. 5.10b, showing an optical resonance with a linewidth $\kappa/2\pi = 3.42$ GHz at a wavelength of $\lambda_c = 1540$ nm. Inefficiencies in the collection and detection of light result in additional uncorrelated shot-noise in the signal and can reduce the squeezing to undetectable levels. For the device studied here, the cavity coupling efficiency, corre-

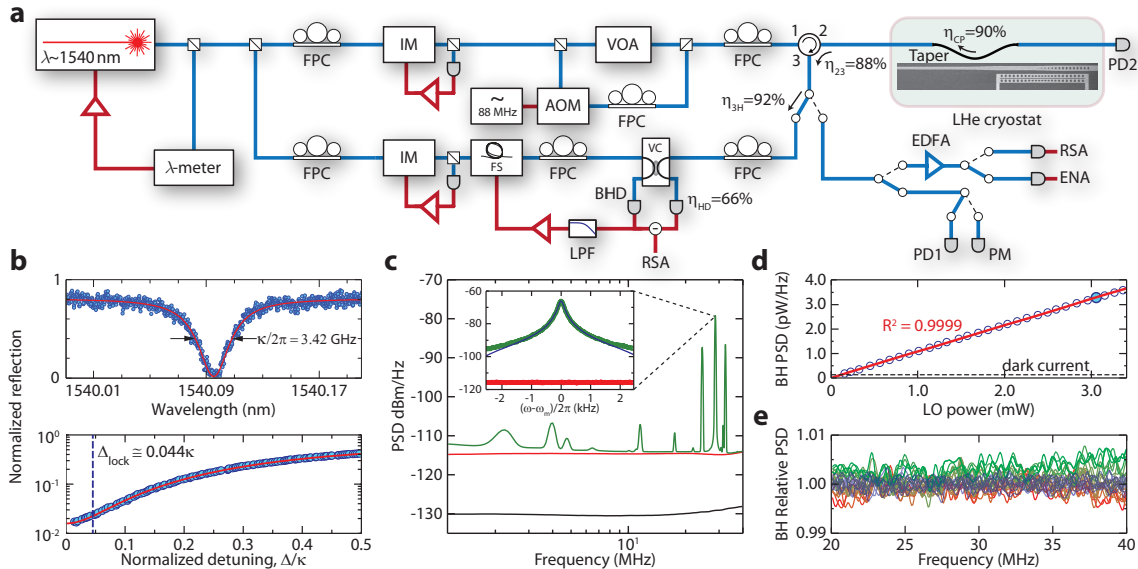


Figure 5.10: Experimental setup and device characterization. **a** The optical signal is derived from an external-cavity diode laser and is sent into a tapered optical fiber inside a liquid Helium cryostat where the silicon sample is cooled to $T \approx 16$ K. The fiber taper is used to evanescently couple light into the silicon optomechanical device. The optical reflection from the device is collected by the same fiber taper and sent to a balanced homodyne detector (BHD) for characterization. For further details of the experimental setup see the Methods Summary. **b** (top) Reflected signal from the optical cavity at low optical power ($\langle n_c \rangle \approx 10$, linewidth $\kappa/2\pi = 3.42$ GHz). (bottom) High-power ($\langle n_c \rangle = 790$) reflected signal, showing the cavity-laser detuning (dashed line) locked to during squeezing measurements. **c** Homodyne noise PSD of the reflected signal showing the transduced thermal Brownian motion of the zipper cavity at $T_b = 16$ K (green curve; $\langle n_c \rangle = 80$). The red curve is the shot noise level and the black curve is the detector's dark noise. The inset shows a zoom-in of the fundamental in-plane differential mechanical mode of the zipper cavity (linewidth $\gamma_i/2\pi = 172$ Hz). **d** Mean value of the PSD of the balanced homodyne detector (averaged over frequencies from 20 to 35 MHz) as a function of the LO power (signal blocked). The filled data point indicates the LO power used in the squeezing measurements. The red and dashed black curves correspond to a linear fit to the data and the detector dark current level, respectively. **e** Noise PSD as a function of θ_{lock} with the signal detuned far off-resonance at $\Delta/\kappa \approx 30$ (shades green to red), referenced to the noise level with the signal blocked (blue).

sponding to the percentage of photons sent into the cavity which are reflected, is determined to be $\eta_\kappa = 0.54$. The fiber-to-chip coupling efficiency is measured at $\eta_{\text{CP}} = 0.90$. A homodyne detection scheme allows for high efficiency detection of arbitrary quadratures of the optical signal field. Characterization and optimization of the efficiency of the entire optical signal path and homodyne detection system results in an overall setup efficiency of $\eta_{\text{setup}} = 0.48$, corresponding to a total signal detection efficiency of $\eta_{\text{tot}} = \eta_{\text{setup}}\eta_\kappa = 0.26$.

Figure 5.10c shows the noise spectrum of the thermal motion of the mechanical resonator obtained by positioning the laser frequency near the cavity resonance and tuning the relative local oscillator (LO) phase of the homodyne detector, θ_{lock} , to measure the quadrature of the reflected signal in

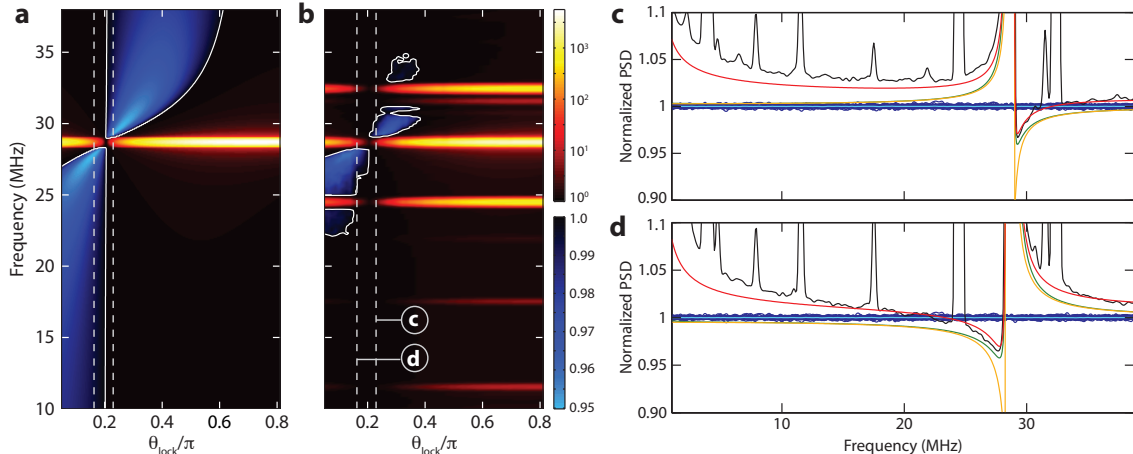


Figure 5.11: **Optomechanical squeezing of light.** **a**, Theoretical model. Density plot of the predicted reflected signal noise PSD, as measured on a balanced homodyne detector and normalized to shot-noise, for a simplified model of the optomechanical system (see section 2.3). Areas below shot-noise are shown in blue shades on a linear scale. Areas with noise above shot-noise are shown in orange shades on a log-scale. The solid white line is a contour delineating noise above and below shot-noise. **b**, Experimental data. Density plot of the measured reflected signal noise PSD for $\langle n_c \rangle = 790$ normalized to the measured shot-noise level. **c**, Slice of the measured density plot in **b** taken at $\theta_{\text{lock}}/\pi = 0.23$. **d**, Slice of the measured density plot in **b** taken at $\theta_{\text{lock}}/\pi = 0.16$. In **c** and **d**, the black curve corresponds to the measured data slice extracted from **b**. The dark blue traces are several measurements of the shot-noise level (average shown in light blue). Also indicated is a model of the squeezing in the absence of thermal noise (orange curve), the same model with thermal noise included (green), and a full noise model including additional phenomenological noise sources (red curve). The vertical white dashed lines of **a** and **b** indicate the data slices shown in **c** and **d**.

which mechanical motion is imprinted. The mechanical spectrum shows the in-plane differential mode of interest at $\omega_m/2\pi = 28$ MHz, as well as several other more weakly coupled mechanical resonances of the nanobeams and coupling waveguide. A high-resolution, narrowband spectrum of the in-plane differential mode is displayed as an inset to Fig. 5.10c, and shows a linewidth of $\gamma_i/2\pi = 172$ Hz, corresponding to a mechanical Q -factor of $Q_m = 1.66 \times 10^5$. The vacuum coupling rate of the in-plane differential mode, measured from the detuning dependence of the optical spring shift and damping, is determined to be $g_0/2\pi = 750$ kHz, in good correspondence with theory. From the calibration of the noise power under the Lorentzian in Fig. 5.10c, the in-plane differential mode is found to thermalize at low optical probe power to a temperature of $T_b \approx 16$ K, corresponding to a thermal phonon occupancy of $\bar{n}(\omega_m) \approx 1.2 \times 10^4$. This yields a ratio $\bar{n}(\omega_m)/Q_m \approx 0.072$, well within the regime where squeezing is possible.

To accurately study the noise properties of the reflected optical signal from the cavity we make a series of measurements to characterize our laser and detection setup. Figure 5.10d shows the measured noise PSD of the balanced homodyne detector for $\omega \approx \omega_m$ as a function of LO power, indicating a linear dependence on power and negligible ($\ll 0.1\%$) added noise above shot-noise. In the

measured squeezing data to follow, a LO power of 3 mW is used. Calibration of the laser intensity and frequency noise over the frequency range of interest ($\omega/2\pi = 1\text{--}40$ MHz) is presented in section B.1.2. The laser intensity noise is measured to be shot-noise dominated over this frequency range, while the laser frequency noise is measured to be roughly flat at a level of $S_{\omega\omega} \sim 5 \times 10^3 \text{ rad}^2 \cdot \text{Hz}$ which contributes insignificantly to the detected noise floor.

Measurement of the noise in the reflected optical signal from the cavity as a function of quadrature angle, frequency, and signal power is presented in Figs. 5.11 and 5.12. These measurements are performed for laser light on resonance with the optical cavity and for input signal powers varying from 252 nW to 3.99 μW , with the maximum signal power corresponding to an average intra-cavity photon number of $\langle n_c \rangle = 3,153$. Positioning of the laser at the appropriate cavity detuning for each signal power is performed by scanning the wavelength across the cavity resonance while monitoring the reflection, and then stepping the laser frequency toward the cavity from the red side until the reflection matches the level that corresponds to a detuning of $\Delta_{\text{lock}}/\kappa \approx 0.04$ (see Methods Summary).

In Fig. 5.11 we plot the theoretically predicted and measured noise PSD versus quadrature angle for a signal power corresponding to $\langle n_c \rangle = 790$ photons. Each quadrature spectrum is the average of 150 traces, and after every other spectrum the signal arm is blocked and the shot-noise PSD measured. The shot-noise level, which represents the noise of the electromagnetic vacuum on the signal arm, is used to normalize the spectra. We find at certain quadrature angles, and for frequencies a few MHz around the mechanical resonance frequency, that the light reflected from the zipper cavity shows a noise PSD below that of vacuum. The density plot of the theoretically predicted noise PSD (Fig. 5.11a) shows the expected wideband squeezing due to the strong optomechanical coupling in these devices, as well as a change in the phase angle where squeezing is observed at below and above the mechanical frequency. This change is due to the change in sign of the mechanical susceptibility and the corresponding change in phase of the mechanical response to RPSN. The measured noise PSD density plot (Fig. 5.11b) shows the presence of several other mechanical noise peaks and a reduced squeezing bandwidth, yet the overall phase- and frequency-dependent characteristics of the squeezing around the strongly-coupled in-plane mechanical mode are clearly present. In particular, Figs. 5.11c and d show two slices of the noise PSD density plot which show the region of squeezing change from being below to above the mechanical resonance frequency.

In Fig. 5.12a we show the measured noise PSD as a function of quadrature angle for a frequency slice at $\omega/2\pi = 27.9$ MHz of the data shown in Fig. 5.11b. The measured squeezing (anti-squeezing) is seen to be smaller (larger) than expected from a model of the optomechanical cavity without thermal noise. We also plot in Fig. 5.12b the maximum measured and modeled squeezing as a function of signal power. The simple theory predicts a squeezing level which monotonically increases with signal power, whereas the measured maximum squeezing saturates at a level of $4.5 \pm 0.2\%$ below the shot-

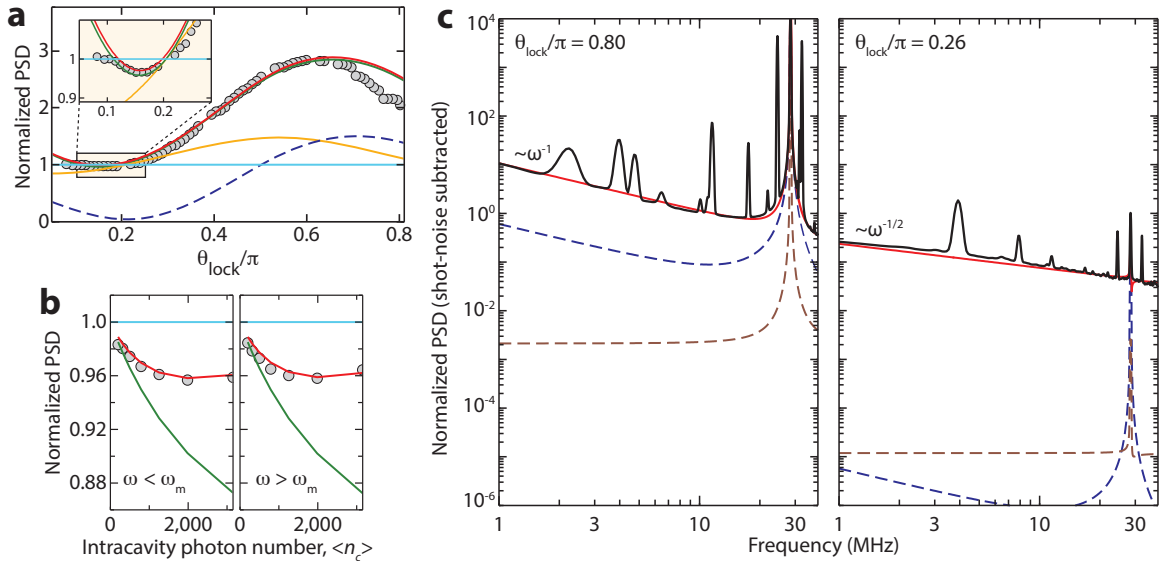


Figure 5.12: **Spectral and power dependence of noise.** **a**, Measured (filled circles) balanced homodyne noise power of the reflected signal at $\omega/2\pi = 27.9$ MHz versus quadrature angle ($\Delta_{\text{lock}}/\kappa = 0.044$ and $\langle n_c \rangle = 790$). The green and red curves corresponds to the single-mode and full noise models, respectively. The orange curve is for a model including the response of the mechanical mode in the absence of thermal noise, i.e., driven by RPSN only, and the dashed blue curve shows the thermal noise component. **b**, Measured (filled circles) minimum noise PSD normalized to shot-noise versus $\langle n_c \rangle$. The left plot is the maximum squeezing for $\omega < \omega_m$ and the right for $\omega > \omega_m$. Also shown is the single-mode noise model (green curve) and the full noise model (red curve). **c**, Balanced homodyne noise PSD of the reflected cavity signal for $\Delta_{\text{lock}}/\kappa = 0.052$ and $\langle n_c \rangle = 3, 153$. Left (right) plot shows phase quadrature corresponding to maximum (minimum) transduction of mechanical motion. The black curve is the measured data with the shot-noise level subtracted. Also shown are the modeled laser phase noise (dashed brown curve), the noise contribution from a single mechanical mode (dashed blue curve), and the full noise model (red curve).

noise at an intracavity power $\langle n_c \rangle = 1,984$ photons. The error in the squeezing is dominated by the uncertainty in the linearity of the detector gain ($\pm 0.15\%$) and the variance of the measured shot-noise level ($\pm 0.1\%$). To understand the processes that limit the bandwidth and magnitude of the measured squeezing, we plot in Fig. 5.12c the noise PSD for phase quadratures that maximize (left plot) and minimize (right plot) the transduction of the mechanical mode peak. Along with the measured data, we also plot the estimated noise due to phase noise of the signal laser, and that for a model of a single mechanical mode coupled to a thermal bath at $T_b = 16$ K. Low frequency noise in the motion quadrature shows an ω^{-1} frequency dependence consistent with structural damping effects [91], but much larger than that of the single-mode noise model. Noise in the quadrature minimizing transduced motion is orders of magnitude larger than the noise predicted by the single-mode model and laser phase noise, and shows an $\omega^{-1/2}$ frequency dependence. The optical power dependence of the low frequency noise in the motion quadrature indicates that optical absorption heats the structure to $T_b \approx 30$ K at the highest measured powers. The red curves in each of the plots

in Fig. 5.12 show a full noise model incorporating structural damping noise from higher frequency mechanical modes, optical absorption heating, and a phenomenological $\omega^{-1/2}$ noise term.

In summary, these measurements show that by reflecting light off a thin-film mechanical resonator undergoing large amplitude thermal motion, light that is in certain respects quieter than vacuum can be obtained. This results from radiation-pressure fluctuations being strongly imprinted on and modified by the motion of the mechanical resonator. The devices in this work utilize lithographic patterning at the nanoscale to transform silicon into a material with an effective quantum optical nonlinearity at a tailorable optical wavelength. The modest level of squeezing realized in this work is limited by both thermal noise and the efficiency with which the reflected light is collected by external optics. The effects of thermal noise and structural damping effects may be substantially reduced by improving the mechanical Q . Measurements of similar silicon devices with different surface treatments have yielded mechanical Q -factors as high as 7×10^5 (see section 3.4), which for the optical power levels used here, should enable on-chip squeezing of 6 dB below shot-noise. Given the microchip form of the devices, and the potential for device integration, squeezed light generated by one device could be directly sent into another device for use as an optical probe. Such an on-chip squeezer and detector could be used as a quantum-enhanced micro-mechanical displacement and force sensor [152]. More generally, we expect future experiments with feedback and strong measurement of the dynamics of a mechanical system to be within reach.

5.3.1 Measurement of optical losses

In order to estimate the total squeezing expected in our setup we carefully characterize all losses in our system. Some of these losses are static (e.g. circulator losses) while others can vary from experiment to experiment (e.g. coupling efficiency of the fiber taper to the waveguide). In figure 5.10 typical losses are shown as efficiencies (η) for various parts of the experiment. The efficiency of sending light from port 1 to 2 of our optical circulator is $\eta_{12} = 85\%$, and $\eta_{23} = 88\%$ for port 2 to 3. In addition, the efficiency from port 3 of the circulator to the homodyne detector is $\eta_{3H} = 92\%$. All these losses are fixed and do not change over time as the components are optically spliced together. Measuring the coupling efficiency of the fiber taper to the waveguide is done every time a new data set is taken. This is accomplished by switching the light that is reflected from the waveguide to a power meter and comparing the reflected power to a known input power with the laser tuned off-resonance from the optical mode (off-resonance the device acts as a near-perfect mirror). Typical achieved efficiencies are around $\eta_{CP} = 90\%$. The efficiency of the homodyne detection strongly depends on the alignment of the polarization between the local oscillator and the signal, as well as by how much the power in the LO overcomes the electronic noise floor of the detector. To determine this efficiency we use an acousto-optic modulator (AOM) inserted in our setup before the circulator in the signal path. The AOM shifts the frequency of the light creating a tone 88 MHz away from the signal with

a fixed, known amplitude, and identical polarization to the signal (we directly measure the power of this tone with a power meter). This tone can now be used to determine the total homodyne efficiency by measuring its power on the spectrum analyzer, taking the other losses into account. Our typical homodyne efficiency is $\eta_{\text{HD}} = 66\%$ resulting in a total setup efficiency (detection efficiency of optical signal photons in the on-chip waveguide) of roughly $\eta_{\text{Setup}} = \eta_{\text{CP}} \cdot \eta_{23} \cdot \eta_{3\text{H}} \cdot \eta_{\text{HD}} \approx 48\%$.

5.3.2 Data collection procedure

Careful calibration of our data is crucial in understanding all noise sources and potential drifts over time in our setup. The losses in our setup are determined before we make a new data run as described in the previous section. We then proceed to record an optical trace of the cavity resonance by switching the light to a photodetector (PD1 in figure 5.10) and scanning the laser wavelength. This trace provides the information to lock the laser to a fixed detuning (typically $0.04 \cdot \kappa$ red of the cavity resonance), which is accomplished using a simple software lock and feedback from the wavemeter (with a resolution of roughly $0.003 \cdot \kappa$) and is described in more detail in the subsection below. As a next step the optical signal is switched to the homodyne detector and the relative phase between the signal and the local oscillator is scanned using the fiber stretcher in the LO arm. The resulting interference is shown in figure 5.13d as the blue trace. The interference signal is used to lock the relative phase between the signal and LO using a Toptica DigiLock 110. The green traces show the properly locked signal, while the red traces are phase set points where the lock failed requiring the associated data to be discarded. We then record the spectra of the homodyne signal and for every trace taken we also save a spectrum of the shot-noise by switching the signal arm away from the homodyne detector and only measure vacuum input to the signal arm of our detector. We re-lock the laser with respect to the cavity every other data point to counteract drift. This procedure is repeated for several different phases and different input powers. We typically took data for 60 different phases for every input power within a range of a little less than $-\pi/2$ to $\pi/2$.

5.3.3 Relation between detuning and quadrature

The laser frequency is positioned at a detuning of roughly $0.04 \cdot \kappa$ by starting at a larger detuning on the red side of the cavity, and stepping the laser blue in 0.1 pm steps (12 MHz) towards the cavity while monitoring the average intensity of the reflected light on PD1. Once the target intensity is reached, the laser is kept at this wavelength during the course of the measurement by the wavemeter lock without further feedback from PD1. The intensity reading gives us an idea of the value of the detuning which is determined more accurately by analysis of our homodyne spectra.

The homodyne spectra are taken at different phase lock points (see Fig. 5.13d) corresponding to quadrature angles θ_{lock} between the reflected signal and the LO. These angles differ from our

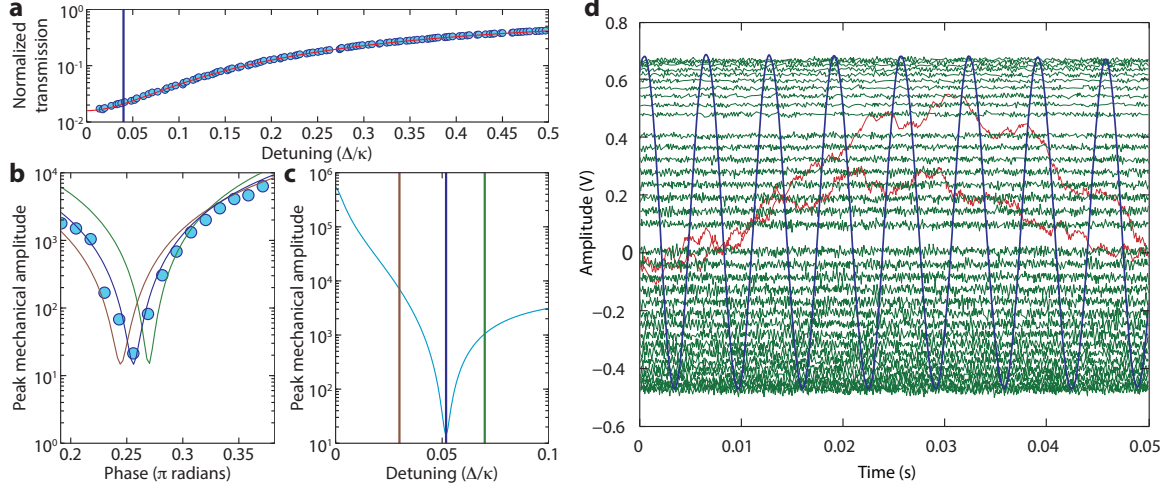


Figure 5.13: **Detuning and phase lock points.** **a**, An optical scan taken before the data run starts is shown. The blue vertical line denotes the target detuning the software lock moves the laser to, determined from the measured reflection intensity. The laser is kept at that detuning via a wavemeter lock, as the light is switched away from PD1 and to the homodyne detector. The measured area under the mechanical mode is plotted in **b** (blue circles) at this detuning. A minimum value is reached for a local-oscillator to reflected signal phase of θ_{lock}^* . Depending on the detuning, different mechanical mode amplitudes can be measured at this phase angle θ_{lock} , according to the model. We obtain an accurate estimate of the detuning by calculating the detuning at which the mechanical mode amplitude is minimized at the measured θ_{lock} as shown in **c**. The expected mode amplitudes for the detunings represented by the red and green lines in **c** are shown by the similarly colored curves in **b**. **d** The blue trace shows the interference signal of the local oscillator and the signal on the homodyne detector when their relative phase is scanned using a fiber stretcher in the local oscillator (LO) arm. The voltage reading here is proportional to $\cos(\theta - \phi)$ where θ is the phase difference between the LO and input to the cavity, and ϕ is the phase imparted by reflection off the cavity. This interference signal is used to actively stabilize the relative phase to different set points (green traces). Occasionally the lock fails, as shown by the red traces, and any associated data is discarded. The range in which the phase can be stably locked is slightly smaller than $-\pi/2$ to $\pi/2$ due to the turning points in the sinusoidal interference curve.

convention in Section 2.3 where the phase θ between the *input* light into the cavity and the local oscillator is considered. They are related to oneanother by the phase imparted on the input light upon reflection from the cavity,

$$\phi(\Delta) = \text{Arg} \left[1 - \frac{\kappa_e}{i\Delta + \kappa/2} \right], \quad (5.9)$$

and the relation

$$\theta_{\text{lock}} = \theta - \phi. \quad (5.10)$$

For a given laser-cavity detuning Δ , we sweep through the different phase lock points (see Fig. 5.13) θ_{lock} , and take mechanical spectra for each phase. The phase that minimizes the mechanical signal

θ_{lock}^* is determined from the recorded spectra. This allows us to solve for Δ using the expression $\theta_{\text{lock}}^* = \theta^*(\Delta) - \phi(\Delta)$ where $\theta^*(\Delta)$ is the phase minimizing the mechanical transduction according to the model in the previous section. To first order (for $\Delta \ll \kappa$) θ^* is 0 since no mechanical signal is observed in the intensity quadrature of the reflected light. This post-processing of the data allows us to determine that across the measured powers the detuning was $\Delta = 0.044 \cdot \kappa \pm 0.006 \cdot \kappa$. For a single measured power, we expect a more accurate determination, with an uncertainty on the order of $0.003 \cdot \kappa$. This level of accuracy in the detuning also determines the uncertainty in quadrature angle of 0.04 rad.

5.3.4 Locking the cavity

A slightly red detuned from resonance lock point is chosen to avoid instabilities of the system due to thermo-optical effects. The laser is locked to this frequency using a wavemeter with a frequency resolution of $\pm 0.0015\kappa$. Drift of the optical cavity resonance over a single noise spectrum measurement (minutes) is found to be negligible. An estimate of the variance of Δ_{lock} is determined from the dependence of the transduction of the mechanical motion on the quadrature phase, indicating that from one lock to another $\Delta_{\text{lock}}/\kappa = 0.044 \pm 0.006$.

Chapter 6

Optomechanical System Proposals

6.1 The basic ideas

6.1.1 Red-side driving and state transfer

By driving a sideband-resolved optomechanical resonator with a red-detuned laser, an effective linear phonon-photon coupling can be induced. This converts the nonlinear interaction Hamiltonian $g_0 \hat{a}^\dagger \hat{a} (\hat{b}^\dagger + \hat{b})$ to:

$$\hat{H}_{\text{eff}} = \Delta \hat{b}^\dagger \hat{b} + G \hat{a}^\dagger \hat{b} + G^* \hat{a} \hat{b}^\dagger \quad (6.1)$$

where G is the dressed optomechanical coupling rate. This so-called “beam-splitter” interaction coherently converts phonons to photons and vice versa. At the simplest level, ignoring all losses, this interaction will cause a Rabi flopping between phonons and photons, with the state of the mechanical resonator being converted to light and back. It is then feasible to use precisely-timed pulses to move the state of the phonon to the photon. This form of state-transfer is not accessible to systems in the weak-coupling regime, where the optical losses κ are much larger than Rabi frequency G . All of the systems studied and presented in this thesis operate in this regime. Fortunately, it is still possible to perform efficient and useful state transfer in the weak-coupling regime, but a slightly different viewpoint must be taken.

6.1.2 Optical damping rate in the weak-coupling regime

In the weak coupling regime, an excitation leaving the mechanical system never returns. The optical cavity will always have a negligible photon population (ignoring the large pump beam), and the mechanical system sees only an enhanced effective loss rate, reminiscent of a Purcell enhancement for atoms. The source of this enhanced loss can be seen as follows. We start from the coupled, linearized equations of motion with \dot{a} set to 0. This constitutes an adiabatic elimination of the

optical cavity, which is valid as long as $\kappa \gg G$. The equations are as follows:

$$\begin{aligned} 0 &= -\frac{\kappa}{2}a - iGb, \\ \dot{b} &= -\frac{\gamma_i}{2}b - iGa, \end{aligned}$$

implying upon inspection that

$$\dot{b} = -\frac{\gamma_i + \gamma_{\text{OM}}}{2}b.$$

The mechanical resonator sees an additional loss channel with rate $\gamma_{\text{OM}} = 4G^2/\kappa$. This loss rate is effectively a coupling between the mechanical system and photons in the optical waveguide at frequency ω_m blue of the driving beam. If only the pump beam is present, vacuum is transferred onto the mechanical system, leading to passive cooling of the mechanical motion as discussed in section 1.3.

6.1.3 Matching to mechanical loss channels

The optomechanical loss rate, γ_{OM} , is the coupling rate between phonons in the mechanical resonator and photons propagating in the *optical waveguide*. The mechanical system can have other loss channels as well, including engineered dissipation into a *mechanical waveguide* at rate γ_e . For now we ignore the intrinsic (or uncontrolled) losses of the mechanical system γ_i , by assuming $\gamma_e \gg \gamma_i$. In the picture with the optical cavity adiabatically removed, we essentially have a single mechanical resonator which is coupled to two different waveguides. By matching the mechanical loss rate to each waveguide (one for photons, the other for phonons), i.e. by setting $\gamma_{\text{OM}} = \gamma_e$, perfect matching between an optical and mechanical waveguides can be achieved. We then have a system element which acts as a coherent interface between photonic and phononic systems, i.e. a phonon-photon translator.

The argument above can be applied just as simply to a mechanical resonator coupled to two optical waveguides, one with an induced loss rate $\gamma_{\text{OM},1}$, the other with loss rate $\gamma_{\text{OM},2}$. In this system, by setting $\gamma_{\text{OM},1} = \gamma_{\text{OM},2}$, two optical waveguides with arbitrarily different frequencies are matched. It is thus possible to convert photons across a vast energy disparity, and in principle, one can convert between microwave and optics. Energy conservation is not an issue, because there are two “pump” laser beams which can give and take photons to the process.

These ideas were first presented by Safavi-Naeini and Painter [5] in the context of optomechanics, and were later demonstrated [6, 159] experimentally. The analogous scheme for converting itinerant photons in the microwave regime has also now been experimentally demonstrated by Abdo et al. [160]. Interestingly enough, the same scheme operates well into the strong coupling scheme [161], where a

different physical picture than that discussed here must be applied.

6.1.4 Dynamic tuning of polaritons

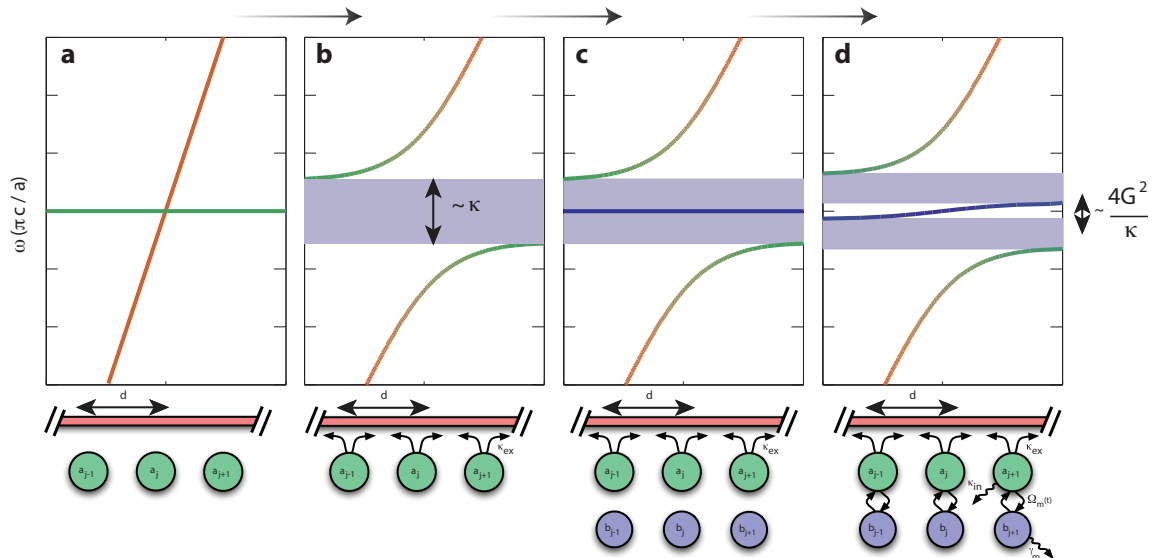


Figure 6.1: **Emergence of polaritons in optomechanical arrays.** The emergence of the polariton bands as different elements are progressively added is shown. **a**, A photonic waveguide (red) and an uncoupled array of optical cavities. **b**, When coupling between the waveguide and the optical cavities is added, the bands mix, and a gap is formed. **c**, Uncoupled arrays of mechanical systems will have no dispersion, since there is no coupling between the mechanical systems. We have plotted this band at an optical frequency, because the nonlinear interaction with the pump beam effectively “pushes” the mechanical system up to higher energies where it interacts linearly with the light in each cavity. **d**, Optomechanical coupling effectively induces a coupling between the mechanical systems, through the optical waveguide, adding some dispersion to the mechanical band. The dispersion of this polariton is tunable through the control beam.

One of the advantages of the phonon-photon translation scheme discussed above is that it does away with the need to be in the driven strong-coupling regime, and having to worry about exact engineering of control pulses. However, even though this scheme can be used to slow light significantly, it provides no way of tuning the delay imposed on the light. Tunable delay lines are important for a variety of applications in the quantum and classical domains. Interestingly, it is possible to create a tunable delay for light using optomechanical systems. By changing the intensity of the pumping laser, the coupling between the optical and mechanical system can be made time-dependent. For a single element system in an EIT setting 5.1, a tunable delay can be created. Since the element generating the delay is a single mechanical resonator, the amount of information which can be stored is fundamentally limited (there is only one degree of freedom). In fact, we showed in section 2.2.1.2 that the delay-bandwidth product, a unitless quantity that approximately represents the number of ‘bits’ one can store in the system, is always on the order of unity.

It is possible to thwart these limits to create long-lived memories for more complex spatio-temporal states of light by using an array of optomechanical elements. To increase the storage of such a quantum memory, we create an array containing many separate mechanical oscillators, coupled through the optical cavities to a waveguide. Light propagating through the waveguide then mixes with the motion and becomes a polariton – part light, part motion. The character of this excitation (and therefore its propagation velocity) can be controlled via the optically controlled interaction rate $G(t)$. At very large values of coupling $G \gg \kappa$, this polaritonic excitation is mainly light, and will thus have a velocity approximately on the same order as that of the group velocity of the waveguide. On other hand, as $G(t)$ is turned down, the bandwidth of the excitation is compressed, down to the linewidth of the mechanical systems, and the state of the photon is transferred into a dark mechanical state that can be read out later by turning up G . This scheme is reminiscent of spin-based quantum optical memories studied over a decade ago [106], with a few subtle differences mainly arising due to the periodic nature of the cavity placement.

6.2 Proposal for an optomechanical phonon-photon translator [5]

Classical and quantum information processing network architectures utilize light (optical photons) for the transmission of information over extended distances, ranging from hundreds of meters to hundreds of kilometers [162, 163]. The utility of optical photons stems from their weak interaction with the environment, large bandwidth of transmission, and resiliency to thermal noise due to their high frequency (~ 200 THz). Acoustic excitations (phonons), though limited in terms of bandwidth and their ability to transmit information farther than a few millimeters, can be delayed and stored for significantly longer times and can interact resonantly with microwave electronic and superconducting systems [27]. This complimentary nature of photons and phonons suggests hybrid phononic-photonic systems as a fruitful avenue of research, where a new class of *optomechanical* circuitry could be made to perform a range of tasks out of reach of purely photonic or phononic systems. A building block of such a hybrid architecture would be elements coherently interfacing optical and acoustic circuits. The optomechanical translator we propose in this paper acts as a chip-scale *transparent, coherent interface* between phonons and photons, and fulfills a key requirement in such a program. In this section, we present a theoretical proposal [5], which provides such an element as a realistic and realizable component.

6.2.1 Photons and phonons on a chip

The snowflake substrate proposed in section 3.2.4, and demonstrated in section 4.2 is unique in its treatment of phonons and photons in a totally symmetric two-dimensional setting. As shown in section 3.3.2.1, a line defect in such a crystal can act as waveguide for phonons, photons, or both. A point defect will also create photonic, and phononic crystal defect state resonances, and we have demonstrated coupling rates on the order of $g_0/2\pi \approx 200$ kHz in these structures (see section 4.2).

We use this coupling to create an interface between phononic and photonic waveguides. The optical loss rate is defined as before to be $\kappa = \kappa_e + \kappa_i$, and the mechanical loss rate is analogously defined as $\gamma_{ie} = \gamma_i + \gamma_e$ (see section 1.2.2). In most optomechanical experiments, the mechanical loss channels are not under the control of the experimentalist. Therefore, typically $\gamma_e = 0$. It is, however, possible to fabricate or engineer a phononic waveguide nearby into which the mechanical motion of the resonator can leak. We will show that designing a structure with independently engineerable values for κ_e and γ_e is possible in section 6.2.2. The linearized equations of motion for such a system are

$$\begin{aligned}\dot{\hat{b}}(t) &= -\left(i\omega_m + \frac{\gamma_{ie}}{2}\right)\hat{b}(t) - iG(\hat{a}(t) + \hat{a}^\dagger(t)) - \sqrt{\gamma_e}\hat{b}_{in}(t) - \sqrt{\gamma_i}\hat{b}_{in,i}(t), \\ \dot{\hat{a}}(t) &= -\left(i\Delta + \frac{\kappa}{2}\right)\hat{a}(t) - iG(\hat{b}(t) + \hat{b}^\dagger(t)) - \sqrt{\kappa_e}\hat{a}_{in}(t) - \sqrt{\kappa_i}\hat{a}_{in,i}(t).\end{aligned}$$

Our goal is to find out how to link input to the the optical (mechanical) waveguide to the output of the mechanical (optical) waveguide. This is easier to express in the Fourier domain where the equations of motion are given by¹

$$\begin{aligned}-i\omega\hat{b}(\omega) &= -\left(i\omega_m + \frac{\gamma_{ie}}{2}\right)\hat{b}(\omega) - iG(\hat{a}(\omega) + \hat{a}^\dagger(\omega)) - \sqrt{\gamma_e}\hat{b}_{in}(\omega) - \sqrt{\gamma_i}\hat{b}_{in,i}(\omega), \\ -i\omega\hat{a}(\omega) &= -\left(i\Delta + \frac{\kappa}{2}\right)\hat{a}(\omega) - iG(\hat{b}(\omega) + \hat{b}^\dagger(\omega)) - \sqrt{\kappa_e}\hat{a}_{in}(\omega) - \sqrt{\kappa_i}\hat{a}_{in,i}(\omega).\end{aligned}$$

Now using the input-output boundary condition (see equation 1.48), we find the following relations for the waveguide outputs:

$$\begin{aligned}\hat{a}_{out}(\omega) &= s_{12}(\omega)\hat{b}_{in}(\omega) + s_{11}(\omega)\hat{a}_{in}(\omega) + n_{12}(\omega)\hat{b}_{in,i}(\omega) + n_{11}(\omega)\hat{a}_{in,i}(\omega) \\ \hat{b}_{out}(\omega) &= s_{21}(\omega)\hat{b}_{in}(\omega) + s_{22}(\omega)\hat{a}_{in}(\omega) + n_{21}(\omega)\hat{b}_{in,i}(\omega) + n_{22}(\omega)\hat{a}_{in,i}(\omega)\end{aligned}$$

¹Here, as in the rest of this thesis, $\hat{a}^\dagger(\omega)$ is the fourier transform of $\hat{a}^\dagger(t)$ and equal to $(\hat{a}(-\omega))^\dagger$.

with

$$s_{11}(\omega) = 1 - \frac{\kappa_e(\gamma_{ie}/2 + i(\omega_m - \omega))}{|G|^2 + (\gamma_{ie}/2 + i(\omega_m - \omega))(\kappa/2 + i(\Delta - \omega))}, \quad (6.2)$$

$$s_{12}(\omega) = \frac{iG^* \sqrt{\gamma_e \kappa_e}}{|G|^2 + (\gamma_{ie}/2 + i(\omega_m - \omega))(\kappa/2 + i(\Delta - \omega))}, \quad (6.3)$$

$$s_{21}(\omega) = s_{12}^*(\omega), \quad (6.4)$$

$$s_{22}(\omega) = 1 - \frac{\gamma_e(\kappa/2 + i(\Delta - \omega))}{|G|^2 + (\gamma_{ie}/2 + i(\omega_m - \omega))(\kappa/2 + i(\Delta - \omega))}, \quad (6.5)$$

and similar expressions for $n_{jk}(\omega)$. We have simplified these equations by ignoring input noise terms from the creation operators $\hat{a}_{in}^\dagger(\omega)$ and $\hat{a}_{in,i}^\dagger(\omega)$. These counter-rotating terms gives rise to the quantum-limit of laser cooling and can be taken into account by using an artificially larger bath temperature [5].

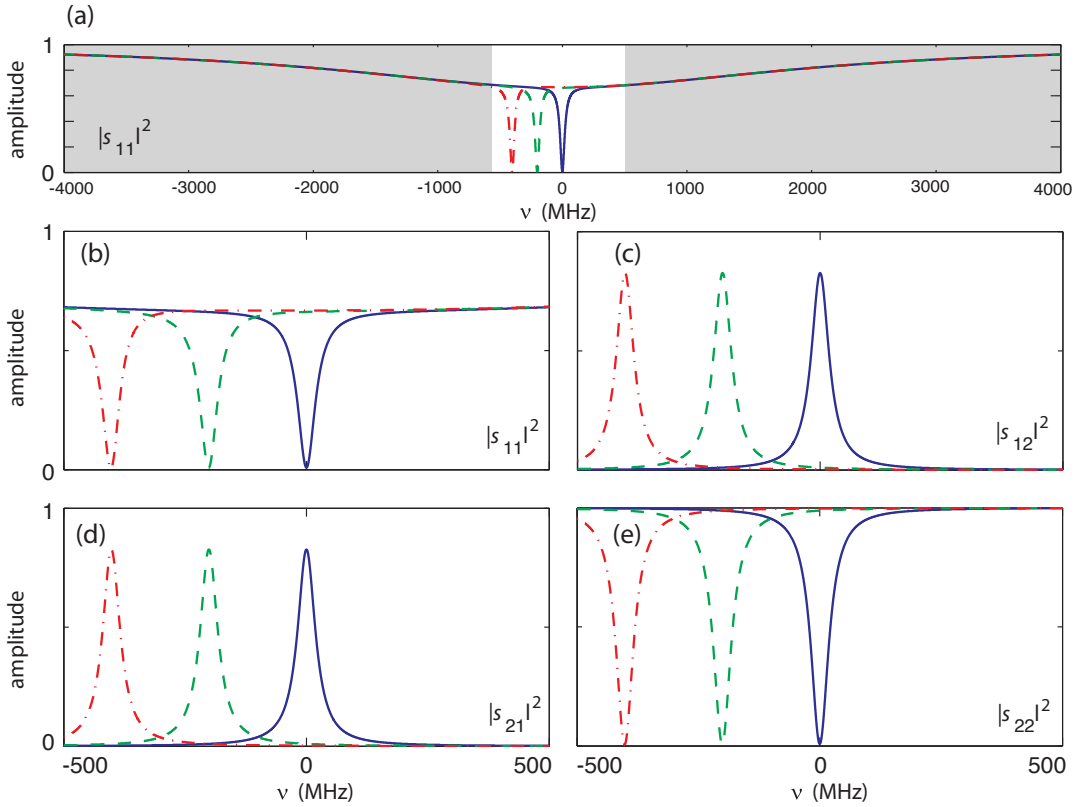


Figure 6.2: **Scattering matrix elements for phonon-photon translator.** Phonon-photon scattering matrix amplitudes for $(\gamma_e, \gamma_i, \kappa_e, \kappa_i, G) = 2\pi \times (20, 2, 4000, 400, 155.6)$ MHz. (a) Plot of the frequency dependence of the optical reflection s_{11} . The broad over-coupled optical line is visible, along with the narrow feature near the center in the unshaded region. This unshaded region is shown in more detail in plots (b), (c), (d), and (e), showing the frequency dependence of the scattering matrix elements s_{11} , s_{12} , s_{21} and s_{22} , respectively. In each plot, the curves (—), (---) and (-·-) represent detunings of $\Delta - \omega_m = 0, 2\pi \times 200$ and $2\pi \times 400$ MHz respectively.

In order to obtain efficient conversion, the cavities must be over-coupled to their respective waveguides, ensuring that the phonon (photon) has a higher chance of leaking into the waveguide continuum modes than escaping into other loss channels. In this regime, $\kappa \approx \kappa_e$ and $\gamma \approx \gamma_e$. In the weak coupling regime, $G < \kappa$, the response of the system exhibits a maximum for s_{12} and s_{21} at $\omega = 0$ and a minimum at the same point for s_{11} and s_{22} . To find the optimal value of G we consider the extrema given by

$$|s_{11}|_{\min} = \left| \frac{4G^2 + \gamma_{ie}\kappa_i - \gamma_{ie}\kappa_e}{4G^2 + \gamma_{ie}\kappa_i + \gamma_{ie}\kappa_e} \right|, \quad (6.6)$$

$$|s_{12}|_{\max} = \left| \frac{4G\sqrt{\gamma_e\kappa_e}}{4G^2 + \gamma_{ie}\kappa} \right|, \quad (6.7)$$

$$|s_{22}|_{\min} = \left| \frac{4G^2 + \kappa\gamma_i - \kappa\gamma_e}{4G^2 + \kappa\gamma_i + \kappa\gamma_e} \right|. \quad (6.8)$$

In the over-coupled approximation and in the case where $\kappa_i = \gamma_i = 0$, it is easy to see that the full translation condition $|s_{12}|_{\max} = 1$ is achievable by setting G equal to

$$2G^o = \sqrt{\gamma_{ie}\kappa}. \quad (6.9)$$

This result has a simple interpretation as a matching requirement. The photonic loss channel viewed from the phononic mode has a loss rate of $4G^2/\kappa$. Matching this to the purely mechanical loss rate of the same phononic mode, γ_{ie} , one arrives at $2G^o = \sqrt{\gamma_{ie}\kappa}$. The same argument can be used for the photonic mode, giving the same result. Under this matched condition, the linewidth of the translation peak in $|s_{12}|^2$ is simply

$$\gamma_{\text{transfer}} = \frac{8|G^o|^2}{\kappa} = 2\gamma_{ie}. \quad (6.10)$$

With intrinsic losses taken into account, either $|s_{11}|$ or $|s_{22}|$ (but not both) can be made exactly 0 by setting $4G^2 = \gamma_{ie}(\kappa_e - \kappa_i)$ or $4G^2 = (\gamma_e - \gamma_i)\kappa$, respectively. The optimal state transfer condition, however, still occurs for $2G^o = \sqrt{\gamma_{ie}\kappa}$. The extremal values ($\omega = \omega_m$) of the scattering matrix are in this case are,

$$|s_{11}|_{\omega=0}^{\text{optimal}} = \frac{\kappa_i}{\kappa_e + \kappa_i}, \quad (6.11)$$

$$|s_{12}|_{\omega=0}^{\text{optimal}} = \sqrt{\frac{\gamma_e\kappa_e}{\gamma_{ie}\kappa}}, \quad (6.12)$$

$$|s_{22}|_{\omega=0}^{\text{optimal}} = \frac{\gamma_i}{\gamma_e + \gamma_i}, \quad (6.13)$$

with corresponding noise matrix elements of,

$$|n_{11}|_{\omega=0}^{\text{optimal}} = \frac{\sqrt{\kappa_i \kappa_e}}{\kappa_e + \kappa_i}, \quad (6.14)$$

$$|n_{12}|_{\omega=0}^{\text{optimal}} = \sqrt{\frac{\gamma_i \kappa_e}{\gamma_{ie} \kappa}}, \quad (6.15)$$

$$|n_{21}|_{\omega=0}^{\text{optimal}} = \sqrt{\frac{\gamma_e \kappa_i}{\gamma_{ie} \kappa}}, \quad (6.16)$$

$$|n_{22}|_{\omega=0}^{\text{optimal}} = \frac{\sqrt{\gamma_i \gamma_e}}{\gamma_e + \gamma_i}. \quad (6.17)$$

For a set of parameters typical of a realistic OMC system, the magnitudes of the scattering matrix elements versus frequency are plotted in Figure 6.2. The normalized optical reflection spectrum ($|s_{11}|^2$) is shown in Figure 6.2(a), in which the broad optical cavity resonance can be seen along with a deeper, narrowband resonance that tunes with Δ . This narrowband resonance is highlighted in Figure 6.2(b), showing that the optical reflection is nearly completely eliminated on resonance. Photons on resonance, instead of being reflected, are being converted into outgoing phonons as can be seen in resonance peak of $|s_{21}|^2$ shown in Figure 6.2(d). A similar reflection dip and transmission peak is visible for the phononic reflection (s_{22}) and phonon to photon translation (s_{12}) curves.

6.2.2 Optomechanical crystal implementation proposal

Up to this point in the analysis of the translator system, the discussion has been kept as general as possible. Such a system is, however, interesting only insofar as it is realizable, and we attempt here to establish the practicality of a phonon-photon translator. Building upon the demonstration of OMCs [101], and the experimental demonstration of localized interacting phonon-photon defect states in snowflake substrates (see section 3.3.2.3), we provide the design of an OMC formed in a silicon microchip that can realize a high phonon-photon translation efficiency.

We limit ourselves here to a two-dimensional (2D) crystal involving only 2D Maxwell's equations for transverse-electric (TE) polarized optical waves and in-plane elastic deformations of an infinitely thick slab. This simplifies the analysis and avoids some of the technical challenges related to achieving high optical Q s in a quasi-2D thin film structure, challenges which have already been studied and met elsewhere [1, 80, 164].

The designed 2D system is shown in Figure 6.3. By creating a line defect optical waveguide, and bringing it near the L2 cavity, the optical cavity resonance is evanescently coupled to the guided modes of the line-defect, as shown in Fig. 6.3b. Control over this coupling rate is achieved at a coarse level by changing the distance (number of unit cells) between the cavity and waveguide. For the structure considered here, a gap of 8 rows is sufficient to achieve a coupling rate κ_e in the desired range. A fine tuning of the coupling rate is accomplished by adjusting the waveguide width

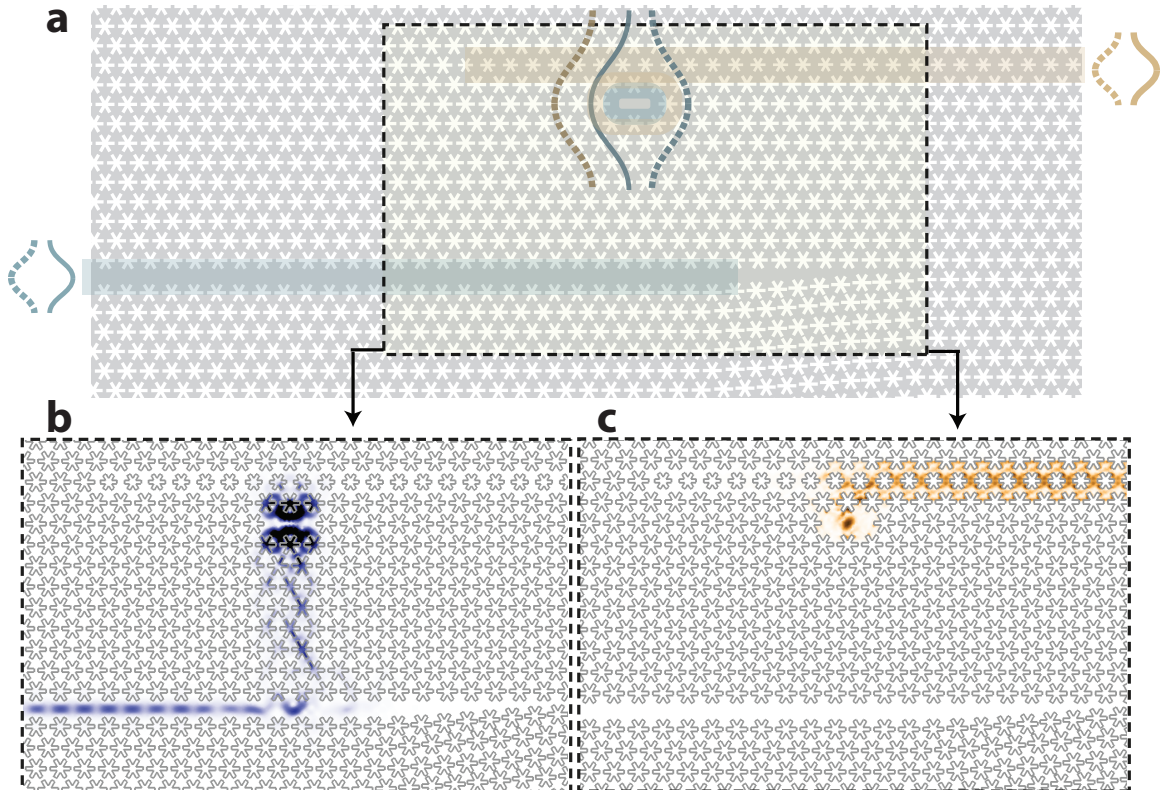


Figure 6.3: **Proposed optomechanical crystal implementation.** **a** The full OMC phonon-photon translator system, consisting of an L2 defect cavity with acoustic and optical waveguide couplers. The waveguide coupling to the cavity, for both optics and acoustics, consists of a pair of horizontal line defect waveguides. The optical waveguide (highlighted in blue) comes from the left side and the acoustic waveguide (highlighted in beige) comes from the right. **b**, The FEM-simulated photonic ($|\langle \mathbf{S}_o \rangle_t|^2$) and **c**, phononic ($|\langle \mathbf{S}_m \rangle_t|^2$) Poynting vectors of the lower cavity-waveguide structure are shown, illustrating the selective optical loading of the lower waveguide and the selective mechanical loading of the upper waveguide on the cavity.

parameter, with a value of $W = 0.135a$ resulting in a loaded optical cavity Q -factor of $Q_{\text{WG,o}} \approx 3 \times 10^5$ (the corresponding external waveguide coupling rate is $\kappa_e/2\pi = 600$ MHz). Considering that intrinsic optical Q -factors as high as 3×10^6 have been achieved in microfabricated thin-film silicon photonic crystal cavities, the calculated optical waveguide loading should put such a cavity structure well into the over-coupled regime ($\kappa_e/\kappa_i \approx 10$). A short section in which W is tapered is used to close off the waveguide on one side.

The same design procedure for the acoustic waveguide results in an evanescently coupled waveguide at a distance of only one row from the L2 cavity. Since the acoustic line-defect waveguide does not support Bloch modes at the optical cavity frequency, no additional loss is calculated for the optical cavity resonance. In this geometry, the mechanical cavity loading is calculated to be $Q_{\text{WG,m}} = 1.3 \times 10^3$, corresponding to an extrinsic coupling rate $\gamma_e/2\pi = 4.4$ MHz. Taking $Q_i \approx 10^4$ (well within what we have demonstrated in this thesis) as an achievable intrinsic mechanical Q -factor,

such a loading also puts the mechanical system in the over-coupling regime ($\gamma_e/\gamma_i \approx 10$).

Simulations of the above cavity-waveguide couplings are performed using FEM [14] with absorbing boundaries at the ends of the waveguide. The resulting time-average electromagnetic Poynting vector $|\langle \mathbf{S}_o \rangle_t|^2 = |\mathbf{E} \times \mathbf{H}^*|/2$ of the optical field leaking from the L2 optical cavity resonance is plotted in Fig. 6.3(b), while the mechanical Poynting vector $|\langle \mathbf{S}_m \rangle_t|^2 = |-\mathbf{v} \cdot \mathbf{T}|^2$ (\mathbf{v} is the velocity field, and \mathbf{T} the stress tensor) of the acoustic waves radiating from the mechanical mode of the L2 cavity is shown in Fig. 6.3(c). It is readily apparent from these two plots that the coupling of the two different waveguides to the L2 cavity act as desired; the acoustic radiation is coupled only to the phononic waveguide, and the optical radiation is coupled only to the photonic waveguide.

6.2.3 Detailed analysis of wavelength conversion [6]

The same matching concept which allows for matching a phononic waveguide to a photonic waveguide can be applied to two optical channels at different optical frequencies, but interacting with the same mechanical resonance. In such a scheme, excitations are converted by the mechanics from one color of light to another. The ‘matching’ requirement in this form of wavelength conversion is simply matching the optomechanically induced damping rates due to each driven optical resonance. Experimentally, it is often easier to do transmission measurements (see section 1.2.2) for purely technical reasons. In such two-sided coupling schemes, at least 50% of the photons are lost at each counter-propagating electromagnetic mode, reducing the total system conversion efficiency to at most 25%. We analyze here the exact transmission spectra and noise properties of a wavelength conversion scheme operating in realistic settings with inefficient couplers, and thermal noise. This work is the theoretical component of an experiment we performed and is presented in more detail in Ref. [6].

We begin by considering the Hamiltonian describing the optomechanical interaction between two distinct optical modes (indexed $k = 1, 2$) coupled to a shared mechanical mode with annihilation operator \hat{b} ,

$$\hat{H} = \sum_k \hbar \delta_k \hat{a}_k^\dagger \hat{a}_k + \hbar \omega_m \hat{b}^\dagger \hat{b} + (\hat{b} + \hat{b}^\dagger) \sum_k \hbar g_k \hat{a}_k^\dagger \hat{a}_k. \quad (6.18)$$

Each optical mode has a frequency ω_k , and is driven by a laser at frequency $\omega_{1,k}$. The Hamiltonian above is written in the interaction picture with $\delta_k = \omega_k - \omega_{1,k}$.

As shown below, strong driving at a mechanical frequency red detuned from each cavity mode, $\delta_k \cong \omega_m$, causes an effective beam splitter interaction to take place between the mechanical mode and each optical cavity mode at an enhanced coupling rate $G_k = g_k |\alpha_k|$, where α_k is the square root of the photon occupation in optical mode k . As long as this coupling is weak with respect to

the optical linewidths κ_k ($G_k \ll \kappa_k$), an adiabatic elimination of the optical cavities results in new effective mechanical loss rates $\gamma_{\text{OM},k}$ into each of the k optical degrees of freedom in the system. This “loss” can provide an effective coupling between the optical cavity modes by allowing the exchange of excitations between the optical resonances through the mechanical motion of the system. We calculate exactly what these conversion rates are by using a scattering matrix formulation to understand the behaviour of the system. Though completely general expressions can be derived, to best understand the processes involved we focus on the parameter regime relevant to this experiment, i.e. the weak-coupling, sideband-resolved case where $\omega_m \gg \kappa \gg \gamma_{\text{OM}}$, and follow a scattering matrix derivation of the induced optomechanical coupling between the optical waveguides coupled to each cavity mode.

The linearized Heisenberg-Langevin equations of motion are found using Eq. (6.18), the displacement $\hat{a}_k \rightarrow \alpha_k + \hat{a}_k$, and the inclusion of the optical input signal ($\hat{a}_{\text{in},k}(t)$), optical vacuum noise ($\hat{a}_{\text{i},k}(t)$), and mechanical thermal fluctuation fields ($\hat{b}_{\text{in}}(t)$):

$$\begin{aligned}\dot{\hat{b}}(t) &= -\left(i\omega_m + \frac{\gamma_i}{2}\right)\hat{b} - i\sum_k G_k(\hat{a} + \hat{a}^\dagger) - \sqrt{\gamma_i}\hat{b}_{\text{in}}(t), \\ \dot{\hat{a}}_k(t) &= -\left(i\delta_k + \frac{\kappa_k}{2}\right)\hat{a}_k - iG_k(\hat{b} + \hat{b}^\dagger) - \sqrt{\kappa_{e,k}/2}\hat{a}_{\text{in},k}(t) - \sqrt{\kappa'_k}\hat{a}_{\text{i},k}(t).\end{aligned}$$

The mechanical loss rate $\gamma_i = \omega_m/Q_m$, determines the coupling of the system to the thermal bath, and provides the most significant contribution in terms of noise processes relevant to the performance of the optomechanical wavelength converter. The other loss rates, κ_k , $\kappa_{e,k}$, and κ'_k are, respectively for optical cavity mode k , the total optical loss rate, the optical loss rate associated with coupling into the waveguide k , and parasitic optical loss rate into all other channels that are undetected representing a loss of information. Due to the local evanescent side-coupling scheme studied here (which bi-directionally couples to the cavity mode), $\kappa_k = \kappa_{e,k}/2 + \kappa'_k$, i.e. only a fraction $\eta_k \equiv \kappa_{e,k}/2\kappa_k$ of the photons leaving the cavity get detected and $\eta_k \leq 1/2$.

The equations of motion are linear and thus the system can be analyzed more simply in the frequency domain. Solving for the spectrum of the mechanical mode $\hat{b}(\omega)$ in terms of the input noise operators, we find:

$$\begin{aligned}\hat{b}(\omega) &= \frac{-\sqrt{\gamma_i}\hat{b}_{\text{in}}(\omega)}{i(\omega_m - \omega) + \gamma/2} + \sum_k \frac{iG_k}{i(\delta_k - \omega) + \kappa_k/2} \frac{\sqrt{\kappa_{e,k}/2}\hat{a}_{\text{in},k}(\omega) + \sqrt{\kappa'_k}\hat{a}_{\text{i},k}(\omega)}{i(\omega_m - \omega) + \gamma/2} \\ &\quad + \sum_k \frac{iG_k}{-i(\delta_k + \omega) + \kappa_k/2} \frac{\sqrt{\kappa_{e,k}/2}\hat{a}_{\text{in},k}^\dagger(\omega) + \sqrt{\kappa'_k}\hat{a}_{\text{i},k}^\dagger(\omega)}{i(\omega_m - \omega) + \gamma/2},\end{aligned}$$

where the mechanical frequency ω_m is now modified by the optical spring, and the mechanical linewidth is given by $\gamma \equiv \gamma_i + \gamma_{\text{OM},1} + \gamma_{\text{OM},2}$. The optomechanical damping terms $\gamma_{\text{OM},k}$ come from

coupling of the mechanical system to the optical mode k , and are given by the relation

$$\begin{aligned}\gamma_{\text{OM},k} &= 2|G_k|^2 \text{Re} \left[\frac{1}{i(\delta_k - \omega_m) + \kappa_k/2} - \frac{1}{-i(\delta_k + \omega_m) + \kappa_k/2} \right] \\ &= \frac{4|G_k|^2}{\kappa_k} \quad \text{for } \delta_k \approx \omega_m.\end{aligned}\tag{6.19}$$

The last expression is a simplification that is often made, and is equivalent to looking at spectral properties at detunings from the mechanical frequency much smaller than κ (so the optical lineshape isn't taken into account). Under this approximation, the optical spectrum is

$$\begin{aligned}\frac{\kappa_k}{2} \hat{a}_k(\omega) &= \frac{iG_k \sqrt{\gamma_i} \hat{b}_{\text{in}}(\omega)}{i(\omega_m - \omega) + \gamma/2} + \sum_j \frac{2G_j G_k}{\kappa_j} \frac{\sqrt{\kappa_{e,j}/2} \hat{a}_{\text{in},j}(\omega) + \sqrt{\kappa'_j} \hat{a}_{i,j}(\omega)}{i(\omega_m - \omega) + \gamma/2} \\ &\quad + \sum_j \frac{iG_j G_k}{2\omega_m} \frac{\sqrt{\kappa_{e,j}/2} \hat{a}_{\text{in},j}^\dagger(\omega) + \sqrt{\kappa'_j} \hat{a}_{i,j}^\dagger(\omega)}{i(\omega_m - \omega) + \gamma/2} \\ &\quad - \sqrt{\kappa_{e,k}/2} \hat{a}_{\text{in},k}(\omega) - \sqrt{\kappa'_k} \hat{a}_{i,k}(\omega).\end{aligned}\tag{6.20}$$

From this expression, we see that there are several noise operators incident on optical mode k . The thermal fluctuations from the environment, $\hat{b}_{\text{in}}(\omega)$, are converted into noise photons over the mechanical bandwidth γ . There is also an induced coupling to the optical mode $j \neq k$, and photons originally incident only on mode j , i.e. $\hat{a}_{\text{in},j}(\omega)$ are now also coupled into \hat{a}_k . Finally, we note that vacuum noise creation operators are also present in this expression. These give rise to quantum noise through spontaneous emission of phonons, though we show below that as ω_m is made very large with respect to κ_k , these terms diminish in importance.

From outside the optomechanical system, we only have access to photons sent into the system, $\hat{a}_{\text{in},j}$, and those leaving the system, $\hat{a}_{\text{out},k}$, on transmission. The relation between these operators is best understood through scattering parameters, and can be derived using the equation for $\hat{a}_k(\omega)$ (Eq. 6.20) and the input-output boundary conditions $\hat{a}_{\text{out},k}(\omega) = \hat{a}_{\text{in},k}(\omega) + \sqrt{\kappa_{e,k}/2} \hat{a}_k(\omega)$. After some algebra, the output operator is expressed as

$$\begin{aligned}\hat{a}_{\text{out},k}(\omega) &= s_{\text{th},k}(\omega) \hat{b}_{\text{in}}(\omega) + t_k(\omega) \hat{a}_{\text{in},k}(\omega) + s_{kj}(\omega) \hat{a}_{\text{in},j}(\omega) + \sum_m n_{\text{opt},m}(\omega) \hat{a}_{i,m}(\omega) \\ &\quad + \sum_m s_{\text{adj},\text{in},m}(\omega) \hat{a}_{\text{in},m}^\dagger(\omega) + \sum_m s_{\text{adj},i,m}(\omega) \hat{a}_{i,m}^\dagger(\omega)\end{aligned}$$

The scattering coefficient $s_{\text{th},k}(\omega)$ is the conversion efficiency of mechanical thermal noise to photons, and is given by

$$s_{\text{th},k}(\omega) = i\sqrt{\eta_k} \frac{\sqrt{\gamma_i \gamma_{\text{OM},k}}}{i(\omega_m - \omega) + \gamma/2}.\tag{6.21}$$

The coefficient $t_k(\omega)$ in our system is transmission amplitude, given by

$$t_k(\omega) = (1 - 2\eta_k) + \eta_k \frac{\gamma_{\text{OM},k}}{i(\omega_m - \omega) + \gamma/2}. \quad (6.22)$$

In principle, this coefficient is the EIT transmission coefficient, though here it is written about the mechanical frequency for detunings on the order of γ and the κ 's are too large ($\kappa \gg \gamma$) for the optical lineshape to be considered in the expression. This is the expected result of the weak coupling approximation. Finally, the most important coefficient is the wavelength conversion coefficient $s_{kj}(\omega)$ which is given by

$$s_{kj}(\omega) = \sqrt{\eta_k \eta_j} \frac{\sqrt{\gamma_{\text{OM},k} \gamma_{\text{OM},j}}}{i(\omega_m - \omega) + \gamma/2}. \quad (6.23)$$

6.2.4 Efficiency, Bandwidth, and Noise

We calculate the spectral density of the output field on port k ($S_{\text{out},k}(\omega)$) assuming an input field spectral density on the opposing optical port j ($S_{\text{in},j}(\omega)$), vacuum inputs on all other optical channels, and thermal noise from a phonon bath with thermal occupation n_b . The spectral densities here have units of photons/Hz \cdot s and can be interpreted as photon flux per unit bandwidth. At first we ignore the field creation operators in the scattering relation Eq. (6.21) (which give rise to quantum back-action heating studied in section 1.4.1) and arrive at the following expression:

$$\begin{aligned} S_{\text{out},k}(\omega) &= \int_{-\infty}^{\infty} d\omega' \langle \hat{a}_{\text{out},k}^\dagger(\omega) \hat{a}_{\text{out},k}(\omega') \rangle \\ &= \int_{-\infty}^{\infty} s_{\text{th},k}^*(-\omega) s_{\text{th},k}(\omega') \langle \hat{b}_{\text{in}}^\dagger(\omega) \hat{b}_{\text{in}}(\omega') \rangle \\ &\quad + t_k^*(-\omega) t_k(\omega') \langle \hat{a}_{\text{in},k}^\dagger(\omega) \hat{a}_{\text{in},k}(\omega') \rangle \\ &\quad + s_{k,j}^*(-\omega) s_{k,j}(\omega') \langle \hat{a}_{\text{in},j}^\dagger(\omega) \hat{a}_{\text{in},j}(\omega') \rangle \\ &\quad + n_{\text{opt},k}^*(-\omega) n_{\text{opt},k}(\omega') \langle \hat{a}_{i,k}^\dagger(\omega) \hat{a}_{i,k}(\omega') \rangle \\ &\quad + n_{\text{opt},j}^*(-\omega) n_{\text{opt},j}(\omega') \langle \hat{a}_{i,j}^\dagger(\omega) \hat{a}_{i,j}(\omega') \rangle d\omega'. \end{aligned}$$

This reduces to,

$$S_{\text{out},k}(\omega) = \eta_k \frac{\gamma_i \gamma_{\text{OM},k}}{(\omega + \omega_m)^2 + (\gamma/2)} n_b + \eta_k \eta_j \frac{\gamma_{\text{OM},k} \gamma_{\text{OM},j}}{(\omega + \omega_m)^2 + (\gamma/2)^2} S_{\text{in},j}(\omega),$$

accounting for the noise autocorrelation functions. From here, we see that the maximum photon wavelength conversion efficiency is given by

$$\eta_{\text{max}} = \eta_1 \eta_2 \frac{4\gamma_{\text{OM},1} \gamma_{\text{OM},2}}{(\gamma_i + \gamma_{\text{OM},1} + \gamma_{\text{OM},2})^2}. \quad (6.24)$$

The conversion process has a bandwidth (BW) equal to the mechanical linewidth

$$\text{BW} \equiv \gamma_i + \gamma_{\text{OM},1} + \gamma_{\text{OM},2}. \quad (6.25)$$

From the same expression, we calculate a value for the optical signal to noise ratio (OSNR), to find

$$\text{OSNR}_{kj}^{\text{classical}} = \eta_j \frac{\gamma_{\text{OM},j}}{\gamma_i n_b} S_{\text{in},j}(\omega). \quad (6.26)$$

Equation (6.26) only takes into account the thermal noise in the system and therefore holds only when $\gamma_i n_b / \gamma_{\text{OM},j} \gg 1$. At higher powers, the quantum noise processes which give rise to the back-action limit in cooling also give rise to excess noise for wavelength conversion. To consider these terms, the creation operators in Eq. (6.21) must not be neglected and the full relation is then found to be

$$\begin{aligned} S_{\text{out},k}(\omega) &= \eta_k \frac{\gamma_{\text{OM},k}}{(\omega + \omega_m)^2 + (\gamma/2)^2} \gamma_i n_b + \eta_k \frac{\gamma_{\text{OM},k}}{(\omega + \omega_m)^2 + (\gamma/2)^2} \gamma_{\text{OM},k} \left(\frac{\kappa_k}{4\omega_m} \right)^2 \\ &+ \eta_k \frac{\gamma_{\text{OM},k}}{(\omega + \omega_m)^2 + (\gamma/2)^2} \gamma_{\text{OM},j} \left(\frac{\kappa_j}{4\omega_m} \right)^2 \\ &+ \eta_k \eta_j \frac{\gamma_{\text{OM},k} \gamma_{\text{OM},j}}{(\omega + \omega_m)^2 + (\gamma/2)^2} S_{\text{in},j}(\omega). \end{aligned} \quad (6.27)$$

The quantum limited OSNR is then found to be

$$\text{OSNR}_{kj} = \frac{\eta_j \gamma_{\text{OM},j} S_{\text{in},j}(\omega)}{\gamma_i n_b + \gamma_{\text{OM},k} \left(\frac{\kappa_k}{4\omega_m} \right)^2 + \gamma_{\text{OM},j} \left(\frac{\kappa_j}{4\omega_m} \right)^2}. \quad (6.28)$$

For the quantum back-action terms to become significant as compared to the thermal noise on the mechanical system, one needs $\gamma_i n_b / \gamma \sim \left(\frac{\kappa}{4\omega_m} \right)^2$. This is a regime that is yet to be reached in experiments and as such the quantum back-action noise terms can be neglected for experiments to date. Perhaps more importantly, we ask ‘‘what is the amount of noise added to a signal of a single photon?’’. We can express the signal to noise ratios as $\text{OSNR}_{kj} = S_{\text{in},j}(\omega) / n_{\text{added}}$, with

$$n_{\text{added}} = \frac{\gamma_i n_b + \gamma_{\text{OM},k} \left(\frac{\kappa_k}{4\omega_m} \right)^2 + \gamma_{\text{OM},j} \left(\frac{\kappa_j}{4\omega_m} \right)^2}{\eta_j \gamma_{\text{OM},j}}. \quad (6.29)$$

Assuming $\kappa_j = \kappa_k = \kappa$, $\gamma_i \ll \gamma$, and $\gamma_{\text{OM},j} = \gamma_{\text{OM},k} = \gamma_{\text{OM}}$, this expression becomes

$$n_{\text{added}} \approx 2\eta_j^{-1} \left(\frac{\gamma_i n_b}{\gamma} + \left(\frac{\kappa}{4\omega_m} \right)^2 \right). \quad (6.30)$$

To achieve the threshold where a single photon incoming on port j is converted, and is more likely to be detected on port k than an upconverted thermal excitation, we require $n_{\text{added}} < 1$. This requirement is equivalent to stating that in the absence of signals on port j and k , a cooled phonon occupation of $\bar{n} = \eta_j/2$ must be achieved. We note that η_k does not make an appearance in this equation, since reduced output coupling efficiency attenuates the thermal noise and signal equivalently. For the same reason, $1/\eta_j$ is present in the noise quanta expression. The factor of two can be understood to come from the fact that for good conversion, we require the photon to enter, and exit the system before a phonon is up converted. The former two processes happen at γ_{OM} , while the latter is given by the thermalization rate $\gamma_i n_b$.

6.3 Proposal for an optomechanical quantum memory [7]

Light is a natural candidate to transmit information across large networks due to its high speed and low propagation losses. A major obstacle to building more advanced optical networks is the lack of an all-optically controlled device that can robustly delay or store optical wave-packets over a tunable amount of time. In the classical domain, such a device would enable all-optical buffering and switching, bypassing the need to convert an optical pulse to an electronic signal. In the quantum realm, such a device could serve as a memory to store the full quantum information contained in a light pulse until it can be passed to a processing node at some later time.

A number of schemes to coherently delay and store optical information are being actively explored. These range from tunable CROW structures [116], where the propagation of light is dynamically altered by modulating the refractive index of the system, to EIT in atomic media [106], where the optical pulse is reversibly mapped into internal atomic degrees of freedom. While these schemes have been demonstrated in a number of experiments, they remain difficult to implement in a practical setting. Here, we present a novel approach to store or stop an optical pulse propagating through a waveguide, wherein coupling between the waveguide and a nearby nano-mechanical resonator array enables one to map the optical field into long-lived mechanical excitations. This process is completely quantum coherent and allows the delay and release of pulses to be rapidly and all-optically tuned. Our scheme combines many of the best attributes of previously proposed approaches, in that it simultaneously allows for large bandwidths of operation, on-chip integration, relatively long delay/storage times, and ease of external control. Beyond light storage, this work opens up the intriguing possibility of a platform for quantum or classical all-optical information processing using mechanical systems.

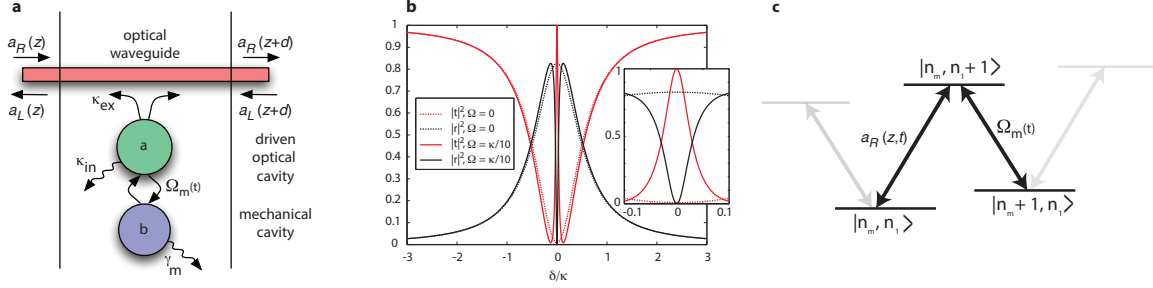


Figure 6.4: **Response of optomechanical array element.**

6.3.1 Description of the system

Fabrication techniques for 2D photonic crystals has matured significantly over the last decade, with experiments on a Si chip [119] demonstrating excellent optical transmission through long ($N > 100$) linear arrays of coupled photonic crystal cavities. Extending these results to planar OMCs provides a natural back-drop for our proposed slow-light scheme.

An array of optomechanical cavities, all with the same optical frequency, mechanical frequency, and coupling rate are considered. A system diagram is shown in Figure 6.5a. All cavities are driven on the red side, so the beam-splitter Hamiltonian is assumed for each cavity, with a tunable phonon-photon coupling rate $G(t) = g_0 \sqrt{n_c(t)}$.

6.3.2 Derivation of dispersion relation

We use a transmission matrix method to find the dispersion relation for photons in the multielement system. The transmission matrix of the system is defined as

$$\begin{pmatrix} a_R(z_j^+) \\ a_L(z_j^+) \end{pmatrix} = M_{om} \begin{pmatrix} a_R(z_j^-) \\ a_L(z_j^-) \end{pmatrix}, \quad (6.31)$$

where $a_R(z_j^\pm)$ and $a_L(z_j^\pm)$ are the noise operators for the right- and left-propagating modes respectively. The \pm super-scripts denote whether the operators are being evaluated on the left (-) or right (+) side of the optomechanical cavity. Free propagation in the waveguide is characterized by the matrix M_f ,

$$\begin{pmatrix} a_R(z+d) \\ a_L(z+d) \end{pmatrix} = M_f \begin{pmatrix} a_R(z) \\ a_L(z) \end{pmatrix}, \quad (6.32)$$

where

$$M_f = \begin{pmatrix} e^{ikd} & 0 \\ 0 & e^{-ikd} \end{pmatrix}. \quad (6.33)$$

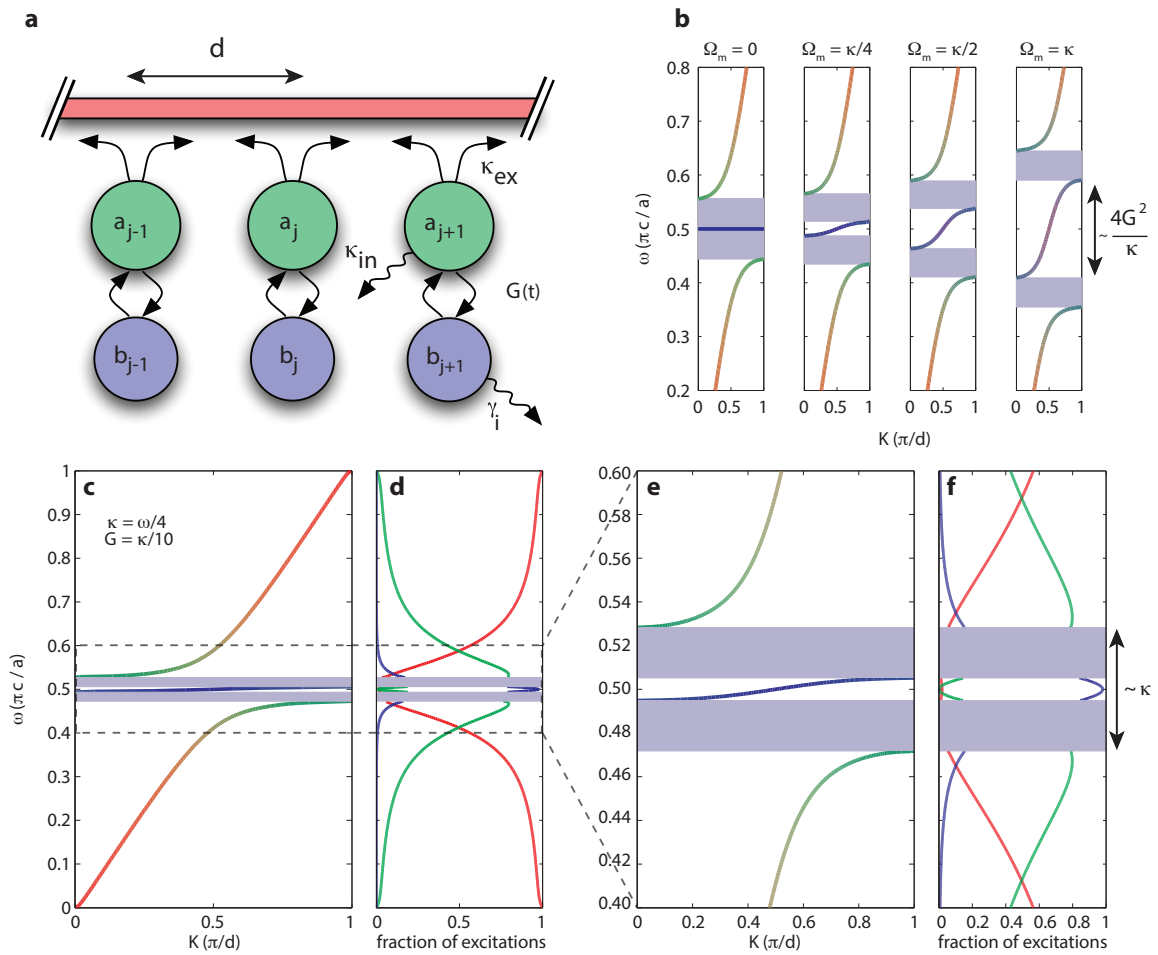


Figure 6.5: **Illustration of band structure of optomechanical crystal array.** **a** Illustration of an OMC array. A two-way optical waveguide is coupled to a periodic array of optomechanical elements spaced by a distance d . The optical cavity modes a_j of each element leak energy into the waveguide at a rate κ_e and have an inherent decay rate κ_i . The mechanical resonator of each element has frequency ω_m and is optomechanically coupled to the cavity mode through a tuning cavity with strength $G(t)$. **b**, The band structure of the system, for a range of driving strengths between $G = 0$ and $G = \kappa$. The blue shaded regions indicate band gaps, while the color of the bands elucidates the fractional occupation (red for energy in the optical waveguide, green for the optical cavity, and blue for mechanical excitations). The dynamic compression of the bandwidth is clearly visible as $G \rightarrow 0$. **c**, Band structure for the case $G = \kappa/10$ is shown in greater detail. **d**, The fractional occupation for each band in **c** is plotted separately. It can be seen that the polaritonic slow-light band is mostly mechanical in nature, with a small mixing with the waveguide modes and negligible mixing with the optical cavity mode. Zoom-ins of figures **c** and **d** are shown in **e** and **f**.

For simplicity, here we work only with the classical equations so that the intrinsic noise terms in the Heisenberg-Langevin equations can be ignored. We begin by transforming the linearized versino of

Eqs. (1.58) and (1.59) to the Fourier domain,

$$0 = \left(i\delta_k - \frac{\kappa}{2}\right)a + iGb + i\sqrt{\frac{\kappa_e}{2}}(a_R(z_j^-) + a_L(z_j^+)), \quad (6.34)$$

$$0 = \left(i\delta_k - \frac{\gamma_m}{2}\right)b + iGa. \quad (6.35)$$

It is then convenient to write the transfer matrix M_{om} in the form

$$M_{om} = \begin{pmatrix} 1 - \beta & -\beta \\ \beta & 1 + \beta \end{pmatrix}, \quad (6.36)$$

with the parameter $\beta(\delta_k)$ given by

$$\beta(\delta_k) = \frac{-i\kappa_e\delta_k}{-i\kappa_i\delta_k + 2(G^2 - \delta_k^2)}. \quad (6.37)$$

The transfer matrix M_{block} describing propagation to the next unit cell can subsequently be diagonalized, $M_{block} = SDS^{-1}$, with the diagonal matrix D given by

$$D = \begin{pmatrix} e^{ik_{\text{eff}}d} & 0 \\ 0 & e^{-ik_{\text{eff}}d} \end{pmatrix}. \quad (6.38)$$

Physically, this diagonalization corresponds to finding the Bloch wavevectors $k_{\text{eff}}(\delta_k)$ of the periodic system. The dispersion relation for the system can be readily obtained through the equation

$$\cos(k_{\text{eff}}(\delta_k)d) = \cos(kd) - i\beta(\delta_k)\sin(kd). \quad (6.39)$$

Writing k in terms of δ_k , we arrive at $kd = \omega_1 d/c + \delta_k d/c$. As described previously, the desirable operation regime of the system is such that the phase imparted in free propagation should be $\omega_1 d/c = (2n + 1)\pi/2$. For concreteness, we set here $\omega_1 d/c = \pi/2$, satisfying this condition. For the frequencies δ_k of interest, which easily satisfy the condition $|\delta_k| \ll d/c$, and ignoring the intrinsic loss κ_i , the simple approximate dispersion formula

$$\cos(k_{\text{eff}}(\delta_k)d) = -\frac{\kappa_e\delta_k}{2(G^2 - \delta_k^2)} \quad (6.40)$$

can be found. This dispersion relation yields two bandgaps, which extend from $\pm\kappa_e/2$ and $\pm 2G^2/\kappa_e$, in the weakly coupled EIT regime ($G \lesssim \kappa_e$). We therefore have three branches in the band structure, with the narrow central branch having a width of $4G^2/\kappa_e$. This branch has an optically tunable width and yields the slow-light propagation.

The dispersive and lossy properties of the array can also be found by analyzing Eq. (6.39)

perturbatively. Expanding Eq. (6.39) as a power series in δ_k , we find

$$k_{\text{eff}}(\delta_k) = k_0 + \frac{\kappa_e \delta_k}{2dG^2} + \frac{i\kappa_e \kappa_i \delta_k^2}{4dG^4} + \frac{(2\kappa_e^3 - 3\kappa_e \kappa_i^2 + 12\kappa_e G^2) \delta_k^3}{24dG^6} + O(\delta_k^4), \quad (6.41)$$

6.3.3 Fractional Occupation Calculation

In our system, the Bloch functions are hybrid waves arising from the mixing of optical waveguide, optical cavity and mechanical cavity excitations. It is therefore of interest to calculate the hybrid, or polaritonic, properties of these waves, by studying the energy distribution of each Bloch mode.

The number of photons n_{WG} in the waveguide can be found by taking the sum of the left- and right-moving photons in a section of the device. Over one unit cell, one obtains

$$n_{\text{WG}} = (|c_j|^2 + |d_j|^2) \frac{d}{c}. \quad (6.42)$$

The relation between this value and the amplitude of the hybrid Bloch wave may be found by considering the symmetry transformation used to diagonalize the unit-cell transmission matrix. Defining C_j to be the amplitude of the Bloch mode of interest, one finds $c_j = s_{11}C_j$ and $d_j = s_{21}C_j$, while from the properties of the symmetry matrix S , $|C_j|^2 = |c_j|^2 + |d_j|^2$. From here we can deduce the number of excitations in the waveguide n_{WG} , the optical cavity n_o and the mechanical cavity n_m for a given Bloch wave amplitude:

$$n_{\text{WG}} = \frac{d}{c} |C_j|^2, \quad (6.43)$$

$$n_o = |a|^2 \quad (6.44)$$

$$= \frac{2|\beta(\delta_k)|^2}{\kappa_e} |c_j + d_j|^2 \quad (6.45)$$

$$= \frac{2|\beta(\delta_k)|^2}{\kappa_e} |s_{11} + s_{21}|^2 |C_j|^2, \quad (6.46)$$

$$n_m = |b|^2 \quad (6.47)$$

$$= \frac{|G|^2}{\delta_k^2 + \gamma_i^2/4} |a|^2. \quad (6.48)$$

We then define the fractional occupation in the mechanical mode by $n_m/(n_{\text{WG}} + n_o + n_m)$ (with analogous definitions for the other components). These relations were used to plot the fractional occupation and colored band diagrams shown in figure 6.5.

6.3.4 Slowing and stopping light

Starting from the approximate dispersion equation (6.41), it is apparent that the group velocity on resonance, $v_g = (dk_{\text{eff}}/d\delta_k)^{-1}|_{\delta_k=0} = 2dG^2/\kappa_e$ can be dramatically slowed by an amount that is tunable through the optomechanical coupling strength G . The quadratic and cubic terms in k_{eff}

characterize pulse absorption and group velocity dispersion, respectively. In the relevant regime where $\kappa_e \gg \kappa_i, \kappa_e \gtrsim G$, these effects are negligible within a bandwidth

$$\Delta\omega \sim \min\left(\frac{2\sqrt{2}G^2}{\sqrt{N\kappa_e\kappa_i}}, \frac{2(6\pi)^{1/3}G^2}{\kappa_e N^{1/3}}\right). \quad (6.49)$$

The second term is the bandwidth over which certain frequency components of the pulse acquire a π -phase shift relative to others, leading to pulse distortion. This yields a bandwidth-delay product of

$$\Delta\omega\tau_{\text{delay}} \sim \min\left(\sqrt{2N\kappa_e/\kappa_i}, (6\pi N^2)^{1/3}\right) \quad (6.50)$$

for static G and negligible mechanical losses. When intrinsic optical cavity losses are negligible, and if one is not concerned with pulse distortion, light can propagate over the full bandwidth $\sim 4G^2/\kappa$ of the slow-light polariton band and the bandwidth-delay product increases to $\Delta\omega\tau_{\text{delay}} \sim N$. On the other hand, we note that if we had operated in a regime where $k_0d = \pi n$, constructive interference in reflection would limit the bandwidth-delay product to $\Delta\omega\tau_{\text{delay}} \sim 1$, independent of system size.

In the static regime, the bandwidth-delay product obtained here is analogous to CROW systems. In the case of EIT, a static bandwidth-delay product of $\Delta\omega\tau_{\text{delay}} \sim \sqrt{\text{OD}}$ results, where OD is the optical depth of the atomic medium. This product is limited by photon absorption and re-scattering into other directions, and is analogous to our result $\Delta\omega\tau_{\text{delay}} \sim \sqrt{N\kappa_e/\kappa_i}$ in the case of large intrinsic cavity linewidth. On the other hand, when κ_i is negligible, photons are never lost and reflections can be suppressed by interference. This yields an improved scaling $\Delta\omega\tau_{\text{delay}} \sim N^{2/3}$ or $\sim N$, depending on whether one is concerned with group velocity dispersion. In atomic media, the weak atom-photon coupling makes achieving $\text{OD} > 100$ very challenging. In contrast, in our system as few as $N \sim 10$ elements would be equivalently dense.

6.3.5 Storage of optical pulse

We now show that the group velocity $v_g(t) = 2dG^2(t)/\kappa_e$ can in fact be adiabatically changed once a pulse is completely localized inside the system, leading to distortion-less propagation at a dynamically tunable speed. In particular, by tuning $v_g(t) \rightarrow 0$, the pulse can be completely stopped and stored.

This phenomenon can be understood in terms of the static band structure of the system (Fig. 6.5) and a ‘‘dynamic compression’’ of the pulse bandwidth. The same physics applies for CROW structures [116], and the argument is re-summarized here. First, under constant G , an optical pulse within the bandwidth of the polariton band completely enters the medium. Once the pulse is inside, we consider the effect of a gradual reduction in $G(t)$. Decomposing the pulse into Bloch wavevector components, it is clear that each Bloch wavevector is conserved under arbitrary changes of G , as it

is fixed by the system periodicity. Furthermore, transitions to other bands are negligible provided that the energy levels are varied adiabatically compared to the size of the gap, which translates into an adiabatic condition $|(d/dt)(G^2/\kappa)| \lesssim \kappa^2$. Then, conservation of the Bloch wavevector implies that the bandwidth of the pulse is dynamically compressed, and the reduction in slope of the polariton band (Fig. 6.5) causes the pulse to propagate at an instantaneous group velocity $v_g(t)$ without any distortion. In the limit that $G \rightarrow 0$, the polaritonic band becomes flat and completely mechanical in character, indicating that the pulse has been reversibly and coherently mapped onto stationary mechanical excitations within the array. We note that since G is itself set by the tuning cavities, its rate of change cannot exceed the optical linewidth and thus the adiabaticity condition is always satisfied in the weak-driving regime.

The maximum storage time is set by the mechanical decay rate, $\sim 1/\gamma_m$. For realistic system parameters $\omega_m/2\pi = 10$ GHz and $Q_m = 10^5$, this yields a storage time of ~ 10 μ s. In CROW structures, light is stored as circulating fields in optical nano-cavities, where state of the art quality factors of $Q \sim 10^6$ limit the storage time to ~ 1 ns. The key feature of our system is that we effectively “down-convert” the high-frequency optical fields to low-frequency mechanical excitations, which naturally decay over much longer time scales. While storage times of ~ 10 ms are possible using atomic media, their bandwidths so far have been limited to < 1 MHz. In our system, bandwidths of ~ 1 GHz are possible for realistic circulating powers in the tuning cavities.

6.3.6 Optomechanical crystal implementation

A line defect on an OMC acts as a waveguide for light [78, 79]. Here, the line defects used consist of a removed row of holes, with the rows above and below shifted towards one another by a distance W . The waveguide was designed such that mechanically, it would have no bands resonant with the cavity frequency and would therefore have no effect on the mechanical Q factors. Optically, it was designed have a single band crossing the cavity frequency and would therefore serve as the single-mode optical waveguide required by the proposal. The design details can be found in Ref. [7].

By bringing the optical waveguide near our cavity, the guided modes of the line-defect are evanescently coupled to the cavity mode, and a coupling between the two may be induced. Control over this coupling rate is achieved at a coarse level by changing the distance between the cavity and waveguide, i.e., the number of unit cells between them. We found a distance of 6 rows to be sufficient in placing our coupling rate κ_e in a desirable range. At this point, a fine tuning of the coupling rate may be accomplished by adjustment

To simulate this coupling rate, we performed FEM simulations using COMSOL where we placed the waveguide near our cavity, and placed absorbing boundaries at the ends of the waveguide away from the cavity. The resulting time-averaged Poynting vector $\langle \mathbf{S} \rangle_t = |\mathbf{E} \times \mathbf{H}^*|/2$ is similar to what is plotted in Fig. 6.3, showing how the power flows out of the system. The resulting simulated

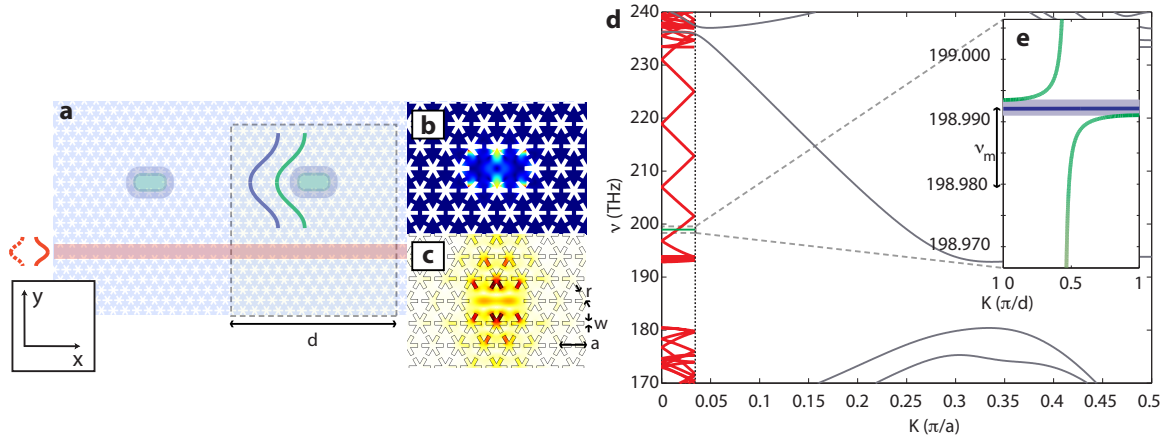


Figure 6.6: **Simulated band structure of optomechanical crystal array.** **a**, Top view of the proposed OMC array, with the superlattice unit-cell of length d highlighted in the center. The unit cell contains an optomechanical cavity (shaded in grey) with a side-coupled linear defect optical waveguide (shaded in red). The displacement field amplitude $|\mathbf{Q}(\mathbf{r})|$ of the mechanical mode and in-plane electric field amplitude $|\mathbf{E}(\mathbf{r})|$ of the optical mode are shown in **b** and **c**, respectively, for the L2 defect cavity. **d**, Bandstructure of the linear-defect waveguide (grey) and the zone folded superlattice of the entire coupled-resonator system (red). The cavity mode (green) crosses the superlattice band at mid-zone, and the waveguide-cavity interaction is shown in more detail in the inset **e**.

structure and its band diagrams are shown in Fig. 6.6 .

Appendix A

Mathematical Definitions and Derivations

A.1 Definitions

Fourier Transforms are defined for operators and variables in the symmetric manner

$$\begin{aligned}\hat{A}(t) &= \frac{1}{\sqrt{2\pi}} \int_{-\infty}^{\infty} d\omega e^{-i\omega t} \hat{A}(\omega), \\ \hat{A}(\omega) &= \frac{1}{\sqrt{2\pi}} \int_{-\infty}^{\infty} dt e^{i\omega t} \hat{A}(t).\end{aligned}\tag{A.1}$$

Spectral densities are defined as

$$S_{AA}(\omega) = \int_{-\infty}^{\infty} d\tau e^{i\omega\tau} \langle \hat{A}^\dagger(t+\tau) \hat{A}(t) \rangle.\tag{A.2}$$

and symmetrized as $\bar{S}_{AA}(\omega) = \frac{1}{2}(S_{AA}(\omega) + S_{AA}(-\omega))$. Here the angular brackets denote expectation values as defined in quantum mechanics $\langle A \rangle = \text{Tr}(A\rho)$. When classical stochastic processes are placed in angular brackets, we refer to a classical ensemble average. In Fourier domain, the various system operators are written in terms of the bath noise operators, and therefore knowledge of the expectation values of form $\langle \hat{A}(\omega) \rangle$ and $\langle \hat{B}(\omega) \hat{A}(\omega') \rangle$ where \hat{A} and \hat{B} are bath field operators is sufficient to calculate spectral densities. These correlations are known from the density matrix of the baths, which in this paper are assumed to be in either a vacuum or thermal state. The Hermitian conjugate of operator $\hat{A}(t)$ is $\hat{A}^\dagger(t)$, and has a Fourier transform denoted as

$$\hat{A}^\dagger(\omega) = \frac{1}{\sqrt{2\pi}} \int_{-\infty}^{\infty} dt e^{i\omega t} \hat{A}^\dagger(t),$$

leading to $(\hat{A}(\omega))^\dagger = \hat{A}^\dagger(-\omega)$. The spectral density may be written also as

$$S_{AA}(\omega) = \int_{-\infty}^{\infty} d\omega' \langle \hat{A}^\dagger(\omega) \hat{A}(\omega') \rangle. \quad (\text{A.3})$$

We use the convention

$$\hat{X}_\theta^{(j)} = \hat{a}_j e^{-i\theta} + \hat{a}_j^\dagger e^{i\theta}. \quad (\text{A.4})$$

to define a measured quadrature of the field. This definition corresponds to having a phase difference of θ between input light and local oscillator.

A.2 Mechanical resonator spectral density

We use mainly the input-output formalism to derive the various spectra which are being measured. For the case of the mechanical resonator, the quantum Langevin equation is given by

$$\dot{\hat{b}}(t) = -\left(i\omega_m + \frac{\gamma_i}{2}\right) \hat{b}(t) - \sqrt{\gamma_i} \hat{b}_{\text{in}}(t), \quad (\text{A.5})$$

With correlation functions for the input noise

$$\langle \hat{b}_{\text{in}}^\dagger(t) \hat{b}_{\text{in}}(t') \rangle = n_b \delta(t - t'), \quad (\text{A.6})$$

$$\langle \hat{b}_{\text{in}}(t) \hat{b}_{\text{in}}^\dagger(t') \rangle = (n_b + 1) \delta(t - t'), \quad (\text{A.7})$$

where n_b is the occupancy of the thermal bath connected to the mechanical resonator. Inherent in the correlation functions above is the assumption that the mechanical resonance bandwidth is very small compared to its resonance frequency (high mechanical Q -factor), such that the bath occupation can be taken as a single number $n_b(\omega_m)$. Additionally, we find for the Fourier transform of the input noise operators,

$$\langle \hat{b}_{\text{in}}^\dagger(\omega) \hat{b}_{\text{in}}(\omega') \rangle = n_b \delta(\omega + \omega'), \quad (\text{A.8})$$

$$\langle \hat{b}_{\text{in}}(\omega) \hat{b}_{\text{in}}^\dagger(\omega') \rangle = (n_b + 1) \delta(\omega + \omega'). \quad (\text{A.9})$$

By solving the Fourier transform of equation (A.5), we find that the mechanical mode annihilation operator will be determined by the input noise as

$$\hat{b}(\omega) = \frac{-\sqrt{\gamma_i} \hat{b}_{\text{in}}(\omega)}{i(\omega_m - \omega) + \gamma_i/2}. \quad (\text{A.10})$$

This can easily be used to calculate the spectral density, and we find,

$$\begin{aligned}
S_{bb}(\omega) &= \int_{-\infty}^{\infty} d\tau e^{i\omega\tau} \langle \hat{b}^\dagger(\tau) \hat{b} \rangle \\
&= \int_{-\infty}^{\infty} d\tau e^{i\omega\tau} \frac{1}{2\pi} \int_{-\infty}^{\infty} d\omega'' \int_{-\infty}^{\infty} d\omega' \\
&\quad \times \langle (\hat{b}(\omega''))^\dagger \hat{b}(\omega') \rangle e^{i\omega''\tau} \\
&= \frac{\gamma_i \bar{n}}{(\omega_m + \omega)^2 + (\gamma_i/2)^2}.
\end{aligned} \tag{A.11}$$

We will sometimes denote this function as $S_{bb}(\omega; \bar{n})$. This spectra density can be thought to represent the ability of the mechanical system to *emit* energy. A similar expression can be found for the creation operators:

$$S_{b^\dagger b^\dagger}(\omega) = \frac{\gamma_i(\bar{n} + 1)}{(\omega_m - \omega)^2 + (\gamma_i/2)^2} \tag{A.12}$$

This spectra density can be thought to represent the ability of the mechanical system to *absorb* energy. Finally, for the position operator, $\hat{x} = x_{\text{zpf}}(\hat{b} + \hat{b}^\dagger)$, we find [36]

$$\begin{aligned}
S_{xx}(\omega) &= x_{\text{zpf}}^2 (S_{bb}(\omega) + S_{b^\dagger b^\dagger}(\omega)) \\
&= x_{\text{zpf}}^2 \left(\frac{\gamma_i \bar{n}}{(\omega_m + \omega)^2 + (\gamma_i/2)^2} + \frac{\gamma_i(\bar{n} + 1)}{(\omega_m - \omega)^2 + (\gamma_i/2)^2} \right).
\end{aligned}$$

A.3 Quantum noise squashing

Assuming perfect detection ($\kappa_e/2 = \kappa$) we find that the normalized heterodyne current is given by

$$\hat{I}(t) = -i\hat{a}_{\text{in}}(t) + i\hat{a}_{\text{in}}^\dagger(t) + \frac{2G}{\sqrt{\kappa}}(\hat{b}(t) + \hat{b}^\dagger(t)) \tag{A.13}$$

Taking the autocorrelation of the detected current,

$$\begin{aligned}
\langle \hat{I}(\tau) \hat{I} \rangle &= \langle \hat{a}_{\text{in}}(\tau) \hat{a}_{\text{in}}^\dagger \rangle + \frac{4|G|^2}{\kappa} \frac{\langle \hat{x}(\tau) \hat{x} \rangle}{x_{\text{zpf}}^2} - \\
&\quad \frac{2iG}{\kappa} \left(\langle \hat{a}_{\text{in}}(\tau) \hat{b}^\dagger \rangle - \langle \hat{b}(\tau) \hat{a}_{\text{in}}^\dagger \rangle \right)
\end{aligned} \tag{A.14}$$

we find $S_{II}(\omega)$ by taking the Fourier transform of the above expression. The first term, due to the fact that the noise is delta correlated gives a constant noise floor. The second term can be thought of as a measurement of position, and we see that the rate at which information is gathered about the system is $4|G|^2/\kappa$, i.e. the optomechanical damping rate, and back-action. The cross-correlation

terms are calculated as such:

$$\begin{aligned} & \int_{-\infty}^{\infty} d\tau e^{i\omega\tau} \langle \hat{a}_{\text{in}}(\tau) \hat{b}^\dagger \rangle = \\ & \frac{1}{2\pi} \int_{-\infty}^{\infty} d\tau e^{i\omega\tau} \int_{-\infty}^{\infty} d\omega' \int_{-\infty}^{\infty} d\omega'' e^{-i\omega'\tau} \langle \hat{a}_{\text{in}}(\omega') (\hat{b}(\omega''))^\dagger \rangle \end{aligned} \quad (\text{A.15})$$

Using the back-action modified mechanical fluctuation operator shown in equation (1.62),

$$\hat{b}(\omega) = \frac{-\sqrt{\gamma_i} \hat{b}_{\text{in}}(\omega)}{i(\omega_m - \omega) + \gamma/2} + \frac{2iG}{\sqrt{\kappa}} \frac{\hat{a}_{\text{in}}(\omega)}{i(\omega_m - \omega) + \gamma/2} \quad (\text{A.16})$$

and the properties of vacuum fluctuation operators, we find

$$\int_{-\infty}^{\infty} d\tau e^{i\omega\tau} \langle \hat{a}_{\text{in}}(\tau) \hat{b}^\dagger \rangle = -\frac{2iG}{\sqrt{\kappa}} \frac{1}{-i(\omega_m - \omega) + \gamma/2}, \quad (\text{A.17})$$

$$\int_{-\infty}^{\infty} d\tau e^{i\omega\tau} \langle \hat{b}(\tau) \hat{a}_{\text{in}}^\dagger \rangle = +\frac{2iG}{\sqrt{\kappa}} \frac{1}{i(\omega_m - \omega) + \gamma/2}. \quad (\text{A.18})$$

From here we calculate the spectral density of the heterodyne signal,

$$\begin{aligned} S_{II}(\omega) &= 1 + \\ & + \frac{4|G|^2}{\kappa} \left(\frac{\gamma \bar{n}}{(\omega_m + \omega)^2 + (\gamma/2)^2} + \frac{\gamma(\bar{n} + 1)}{(\omega_m - \omega)^2 + (\gamma/2)^2} \right) \\ & - \frac{4|G|^2}{\kappa} \frac{\gamma}{(\omega_m - \omega)^2 + (\gamma/2)^2} \\ & = 1 + \frac{8|G|^2}{\kappa} \bar{S}_{bb}(\omega). \end{aligned}$$

A.4 Scattering matrix elements

By algebraic manipulation of the Heisenberg equations of motion in Fourier domain, and an additional input-output boundary condition $\hat{a}_{\text{out}} = \hat{a}_{\text{in}} + \sqrt{\kappa_e/2} \hat{a}$, we arrive at scattering relations

$$\hat{a}_{\text{out}}(\omega)|_{\Delta=-\omega_m} \approx t(\omega; \Delta) \hat{a}_{\text{in}}(\omega) + n_{\text{opt}}(\omega; \Delta) \hat{a}_{\text{in},i}(\omega) + s_{12}(\omega; \Delta) \hat{b}_{\text{in}}^\dagger(\omega) \quad (\text{A.19})$$

and

$$\hat{a}_{\text{out}}(\omega)|_{\Delta=\omega_m} \approx t(\omega; \Delta) \hat{a}_{\text{in}}(\omega) + n_{\text{opt}}(\omega; \Delta) \hat{a}_{\text{in},i}(\omega) + s_{12}(\omega; \Delta) \hat{b}_{\text{in}}(\omega), \quad (\text{A.20})$$

for blue- and red-side laser pumping, respectively. In the driven weak coupling regime ($\gamma_{\text{OM}} \ll \kappa$), these scattering coefficients have simple algebraic forms which are presented below.

A.4.1 Red-side driving: $\Delta = \omega_m$

The red-side scattering matrix elements for values of ω about the mechanical frequency ($\omega - \omega_m \ll \kappa$) are:

$$t(\omega; \Delta = \omega_m) = 1 - \frac{\kappa_e}{\kappa} + \frac{|\gamma_{\text{OM}}| \kappa_e}{2\kappa} \frac{1}{i(\omega_m - \omega) + \gamma/2}, \quad (\text{A.21})$$

$$n_{\text{opt}}(\omega; \Delta = \omega_m) = \sqrt{\frac{2\kappa' \kappa_e}{\kappa^2}} \left(\frac{|\gamma_{\text{OM}}|/2}{i(\omega_m - \omega) + \gamma/2} - 1 \right), \quad (\text{A.22})$$

and

$$s_{12}(\omega; \Delta = \omega_m) = \sqrt{\frac{\kappa_e}{2\kappa}} \frac{i\sqrt{\gamma_i |\gamma_{\text{OM}}|}}{i(\omega_m - \omega) + \gamma/2} \quad (\text{A.23})$$

A.4.2 Blue-side driving: $\Delta = -\omega_m$

The blue-side scattering matrix elements for values of ω about the mechanical frequency ($\omega + \omega_m \ll \kappa$) are:

$$t(\omega; \Delta = -\omega_m) = 1 - \frac{\kappa_e}{\kappa} - \frac{|\gamma_{\text{OM}}| \kappa_e}{2\kappa} \frac{1}{-i(\omega_m + \omega) + \gamma/2} \quad (\text{A.24})$$

$$n_{\text{opt}}(\omega; \Delta = -\omega_m) = -\sqrt{\frac{2\kappa' \kappa_e}{\kappa^2}} \left(\frac{|\gamma_{\text{OM}}|/2}{-i(\omega_m + \omega) + \gamma/2} + 1 \right) \quad (\text{A.25})$$

$$s_{12}(\omega; \Delta = -\omega_m) = \sqrt{\frac{\kappa_e}{2\kappa}} \frac{i\sqrt{\gamma_i |\gamma_{\text{OM}}|}}{-i(\omega_m + \omega) + \gamma/2} \quad (\text{A.26})$$

Appendix B

Characterization of laser phase noise in semiconductor diode lasers

B.1 Laser phase noise measurement at megahertz frequencies

B.1.1 Homodyne measurement with laser noise

A homodyne measurement is designed to measure the spectral density of the fluctuations of the optical field exiting the cavity. However any real laser system will have technical noise, in addition to the quantum noise associated with an vacuum, which adds to the detected noise level. Both the signal and local oscillator arm of our setup contain this noise which must be taken into account. The noise on the signal arm can also be modified non-trivially by propagation through the optomechanical system. Laser phase and intensity noise have differing effects on the detected noise floor. In a measurement with a cavity, where the signal and local oscillator contain the same phase noise, phase noise cannot be detected. This is because the local oscillator phase sets the frame of reference where the signal phase is measured. Thus fluctuations in this frame of reference, if accompanied by the same fluctuations in the signal, will not be detected. In the case of an extra cavity in the signal path, an additional frequency reference is provided, thus phase noise will appear in the intensity quadrature of the signal detected with a noisy local oscillator.

B.1.1.1 Without optical cavity

We start by reproducing known results on the operation of an ideal, balanced homodyne detection system with signal and local oscillator input fields \hat{a}_s and \hat{a}_{LO} respectively, under the influence of noise [165–167]. Most generally, these fields consist of coherent tones α_s and α_{LO} , technical (or

classical) noise components $a_{s,N}(t)$ and $a_{LO,N}(t)$, and quantum fluctuations $\hat{a}_{s,vac}(t)$ and $\hat{a}_{LO,vac}(t)$:

$$\hat{a}_s = \alpha_s + a_{s,N}(t) + \hat{a}_{s,vac}(t), \quad (\text{B.1})$$

$$\hat{a}_{LO} = \alpha_{LO} + a_{LO,N}(t) + \hat{a}_{LO,vac}(t). \quad (\text{B.2})$$

Since both the local oscillator field and the signal field are generated by the same laser, the technical noise on the signal and local oscillator will be correlated, and these correlations must be accounted for in the analysis. For the simplest case, where the signal arm does not experience the complex dispersion from interaction with an optomechanical system (e.g. being reflected off the end-mirror far detuned from the optical resonator), we expect

$$a_{s,N}(t) = \alpha_s \xi(t) \quad \text{and} \quad a_{LO,N}(t) = \alpha_{LO} \xi(t). \quad (\text{B.3})$$

The function $\xi(t)$ is related to the intensity and phase fluctuations of the laser light ($n(t)$ and $\phi(t)$ respectively):

$$\begin{aligned} a(t) &= a_0(1 + n(t))e^{i\phi(t)} \approx a_0(1 + n(t) + i\phi(t)) \\ \xi(t) &= n(t) + i\phi(t) \end{aligned} \quad (\text{B.4})$$

The difference of the photocurrent in the homodyne detector is given by

$$\hat{I}(t) = \hat{a}_s \hat{a}_{LO}^\dagger + \hat{a}_s^\dagger \hat{a}_{LO}, \quad (\text{B.5})$$

which, considering only the technical noise, reduces to

$$\hat{I}(t) = |\alpha_{LO}| \hat{X}_\theta^{(s,vac)} + I_{DC}(1 + 2\text{Re}\{\xi(t)\}), \quad (\text{B.6})$$

under the assumption that $\alpha_{LO} \gg \alpha_s$, using the definitions in equation (B.3), and taking the DC current $I_{DC} = 2\text{Re}\{\alpha_s^* \alpha_{LO}\} = 2|\alpha_s \alpha_{LO}| \cos(\theta)$, where θ is the relative phase between the signal and local oscillator. From this equation we see that the phase noise $\phi(t)$ cannot be detected on a balanced homodyne setup. This can be understood as being from the detectors fundamental insensitivity to phase noise on the laser, as the only phase reference in the system is the local oscillator, which contains the same phase fluctuations as the signal. Secondly, for the local oscillator phase which makes $I_{DC} = 0$, intensity noise is not detected. In a real homodyne detector this is only true for a perfect common mode rejection ratio (CMRR), which is the case in our setup (see section 5.3) as the intensity noise is negligible and the CMRR is > 25 dB.

B.1.1.2 With optical cavity

Following the derivation in section 2.3.3 and taking the classical noise component of the field input to the cavity to be $a_{\text{in}}^{(\text{N})}(\omega) = i\alpha_{\text{in}}\phi(\omega)$ (with a corresponding LO phase noise of $a_{\text{LO}}^{(\text{N})}(\omega) = i\alpha_{\text{LO}}\phi(\omega)$), we arrive at an expression for the output noise due to input phase noise from the cavity:

$$a_{\text{out}}^{(\text{N})}(\omega) = i\alpha_{\text{in}}(1 + A_1(\omega) - A_2(\omega))\phi(\omega). \quad (\text{B.7})$$

Without optomechanical interaction ($G = 0$) we find $A_1(\omega) = -\kappa/(i(\Delta - \omega) + \kappa/2)$, and $A_2(\omega) = 0$. We calculate the expression for the current noise due to laser phase noise using this expression:

$$\begin{aligned} I^{(\text{N})}(\omega) &= \alpha_{\text{LO}}^* a_{\text{out}}^{(\text{N})}(\omega) + \alpha_{\text{LO}} [a_{\text{out}}^{(\text{N})}(-\omega)]^* \\ &\quad + \alpha_{\text{out}}^* a_{\text{LO}}^{(\text{N})}(\omega) + \alpha_{\text{out}} [a_{\text{LO}}^{(\text{N})}(-\omega)]^* \\ &= F(\omega)\phi(\omega) \end{aligned} \quad (\text{B.8})$$

with $F(\omega) = i|\alpha_{\text{LO}}\alpha_{\text{in}}|[e^{-i\theta}(r(\omega) - r(0)) + e^{i\theta}(r(-\omega) - r(0))^*]$. The PSD of the photocurrent due to phase noise is found to be

$$S_{II}^{(\text{N})}(\omega) = |F(\omega)|^2 S_{\phi\phi}(\omega). \quad (\text{B.9})$$

For a system with no dispersion, $r(\omega) = \text{const.}$, it can be easily shown that $F(\omega) = 0$ as expected. For an over-coupled cavity with no optomechanical coupling, $r(\omega) = 1 - \kappa/(i(\Delta - \omega) + \kappa/2)$, so $r(\omega) - r(0) \approx 4i\omega/\kappa$, and we have $F(\omega) = 8i|\alpha_{\text{LO}}\alpha_{\text{in}}|\sin(\theta)(\omega/\kappa)$. The ω dependence of $F(\omega)$ means that a flat frequency fluctuation spectrum ($S_{\phi\phi} \propto \omega^{-2}$, as we observe) adds a flat noise floor to the detected signal.

Finally we note that phase noise on the laser can drive the mechanical motion and cause heating. This effect is negligible when tuned near resonance, where only the intensity fluctuations affect the mechanics.

B.1.2 Measurement and characterization of laser noise

In this section we discuss the procedure used for characterization of our laser (New Focus TLB-6728-P-D). This characterization was done using an independent setup, a variant of what is shown in figure B.2, and involved two measurements directly detecting the light.

The first measurement is to characterize the intensity noise where the laser light is sent directly onto a photodetector with the incident power varied. From the theory we expect for the detector

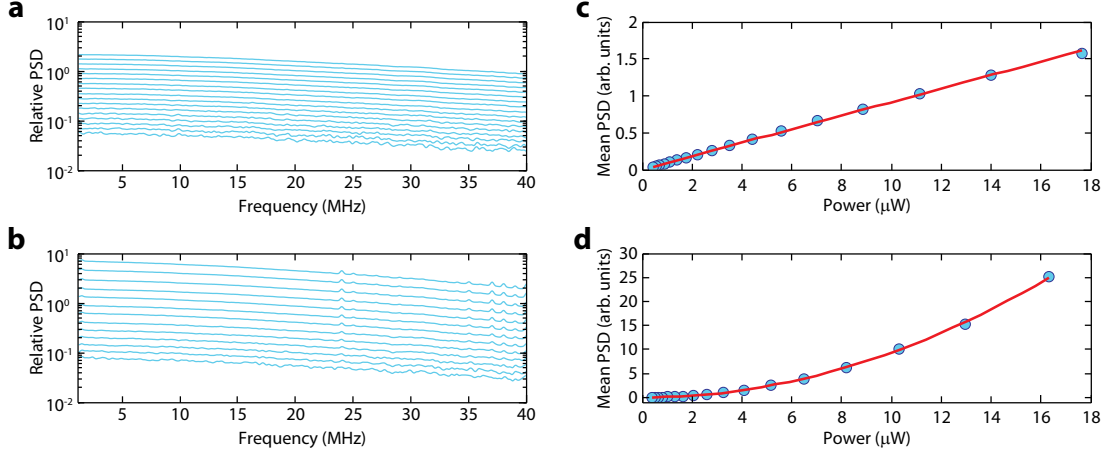


Figure B.1: **Laser noise characterization.** **a**, We measure the PSD of our laser for several powers, normalize to and then subtract it from the dark current of the detector. The same measurement is performed using a Mach-Zehnder interferometer locked at half of the fringe amplitude in order to convert any frequency noise to intensity noise to allow detection and is shown in **b**. **c**, Plot of the mean value of the PSD around the mechanical frequency ω_m from the measurement done in **a** as a function of power. The good linear fit (red line) indicates that no intensity noise is present. **d**, Mean PSD of the measurement in **b**. The quadratic fit (red line) shows that phase noise is indeed present (see text for more details).

photocurrent

$$\begin{aligned}
 I(t) &= (\alpha_{\text{LO}} + a_{\text{LO},N}(t) + \hat{a}_{\text{LO},\text{vac}}(t))^\dagger (\text{h.c.}) \\
 &= |\alpha_{\text{LO}}| \hat{X}_{\theta=0}^{(\text{LO},\text{vac})} + I_{\text{DC}} (1 + 2\text{Re}\{\xi(t)\}), \\
 \text{with } I_{\text{DC}} &= |\alpha_{\text{LO}}|^2.
 \end{aligned} \tag{B.10}$$

The spectral density of the current is then given by

$$S_{II}(\omega) = |\alpha_{\text{LO}}|^2 (1 + |\alpha_{\text{LO}}|^2 S_{nn}(\omega)), \tag{B.11}$$

where $S_{nn}(\omega)$ is the PSD of the intensity noise fluctuations. For a real detector, this equation is modified by the presence of a dark current $S_{\text{dark}}(\omega)$ and non-unity efficiency ($\eta_{\text{det}} < 1$):

$$S_{II}(\omega) = S_{\text{dark}}(\omega) + |\alpha_{\text{LO}}|^2 (1 + \eta_{\text{det}} |\alpha_{\text{LO}}|^2 S_{nn}(\omega)). \tag{B.12}$$

We subtract the dark current (measured with the laser turned off) from the data, and set bounds on the magnitude of the intensity noise present in the laser by examining the linear and quadratic dependence of the noise floor with respect to power. The linear component is due to shot-noise, while the quadratic variance is due to the intensity noise fluctuations (see equation (B.12)). The

results are shown in figure B.1a and c. The noise floor was seen to only increase linearly with laser power, confirming the absence of intensity noise at the frequencies of interest.

A second measurement is done to characterize the phase noise properties of the system. By sending the laser through a Mach-Zehnder interferometer (MZI) with transfer function $I(t) = I_0(1 + \sin(2\pi\omega/\omega_{\text{FSR}}))$, the intensity of the transmitted light will contain fluctuations related to the frequency fluctuations of the light (see figure B.1). The free spectral range (FSR) of the MZI is $\omega_{\text{FSR}}/2\pi = 115$ MHz. For a real detector, and assuming $\omega \ll \omega_{\text{FSR}}$, we arrive at

$$S_{II}(\omega) = S_{\text{dark}}(\omega) + |\alpha_{\text{LO}}|^2 \left(1 + \eta_{\text{det}} \frac{|\alpha_{\text{LO}}|^2}{\omega_{\text{FSR}}^2} S_{\phi\phi}(\omega) \right).$$

Some phase noise was detected, as shown in figure B.1b and d and the quadratic dependence of the PSD on signal power. The spectral densities show a roll-off due to the FSR of the MZI. It was found that in the frequency range of interest, $1 \text{ MHz} < \omega/2\pi < 40 \text{ MHz}$, the frequency noise spectral density, $S_{\omega\omega}(\omega) = \omega^2 S_{\phi\phi}(\omega)$, is flat, and roughly equal to $3 - 6 \times 10^3 \text{ rad}^2 \cdot \text{Hz}$, in agreement with previous characterization of the same lasers at higher frequencies [4], as presented below.

B.2 Laser phase noise measurement at gigahertz frequencies

The constraints of silicon nanofabricated devices, i.e. their single-mode nature, and their spread in parameters such as optical cavity frequency caused by fabrication imperfections, mean that wideband tunable external cavity diode lasers (ECDL) are invaluable for experiments in optomechanics with mechanical systems operating in the GHz range. As such, they have been used extensively by our group as well as others [118, 168–170]. Phase and frequency noise at higher frequencies have been of concern in these types of lasers, and it is therefore important to evaluate the laser noise properties.

Here we present a measurement of $S_{EE}(\omega)$ based on a measurement of the phase noise spectral density $S_{\phi\phi}(\omega)$ and relation (2.36). A Mach-Zehnder interferometer (MZI) is an optical component where the detected intensity of the transmitted light is dependent on the frequency of the light, and given by $T(\omega) = 1 + \sin(\omega/\omega_{\text{FSR}})$, where ω_{FSR} is the free spectral range of the interferometer (20.1 GHz in our case). For the moment, we linearize this relation as, $T(\omega) = 1 + \omega/\omega_{\text{FSR}}$ (the full relation is used for the presented data). Assuming that the laser frequency $\omega_L = \omega_L(t)$, is a stochastic process representing the instantaneous frequency of the laser light, the detected intensity will be given by $I(t) = \dot{N} + \dot{N}\omega_L(t)/\omega_{\text{FSR}} + n_{\text{SN}}(t)$. The term \dot{N} is the average flux of photons incident on the detector, while the last term $n_{\text{SN}}(t)$, is the white shot-noise of the laser with amplitude proportional to $\dot{N}^{1/2}$. The spectral density of the detected signal is then given by,

$$S_{II}(\omega) = \dot{N} + \frac{\dot{N}^2}{\omega_{\text{FSR}}^2} \bar{S}_{\omega\omega}(\omega). \quad (\text{B.13})$$

Therefore, using the shot noise as a reference level, we can define a signal-to-noise ratio as,

$$\text{SNR} = \frac{\dot{N}}{\omega_{\text{FSR}}^2} \bar{S}_{\omega\omega}(\omega), \quad (\text{B.14})$$

where the “signal” is the classical laser frequency noise and the “noise” is shot-noise. This shot-noise based calibration method can be performed by a set-up such as the one shown in Figure 5.5b. Such measurement of shot-noise however depends on knowledge of the detector quantum efficiency.

An alternate calibration method, free of any need to measure absolute powers and detector efficiencies, or to model the optical component transducing the phase noise (here the MZI), is shown schematically in Figure 5.5a. A phase modulator is used to generate a tone with a large modulation index β at the frequency of interest. This unitless modulation index is directly obtained by measuring the power of the generated sidebands, using a scanning Fabry-Pérot filter in our case. These powers are related to each other by the appropriate Bessel function with argument β . Measuring the tone passing through the MZI provides us with a calibration of $\bar{S}_{\omega\omega}(\omega)$.

Both methods give nominally the same results for the calibration of laser frequency noise, which we plot in Fig. B.3a-c for three different New Focus Velocity series external-cavity semiconductor diode lasers used in the work presented here and in recent cavity-optomechanical experiments with GHz-frequency OMCs [3, 46]. In these plots, the detector noise at zero input power (Noise Equivalent Power (NEP)) and the laser shot noise, are subtracted from raw measured noise spectra. Spectra showing the raw data at various stages of the processing are shown in Fig. B.4.

B.2.1 Phase noise calibration

Here we describe the phase noise calibration method (with the setup shown in Fig. 5.5a) used to characterize the lasers. An electro-optic phase modulator is used to generate sidebands on the optical laser signal at ω_L , by creating a phase modulation of

$$\phi(t) = \beta \cos(\omega_c t). \quad (\text{B.15})$$

The ratio of the power between the carrier at ω_L and the first order sideband is given by

$$\frac{P_1}{P_0} = \left| \frac{J_1(\beta)}{J_0(\beta)} \right|^2. \quad (\text{B.16})$$

Using a scanning Fabry-Pérot filter with a bandwidth much smaller than ω_c , we select out each sideband individually, and measure the powers $P_{0,1}$ in the carrier and sidebands to obtain a value for β .

The frequency noise spectrum for a known modulation $\phi(t)$ can be calculated from the Fourier transform of the autocorrelation function $\langle \dot{\phi}(t)\dot{\phi}(t + \tau) \rangle$. For the case of sinusoidal phase modulation

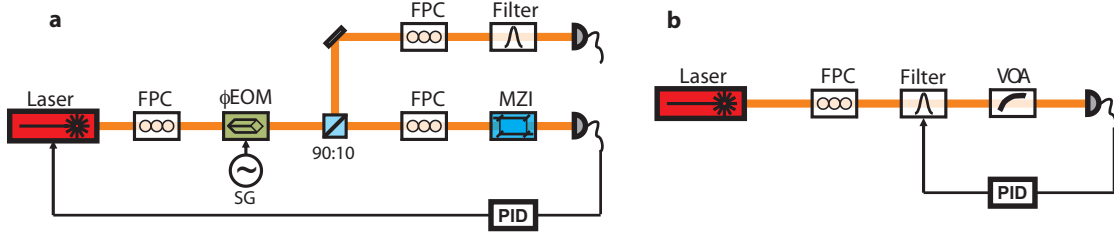


Figure B.2: **High-frequency phase noise measurement setup.** **a** The experimental setup used for measurement and calibration of laser phase noise. Light from the laser under test is sent into an electro-optical phase modulator (ϕ EOM), generating a pure phase modulation which is used to calibrate the system response. Most of the light is then taken from the 90% end of a beam splitter, and sent through an all-fiber imbalanced ($\Delta L \sim 2$ cm) Mach-Zehnder interferometer (MZI), with a free spectral range of 20.1 GHz (measured using calibrated Toptica wavemeter). The MZI converts frequency fluctuations into intensity fluctuations, which are detected on a high speed photodetector (New Focus 1544-B). The DC output of the photodetector is used to perform a low-frequency lock of the laser frequency to the mid-point of the MZI sinusoidal transfer function. The 10% split-off signal is sent through a scannable optical filter (bandwidth 50MHz), which allows one to independently measure the modulation index of the phase modulated calibration tone by sweeping the filter across the carrier and sidebands, comparing their optical power. Fiber polarization controllers (FPCs) are used to adjust the optical field polarization. **b** For an alternate calibration of the laser phase noise, the shot noise level of the detected laser signal is measured. This is accomplished by sending the laser through a narrow optical filter (50 MHz bandwidth), followed by a variable optical attenuator (VOA), to obtain the shot noise level of the photodetected signal at GHz frequencies. The optical filter is used to remove classical laser noise at these frequencies.

we have $\langle \dot{\phi}(t)\dot{\phi}(t+\tau) \rangle = \omega^2 \beta^2 \cos(\omega_c \tau)/2$, with a corresponding frequency noise power spectral density of (in units of rad^2Hz),

$$\bar{S}_{\omega\omega}^{\text{cal}}(\omega) = \frac{\pi\omega^2\beta^2}{2} (\delta(\omega - \omega_c) + \delta(\omega + \omega_c)). \quad (\text{B.17})$$

By comparing the raw measured noise of the laser frequency noise ($S_{\text{meas}}(\omega)$) to that of the raw measured noise in the calibration signal peak ($S_{\text{meas}}^{\text{cal}}(\omega)$), one can calibrate the measured laser frequency noise in units of rad^2Hz . Specifically, we have that $A(\omega_c) \int_{\omega_c - \Delta\omega}^{\omega_c + \Delta\omega} S_{\text{meas}}^{\text{cal}}(\omega) d\omega = \pi\omega^2\beta^2/2$, where $A(\omega_c)$ is the conversion coefficient (at frequency ω_c) between measured electrical noise power density and (symmetrized) frequency noise power density for our experimental apparatus. The corresponding laser frequency noise at ω_c can then be related to the measured electrical noise and the noise power in the phase modulation calibration tone as,

$$\bar{S}_{\omega\omega}(\omega_c) = \frac{\pi\omega_c^2\beta^2}{2} \frac{S_{\text{meas}}(\omega_c)}{\int_{\omega_c - \Delta\omega}^{\omega_c + \Delta\omega} S_{\text{meas}}^{\text{cal}}(\omega) d\omega}. \quad (\text{B.18})$$

In order to generate the calibrated laser frequency noise spectra of Fig. B.3 we measured the conversion coefficient, $A(\omega_c)$, at ~ 50 MHz intervals across the entire frequency span of the measurement.

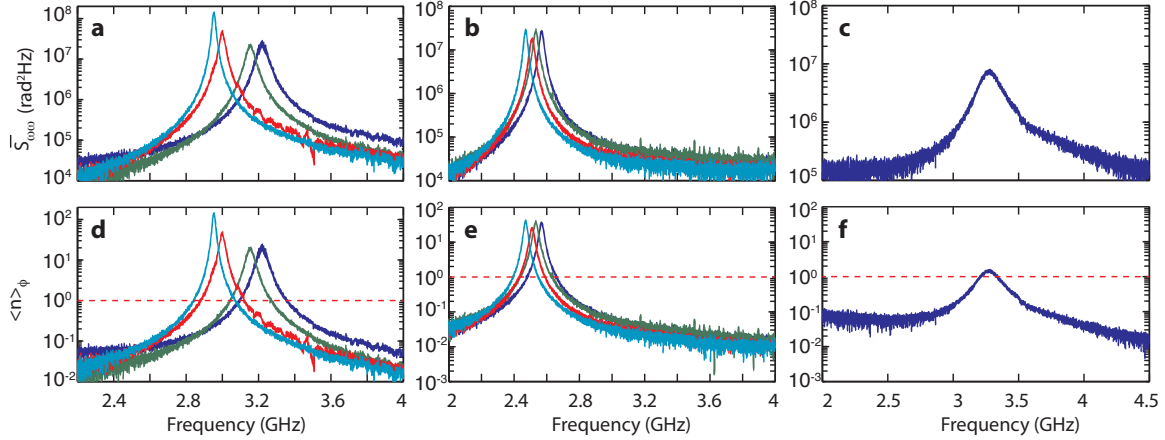


Figure B.3: **High-frequency phase noise measurements.** **a**, **b** and **c** are the calibrated frequency noise $\bar{S}_{\omega\omega}$ for Lasers 1 (Model 6328, Serial #286), 2 (Model 6728), and 3 (Model 6326, Serial #19), respectively. In **a**, **b** the different color curves are for measurements made at different laser wavelengths, with $\{\text{blue, green, red, cyan}\}$ corresponding to $\lambda = \{1520, 1537, 1550, 1570\}$ nm, respectively. Laser 3 is a 1400nm band laser which was only operated at $\lambda = 1460$ nm. The plots shown in **d**, **e** show the corresponding level of laser phase noise heating (\bar{n}_ϕ) in units of phonons for the device parameters and maximum cooling laser power ($n_c = 2000$ intra-cavity cooling beam photons, $\kappa_c/2\pi = 65$ MHz, $\kappa/2\pi = 488$ MHz, $\omega_m/2\pi = 3.68$ GHz) of Ref. [46]. In **f** we show the same for the device parameters and maximum cooling beam power ($n_c = 330$, $\kappa_c/2\pi = 45$ MHz, $\kappa/2\pi = 300$ MHz, $\omega_m/2\pi = 3.99$ GHz) of Ref. [3].

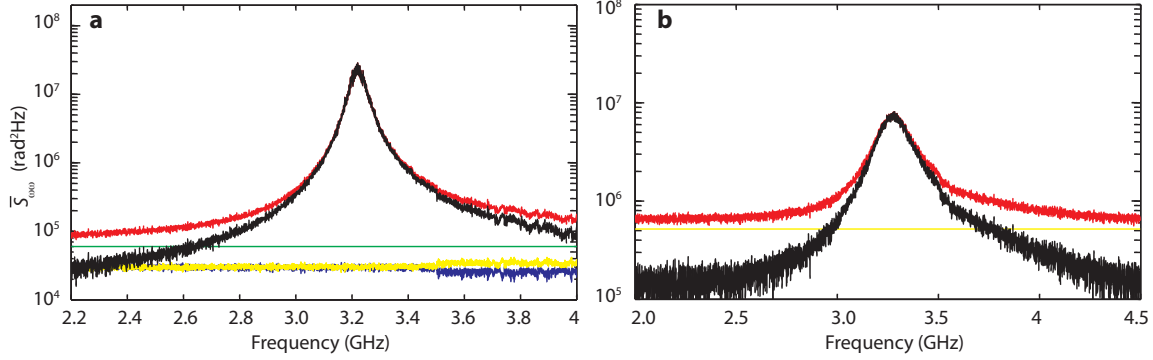


Figure B.4: **Contributions to measured frequency noise results.** **a**, Measured total noise spectrum (red curve), along with the shot noise (blue curve) and detector NEP (yellow curve), used to generate the laser frequency noise spectrum of Fig. B.3a (only 1520 nm wavelength shown). The detector NEP is measured by simply blocking the laser (zero optical power) and measuring the noise spectrum (note that the detector NEP is well above the intrinsic noise level of the spectrum analyzer). The shot-noise is measured independently for an identical laser power and wavelength using the set-up of Fig. 5.5b. The green line corresponding to the sum of average NEP and shot noise levels. The black curve is the measured signal with the shot noise and NEP background levels subtracted, and represents the component of the measured noise which we attribute to laser frequency noise in Fig. B.3a. **b**, Measured total noise spectrum (red curve) and detector NEP (yellow curve) used to generate the laser frequency noise spectrum of Fig. B.3c. The shot-noise level (not shown) for this measurement is far below the NEP level. The black curve is the measured signal with the NEP subtracted, and is the resulting laser frequency noise spectrum plotted in Fig. B.3c.

Appendix C

Definitions

C.1 Acronyms

EIT Electromagnetically Induced Transparency

NEP Noise Equivalent Power

RPSN Radiation Pressure Shot-Noise

FEM Finite-Element Method

PSD Power Spectral Density

CROW Coupled Resonator Optical Waveguide

OMC Optomechanical Crystal

EIA Electromagnetically Induced Absorption

Appendix D

Publications

Papers where the author has made a major contribution:

1. A. H. Safavi-Naeini, S. Groeblacher, J. T. Hill, J. Chan, M. Aspelmeyer, and O. Painter, “Squeezing of light via reflection from a silicon micromechanical resonator,” *arXiv:1302.6179* (2013).
2. A. H. Safavi-Naeini, J. Chan, J. T. Hill, S. Groeblacher, H. Miao, Y. Chen, M. Aspelmeyer, and O. Painter, “Laser noise in cavity-optomechanical cooling and thermometry,” *New Journal of Physics* **15**, 035007– (2013).
3. J. T. Hill, A. H. Safavi-Naeini, J. Chan, and O. Painter, “Coherent optical wavelength conversion via cavity optomechanics,” *Nature communications* **3**, 1196 (2012).
4. J. Chan, A. H. Safavi-Naeini, J. T. Hill, S. Meenehan, and O. Painter, “Optimized optomechanical crystal cavity with acoustic radiation shield,” *App. Phys. Lett.* **101**, 081115 (2012).
5. A. H. Safavi-Naeini, J. Chan, J. T. Hill, T. P. M. Alegre, A. Krause, and O. Painter, “Observation of quantum motion of a nanomechanical resonator,” *Phys. Rev. Lett.* **108**, 033602– (2012).
6. J. Chan, T. P. M. Alegre, A. H. Safavi-Naeini, J. T. Hill, A. Krause, S. Gröblacher, M. Aspelmeyer, and O. Painter, “Laser cooling of a nanomechanical oscillator into its quantum ground state,” *Nature* **478**, 89–92 (2011).

7. A. H. Safavi-Naeini, J. Chan, M. Eichenfield, Q. Lin, J. T. Hill, D. Chang, and O. Painter, “Electromagnetically induced transparency and slow light with optomechanics,” *Nature* **472**, 69–73 (2011).
8. T. P. M. Alegre, A. H. Safavi-Naeini, M. Winger, and O. Painter, “Quasi-two-dimensional optomechanical crystals with a complete phononic bandgap,” *Opt. Express* **19**, 5658-5669 (2011).
9. D. Chang, A. H. Safavi-Naeini, Mohammad Hafezi and O. Painter, “Slowing and stopping light using an optomechanical crystal array,” *New J. Phys.* **13**, 023003 (2011).
10. A. H. Safavi-Naeini and O. Painter, “Proposal for an Optomechanical Traveling Wave Phonon-Photon Translator,” *New J. Phys.* **13**, 013017 (2011).
11. A. H. Safavi-Naeini, T. P. M. Alegre, M. Winger, and O. Painter, “Optomechanics in an ultrahigh-Q slotted 2D photonic crystal cavity,” *Appl. Phys. Lett.* **97**, 181106 (2010).
12. A. H. Safavi-Naeini and O. Painter, “Design of Optomechanical Cavities and Waveguides on a Simultaneous Bandgap Phononic-Photonic Crystal Slab,” *Opt. Express* **18**, 14926-14943 (2010).

Other results where the author has contributed:

1. F. Y. Khalili, H. Miao, H. Yang, A. H. Safavi-Naeini, O. Painter, and Y. Chen, “Quantum back-action in measurements of zero-point mechanical oscillations,” *Physical Review A* **86**, 033840 (2012).
2. M. Davanco, J. Chan, A. H. Safavi-Naeini, O. Painter, and K. Srinivasan, “Slot-mode-coupled optomechanical crystals,” *Optics Express* **20**, 24394–24410 (2012).
3. M. Ludwig, A. H. Safavi-Naeini, O. Painter, and F. Marquardt, “Enhanced Quantum Nonlinearities in a Two-Mode Optomechanical System,” *Physical Review Letters* **109**, 063601 (2012).

4. M. Winger, T. Blasius, T. P. M. Alegre, A. H. Safavi-Naeini, S. Meenehan, J. Cohen, S. Stobbe, and O. Painter, “A chip-scale integrated cavity-electro-optomechanics platform,” *Opt. Express* **19**, 24905-24921 (2011).
5. R. Perahia, T. P. M. Alegre, A. H. Safavi-Naeini, and O. Painter, “Surface-plasmon mode hybridization in sub-wavelength microdisk lasers,” *Appl. Phys. Lett.* **95**, 201114 (2009).
6. M. Eichenfield, J. Chan, A. H. Safavi-Naeini, K. J. Vahala, and O. Painter, “Modeling dispersive coupling and losses of localized optical and mechanical modes in optomechanical crystals,” *Opt. Express* **17**, 20078–20098 (2009).

Bibliography

- [1] A. H. Safavi-Naeini, T. P. M. Alegre, M. Winger, and O. Painter, “Optomechanics in an ultrahigh-Q slotted 2D photonic crystal cavity,” *Appl. Phys. Lett.* **97**, 181106 (2010).
- [2] A. H. Safavi-Naeini, T. P. M. Alegre, J. Chan, M. Eichenfield, M. Winger, Q. Lin, J. T. Hill, D. Chang, and O. Painter, “Electromagnetically induced transparency and slow light with optomechanics,” *Nature* **472**, 69–73 (2011).
- [3] A. H. Safavi-Naeini, J. Chan, J. T. Hill, T. P. M. Alegre, A. Krause, and O. Painter, “Observation of Quantum Motion of a Nanomechanical Resonator,” *Phys. Rev. Lett.* **108**, 033602 (2012).
- [4] A. H. Safavi-Naeini, J. Chan, J. T. Hill, S. Groeblacher, H. Miao, Y. Chen, M. Aspelmeyer, and O. Painter, “Laser noise in cavity-optomechanical cooling and thermometry,” *New J. Phys.* **15**, 035007– (2013).
- [5] A. H. Safavi-Naeini and O. Painter, “Proposal for an optomechanical traveling wave phonon-photon translator,” *New J. Phys.* **13**, 013017 (2011).
- [6] J. T. Hill, A. H. Safavi-Naeini, J. Chan, and O. Painter, “Coherent optical wavelength conversion via cavity optomechanics,” *Nature communications* **3**, 1196 (2012).
- [7] D. Chang, A. H. Safavi-Naeini, M. Hafezi, and O. Painter, “Slowing and stopping light using an optomechanical crystal array,” *New J. Phys.* **13**, 023003 (2011).
- [8] P. Rabl, “The photon blockade effect in optomechanical systems,” *arXiv:1102.0278* (2011).
- [9] A. Nunnenkamp, K. Borkje, and S. Girvin, “Single-photon optomechanics,” *Phys. Rev. Lett.* **107**, 63602 (2011).
- [10] M. J. Collett and C. W. Gardiner, “Squeezing of intracavity and traveling-wave light fields produced in parametric amplification,” *Phys. Rev. A* **30**, 1386–1391 (1984).
- [11] C. W. Gardiner and M. J. Collett, “Input and output in damped quantum systems: Quantum stochastic differential equations and the master equation,” *Phys. Rev. A* **31**, 3761–3774 (1985).

- [12] A. D. O’Connell, M. Hofheinz, M. Ansmann, R. C. Bialczak, M. Lenander, E. Lucero, M. Neeley, D. Sank, H. Wang, M. Weides, J. Wenner, J. M. Martinis, and A. N. Cleland, “Quantum ground state and single-phonon control of a mechanical resonator,” *Nature* **464**, 697–703 (2010).
- [13] J. V. Bladel, *Electromagnetic Fields, 2ed* (IEEE Press. Wiley-Interscience, 2007).
- [14] *COMSOL Multiphysics 3.5* (2009).
- [15] S. Haroche and J.-M. Raimond, *Exploring the Quantum: Atoms, Cavities, and Photons* (Oxford University Press, 2006).
- [16] C. Kittel, *Introduction to Solid State Physics* (John Wiley, 2005).
- [17] A. R. Cowan and J. F. Young, “Optical bistability involving photonic crystal microcavities and Fano line shapes,” *Phys. Rev. E* **68**, 046606– (2003).
- [18] S. Hughes and H. Kamada, “Single-quantum-dot strong coupling in a semiconductor photonic crystal nanocavity side coupled to a waveguide,” *Phys. Rev. B* **70**, 195313– (2004).
- [19] M. Wubs, L. G. Suttorp, and A. Lagendijk, “Multiple-scattering approach to interatomic interactions and superradiance in inhomogeneous dielectrics,” *Phys. Rev. A* **70**, 053823– (2004).
- [20] J. Joannopoulos, S. Johnson, J. Winn, and R. Meade, *Photonic Crystals: Molding the Flow of Light*, Princeton University Press (2008).
- [21] S. G. Johnson, M. Ibanescu, M. A. Skorobogatiy, O. Weisberg, J. D. Joannopoulos, and Y. Fink, “Perturbation theory for Maxwell’s equations with shifting material boundaries,” *Phys. Rev. E* **65**, 066611– (2002).
- [22] C. Cohen-Tannoudji, J. Dupont-Roc, and G. Grynberg, *Atom-Photon Interactions: Basic Processes and Applications* (Wiley-Interscience, 1992).
- [23] M. Eichenfield, J. Chan, A. H. Safavi-Naeini, K. J. Vahala, and O. Painter, “Modeling dispersive coupling and losses of localized optical and mechanical modes in optomechanical crystals,” *Opt. Express* **17**, 20078–20098 (2009).
- [24] J. Chan, A. H. Safavi-Naeini, J. T. Hill, S. Meenehan, and O. Painter, “Optimized optomechanical crystal cavity with acoustic radiation shield,” *App. Phys. Lett.* **101**, 081115 (2012).
- [25] A. Yariv and P. Yeh, *Optical waves in crystals*, Vol. 5 (Wiley New York, 1984).
- [26] C. W. Gardiner and P. Zoller, *Quantum Noise, 3rd ed.* (Springer, 2004).
- [27] D. M. Pozar, *Microwave Engineering, 3ed* (Wiley, 2004).

- [28] H. A. Haus, *Waves and Fields in Optoelectronics* (Prentice-Hall, Inc., 1984).
- [29] H. Haus and Y. Lai, “Narrow-band optical channel-dropping filter,” *Lightwave Technology, Journal of* **10**, 57–62 (1992).
- [30] B. Little, S. Chu, H. Haus, J. Foresi, and J.-P. Laine, “Microring resonator channel dropping filters,” *Lightwave Technology, Journal of* **15**, 998–1005 (1997).
- [31] C. Manolatou, M. Khan, S. Fan, P. Villeneuve, H. Haus, and J. Joannopoulos, “Coupling of modes analysis of resonant channel add-drop filters,” *Quantum Electronics, IEEE Journal of* **35**, 1322–1331 (1999).
- [32] P. E. Barclay, K. Srinivasan, and O. Painter, “Design of photonic crystal waveguides for evanescent coupling to optical fiber tapers and integration with high-Q cavities,” *J. Opt. Soc. Am. B* **20**, 2274–2284 (2003).
- [33] S. M. Spillane, T. J. Kippenberg, O. J. Painter, and K. J. Vahala, “Ideality in a Fiber-Taper-Coupled Microresonator System for Application to Cavity Quantum Electrodynamics,” *Phys. Rev. Lett.* **91**, 043902– (2003).
- [34] P. Barclay, K. Srinivasan, and O. Painter, “Nonlinear response of silicon photonic crystal microresonators excited via an integrated waveguide and fiber taper,” *Opt. Express* **13**, 801–820 (2005).
- [35] M. Ludwig, B. Kubala, and F. Marquardt, “The optomechanical instability in the quantum regime,” *New J. Phys.* **10**, 23 (2008).
- [36] A. A. Clerk, M. H. Devoret, S. M. Girvin, F. Marquardt, and R. J. Schoelkopf, “Introduction to quantum noise, measurement, and amplification,” *Rev. Mod. Phys.* **82**, 1155–1208 (2010).
- [37] I. Wilson-Rae, N. Nooshi, W. Zwerger, and T. J. Kippenberg, “Theory of ground state cooling of a mechanical oscillator using dynamical back-action,” *Phys. Rev. Lett.* **99**, 093901 (2007).
- [38] I. Wilson-Rae, N. Nooshi, J. Dobrindt, T. J. Kippenberg, and W. Zwerger, “Cavity-assisted backaction cooling of mechanical resonators,” *New J. Phys.* **10**, 095007 (2008).
- [39] F. Marquardt, J. P. Chen, A. A. Clerk, and S. M. Girvin, “Quantum Theory of Cavity-Assisted Sideband Cooling of Mechanical Motion,” *Phys. Rev. Lett.* **99**, 093902 (2007).
- [40] A. H. Safavi-Naeini, S. Groeblacher, J. T. Hill, J. Chan, M. Aspelmeyer, and O. Painter, “Squeezing of light via reflection from a silicon micromechanical resonator,” *arXiv:1302.6179* (2013).

- [41] F. Y. Khalili, H. Miao, H. Yang, A. H. Safavi-Naeini, O. Painter, and Y. Chen, “Quantum back-action in measurements of zero-point mechanical oscillations,” *Phys. Rev. A* **86**, 033840 (2012).
- [42] F. Massel, T. T. Heikkilä, J.-M. Pirkkalainen, S. U. Cho, H. Saloniemi, P. J. Hakonen, and M. A. Sillanpää, “Microwave amplification with nanomechanical resonators,” *Nature* **480**, 351–354 (2011).
- [43] F. Hocke, X. Zhou, A. Schliesser, T. J. Kippenberg, H. Huebl, and R. Gross, “Electromechanically induced absorption in a circuit nano-electromechanical system,” *New J. Phys* **14**, 123037– (2012).
- [44] A. Schliesser, P. Del’Haye, N. Nooshi, K. J. Vahala, and T. J. Kippenberg, “Radiation Pressure Cooling of a Micromechanical Oscillator Using Dynamical Backaction,” *Phys. Rev. Lett.* **97**, 243905 (2006).
- [45] Y.-S. Park and H. Wang, “Resolved-sideband and cryogenic cooling of an optomechanical resonator,” *Nature Phys.* **5**, 489–493 (2009).
- [46] J. Chan, T. P. M. Alegre, A. H. Safavi-Naeini, J. T. Hill, A. Krause, S. Gröblacher, M. Aspelmeyer, and O. Painter, “Laser cooling of a nanomechanical oscillator into its quantum ground state,” *Nature* **478**, 89–92 (2011).
- [47] C. Fabre, M. Pinard, S. Bourzeix, A. Heidmann, E. Giacobino, and S. Reynaud, “Quantum-noise reduction using a cavity with a movable mirror,” *Phys. Rev. A* **49**, 1337–1343 (1994).
- [48] K. Borkje, A. Nunnenkamp, B. M. Zwickl, C. Yang, J. G. E. Harris, and S. M. Girvin, “Observability of radiation-pressure shot noise in optomechanical systems,” *Phys. Rev. A* **82**, 013818– (2010).
- [49] T. P. Purdy, R. W. Peterson, and C. A. Regal, “Observation of Radiation Pressure Shot Noise on a Macroscopic Object,” *Science* **339**, 801–804 (2013).
- [50] A. Schliesser, O. Arcizet, R. Rivière, G. Anetsberger, and T. J. Kippenberg, “Resolved-sideband cooling and position measurement of a micromechanical oscillator close to the Heisenberg uncertainty limit,” *Nature Phys.* **5**, 509–514 (2009).
- [51] S. Gröblacher, J. B. Hertzberg, M. R. Vanner, S. Gigan, K. C. Schwab, and M. Aspelmeyer, “Demonstration of an ultracold micro-optomechanical oscillator in a cryogenic cavity,” *Nature Phys.* **5**, 485–488 (2009).

- [52] F. Marquardt, J. G. E. Harris, and S. M. Girvin, “Dynamical Multistability Induced by Radiation Pressure in High-Finesse Micromechanical Optical Cavities,” *Phys. Rev. Lett.* **96**, 103901 (2006).
- [53] T. Botter, D. W. C. Brooks, N. Brahms, S. Schreppler, and D. M. Stamper-Kurn, “Linear amplifier model for optomechanical systems,” *Phys. Rev. A* **85**, 013812– (2012).
- [54] A. A. Clerk, F. Marquardt, and K. Jacobs, “Back-action evasion and squeezing of a mechanical resonator using a cavity detector,” *New Journal of Physics* **10**, 095010 (2008).
<http://www.citebase.org/abstract?id=oai:arXiv.org:0802.1842>
- [55] T. Rocheleau, T. Ndukum, C. Macklin, J. B. Hertzberg, A. A. Clerk, and K. C. Schwab, “Preparation and detection of a mechanical resonator near the ground state of motion,” *Nature* **463**, 72–75 (2010).
- [56] T. Kippenberg, A. Schliesser, and M. Gorodetsky, “Phase noise measurement of external cavity diode lasers and implications for optomechanical sideband cooling of GHz mechanical modes,” *arXiv:1112.6277* (2011).
- [57] P. Rabl, C. Genes, K. Hammerer, and M. Aspelmeyer, “Phase-noise induced limitations on cooling and coherent evolution in optomechanical systems,” *Phys. Rev. A* **80**, 063819 (2009).
- [58] G. A. Phelps and P. Meystre, “Laser phase noise effects on the dynamics of optomechanical resonators,” *Phys. Rev. A* **83**, 063838– (2011).
- [59] M. Abdi, S. Barzanjeh, P. Tombesi, and D. Vitali, “Effect of phase noise on the generation of stationary entanglement in cavity optomechanics,” *Phys. Rev. A* **84**, 032325– (2011).
- [60] R. Ghobadi, A. R. Bahrapour, and C. Simon, “Optomechanical Entanglement in the Presence of Laser Phase Noise,” (2011).
- [61] D. Meschede, *Optics, Light and Lasers* (Wiley-VCH, 2004).
- [62] M. Poggio, C. L. Degen, H. J. Mamin, and D. Rugar, “Feedback cooling of a cantilever’s fundamental mode below 5 mK,” *Phys. Rev. Lett.* **99**, 017201 (2007).
- [63] G. S. Agarwal and S. Huang, “Electromagnetically induced transparency in mechanical effects of light,” *Phys. Rev. A* **81**, 041803– (2010).
- [64] S. Weis, R. Rivière, S. Deléglise, E. Gavartin, O. Arcizet, A. Schliesser, and T. J. Kippenberg, “Optomechanically Induced Transparency,” *Science* **330**, 1520–1523 (2010).
- [65] J. D. Teufel, D. Li, M. S. Allman, K. Cicak, A. J. Sirois, J. D. Whittaker, and R. W. Simmonds, “Circuit cavity electromechanics in the strong-coupling regime,” *Nature* **471**, 204–208 (2011).

- [66] P. R. Saulson, “Thermal noise in mechanical experiments,” *Phys. Rev. D* **42**, 2437 (1990).
- [67] A. Gillespie and F. Raab, “Thermal noise in the test mass suspensions of a laser interferometer gravitational-wave detector prototype,” *Phys. Lett. A* **178**, 357–363 (1993).
- [68] A. Heidmann, Y. Hadjar, and M. Pinard, “Quantum nondemolition measurement by optomechanical coupling,” *Appl. Phys. B* **64**, 173–180 (1997).
- [69] P. Verlot, A. Tavernarakis, T. Briant, P.-F. Cohadon, and A. Heidmann, “Scheme to Probe Optomechanical Correlations between Two Optical Beams Down to the Quantum Level,” *Phys. Rev. Lett.* **102**, 103601 (2009).
- [70] A. Jayich, J. Sankey, K. Borkje, D. Lee, C. Yang, M. Underwood, L. Childress, A. Petrenko, S. Girvin, and J. Harris, “Cryogenic Optomechanics with a Si₃N₄ Membrane and Classical Laser Noise,” *arXiv:1209.2730* (2012).
- [71] B.-S. Song, S. Noda, T. Asano, and Y. Akahane, “Ultra-high-Q photonic double-heterostructure nanocavity,” *Nat Mater* **4**, 207–210 (2005).
<http://dx.doi.org/10.1038/nmat1320>
- [72] P. B. Deotare, M. W. McCutcheon, I. W. Frank, M. Khan, and M. Loncar, “High quality factor photonic crystal nanobeam cavities,” *Appl. Phys. Lett.* *Phys. Lett.* **94**, 121106–121106–3 (2009).
- [73] S. Mohammadi, A. Eftekhar, and A. Adibi, “Large simultaneous band gaps for photonic and phononic crystal slabs,” in *Conference on Lasers and Electro-Optics* (2008).
- [74] S. Mohammadi, A. Eftekhar, A. Khelif, and A. Adibi, “Simultaneous two-dimensional phononic and photonic band gaps in opto-mechanical crystal slabs,” *Opt. Express* **18**, 9164–9172 (2010).
- [75] S. Nemat-Nasser and M. Hori, *Micromechanics: overall properties of heterogeneous materials*, Vol. 2 (Elsevier Amsterdam, 1999).
- [76] S. G. Johnson and J. D. Joannopoulos, “Block-iterative frequency-domain methods for Maxwell’s equations in a planewave basis,” *Opt. Express* **8**, 173–190 (2001).
- [77] A. H. Safavi-Naeini and O. Painter, “Design of Optomechanical Cavities and Waveguides on a Simultaneous Bandgap Phononic-Photonic Crystal Slab,” *1003.5265* (2010).
- [78] A. Chutinan and S. Noda, “Waveguides and waveguide bends in two-dimensional photonic crystal slabs,” *Phys. Rev. B* **82**, 4488–4492 (2000).

- [79] S. G. Johnson, P. R. Villeneuve, S. Fan, and J. D. Joannopoulos, “Linear waveguides in photonic-crystal slabs,” *Phys. Rev. B* **62**, 8212–8222 (2000).
- [80] E. Kuramochi, M. Notomi, S. Mitsugi, A. Shinya, T. Tanabe, and T. Watanabe, “Ultra-high-Q photonic crystal nanocavities realized by the local width modulation of a line defect,” *Appl. Phys. Lett.* **88**, 041112–3 (2006).
- [81] M. S. Kang, A. Nazarkin, A. Brenn, and P. S. J. Russell, “Tightly trapped acoustic phonons in photonic crystal fibres as highly nonlinear artificial Raman oscillators,” *Nat Phys* **5**, 276–280 (2009).
- [82] P. Dainese, P. S. J. Russell, G. S. Wiederhecker, N. Joly, H. L. Fragnito, V. Laude, and A. Khelif, “Raman-like light scattering from acoustic phonons in photonic crystal fiber,” *Opt. Express* **14**, 4141–4150 (2006).
- [83] R. W. Boyd, *Nonlinear Optics, 3ed* (Academic Press, 2008).
- [84] M. Eichenfield, R. Camacho, J. Chan, K. J. Vahala, and O. Painter, “A picogram- and nanometre-scale photonic-crystal optomechanical cavity,” *Nature* **459**, 550–555 (2009).
- [85] G. H. Wannier, “Dynamics of Band Electrons in Electric and Magnetic Fields,” *Rev. Mod. Phys.* **34**, 645–655 (1962).
- [86] M. Charbonneau-Lefort, E. Istrate, M. Allard, J. Poon, and E. Sargent, “Photonic crystal heterostructures: Waveguiding phenomena and methods of solution in an envelope function picture,” *Phys. Rev. B* **65**, – (2002).
- [87] E. Istrate, M. Charbonneau-Lefort, and E. Sargent, “Theory of photonic crystal heterostructures,” *Phys. Rev. B* **66**, – (2002).
- [88] O. Painter, K. Srinivasan, and P. E. Barclay, “Wannier-like equation for the resonant cavity modes of locally perturbed photonic crystals,” *Phys. Rev. B* **68**, 035214– (2003).
- [89] Y. Levin, “Internal thermal noise in the LIGO test masses: A direct approach,” *Phys. Rev. D* **57**, 659 (1998).
- [90] V. B. Braginsky, M. L. Gorodetsky, and S. P. Vyatchanin, “Thermodynamical fluctuations and photo-thermal shot noise in gravitational wave antennae,” *Phys. Lett. A* **264**, 1–10 (1999).
- [91] Y. T. Liu and K. S. Thorne, “Thermoelastic noise and homogeneous thermal noise in finite sized gravitational-wave test masses,” *Phys. Rev. D* **62**, 122002 (2000).
- [92] M. L. Gorodetsky and I. S. Grudin, “Fundamental thermal fluctuations in microspheres,” *J. Opt. Soc. Am. B* **21**, 697–705 (2004).

- [93] A. Schliesser, G. Anetsberger, R. Rivière, O. Arcizet, and T. J. Kippenberg, “High-sensitivity monitoring of micromechanical vibration using optical whispering gallery mode resonators,” *New J. Phys.* **10**, 095015 (2008).
- [94] J. Komma, C. Schwarz, G. Hofmann, D. Heinert, and R. Nawrodt, “Thermo-optic coefficient of silicon at 1550 nm and cryogenic temperatures,” *Appl. Phys. Lett.* **101**, 041905 (2012).
- [95] A. Di Falco, L. OFaolain, and T. Krauss, “Dispersion control and slow light in slotted photonic crystal waveguides,” *App. Phys. Lett.* **92**, 083501–083501–3 (2008).
- [96] J. Gao, J. McMillan, M. Wu, J. Zheng, S. Assefa, and C. Wong, “Demonstration of an air-slot mode-gap confined photonic crystal slab nanocavity with ultrasmall mode volumes,” *App. Phys. Lett.* **96**, 051123–051123–3 (2010).
- [97] A. Di Falco, L. OFaolain, and T. Krauss, “Chemical sensing in slotted photonic crystal heterostructure cavities,” *App. Phys. Lett.* **94**, 063503–063503–3 (2009).
- [98] M. Borselli, T. J. Johnson, and O. Painter, “Measuring the role of surface chemistry in silicon microphotonic,” *App. Phys. Lett.* **88**, 131114 (2006).
- [99] C. P. Michael, M. Borselli, T. J. Johnson, C. Chrystal, and O. Painter, “An optical fiber-taper probe for wafer-scale microphotonic device characterization,” *Opt. Express* **15**, 4745–4752 (2007).
- [100] T. J. Kippenberg and K. J. Vahala, “Cavity Optomechanics: Back-Action at the Mesoscale,” *Science* **321**, 1172–1176 (2008).
- [101] M. Eichenfield, J. Chan, R. Camacho, K. Vahala, and O. Painter, “Optomechanical crystals,” *Nature* **462**, 78–82 (2009).
- [102] I. Favero and K. Karrai, “Optomechanics of deformable optical cavities,” (2009).
- [103] V. Braginsky and A. Manukin, *Measurement of weak forces in Physics experiments* (Univ. of Chicago Press, 1977).
- [104] S. Gröblacher, K. Hammerer, M. R. Vanner, and M. Aspelmeyer, “Observation of strong coupling between a micromechanical resonator and an optical cavity field,” *Nature* **460**, 724–727 (2009).
- [105] L. V. Hau, S. E. Harris, Z. Dutton, and C. H. Behroozi, “Light speed reduction to 17 metres per second in an ultracold atomic gas,” *Nature* **397**, 594–598 (1999).
- [106] M. Fleischhauer, A. Imamoglu, and J. P. Marangos, “Electromagnetically induced transparency: Optics in coherent media,” *Rev. Mod. Phys.* **77**, 633 (2005).

- [107] H. Kimble, “The quantum internet,” *Nature* **453**, 1023–1030 (2008).
- [108] D. E. Chang, C. A. Regal, S. B. Papp, D. J. Wilson, J. Ye, O. Painter, H. J. Kimble, and P. Zoller, “Cavity opto-mechanics using an optically levitated nanosphere,” *PNAS* **107**, 1005–1010 (2010).
- [109] U. Schnorrberger, J. Thompson, S. Trotzky, R. Pugatch, N. Davidson, S. Kuhr, and I. Bloch, “Electromagnetically induced transparency and light storage in an atomic mott insulator,” *Phys. Rev. Lett.* **103**, 033003 (2009).
- [110] B. Wu, J. F. Hulbert, E. J. Lunt, K. Hurd, A. R. Hawkins, and H. Schmidt, “Slow light on a chip via atomic quantum state control,” *Nature Photonics* **4**, 776–779 (2010).
- [111] C. Santori, P. Tamarat, P. Neumann, J. Wrachtrup, D. Fattal, R. G. Beausoleil, J. Rabeau, P. Olivero, A. D. Greentree, and S. Praver, “Coherent population trapping of single spins in diamond under optical excitation,” *Phys. Rev. Lett.* **97**, 247401 (2006).
- [112] L. Thevenaz, “Slow and fast light in optical fibres,” *Nature Photonics* **2**, 474–481 (2008).
- [113] M. S. Bigelow, N. N. Lepeshkin, and R. W. Boyd, “Superluminal and slow light propagation in a room-temperature solid,” *Science* **301**, 200–202 (2003).
- [114] M. Afzelius, C. Simon, H. de Riedmatten, and N. Gisin, “Multimode quantum memory based on atomic frequency combs,” *Phys. Rev. A* **79**, 052329 (2009).
- [115] H. De Riedmatten, M. Afzelius, M. U. Staudt, C. Simon, and N. Gisin, “A solid-state light-matter interface at the single-photon level,” *Nature* **456**, 773–777 (2008).
- [116] M. F. Yanik and S. Fan, “Stopping light all optically,” *Phys. Rev. Lett.* **92**, 083901 (2004).
- [117] Q. Xu, S. Sandhu, M. L. Povinelli, J. Shakya, S. Fan, and M. Lipson, “Experimental realization of an on-chip all-optical analogue to electromagnetically induced transparency,” *Phys. Rev. Lett.* **96**, 123901 (2006).
- [118] M. Li, W. H. P. Pernice, C. Xiong, T. Baehr-Jones, M. Hochberg, and H. X. Tang, “Harnessing optical forces in integrated photonic circuits,” *Nature* **456**, 480–484 (2008).
- [119] M. Notomi, E. Kuramochi, and T. Tanabe, “Large-scale arrays of ultrahigh-Q coupled nanocavities,” *Nature photonics* **2**, 741–747 (2008).
- [120] A. Lezama, S. Barreiro, and A. Akulshin, “Electromagnetically induced absorption,” *Phys. Rev. A* **59**, 4732 (1999).
- [121] C.-C. Nguyen, “MEMS technology for timing and frequency control,” *Ultrasonics, Ferroelectrics and Frequency Control, IEEE Transactions on* **54**, 251–270 (2007).

- [122] K. M. Lakin, G. R. Kline, and K. T. McCarron, “Development of miniature filters for wireless applications,” *Microwave Theory and Techniques, IEEE Transactions on* **43**, 2933–2939 (1995).
- [123] R. W. Boyd and D. J. Gauthier, “Controlling the velocity of light pulses,” *Science* **326**, 1074–1077 (2009).
- [124] K. Stannigel, P. Rabl, A. S. Sørensen, P. Zoller, and M. D. Lukin, “Optomechanical Transducers for Long-Distance Quantum Communication,” *Phys. Rev. Lett.* **105**, 220501 (2010).
- [125] F. Diedrich, J. C. Bergquist, W. M. Itano, and D. J. Wineland, “Laser Cooling to the Zero-Point Energy of Motion,” *Phys. Rev. Lett.* **62**, 403– (1989).
- [126] P. S. Jessen, C. Gerz, P. D. Lett, W. D. Phillips, S. L. Rolston, R. J. C. Spreeuw, and C. I. Westbrook, “Observation of quantized motion of Rb atoms in an optical field,” *Phys. Rev. Lett.* **69**, 49–52 (1992).
- [127] C. Monroe, D. M. Meekhof, B. E. King, S. R. Jefferts, W. M. Itano, D. J. Wineland, and P. Gould, “Resolved-Sideband Raman Cooling of a Bound Atom to the 3D Zero-Point Energy,” *Phys. Rev. Lett.* **75**, 4011–4014 (1995).
- [128] C. A. Blockley, D. F. Walls, and H. Risken, “Quantum Collapses and Revivals in a Quantized Trap,” *EPL (Europhysics Letters)* **17**, 509 (1992).
- [129] J. I. Cirac and P. Zoller, “Quantum Computations with Cold Trapped Ions,” *Phys. Rev. Lett.* **74**, 4091– (1995).
- [130] A. Steane, “The ion trap quantum information processor,” *Applied Physics B: Lasers and Optics* **64**, 623–643 (1997), 10.1007/s003400050225.
- [131] J. D. Teufel, T. Donner, D. Li, J. H. Harlow, M. S. Allman, K. Cicak, A. J. Sirois, J. D. Whittaker, K. W. Lehnert, and R. W. Simmonds, “Sideband Cooling Micromechanical Motion to the Quantum Ground State,” *arXiv:1103.2144* (2011).
- [132] E. Verhagen, S. Deleglise, S. Weis, A. Schliesser, and T. J. Kippenberg, “Quantum-coherent coupling of a mechanical oscillator to an optical cavity mode,” *Nature* **482**, 63–67 (2012).
- [133] C. M. Caves, K. S. Thorne, R. W. P. Drever, V. D. Sandberg, and M. Zimmermann, “On the measurement of a weak classical force coupled to a quantum-mechanical oscillator. I. Issues of principle,” *Rev. Mod. Phys.* **52**, 341–392 (1980).
- [134] C. A. Regal, J. D. Teufel, and K. W. Lehnert, “Measuring nanomechanical motion with a microwave cavity interferometer,” *Nature Phys.* **4**, 555–560 (2008).

- [135] D. W. C. Brooks, T. Botter, S. Schreppler, T. P. Purdy, N. Brahms, and D. M. Stamper-Kurn, “Non-classical light generated by quantum-noise-driven cavity optomechanics,” *Nature* **488**, 476–480 (2012).
- [136] M. Wallquist, K. Hammerer, P. Rabl, M. Lukin, and P. Zoller, “Hybrid quantum devices and quantum engineering,” *Physica Scripta* **2009**, 014001 (2009).
- [137] S. Camerer, M. Korppi, A. Jckel, D. Hunger, T. W. Hensch, and P. Treutlein, “Realization of an optomechanical interface between ultracold atoms and a membrane,” *arXiv:1107.3650* (2011).
- [138] V. Braginsky and F. Khalili, *Quantum Measurements* (Cambridge University Press, 1995).
- [139] C. M. Caves, “Quantum-mechanical noise in an interferometer,” *Phys. Rev. D* **23**, 1693–1708 (1981).
- [140] S. Mancini and P. Tombesi, “Quantum noise reduction by radiation pressure,” *Phys. Rev. A* **49**, 4055–4065 (1994).
- [141] H. P. Yuen, “Two-photon coherent states of the radiation field,” *Phys. Rev. A* **13**, 2226–2243 (1976).
- [142] J. N. Hollenhorst, “Quantum limits on resonant-mass gravitational-radiation detectors,” *Phys. Rev. D* **19**, 1669–1679 (1979).
- [143] D. F. Walls, “Squeezed states of light,” *Nature* **306**, 141–146 (1983).
- [144] R. E. Slusher, L. W. Hollberg, B. Yurke, J. C. Mertz, and J. F. Valley, “Observation of Squeezed States Generated by Four-Wave Mixing in an Optical Cavity,” *Phys. Rev. Lett.* **55**, 2409–2412 (1985).
- [145] R. M. Shelby, M. D. Levenson, S. H. Perlmutter, R. G. DeVoe, and D. F. Walls, “Broad-Band Parametric Deamplification of Quantum Noise in an Optical Fiber,” *Phys. Rev. Lett.* **57**, 691–694 (1986).
- [146] L.-A. Wu, H. J. Kimble, J. L. Hall, and H. Wu, “Generation of Squeezed States by Parametric Down Conversion,” *Phys. Rev. Lett.* **57**, 2520–2523 (1986).
- [147] P. Grangier, R. E. Slusher, B. Yurke, and A. LaPorta, “Squeezed-Light-Enhanced Polarization Interferometer,” *Phys. Rev. Lett.* **59**, 2153–2156 (1987).
- [148] M. Mehmet, S. Ast, T. Eberle, S. Steinlechner, H. Vahlbruch, and R. Schnabel, “Squeezed light at 1550 nm with a quantum noise reduction of 12.3 dB,” *Opt. Express* **19**, 25763–25772 (2011).

- [149] M. Xiao, L.-A. Wu, and H. J. Kimble, “Precision measurement beyond the shot-noise limit,” *Phys. Rev. Lett.* **59**, 278–281 (1987).
- [150] The LIGO Scientific Collaboration, “A gravitational wave observatory operating beyond the quantum shot-noise limit,” *Nature Phys.* **7**, 962–965 (2011).
- [151] M. A. Taylor, J. Janousek, V. Daria, J. Knittel, B. Hage, H.-A. Bachor, and W. P. Bowen, “Biological measurement beyond the quantum limit,” *Nature Photon. (Advanced Online Publication)* (2013).
- [152] U. B. Hoff, G. I. Harris, L. S. Madsen, H. Kerdoncuff, M. Lassen, B. M. Nielsen, W. P. Bowen, and U. L. Andersen, “Quantum-enhanced micro-mechanical displacement sensitivity,” *arXiv:1302.0867* (2013).
- [153] C. M. Caves, “Quantum-Mechanical Radiation-Pressure Fluctuations in an Interferometer,” *Phys. Rev. Lett.* **45**, 75–79 (1980).
- [154] B. Abbott et al., “Observation of a kilogram-scale oscillator near its quantum ground state,” *New J. Phys.* **11**, 073032 (2009).
- [155] S. Gigan, H. R. Böhm, M. Paternostro, F. Blaser, G. Langer, J. B. Hertzberg, K. C. Schwab, D. Bäuerle, M. Aspelmeyer, and A. Zeilinger, “Self-cooling of a micromirror by radiation pressure,” *Nature* **444**, 67–70 (2006).
- [156] O. Arcizet, P.-F. Cohadon, T. Briant, M. Pinard, and A. Heidmann, “Radiation-pressure cooling and optomechanical instability of a micromirror,” *Nature* **444**, 71–74 (2006).
- [157] T. Corbitt, Y. B. Chen, F. Khalili, D. Ottaway, S. Vyatchanin, S. Whitcomb, and N. Mavalvala, “Squeezed-state source using radiation-pressure-induced rigidity,” *Physical Review A* **73**, 023801 (2006).
- [158] K. W. Murch, K. L. Moore, S. Gupta, and D. M. Stamper-Kurn, “Observation of quantum-measurement backaction with an ultracold atomic gas,” *Nature Phys.* **4**, 561–564 (2008).
- [159] C. Dong, V. Fiore, M. C. Kuzyk, and H. Wang, “Optomechanical Dark Mode,” *Science* **338**, 1609–1613 (2012).
- [160] B. Abdo, K. Sliwa, F. Schackert, N. Bergeal, M. Hatridge, L. Frunzio, A. D. Stone, and M. Devoret, “Full Coherent Frequency Conversion between Two Propagating Microwave Modes,” *Phys. Rev. Lett.* **110**, 173902– (2013).
- [161] Y.-D. Wang and A. A. Clerk, “Using Interference for High Fidelity Quantum State Transfer in Optomechanics,” *Phys. Rev. Lett.* **108**, 153603– (2012).

- [162] G. P. Agrawal, *Fiber-Optic Communication Systems, 3ed* (Wiley-Interscience, 2002).
- [163] L.-M. Duan, M. D. Lukin, J. I. Cirac, and P. Zoller, “Long-distance quantum communication with atomic ensembles and linear optics,” *Nature* **414**, 413–418 (2001).
- [164] B.-S. Song, T. Asano, Y. Akahane, Y. Tanaka, and S. Noda, “Multichannel Add/Drop Filter Based on In-Plane Hetero Photonic Crystals,” *J. Lightwave Technol.* **23**, 1449– (2005).
- [165] H. P. Yuen and V. W. S. Chan, “Noise in homodyne and heterodyne detection,” *Opt. Lett.* **8**, 177–179 (1983).
- [166] B. L. Schumaker, “Noise in homodyne detection,” *Opt. Lett.* **9**, 189–191 (1984).
- [167] J. H. Shapiro, “Quantum noise and excess noise in optical homodyne and heterodyne receivers,” *IEEE J. Quantum Elect.* **21**, 237–250 (1985).
- [168] L. Ding, C. Baker, P. Senellart, A. Lemaitre, S. Ducci, G. Leo, and I. Favero, “High Frequency GaAs Nano-Optomechanical Disk Resonator,” *Phys. Rev. Lett.* **105**, 263903– (2010).
- [169] E. Gavartin, R. Braive, I. Sagnes, O. Arcizet, A. Beveratos, T. J. Kippenberg, and I. Robert-Philip, “Optomechanical Coupling in a Two-Dimensional Photonic Crystal Defect Cavity,” *Phys. Rev. Lett.* **106**, 203902– (2011).
- [170] K. Srinivasan, H. Miao, M. T. Rakher, M. Davanco, and V. Aksyuk, “Optomechanical Transduction of an Integrated Silicon Cantilever Probe Using a Microdisk Resonator,” *Nano Lett.* **11**, 791–797 (2011).